REPORT DOCUMENTATION PAGE

Public reporting burden for this collection of information is estimated to average 1 hour per response, including the time for reviewing instructions, searching existing data sources, gathering and maintaining the data needed, and completing and reviewing this collection of information. Send comments regarding this burden estimate or any other aspect of this collection of information, including suggestions for reducing this burden to Department of Defense, Washington Headquarters Services, Directorate for Information Operations and Reports (0704-0188), 1215 Jefferson Davis Highway, Suite 1204, Arlington, VA 22202-4302. Respondents should be aware that notwithstanding any other provision of law, no person shall be subject to any penalty for failing to comply with a collection of information if it does not display a currently valid OMB control number. **PLEASE DO NOT RETURN YOUR FORM TO THE ABOVE ADDRESS.**

1. REPORT DATE (DD-MM-YYYY)	2. REPORT TYPE	3. DATES COVERED (From - To)
14-01-2004	Thesis	

4. TITLE AND SUBTITLE	5a. CONTRACT NUMBER
Computational Scattering Models for Elastic and Electromagnetic Waves in Particulate Media	5b. GRANT NUMBER
	5c. PROGRAM ELEMENT NUMBER

6. AUTHOR(S)	5d. PROJECT NUMBER
Timothy Edwin Doyle (Utah State University)	5e. TASK NUMBER
	5f. WORK UNIT NUMBER

7. PERFORMING ORGANIZATION NAME(S) AND ADDRESS(ES)	8. PERFORMING ORGANIZATION REPORT NUMBER
ATK Thiokol Propulsion P.O. Box 707, M/S 200 Brigham City UT 84302-0707	

9. SPONSORING / MONITORING AGENCY NAME(S) AND ADDRESS(ES)	10. SPONSOR/MONITOR'S ACRONYM(S)
ATK Thiokol Propulsion P.O. Box 707, M/S 200 Brigham City UT 84302-0707	11. SPONSOR/MONITOR'S NUMBER(S)

12. DISTRIBUTION / AVAILABILITY STATEMENT

Approved for public release; distribution unlimited.

13. SUPPLEMENTARY NOTES

A dissertation submitted in partial fulfillment of the requirements for the degree of Doctor of Philosophy in Physics at Utah State University. AFRL/PR-West reviewed and assigned tracking number AFRL-PR-ED-TP-2004-008.

14. ABSTRACT

20040225 098

15. SUBJECT TERMS

16. SECURITY CLASSIFICATION OF:			17. LIMITATION OF ABSTRACT	18. NUMBER OF PAGES	19a. NAME OF RESPONSIBLE PERSON Leilani Richardson
a. REPORT	b. ABSTRACT	c. THIS PAGE	A	221	19b. TELEPHONE NUMBER (include area code) (661) 275-5015
Unclassified	Unclassified	Unclassified			

COMPUTATIONAL SCATTERING MODELS FOR ELASTIC AND ELECTROMAGNETIC WAVES

IN PARTICULATE MEDIA

by

Timothy Edwin Doyle

A dissertation submitted in partial fulfillment
of the requirements for the degree

of

DOCTOR OF PHILOSOPHY

in

Physics

Approved:

_____
J. R. Dennison
Major Professor

_____
I. Lee Davis
Committee Member

_____
Joseph Koebbe
Committee Member

_____
David Peak
Committee Member

_____
D. Mark Riffe
Committee Member

_____
Thomas Kent
Dean of Graduate Studies

UTAH STATE UNIVERSITY
Logan, Utah

2003

ABSTRACT

Computational Scattering Models for Elastic and Electromagnetic Waves

in Particulate Media

by

Timothy Edwin Doyle, Doctor of Philosophy

Utah State University, 2003

Major Professor: Dr. J. R. Dennison
Department: Physics

Numerical models were developed to simulate the propagation of elastic and electromagnetic

waves in an arbitrary, dense dispersion of spherical particles. The scattering interactions were modeled

with vector multipole fields using pure-orbital vector spherical harmonics, and solved using the full vector

form of the boundary conditions. Multiple scattering was simulated by translating the scattered wave fields

from one particle to another with the use of translational addition theorems, summing the multiple

scattering contributions, and recalculating the scattering in an iterative fashion to a convergent solution.

The addition theorems were rederived in this work using an integral method, and were shown to be

numerically equivalent to previously published theorems. Both ordered and disordered collections of up to

5,000 spherical particles were used to demonstrate the ability of the scattering models to predict the spatial

and frequency distributions of the transmitted waves.

The results of the models show that they are qualitatively correct for many particle configurations

and material properties, displaying predictable phenomena such as refractive focusing, mode conversion,

and photonic band gaps. However, the elastic wave models failed to converge for specific frequency

regions, possibly due to resonance effects. Additionally, comparison of the multiple scattering simulations

with those using only single particle scattering showed that the multiple scattering computations are

quantitatively inaccurate. The inaccuracies arise from nonconvergence of the translational addition

theorems, introducing errors into the translated fields which minimize the multiple scattering contributions

and bias the field amplitudes towards single scattering contributions. The addition theorems are shown to converge very slowly, and to exhibit plateaus in convergence behavior that can lead to false indications of convergence.

The theory and algorithms developed for the models are broad-based, and can accommodate a variety of structures, compositions, and wave modes. The generality of the approach also lends itself to the modeling of static fields and currents. Suggestions are presented for improving and implementing the models, including extension to nonspherical particles, efficiency improvements for the algorithms, and specific applications in a variety of fields.

(203 pages)

ACKNOWLEDGMENTS

My continuing journey through work and education has been enriched by many people. Foremost is my wife, Christine, who has supported, encouraged, and shared my endeavors for the last 20 years. I could not have found a better lifelong companion, friend, and partner.

Throughout my career as a physicist there has been a handful of individuals who have had a continuing and powerful influence on my path. Drs. J.R. Dennison and I. Lee Davis are two such people. Their support, optimism, wisdom, and guidance have profoundly shaped my career, and have been the fertile ground that has allowed my lifelong dream of pursuing important scientific questions to grow, blossom, and bear fruit. I will be always grateful for their generosity, friendship, and valued advice. Most importantly, they have been examples of the type of scientist and person I would like to be.

Drs. Mark Riffe and Joseph Koebbe have contributed many helpful suggestions for my work and graduate education, and their input has been greatly appreciated. My conversations with Dr. David Peak have helped to maintain my enthusiasm over the past five years, and have showed me the breadth and possibilities of applying physics to complex systems beyond the traditional realm of the physicist.

Dr. Jim Wheeler has shown me the beauty and elegance of quantum theory, a view of the towering triumph of 20th century physics (the Standard Model) and a glimpse of the future of physics (string theory and biconformal gauge theory). His generosity with his time and insights have been greatly valued, and I will continue to try to emulate his adventurous yet rigorous approach to physics.

The Physics department at USU continues to be a source of kindness and humanity, and a focal point for my timeline in this universe. Dr. Farrell Edwards has been a continuing source of inspiration and confidence since my first physics course in college 25 years ago. I would also like to thank Jason Kite for his help and friendship during our preparation for the comprehensive exams. Deborah Reece, Karalee Ransom,and Sharon Jensen have supplied invaluable help and information from the department office, and their efforts are much appreciated.

This work would not have been possible without the tremendous understanding, support, and vision from Thiokol. I would like to thank Drs. Lee Pearson and Dennis Fife for their help and encouragement of my educational goals during my employment at Thiokol, and Scott Hyde for his

unflagging support of the scattering model development. I have never worked with better, more thoughtful, or more supportive people. I would also like to extend my appreciation to Dr. Gregory Ruderman of the Air Force Propulsion Directorate for his continuing interest, encouragement, and sponsorship of the work.

Finally, I would like to thank my brother, Thaddeus Doyle, whose untimely death in 1998 made me realize that life is too short to postpone the pursuit of your dreams. The completion of this work and my formal education should be credited in part to this kind and hard-working man. I will continue to miss him.

Timothy Edwin Doyle

CONTENTS

LIST OF TABLES

Table

LIST OF FIGURES

SYMBOLS AND NOTATION

A_{nm}, B_{nm}, C_{nm} — Incoming wavefield coefficients of order n,m for longitudinal, shear-electric, and shear-magnetic elastic waves respectively

D_{nm}, E_{nm}, F_{nm} — Interior wavefield coefficients of order n,m for longitudinal, shear-electric, and shear-magnetic elastic waves respectively

G_{nm}, H_{nm}, I_{nm} — Outgoing wavefield coefficients of order n,m for longitudinal, shear-electric, and shear-magnetic elastic waves respectively

a_{nm}, b_{nm} — Incoming wavefield coefficients of order n,m for electric-type and magnetic-type electromagnetic waves respectively

c_{nm}, d_{nm} — Interior wavefield coefficients of order n,m for electric-type and magnetic-type electromagnetic waves respectively

e_{nm}, f_{nm} — Outgoing wavefield coefficients of order n,m for electric-type and magnetic-type electromagnetic waves respectively

$\mathbf{A}_{nm}(r;L)$, $\mathbf{A}_{nm}(r;E)$, $\mathbf{A}_{nm}(r;M)$ — Longitudinal, electric, and magnetic-type vector multipole functions of order n,m

$\mathbf{L}_{nm}$, $\mathbf{N}_{nm}$, $\mathbf{M}_{nm}$ — Longitudinal, electric, and magnetic-type vector spherical wave functions of order n,m

$\mathbf{U}_{nm}$, $\mathbf{V}_{nm}$, $\mathbf{W}_{nm}$ — Modified longitudinal, electric, and magnetic-type vector multipole functions of order n,m

$\Pi_{\lambda,\nu,\mu}^{l,n,m}(\mathbf{R}_{\alpha\beta})$ — Vector off-center expansion coefficients

$Z_{\nu,\mu}^{n,m}(\mathbf{R}_{\alpha\beta})$ — $j_\nu(ka_\beta)$-normalized scalar off-center expansion coefficients

$Z_{\lambda,\nu,\mu}^{l,n,m}(\mathbf{R}_{\alpha\beta})$ — $j_\lambda(ka_\beta)$-normalized vector off-center expansion coefficients

$C_{a,\alpha,b,\beta}^{c,\gamma}$ — Clebsch-Gordan coefficient

$P_n^m(\cos\theta)$ — Normalized Legendre polynomial of order n,m

$Y_{nm}(\theta,\varphi)$ — Scalar spherical harmonic function of order n,m

$\mathbf{Y}_{nm}^l(\theta,\varphi)$ — Vector spherical harmonic function of order n,m and vector l

$h_n^{(1)}(kr)$	Spherical Hankel function of first kind
$h_n^{(2)}(kr)$	Spherical Hankel function of second kind
$j_n(kr)$	Spherical Bessel function
$y_n(kr)$	Spherical Neumann function
$z_n(kr)$	Generic spherical radial function (either of Bessel, Neumann, or Hankel type)
G_{N0}, H_{N0}, J_{N0} G_{N1}, H_{N1}, J_{N1}	Symbolic substitutions for terms in the electromagnetic boundary condition equations
$T_1(j)$, $T_1(h)$, $T_1(g)$ $T_2(j)$, $T_2(h)$, *etc.*	Symbolic substitutions for terms in the elastic wave boundary condition equations
$\mathbf{u}_L$	Longitudinal displacement vector
$\mathbf{u}_S$	Shear displacement vector
Φ	Scalar potential for longitudinal elastic field
Ψ	Vector potential for shear elastic fields
k_L	Longitudinal wavevector
k_S	Shear wavevector
c_L	Longitudinal wavespeed
c_S	Shear wavespeed
ρ	Density
λ, μ	Lame constants
η	Electromagnetic index of refraction

CHAPTER 1

INTRODUCTION

1.1 Background

A particulate medium is inhomogeneous matter comprised of discrete particles suspended in a matrix. Particulate media are ubiquitous. They comprise a large portion of the earth's crust, and are found in interstellar nebulae, interplanetary plasmas, dust-strewn atmospheres, cloud formations, and ocean seabeds. Biological systems are also particulate in character, consisting of macromolecular suspensions, organelles, cells, and tissues. Humanity has also engineered materials that use particulates to enhance strength (concrete, rubber tires, nanocomposites), provide chemical energy (alkaline batteries, solid rocket propellants), or impart new properties (photonic band gap materials, electrorheological fluids).

The propagation of waves through particle-filled media is an important yet difficult problem which has challenged physicists for over a century. An analysis of the propagation of waves through a particle-filled medium is a study in *scattering*. If the particles are widely dispersed the scattering is dominated by *single particle scattering*, where the waves are scattered only once by a particle. At low particle concentrations, the single-scatterer approximation is usually sufficient to describe the propagation of a wave through a particulate medium and to predict the resultant wave properties.

At high particle concentrations the single-scatterer approximation is no longer valid. As the particles become more closely packed, a larger portion of the waves scatter from one particle to another in a process known as *multiple scattering*. Important problems in understanding wave propagation in particulate media include determining under what conditions single particle scattering is valid, under what conditions multiple scattering must be considered, and determining the extent and effects of multiple scattering.

Multiple scattering is a notorious problem in physics because it is a many-body problem. There are special cases where multiple scattering is exactly solvable, including those involving just a few particles or symmetric geometries such as molecular structures or ordered lattices. However, the multiple scattering problem is not solvable in an exact, closed, analytical form for arbitrary scatterer numbers, properties, and arrangements. Statistical, approximation, or computational methods must therefore be employed to

physically describe how waves propagate through the particulate medium, and to predict the changes in wave properties as a result of the multiple interactions. Many approximate and statistical solutions have been advanced and are successful at predicting the general, overall propagation properties of particulate matter. However, these methods replace the detailed physics of the scattering mechanisms with simplistic mathematical idealizations, and are often not a satisfactory substitute for a complete mechanistic description of the scattering.

To date, wave propagation has been most successfully treated for dilute particle dispersions where multiple scattering is minimized.[1,2] Statistical and approximation methods work quite well for these cases, but typically also require particles of uniform size, uniform properties, and low contrast with respect to the matrix properties. Current statistical and approximation methods fail, however, for moderate-to-high particle concentrations (above 15% for solid particles in a solid matrix) and high frequency (small wavelength) scattering.[1,2]

Another deficiency of current statistical and approximation methods is that they are not sensitive to the details of the microstructure. Such details include particle size distributions, mixed particle types (*i.e.*, particles of different materials), and various degrees of order and disorder in the spatial distribution of the particles.[1] Statistical and approximation methods typically use an effective medium approximation to model the particulate medium. Such approaches are useful for qualitative analysis of the general behavior of the medium, but fall short of a quantitative determination of properties based on the microstructure (*i.e.*, particle sizes, properties, and spatial distributions). Additionally, dense particle dispersions and close random packs have yet to be reasonably treated with an exact, first principles approach.

Computational physics has grown into a major area of research over the last quarter century, complementing both experimental physics and theoretical physics. Computational models allow simulation of many phenomena not approachable with analytic methods, including many-body systems (molecules, polymers, amorphous structures, planetary and stellar systems), continuous systems (atmospheric circulation, material stress states, thermal properties), and complex or chaotic systems (biological structures, neural networks, cellular automata, coupled dynamical systems).

Due to the phenomenal increase in computational speed, capability, and accessibility in the past few decades, computational simulations in condensed matter and materials physics have become powerful and useful alternatives to statistical and approximation methods. Computational models have allowed the numerical solution of problems and simulation of physical systems which were previously unsolvable and beyond analysis. They additionally offer the following advantages:[3]

1. They are ideally suited for many-body problems, providing exact and detailed information on the microscopic processes, and deriving macroscopic properties from these processes in an *ab initio* first-principles manner.

2. They are a more physics-based, mechanistic approach as compared to empirical approaches since they directly calculate the relevant interactions to arrive at the final solution.

3. They are flexible, allowing a wide range of variables and virtual experiments to be tested in the model, thereby increasing our fundamental understanding of the physical behavior of the studied system.

4. They represent virtual instruments, allowing close-up (virtual microscope), distant (virtual telescope), or spectral (virtual spectrometer) views of the studied system.

Development of computational models for multiple scattering in particulate media was therefore the focus of this research. Although such models have been developed in the past, opportunities for improvements in both theory and implementation existed to increase their versatility, accuracy, and usefulness. Additionally, the exponential growth in computer capabilities and increasing access to those capabilities over the past two decades has made the first-principles modeling of wave propagation in extended particulate media inexpensive and practical.

This dissertation presents the development of analytical expressions and numerical algorithms for computation of multiple scattering in particulate media. These computational models are based on a *Vector Multipole Iterative Scattering Technique* (VMIST). The models simulate particle-filled media with mixed, arbitrary particle sizes, particle properties, and packing structures. The particles are modeled as spheres, with vector spherical harmonics used as basis functions for the fundamental excitations of the particles.

These functions are general in character and can be applied to both electromagnetic and elastic waves. The VMIST models compute the propagation of waves through a particulate medium by using single particle scattering solutions to obtain the primary scattered fields. The scattered fields are then translated from one particle to another using *translational addition theorems*. The single particle scattering solutions are then applied again to yield the secondary scattering contributions. This process of scattering-translating-scattering is repeated over and over again via iteration until the scattered field solutions converge to a specified criterium.

1.2 Objectives

The primary objective of this research was to develop *ab initio* computational models to describe how elastic and electromagnetic waves propagate through a particle-filled medium. The models developed were intended to be used as tools for various purposes, and were designed with generality to address the broad-ranging media and applications that can be profitably addressed with this approach. This generality includes the ability to model a three-dimensional system of particles with various sizes, properties, and packing densities. The particles can also be arranged in any arbitrary configuration including periodic, quasicrystalline, and random. The generality also extends to a full range of wavelengths—no long or short wavelength approximations are made.

Important questions that this research was intended to address included the following:

1. Can elastic and electromagnetic waves be modeled using the same mathematical formalisms, solution methods, and program code structure?

2. Does the use of pure-orbital vector spherical harmonics confer an advantage in the development of the multiple scattering theory?

3. How efficient and accurate are the translational addition theorems, and for what spherical particle configurations (radii, distances, and angular orientations)?

4. Are the translational addition theorems fast and accurate enough for media and material simulations containing large numbers of particles (10^3-10^5)?

5. How well do simulations using nearest neighbor and single scatterer approximations compare to multiple scattering simulations?

Scattering models are tools used for a wide variety of purposes in many scientific and engineering disciplines. From a broad perspective, there are three reasons for developing scattering models for particulate media:

1. <u>To discover the interactions of matter with energy as a function of structure.</u>

By determining how waves behave in an arbitrary arrangement of particles, we can discover new phenomena and physics by studying configurations with varying degrees of order-disorder, complexity, anisotropy, and packing density (particle concentration). Currently such studies are limited by the types of experimental samples that can be manufactured and tested, or by the accuracy of approximation or statistical approaches. Computational methods based on first principles are necessary for pushing our knowledge of these physical systems and their interactions with classical fields further.

2. <u>To determine the structure of matter that is remote or inaccessible.</u>

By modeling how waves are altered as they travel through a particle-filled material or medium, we can find out more about the structure and properties of that material or medium. This is the goal in nondestructive evaluation, remote sensing, seismic exploration, astrophysical observations, and medical imaging. The properties we wish to discover include internal variations in elastic or electromagnetic properties, particle size distributions, particle number densities, and microstructure. Knowing such properties allows the discovery of tumors and disease in people, petroleum or gas in rocks, plankton blooms in the ocean, material degradation and aging in particulate composites, precipitation in clouds, and dust particles in deep space.

3. <u>To modify the structure of matter for new materials and tools.</u>

By predicting how waves will behave in a particle-filled material or medium, we can custom design such a material or medium to have useful and unique electromagnetic and acoustic properties. This is the goal in the development of photonic and acoustic band gap materials, radiation-absorbing paints and coatings, advanced or multi-functional particulate composites, nanocomposites, ultrasonic transducers and

contrast agents, nano-dusts (collections of very small sensors or robotic elements), nonlinear optical and laser materials, and new biomaterials. Having the capability to predict how waves interact in a particle-filled medium will allow us to computationally design these new materials and devices based on the complex physical interactions that occur in particle-filled materials.

1.3 Scope

The approach for developing the VMIST computational models involved three steps:

1. Derive the mathematical expressions for single particle scattering from the fundamental field equations

2. Derive and test the equations for translating the scattered fields from one particle to another.

3. Design, build, and test algorithms for computing the multiple scattering.

Both elastic and electromagnetic fields were modeled in this work since they are both vector fields arising from the vector Helmholtz equation. The scattering theories for both types of fields can therefore use the same wave functions, translational addition theorems, and mathematical methods.

Several key areas were focal in developing and improving upon the scattering models. These areas included (1) a review of the vector spherical wave functions used to date for scattering, (2) a reformulation of the single sphere scattering problem using pure-orbital vector spherical harmonics, (3) rigorous solution of the scattered and transmitted field amplitude coefficients using the method of boundary conditions, (4) rederivation of the translational addition theorems using pure-orbital spherical harmonics and an integral approach, (5) numerical testing and comparison of the rederived addition theorems with previously published versions, and (6) coding, testing, and demonstration of the scattering models in Fortran programs. Each of these topics will be presented in the following chapters in the indicated order.

For the purposes of this monograph, a *particulate* medium is defined as a collection of particles of one or more material compositions, dispersed in a medium (the matrix) of different composition, structure, or phase (Figure 1-1, left). The microstructure of such a particulate state is known as a *dispersion* microstructure, and can be differentiated from the *granular* state by the observation that the granular state is characterized by closely-packed particles in contact, but without a substantial matrix affecting the particle

behavior (Figure 1-1, middle). It is the nature of the physical contacts, packing structure, and resultant dynamics that are of interest in granular physics. A particulate medium can also be differentiated from the *polycrystalline* state that is typical of metals, ceramics, and many rocks (Figure 1-1, right). The polycrstalline state is comprised of a mosaic of individual, interlocking grains of various crystalline phase and/or composition. Although this definition for particulate media appears restrictive and limited in application, there exists numerous materials and states of matter that are described well with a dispersion microstructure (see Chapter 7).

The scattering models developed in this work are limited to dispersion-type microstructures consisting of spherical particles embedded in a matrix. They are therefore not applicable to polydomain-type microstructures such as the grain structure in metals, or to granular materials such as sand. The material properties of the particles are assumed to be isotropic, homogeneous, and linear within the particle (although extension of the models to concentrically layered spheres would be straightforward). The material properties of the matrix are also isotropic, homogeneous, and linear.
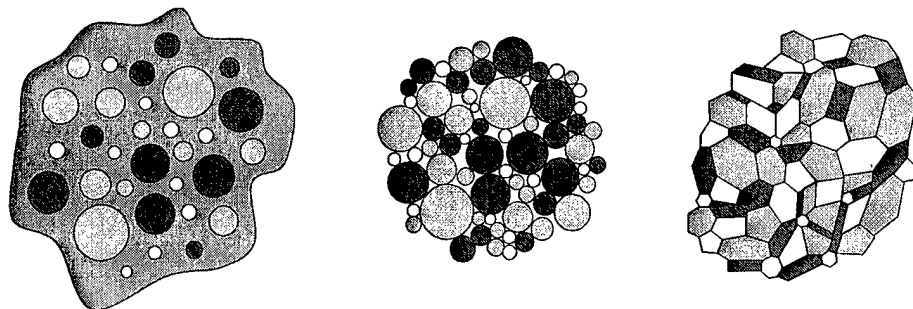
FIGURE 1-1. Illustrations of dispersion (left), granular (middle), and polycrystalline (right) microstructures.

1.4 Originality and Significance of Contribution

The use of multipole translations and iteration to model multiple scattering in many-particle systems is not new, and has been reported by several groups over the past 30 years. Many opportunities exist, however, to improve upon the previously published approaches, to extend the application of the models to more complex material systems or wave propagation modes, and to test the accuracy and convergence of such approaches. Such improvements, applications, and evaluations comprise the original contributions of this work. These contributions include the following:

1. Reformulation of the multiple scattering formalism using pure-orbital vector spherical harmonics and associated vector multipole fields.

2. A comparison of vector multipole functions used for spherical scattering, and introduction of a modification that reconciles the two most widely-used definitions and is congruent with the use of translational addition theorems.

3. A clear and rigorous solution of the boundary conditions for spherical scattering using pure-orbital vector spherical harmonics, showing that solution of the boundary conditions requires application of orthogonality conditions for vector functions as opposed to scalar functions.

4. A new and more straightforward derivation of the translational addition theorems for vector multipole fields based on pure-orbital vector spherical harmonics and an integral method.

5. Two new and numerically equivalent methods for deriving and computing the field translation coefficients, based (1) on direct translation of the fields, and (2) on translation of the potentials and subsequent calculation of the fields using the gradient and curl operators.

6. A numerical comparison of published addition theorems, showing the equivalence of this work's rederived form with the most widely-cited theorems, but showing significant numerical inaccuracies for other recently published theorems. (These tests appear to be the first comparisons of addition theorems in the literature.)

7. Evaluation of the convergence behavior of the addition theorems in a more direct and accurate manner than presented in the literature. The results indicate that other researchers have grossly

underestimated the number of multipole expansion terms (maximum multipole order) required for convergence.

8. Application of the multiple scattering formalism to the scattering of full elastic waves (longitudinal + shear modes) and electromagnetic waves in random particle systems (previous studies were limited to either longitudinal waves or ordered particle systems).

9. Comparison of scattering model results for multiple scattering with those using single particle scattering and nearest neighbor approximations, and preliminary determination of the limits of validity for the multiple scattering models.

10. Quantitative testing of the multiple scattering theory and identification of deficiencies in the approach, with emphasis on convergence and multipole expansion truncation errors.

CHAPTER 2

REVIEW OF PREVIOUS WORK

2.1 Single Sphere Scattering

Although Mie is credited as having solved the problem of electromagnetic scattering by a sphere in 1908 (and hence given immortal status with the universal use of the term "Mie scattering"), other notable scientist made important contributions to the problem prior to 1900, most notably Lorenz and Thompson.[4-6] Debye also published solutions in 1909.[7] Stratton established the modern form of the solution with the use of the vector spherical wave functions **M** and **N**, and later solutions follow this format.[8-14] Logan presents the early history of the electromagnetic solution for the single sphere, with emphasis on the contributions prior to and concurrent with Mie's work.[15,16]

The scattering of elastic waves by a single sphere also had beginnings in the 19th century, starting with Clebsch and Lord Rayleigh.[17,18] These early attempts were only partial solutions, however, in that they were constrained to acoustic (sound) waves in a fluid such as air, which can only support longitudinal waves. Clebsch's work, although forgotten and lost for a century, established the foundations for solving this class of problems in 1863 with the use of separation of variables and boundary conditions.[16] In 1877, Lord Rayleigh (John William Strut) introduced the concepts of spherical surface harmonics S_n and spherical harmonics ψ_n; however, these functions were not of the modern form physicists are now familiar with. He also used normal Bessel functions and Legendre polynomials. The specific problems Lord Rayleigh solved included air vibrations emitted by a vibrating sphere, air vibrations inside a spherical enclosure, air vibrations between concentric spherical shells, and the scattering of plane wave air vibrations from a spherical obstacle.

Progress was slow, however, for the single sphere elastic wave problem. In the mid-20th century Faran extended the scattering work to solid spheres within which both shear and longitudinal waves can exist.[19] Substantial progress was not seen for the single sphere elastic scattering problem until 1956, when Ying and Truell published their benchmark paper.[20] Ying and Truell's paper became the most-cited and well-known work on the scattering of elastic waves by a spherical particle. The article solved the scattering

problem for a sphere within an elastic solid, and treated three cases: scattering by a rigid sphere, an elastic sphere, and a spherical cavity. Their work was based on methods used for the solution of Mie scattering—boundary condition solutions and wave functions based on spherical Bessel functions and Legendre polynomials. Their work also addressed important issues in particle scattering such as mode conversion and the frequency dependence of the scattering. Numerous subsequent papers published up to the 1990's have verified, extended, and generalized this work.[21-34] Other approaches to the single sphere elastic wave scattering problem have included resonance and ray tracing methods.[35-39]

Although the sum of the work on single sphere scattering ranks as a substantial and important contribution to science, much of it is presented with cumbersome notation and definitions. Specifically, there is a widespread reliance on the vector spherical wave functions defined by Stratton (**L**, **M**, and **N** for the longitudinal and two transverse modes of propagation), which are constructed from scalar functions (spherical Bessel, Legendre, and trigonometric functions). Very little work has been found in the literature which solves the single sphere scattering problem with the use of more modern (pure-orbital or pure-spin) vector spherical harmonics. The value of such an approach will be demonstrated in following chapters.

2.2 Mathematical Tools

The vector spherical wave functions presented by Stratton—**L**, **M**, and **N**—have been and are still widely used for both electromagnetic and elastic (acoustic) scattering theories for spherical coordinate systems.[9] These definitions have also been used in such venerable texts as Morse and Feshbach, and Jackson.[40,41] Closely-related functions are those defined by Hill.[42,43]

A more elegant definition for these functions are the vector multipoles presented by Rose in 1957, and used by Greiner and Maruhn.[44,45] Whereas the vector spherical wave functions **L**, **M**, and **N** are defined component-by-component using scalar spherical harmonics (or Legendre functions + sine/cosine functions), the vector multipoles are more simply expressed using vector spherical harmonics. There are several types of vector spherical harmonics, the most useful being the pure-spin and pure-orbital harmonics.[46,47] The pure-orbital vector spherical harmonics were defined by Edmonds in 1957, and are presented in current mathematical physics texts.[48,49]

Greiner and Maruhn present a very good discourse and introduction on vector spherical harmonics and vector multipole fields (longitudinal, electric, and magnetic) in terms of modern vector spherical harmonic notation (pure-orbital harmonics).[45] Thorne presents a very good review of vector spherical harmonics with modern notation (pure-spin and pure-orbital harmonics) and vector multipole fields.[46] Varshalovich et al. is also a very useful reference providing extensive detail on the relationships, properties, and forms of scalar, vector, and tensor spherical harmonics. Varshalovich et al. additionally includes chapters on Clebsch-Gordan coefficients, Wigner-3J coefficients, and other mathematical forms useful in describing spherical functions in classical theory and angular momentum in quantum theory.[47] Arfken and Weber has been updated with fairly good sections on vector spherical harmonics, spherical Bessel functions, and solution of the Helmholtz equation.[49]

The use of both Stratton's vector spherical wave functions ($\mathbf{L}$, $\mathbf{M}$, and $\mathbf{N}$) and Rose's vector multipoles in the literature raises the following questions that are addressed by this dissertation:

1. Which formalism is most useful and concise for both electromagnetic and elastic wave scattering problems?

2. What is the relationship between these two formalisms, and would it be useful to modify one or the other to make them more compatible?

The radial functions in both the vector spherical wave functions and vector multipoles are the spherical Bessel functions. These are defined in numerous texts.[49,50] Abramowitz and Stegun are an indenspensable resource for mathematical formulae, especially recursive relations for calculating spherical Bessel functions.[50] Gillman and Fiebig present a simple computer program that resolves the appearance and growth of large errors (for large n) in the spherical Bessel function $j_n(x)$ by using a downward instead of upward recursion algorithm.[51] This algorithm was found essential in the programming of the VMIST computations.

Translational addition theorems for spherical harmonics are the core mathematical tools for a multipole approach to multiple scattering. Addition theorems for the scalar spherical harmonics were first derived by Friedman and Russek, and were also presented by Rose.[52,53] Stein corrected the scalar addition

theorems of Friedman and Russek, and also introduced addition theorems for the vector spherical wave functions **M** and **N**.[54] Cruzan furthered the development of the vector addition theorems and essentially rederived them (however, still in the cumbersome notation of Stratton's **M** and **N** multipoles) in 1962.[55]

Numerous papers have been published since Cruzan that rederive or reformulate the scalar and vector translational addition theorems.[56-69] However, Cruzan's derivations remain the benchmark and are the most widely used form of the translational addition theorems. Although the scalar addition theorem presented by Cruzan is straightforward, other published versions are not as approachable. The confusion in the literature for the vector addition theorems is even worse. The number and variety of translational addition theorems published over the past 50 years introduces the following problems:

1. Most of the theorems, including Cruzan's, use notation and functions specific only to the paper. This specialized notation makes comparison of the different theorems difficult, and the inability to adhere to standard mathematical usage impedes their interpretation.

2. Much of the notation used in the theorems is unwieldy, cumbersome, unfamiliar, or vague.

3. Many of the theorems use uncommon spherical harmonic definitions and normalizations, or alternate vector spherical harmonic definitions.

4. Many of the theorems differ both in derivation method and mathematical content. Even a cursory examination reveals discrepancies between theorems that can only be interpreted as that some of the published theorems are incorrect.

A review of the literature revealed that the following work was needed to resolve these issues:

1. A new, more straightforward and mathematically rigorous derivation method for the vector addition theorems.

2. Vector addition theorems that exclusively use standard mathematical usage.

3. Vector addition theorems that are applicable to both Stratton's vector spherical wave functions and Rose's vector multipole notation.

4. Verification and comparison testing of the theorems to test their correctness, convergence, and computational efficiency.

Since having correct and compatible translational addition theorems are necessary for constructing a multiple scattering computational model, these tasks were each addressed in this dissertation.

2.3 Two-Sphere and Sphere-Plane Scattering

Liang and Lo were one the first groups to solve the two-sphere problem for electromagnetic scattering using multipole translations.[70] They applied Cruzan's translational addition theorems for vector spherical wave functions, but limited the problem to spheres along the z-axis to simplify the addition theorems. Bruning and Lo generalized the solution to spheres with arbitrary orientation and distance.[71,72] New and Eisler solve the two-sphere problem for acoustic scattering (pressure or longitudinal waves only) using the method of Green's functions and Sack's addition theorems.[73,56] Other two-sphere solution methods have used Green's function in bispherical coordinates, the generalized multipole technique, far-field approximations, dipole approximations, model analysis, and the T-matrix (transfer matrix) approach.[74-79] Other multipole solution methods for the acoustic scattering by two spheres have also been presented.[80,81]

A closely related problem is the scattering by a sphere close to a plane boundary or surface. Gaunaurd and Huang solved this problem for acoustic (longitudinal) scattering using the scalar addition theorem, and applied it to the scattering of sound by air bubbles near the ocean surface.[82,83] A ray-acoustic (analogous to ray-optic) approach has also been applied to near-surface ocean bubbles.[84] Electromagnetic scattering of spherical particles near surfaces have been modeled as well, and an interesting application is the detection of contaminants and defects on electronic materials.[85,86]

2.4 Multiple Scattering with Multipoles

There are many computational methods that use multipole expansions for the multiple scattering of waves from a collection of spheres. In addition to the iterative approach, there are the order-of-scattering, matrix, fast multipole, multiple multipole, and dipole approximation methods. Comberg and Wriedt review the various multipole methods and compare three of them (order-of-scattering, multiple multipole, and dipole approximation methods).[87]

Iterative computation of multiple scattering for electromagnetic waves has been reported by Hamid *et al.*, Mackowski, and de Daran *et al.* using Cruzan's vector addition theorems and Stratton's **N** and **M** wave functions.[88-92] Mackowski rederived the addition theorems and found recursive expressions to simplify their computation.[91] Fuller and Kattawar use the order-of-scattering method, which is also an iterative solution, but one that separates the scattered fields into first reflection, second reflection, *etc.* and sums the scattered field coefficients separately based on this order of reflection.[93,94]

Borghese *et al.* first reported a scalar approach using Debye potentials, but shifted to vector functions and a matrix solution approach in subsequent studies.[95-98] The matrix approach essentially treats the particle-to-particle interactions and their scattered field coefficients as a linear algebra problem. With N spheres and two scattered field components (**N** and **M**) for each sphere, the problem becomes one of solving $2N$ equations with $2N$ unknowns. As expected, solutions for large N are problematic, and Borghese *et al.* limited their models to small (2-4) clusters of spheres. Quinten and Krebig also use a linear solution approach for small (2-5) clusters of spheres.[99] Mackowski also adopts the matrix approach.[100]

It is clear from the number of respective articles published for each method that the matrix approach has been much more thoroughly studied and applied than the iterative approach. The matrix approach sees full implementation in the T-matrix (transfer matrix) method developed by Waterman for both electromagnetic and elastic wave scattering.[101-104] Again, the T-matrix approach uses multipole expansions and translations via addition theorems. However, the T-matrix method is more generalized, and allows arbitrary scattering geometries to be formulated and solved, including layered particles, nonspherical particles, and point scatterers.[105-117] Again, the drawbacks of the T-matrix approach are that the matrices become intractable for large numbers of particles and are often sparse. This makes inversion and solution of the matrices difficult for realistic simulations of a particulate medium. Stout *et al.* address these problems and present a remedy with a recursive T-matrix method.[118]

The most relevant application of the T-matrix approach to the problem addressed by this dissertation (the scattering of elastic and electromagnetic waves in a random particulate media) was recently published by Gumerov and Duraiswami.[119] However, their work only addresses acoustic (sound) waves in air, and therefore only requires the scalar addition theorem to translate the potential of the

longitudinal (compressional) field. A computational solution for full (longitudinal + shear) elastic wave scattering in a random ensemble of spheres was not found after a thorough literature search. Part of the reason for this is that the full elastic wave solution is more complicated than that for either purely compressional sound waves or electromagnetic waves. Elastic waves have three fields to be specified (1 longitudinal + 2 shear), whereas sound waves only have one field (longitudinal) and electromagnetic waves have two (electric + magnetic). Additionally, the longitudinal field is coupled in the solution matrix by the boundary conditions to one of the shear fields. This coupling is minimized in the case of sound scattering (the only shear fields are inside the particle), and absent in electromagnetic scattering.

Another reason for the absence of elastic wave scattering models for particulate media is due to the emphasis on the T-matrix approach in the literature. Solution of the elastic wave scattering problem for large numbers of particles is currently not practical with the T-matrix approach due to the large size and complexity of the matrices ($3N \times 3N$ since there are three external fields for each particle). The iterative approach does not have this limitation, however, and can be advantageously applied to the elastic wave scattering problem (as will be shown in this work).

The limitations of the T-matrix approach have spurred the development of more efficient but less exact multipole computation methods. The fast multipole method (FMM) is one such example.[120-124] The FMM uses a hierarchal approach that first models a small ensemble of particles and computes the scattered fields for the particle-to-particle interactions. The FMM then constructs a second-order ensemble using the small ensemble as the building blocks. The scattered fields from the small ensemble interact with the scattered fields from other small ensembles to yield the scattered fields for the second-order ensemble. Even higher-order ensembles can then be constructed and the computational process continued until the total scattering field is calculated. Note that the FMM is an approximation in that the scattering interactions are approximated by progressively increasing the scale of the scattering volume/entity.

Another approximate multipole method is the multiple multipole method.[125-128] In the multiple multipole method, the scatterers are much smaller than the wavelength. Therefore, multiple scattering is accounted for with simplified, non-orthogonal multipole expansions from various expansion points

distributed throughout the medium. The advantage of the multiple multipole method is that it converges faster than methods which use conventional multipole moments tied to the particles.

There are various other multipole approximation methods. The discrete dipole approximation use the superposition of dipole fields from a large array of dipoles to model the scattered fields from arbitrarily shaped objects and particles.[129] Other methods include indirect mode matching (IMM) of the multipole fields, far-field dipole-dipole coupling approximations, and ray theory.[130-133]

2.5 Non-Multipole Multiple Scattering Methods

2.5 (a) Other Computational Methods

The most popular computation methods in engineering disciplines are the finite element and finite difference methods, so it is not surprising that these have been applied to multiple scattering in particulate media.[134-140] The primary drawback of these methods is the amount of computation required to perform simulations of even modest microstructures. For example, to model a collection of spherical particles in a material, both the spheres and the matrix must first be divided (*discretized*) into polyhedral cells or volume units (the *grid mesh*) that approximate the microstructure. An enormous number of cells are required to model three dimension problems. Even with the problem reduced to two dimensions, the number of cells for a single particle ranges in the hundreds. There are trade-offs involved in selecting a mesh size as well—a finer mesh will provide a higher fidelity solution, but at the cost of an increased computational burden.

To date, most finite methods have been applied to only single particle scattering or to scattering in lattices where the microstructure can be simplified with repeating structural units.[136,137] To retain computational tractability, scattering in random microstructures has been limited to either two-dimensional simulations or the use of a repeating disordered cell containing only a few particles.[134,138-140] A related method, the boundary element method, has been used extensively in ultrasonic scattering, but has yet found utility in the multiple scattering problem.[141]

An interesting and unusual computational method to be applied to multiple scattering in heterogeneous media is the lattice-Boltzmann approach.[142-144] This approach models the particles on a

discrete lattice with both wave and phonon-like interactions, and has been used to simulate seismic wave propagation through rock. The approach greatly simplifies the microphysical interactions, but may be applicable to studying how microfractures, pores, and grain texture in rocks affect macroscopic wave properties such as anisotropy and attenuation.

2.5 (b) Statistical and Approximation Methods

Due to the complexity of the multiple scattering problem, the lack of computational capability, and a desire for elegant, practical solutions, numerous statistical, approximation, and integral methods were devised in the mid-20th century and continue to be developed up to the present.[145-187] Since these methods are not multipole-based simulations but do present competing solutions to the multiple scattering problem, they will be briefly summarized.

Foldy was one of the first to address the problem of the multiple scattering of scalar waves from randomly distributed particles based on a simple statistical approach that averaged over particle configurations using probability distribution functions.[145] Lax obtained an effective field description using a proportionality constant (instead of an iterative equation with successive scattering terms) and a quasi-crystalline approximation (named such since it is only rigorously valid for crystalline particle configurations).[146-147]

Epstein and Carhart calculated the attenuation of acoustic waves in fog due to viscosity and thermal losses as well as scattering losses.[148] The scattering losses, however, were determined from single particle scattering, and no multiple scattering was assumed. Waterman and Truell, and Fikioris and Waterman, also used a configurational averaging approach to obtain the complex propagation constant (wave vector $\kappa(\omega,\rho)$, from which velocity and attenuation can be obtained) for a medium with randomly distributed scatterers.[149,150] Devaney used the self-consistent method of Lax and ensemble averaged over the Green tensor.[151]

Drolen and Tien treated multiple scattering using the form factor technique from X-ray scattering theory. The technique uses a pair distribution function to correlate the relative positions of the particles in the system.[152] Yuen and Dunaway described multiple scattering with a successive approximation procedure, and is valid for very generalized scattering.[153] Sabina and Willis used an embedding scheme

with approximate solutions for the single particle scattering and explicit equations for the multiple scattering which are solved by iteration.[154]

Beltzer presented an effective medium approach for acoustic waves in random composites that used a differential scheme.[156] The method first computes the effective properties for small particles in the matrix, thus generating an first-order effective matrix. Effective properties for particles of larger size embedded in this first-order effective matrix are then computed, yielding a second-order effective matrix. The process is continued until the macroscopic effective properties are acquired.

Some of the other more significant multiple scattering theories include those based on the density-of-states approach,[157-161] variational/quantum mechanical approaches,[162-165] radiative transfer and Dyson equations,[166-171] diffusion approaches,[172-174] path integral approaches,[175-182] and the Lippmann-Schwinger equation.[183-185] The most notable density-of-states approach is by Lloyd and Berry, whose scattering expressions are used frequently for acoustic applications.[160] The radiative transfer/Dyson equation approach is analogous to electromagnetic (optical) radiative transfer theory, but assumes weak material heterogeneity.[166-171]

van Rossum and Nieuwenhuizen developed a multiple scattering description using diffusion theory plus corrections derived from radiative transfer equations for mesoscopic scales.[172] They also discussed the relationship of diffusion-type multiple scattering to weak and Anderson localization. Feynman introduced the path integral approach to quantum mechanics, which has been applied to the multiple scattering of classical waves.[175] Flatté et al. applied the path integral approach to scattering environments where the variations in acoustic properties are smooth and not large, including ocean and seismic scattering.[176,177]

Several researchers use a combination of multiple scattering theories and approaches to refine the approximation. For example, Mishchenko developed a statistical approach to electromagnetic scattering in particulate media by first beginning with the Lippmann-Schwinger equations.[185] He then uses the averaging equations developed by Foldy and Lax, and further applies other approximations such as the far-field approximation. Although such a course may improve upon previous statistical theories and approximations, one wonders how far from physical reality it may take us.

Two very good reviews on multiple scattering theories for ultrasound are found in Povey and

McClements, and Povey.[186,187] Povey and McClements present a wide range of contributed articles on the

theory, applications, and experimental measurements of ultrasound propagation through suspensions and

other heterogeneous systems.[186] The theories focus on effective medium and statistical approaches such as

those by Foldy, Lax, and Lloyd and Berry. Povey also presents a review of the theory, experimental

methods, and applications of ultrasonic propagation specifically through suspensions.[187] The theory is

based on the development and results from Ying and Truell for single particle scattering along with

expressions for multiple scattering from Waterman and Truell, Fikioris and Waterman, and Lloyd and

Berry.

Table 2-1 summarizes the state of the art for some of the more popular scattering models

reviewed, and compares them to the accomplishments and limitations revealed by this work.

TABLE 2-1. State of the art for electromagnetic and elastic wave scattering models, and achievements and limitations of this work.

Model Type	State of the Art 2003	Achievements and Limitations of this Work
Effective medium and integral approaches	Approximations valid for • Dilute particle concentrations • Uniform particle size and type • No viscoelastic or shear properties	
Finite element and difference methods	Computationally intractable without simplified microstructure (repeating cell, *etc.*)	
Multipole approaches	Current results: • Longitudinal waves in dilute disordered media • Longitudinal and shear waves in simple lattices • Electromagnetic waves for modest clusters and particle packings T-matrix, fast multipole, and recursion methods increase computation speed	Electromagnetic and both longitudinal and shear waves modeled for • Dense packings (up to 50%) • Large packings (up to 12,800 particles) • Highly disordered • Variable particle sizes and types Methods are slow due to direct translation of fields and iteration

CHAPTER 3

APPROACH

3.1 First Principles: The Fundamental Equations

3.1 (a) Electromagnetic Waves from Maxwell's Equations

VMIST is a first-principles approach. It is therefore appropriate that we begin with the fundamental equations of physics and develop the theory that underlie the VMIST computations. The fundamental equations for classical electromagnetism are the Maxwell equations. The Maxwell equations for a dielectric medium with no free charges or currents are the following:

$$\nabla \times \mathbf{H} = \frac{1}{c}\frac{\partial \mathbf{D}}{\partial t} \qquad (3.1) \qquad\qquad \nabla \times \mathbf{E} = -\frac{1}{c}\frac{\partial \mathbf{B}}{\partial t} \qquad (3.2)$$

$$\nabla \cdot \mathbf{D} = 0 \qquad (3.3) \qquad\qquad \nabla \cdot \mathbf{B} = 0 \qquad (3.4)$$

These are Maxwell's macroscopic equations, where $\mathbf{D} = \varepsilon \mathbf{E}$ and $\mathbf{H} = \frac{1}{\mu}\mathbf{B}$. Taking the curl of Eqs. 3.1 and 3.2 yields

$$\nabla \times (\nabla \times \mathbf{H}) = \frac{1}{c}\frac{\partial}{\partial t}(\nabla \times \mathbf{D}) \qquad (3.5)$$

$$\nabla \times (\nabla \times \mathbf{E}) = -\frac{1}{c}\frac{\partial}{\partial t}(\nabla \times \mathbf{B}) \qquad (3.6)$$

Substituting Eqs. 3.1 and 3.2 back into Eqs. 3.5 and 3.6, and converting $\mathbf{D}$ to $\mathbf{E}$ and $\mathbf{B}$ to $\mathbf{H}$, gives

$$\nabla \times (\nabla \times \mathbf{H}) = -\frac{\varepsilon\mu}{c^2}\frac{\partial^2 \mathbf{H}}{\partial t^2} \qquad (3.7)$$

$$\nabla \times (\nabla \times \mathbf{E}) = -\frac{\varepsilon\mu}{c^2}\frac{\partial^2 \mathbf{E}}{\partial t^2} \qquad (3.8)$$

Finally, we use the vector identity $\nabla \times (\nabla \times \mathbf{A}) = \nabla(\nabla \cdot \mathbf{A}) - \nabla^2 \mathbf{A}$ and Eqs. 3.3 and 3.4 to arrive at wave equations for the electric and magnetic fields:

$$\nabla^2 \mathbf{H} - \frac{\varepsilon\mu}{c^2}\frac{\partial^2 \mathbf{H}}{\partial t^2} = 0 \qquad (3.9)$$

$$\nabla^2 \mathbf{E} - \frac{\varepsilon\mu}{c^2}\frac{\partial^2 \mathbf{E}}{\partial t^2} = 0 \qquad (3.10)$$

Assuming a purely sinusoidal, steady-state time dependence for the electric and magnetic fields of

the form $\mathbf{E}(\mathbf{x},t) = \mathbf{E}(\mathbf{x})e^{-i\omega t}$, Eqs. 3.9 and 3.10 become the familiar Helmholtz equations:

$$(\nabla^2 + k^2)\mathbf{H} = 0 \qquad (3.11)$$

$$(\nabla^2 + k^2)\mathbf{E} = 0 \qquad (3.12)$$

The wavevector k is defined as $k = \frac{\omega}{c}\sqrt{\varepsilon\mu}$. We can also define an index of refraction η as $\eta = \sqrt{\frac{\varepsilon}{\mu}}$.

Solutions to Eqs. 3.11 and 3.12 traditionally take the form of vector spherical wave functions.

Substituting the time dependence back into the Maxwell equations (Eqs. 3.1 and 3.2) yields conditions

which must be satisfied by the form of the vector spherical wave functions that are used:

$$\nabla \times \mathbf{H} = \frac{-i\omega\varepsilon}{c}\mathbf{E} = -ik\eta\mathbf{E} \qquad (3.13)$$

$$\nabla \times \mathbf{E} = \frac{i\omega\mu}{c}\mathbf{H} = i\frac{k}{\eta}\mathbf{H} \qquad (3.14)$$

3.1 (b) Elastic Waves from the Navier Equation

The fundamental equation for elastic waves is the Navier or elastic wave equation. The elastic

wave equation for linear, homogeneous materials is the following:

$$\rho\frac{\partial^2 \mathbf{u}}{\partial t^2} = (\lambda + 2\mu)\nabla(\nabla \cdot \mathbf{u}) - \mu\nabla \times (\nabla \times \mathbf{u}) \qquad (3.15)$$

The vector $\mathbf{u}$ is the displacement, and can be separated into a longitudinal (dilatational) part, $\mathbf{u}_L$, and a shear

(transverse) part, $\mathbf{u}_S$:

$$\mathbf{u} = \mathbf{u}_L + \mathbf{u}_S \qquad (3.16)$$

These two vectors have the following properties, which allow the elastic wave equation to be separated into two equations:

$$\nabla \times \mathbf{u}_L = 0 \quad (3.17) \qquad\qquad \nabla \cdot \mathbf{u}_S = 0 \quad (3.18)$$

Substituting $\mathbf{u}_L$ and $\mathbf{u}_S$ back into the elastic wave equation (Eq. 3.15) we get

$$\rho \frac{\partial^2 \mathbf{u}_L}{\partial t^2} = (\lambda + 2\mu)\nabla(\nabla \cdot \mathbf{u}_L) - \mu\nabla \times (\nabla \times \mathbf{u}_L) \qquad (3.19)$$

$$\rho \frac{\partial^2 \mathbf{u}_S}{\partial t^2} = (\lambda + 2\mu)\nabla(\nabla \cdot \mathbf{u}_S) - \mu\nabla \times (\nabla \times \mathbf{u}_S) \qquad (3.20)$$

Making use of Eqs. 3.17 and 3.18 yields the following:

$$\rho \frac{\partial^2 \mathbf{u}_L}{\partial t^2} = (\lambda + 2\mu)\nabla(\nabla \cdot \mathbf{u}_L) \qquad (3.21)$$

$$\rho \frac{\partial^2 \mathbf{u}_S}{\partial t^2} = -\mu\nabla \times (\nabla \times \mathbf{u}_S) \qquad (3.22)$$

We again use the vector identity $\nabla \times (\nabla \times \mathbf{A}) = \nabla(\nabla \cdot \mathbf{A}) - \nabla^2 \mathbf{A}$ and the conditions given by Eqs. 3.17 and 3.18 to convert Eqs. 3.21 and 3.22 into solvable differential equations:

$$\rho \frac{\partial^2 \mathbf{u}_L}{\partial t^2} = (\lambda + 2\mu)\nabla^2 \mathbf{u}_L \qquad (3.23)$$

$$\rho \frac{\partial^2 \mathbf{u}_S}{\partial t^2} = \mu\nabla^2 \mathbf{u}_S \qquad (3.24)$$

For time-independent (static) problems, we get Laplace's Equation for the longitudinal field ($\nabla^2 \mathbf{u}_L = 0$) and for the shear field ($\nabla^2 \mathbf{u}_S = 0$). For time-dependent problems we get wave equations for the two vectors. Here, c_L and c_S are the longitudinal and shear wavespeeds, respectively.

$$c_L^2 \nabla^2 \mathbf{u}_L - \frac{\partial^2 \mathbf{u}_L}{\partial t^2} = 0 \quad (3.25) \qquad\qquad c_S^2 \nabla^2 \mathbf{u}_S - \frac{\partial^2 \mathbf{u}_S}{\partial t^2} = 0 \quad (3.26)$$

$$c_L^2 = \frac{\lambda + 2\mu}{\rho} \quad (3.27) \qquad\qquad c_S^2 = \frac{\mu}{\rho} \qquad (3.28)$$

As in the electromagnetic case, we assume a purely sinusoidal, steady-state time dependence for $\mathbf{u}_L$ and $\mathbf{u}_S$ of the $\mathbf{u}(\mathbf{x}, t) = \mathbf{u}(\mathbf{x})e^{-i\omega t}$ form. Eqs. 3.25 and 3.26 then become the familiar Helmholtz equations, where k_L and k_S are the longitudinal and shear wavevectors, respectively.

$$(\nabla^2 + k_L^2)\mathbf{u}_L = 0 \qquad (3.29) \qquad\qquad (\nabla^2 + k_S^2)\mathbf{u}_S = 0 \qquad (3.30)$$

$$k_L^2 = \frac{\omega^2}{c_L^2} \qquad (3.31) \qquad\qquad k_S^2 = \frac{\omega^2}{c_S^2} \qquad (3.32)$$

In contrast to the electromagnetic vector Helmholtz equations, Eqs. 3.29 and 3.30 are usually not solved using vector functions. Rather, the vectors $\mathbf{u}_L$ and $\mathbf{u}_S$ are expressed as a scalar potential Φ and vector potential Ψ:

$$\mathbf{u}_L = \nabla\Phi \qquad (3.33) \qquad\qquad\qquad \mathbf{u}_S = \nabla \times \Psi \qquad (3.34)$$

Waves of the shear displacement field $\mathbf{u}_S$ are transverse waves and are therefore polarized in one direction. This implies that two shear displacement fields can exist perpendicular to and independent of each other. We can therefore define a second shear displacement field from the vector potential Ψ which is perpendicular to the one defined in Eq. 3.34:

$$\mathbf{u}_S = \nabla \times (\nabla \times \Psi) \qquad\qquad\qquad (3.35)$$

These two shear fields are analogous to the electric and magnetic fields since they are transverse and normally perpendicular to one another. In most applications, these two shear fields are denoted as the vertical shear field and horizontal shear field. These names arose from a very important problem in elastic wave scattering—reflection and refraction from a planar boundary, where the shear wave components are either vertical or horizontal to the plane. This distinction is meaningless, however, when considering reflections and refractions from spheres. Due to the analogy with electromagnetism, and the lack of any other designation that would make sense, we will therefore refer to the two shear fields as the shear-electric (SE) field and shear-magnetic (SM) field. These designations will become more meaningful when the vector spherical wave functions are assigned. The electric and SE multipole fields will use the same vector spherical wave function, as will the magnetic and SM multipole fields.

For most acoustic scattering problems, the vector potential Ψ is further reduced to one or two scalar functions using symmetry or other conveniences of the particular problem. Although this simplifies the mathematics to some extent, generality is also lost. Additionally, solution of the boundary conditions requires the potentials to be re-transformed back into the components of the displacements. The boundary condition calculations therefore become unwieldy due to the presence of derivatives and cross-products (gradients and curls) in the solutions.

To solve Eqs. 3.29 and 3.30 using vector functions, we need to express $\mathbf{u}_L$ and $\mathbf{u}_S$ in the appropriate basis. Since our coordinate system is spherical polar, the solutions to the Helmholtz equation are spherical harmonics for the angular part and spherical Bessel functions for the radial part. Vectors $\mathbf{u}_L$ and $\mathbf{u}_S$ will therefore be comprised of a product of spherical Bessel functions and vector spherical harmonics, and are known as vector spherical wave functions. Note that the vector spherical wave functions must also satisfy the conditions in Eqs. 3.17 and 3.18.

Since we have removed the time dependence from the fundamental equations, our solutions will be steady-state solutions. This means that the solutions—the vector spherical wave functions—will intrinsically contain both the amplitude and phase information of the waves (the phase information is usually carried by the kr argument in the spherical Bessel functions). This is an important feature to remember when we start scattering waves from one sphere to another—the wave functions and translation equations will take care of the phase factors, so no extra effort will be required to account for the phase of the waves.

3.2 Spherical Wave Functions for the Vector Helmholtz Equation

A goal in developing the VMIST computational model was to develop scattering theories for both electromagnetic and elastic waves based on a compatible mathematical formalism. This goal required finding a set of spherical wave functions that solved the Helmholtz equations and other conditions for both types of waves, were consistent with the translational addition theorems, were consistent with previous usage, and were not overly complex or elaborate.

The terms "vector spherical harmonic", "vector spherical wave function", and "vector multipole function" have been used interchangeably in the literature, which may give rise to confusion. In this work we will be more precise and reserve the use of the term "vector spherical harmonic" for functions with only an angular dependence, primarily the pure-orbital and pure-spin vector spherical harmonics. "Vector spherical wave functions" are oscillatory functions with both angular and radial dependencies, but are not necessarily constructed from vector spherical harmonics. For example, Stratton constructed the **L**, **M**, and **N** vector spherical wave functions using only Legendre polynomials, sines, and cosines.[9] Finally, "vector multipole functions" will refer to a specific type of vector spherical wave function comprised of vector spherical harmonics as defined above. This usage is consistent with many modern authorities on the subject.[41,45-47,49]

Although the vector spherical wave functions have taken many forms in the literature, there is universal agreement as to the form of the scalar spherical wave functions. The scalar spherical wave functions are simply defined as expansions of the product of a spherical radial function with a spherical harmonic:

$$\Phi = \sum_{n=0}^{\infty} \sum_{m=-n}^{+n} z_n(kr) Y_{nm}(\theta, \varphi) \tag{3.36}$$

The $z_n(kr)$ represents a spherical radial function dependent on the type of waves to be described (a spherical Bessel function $j_n(kr)$ for standing waves, a spherical Hankel function of the first kind $h_n^{(1)}(kr)$ for outward propagating waves, or a spherical Hankel function of the second kind $h_n^{(2)}(kr)$ for inward propagating waves). The spherical harmonic can alternately be replaced with Legendre polynomials for the θ dependence and sine-cosine expansions for the φ dependence. The scalar spherical wave functions are most useful for modeling scalar potentials.

There are two sets of definitions for vector spherical wave function that have been extensively used in the literature and for which translational addition theorems have been derived. The **L**, **N**, and **M** wave functions defined by Stratton are the older of the two sets, but are still in wide use today, especially in the field of optical scattering.[9] (For brevity, these functions will be referred to collectively as **LNM** wave functions.) In spherical polar coordinates these functions are given as

$$\mathbf{L}_{nm} = \frac{\partial}{\partial r} z_n(kr) P_n^m(\cos\theta) \exp(im\varphi)\hat{e}_r$$

$$+ \frac{1}{r} z_n(kr) \frac{\partial P_n^m(\cos\theta)}{\partial\theta} \exp(im\varphi)\hat{e}_\theta \qquad (3.37)$$

$$+ \frac{im}{r\sin\theta} \frac{\partial}{\partial r} z_n(kr) P_n^m(\cos\theta) \exp(im\varphi)\hat{e}_\phi$$

$$\mathbf{N}_{nm} = \frac{n(n+1)}{kr} z_n(kr) P_n^m(\cos\theta) \exp(im\varphi)\hat{e}_r$$

$$+ \frac{1}{kr} \frac{\partial}{\partial r}[rz_n(kr)] \frac{\partial P_n^m(\cos\theta)}{\partial\theta} \exp(im\varphi)\hat{e}_\theta \qquad (3.38)$$

$$+ \frac{im}{kr\sin\theta} \frac{\partial}{\partial r}[rz_n(kr)] P_n^m(\cos\theta) \exp(im\varphi)\hat{e}_\phi$$

$$\mathbf{M}_{nm} = \frac{im}{\sin\theta} z_n(kr) P_n^m(\cos\theta) \exp(im\varphi)\hat{e}_\theta$$

$$- z_n(kr) \frac{\partial P_n^m(\cos\theta)}{\partial\theta} \exp(im\varphi)\hat{e}_\phi \qquad (3.39)$$

For convenience we have replaced the original even and odd function notation—$\cos(m\varphi)$ and $\sin(m\varphi)$—with the more modern exponential notation—$\exp(im\varphi)$. Stratton defined the LNM wave functions as solutions to the vector Helmholtz equation for electromagnetic fields.[9] The electric and magnetic fields are given by a linear combination of the N and M wave functions.

The more modern solutions for the vector Helmholtz equation in spherical coordinates are the vector multipole fields which use pure-orbital vector spherical harmonics. The spherical wave functions defined by the vector multipole fields are the longitudinal, electric, and magnetic multipole fields, respectively:[44,45]

$$\mathbf{A}_{nm}(r;L) = \sqrt{\frac{n}{2n+1}} z_{n-1}(kr) \mathbf{Y}_{nm}^{n-1}(\theta,\varphi) + \sqrt{\frac{n+1}{2n+1}} z_{n+1}(kr) \mathbf{Y}_{nm}^{n+1}(\theta,\varphi) \qquad (3.40)$$

$$\mathbf{A}_{nm}(r;E) = \sqrt{\frac{n+1}{2n+1}} z_{n-1}(kr) \mathbf{Y}_{nm}^{n-1}(\theta,\varphi) - \sqrt{\frac{n}{2n+1}} z_{n+1}(kr) \mathbf{Y}_{nm}^{n+1}(\theta,\varphi) \qquad (3.41)$$

$$\mathbf{A}_{nm}(r;M) = z_n(kr) \mathbf{Y}_{nm}^n(\theta,\varphi) \qquad (3.42)$$

The notation for the multipole fields are from Greiner and Maruhn, and for the vector spherical harmonics from Varshalovich.[45,47] In the literature, these vector spherical harmonics are either equivalent or closely related to the V vector spherical harmonics of Edmonds,[48] the T vector spherical harmonics of Rose,[44] and the X vector spherical harmonics of Jackson.[41] The vector multipole fields are directly related to the electromagnetic vector potential. In terms of the vector multipole fields, the electric and magnetic fields are the following:

$$\mathbf{E}(r) = ik\big[\mathbf{A}(r;E) + \mathbf{A}(r;M)\big] \tag{3.43}$$

$$\mathbf{H}(r) = ik\big[\mathbf{A}(r;E) - \mathbf{A}(r;M)\big] \tag{3.44}$$

By converting the Legendre and exponential functions in the **LNM** wave functions to spherical harmonics, we can find how the **LNM** wave functions are related to the vector multipole fields. We find that the vector multipole fields are related to the **LNM** wave functions by the following normalization constants:

$$\mathbf{A}_{nm}(r;L) = \mathbf{L}_{nm}\frac{1}{k}(-1)^m\sqrt{\frac{2n+1}{4\pi}\frac{(n-m)!}{(n+m)!}} \tag{3.45}$$

$$\mathbf{A}_{nm}(r;E) = \mathbf{N}_{nm}\frac{1}{\sqrt{(n)(n+1)}}(-1)^m\sqrt{\frac{2n+1}{4\pi}\frac{(n-m)!}{(n+m)!}} \tag{3.46}$$

$$\mathbf{A}_{nm}(r;M) = \mathbf{M}_{nm}\frac{i}{\sqrt{(n)(n+1)}}(-1)^m\sqrt{\frac{2n+1}{4\pi}\frac{(n-m)!}{(n+m)!}} \tag{3.47}$$

Note that the normalization constants differ for each of the fields, rising from the differences in definitions between the two formulations. The **LNM** wave functions and vector multipole fields are therefore not the same functions!

Both the **LNM** wave functions and vector multipole fields are suitable for electromagnetic wave functions. The vector multipole formulation is preferred, however, since the vector spherical harmonics are more concise and have useful orthogonality properties, vector differentiation formulas, and integral solutions in the form of Clebsch-Gordan coefficients. Both Stratton's **LNM** wave functions and Rose's vector multipole fields have been used for elastic wave functions as well, but mostly for simple scattering

problems such as that for a single sphere. Consistency problems arise, however, when both sets of formalisms are applied simultaneously to electromagnetic and elastic scattering theory, or when they are combined with translational addition theorems.

The first inconsistency arises from our definition of the shear displacement fields as derived from the Navier equation:

$$\mathbf{u}_{SE} = \frac{1}{k} \nabla \times \mathbf{\Psi} \tag{3.48}$$

$$\mathbf{u}_{SM} = \frac{1}{k^2} \nabla \times \left(\nabla \times \mathbf{\Psi} \right) \tag{3.49}$$

Note the inclusion of the $1/k$ and $1/k^2$ factors to normalize the derivatives of the spherical Bessel functions. To have $\mathbf{u}_{SE}$ and $\mathbf{u}_{SM}$ in vector multipole form, we start from a definition for the vector potential $\mathbf{\Psi}$ that uses a vector spherical harmonic and a form similar to that of the scalar potential Φ (Eq. 3.36):

$$\mathbf{\Psi} = \sum_{n=0}^{\infty} \sum_{m=-n}^{+n} z_n(kr) \mathbf{Y}_{nm}^n(\theta, \varphi) \tag{3.50}$$

This vector potential does not, however, give rise to the standard vector multipole fields when put into the definitions for the shear displacement fields. Although $\mathbf{u}_{SM}$ results in the same magnetic multipole field (Eq. 3.52), $\mathbf{u}_{SE}$ results in a modified form where the $\mathbf{A}_{nm}(r;E)$ is multiplied by an i (Eq. 3.51):

$$\frac{1}{k} \nabla \times \mathbf{\Psi}_{nm} = i \mathbf{A}_{nm}(r;E) \tag{3.51}$$

$$\frac{1}{k^2} \nabla \times \left(\nabla \times \mathbf{\Psi}_{nm} \right) = \mathbf{A}_{nm}(r;M) \tag{3.52}$$

The second inconsistency arises from the translational addition theorems. The translation of the $\mathbf{N}$ and $\mathbf{M}$ vector spherical wave functions from one coordinate system to another is expressed in the following symmetric form:

$$\mathbf{N}_{nm} = \sum_{\nu=0}^{\infty} \sum_{\mu=-\nu}^{\nu} \left(S_{\nu\mu}^{nm} \mathbf{N}'_{\nu\mu} + T_{\nu\mu}^{nm} \mathbf{M}'_{\nu\mu} \right) \tag{3.53}$$

$$\mathbf{M}_{nm} = \sum_{\nu=0}^{\infty} \sum_{\mu=-\nu}^{\nu} \left(S_{\nu\mu}^{nm} \mathbf{M}'_{\nu\mu} + T_{\nu\mu}^{nm} \mathbf{N}'_{\nu\mu} \right) \tag{3.54}$$

The $S_{\nu\mu}^{nm}$ coefficient is a "direct" translation coefficient, expanding field **N** in terms of **N'**, and field **M** in terms of **M'**. The $T_{\nu\mu}^{nm}$ coefficient is an "indirect" translation coefficient, expanding field **N** in terms of **M'**, and field **M** in terms of **N'**. Note that this transformation is symmetric with respect to **N** and **M**. This symmetry is not preserved, however, with the vector multipole definitions of Eqs. 3.40-3.42. For the standard vector multipole field formalism, two independent "indirect" translation coefficients (differing by a factor of i) are required to translate between electric and magnetic multipole fields.

This conclusion has been verified with numerical testing of the translational addition theorems, which has shown that the symmetric form of the theorems is consistent with the definition of the **L**, **N**, and **M** wave functions, but not with the original definition of Rose's vector multipole fields.

To be consistent with definitions for both the electromagnetic fields and shear displacement fields, and to be able to use the translational addition theorems in the simpler symmetric form, we need to modify the definitions for the vector multipoles as follows:

$$\mathbf{U} = \frac{1}{k}\nabla\Phi \tag{3.55}$$

$$\mathbf{V} = \frac{1}{k}\nabla\times\Psi \tag{3.56}$$

$$\mathbf{W} = \frac{1}{k^2}\nabla\times\left(\nabla\times\Psi\right) \tag{3.57}$$

To avoid confusion with the **LNM** wave functions and vector multipoles in Eqs. 3.40-3.42, we shall call these functions **UVW** multipole fields. They are solutions to the Navier equation as well as the Maxwell equations. The electric (**V**) and magnetic (**W**) multipole fields correspond to the SE and SM shear displacement fields in the elastic wave problem, Figure 3-1, whereas the longitudinal multipole field (**U**) naturally corresponds to a dilatational displacement field, Figure 3-2.
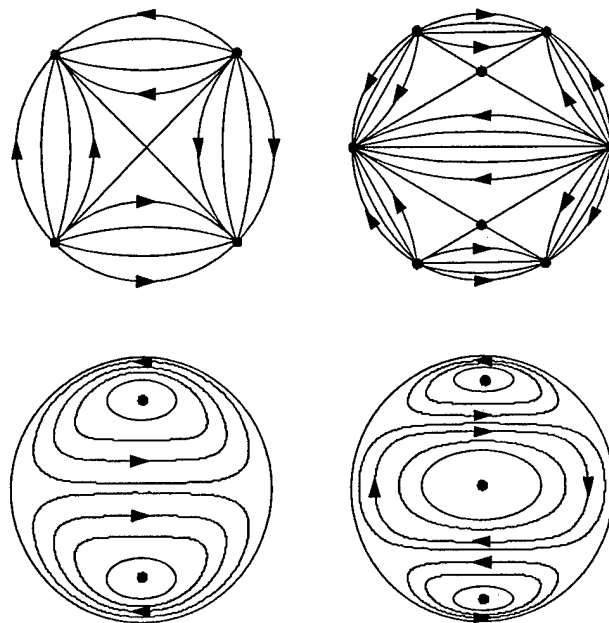
FIGURE 3-1. Electric or **V** multipole fields (top), and magnetic or **W** multipole fields (bottom). Adapted from Mie (1908).[6]
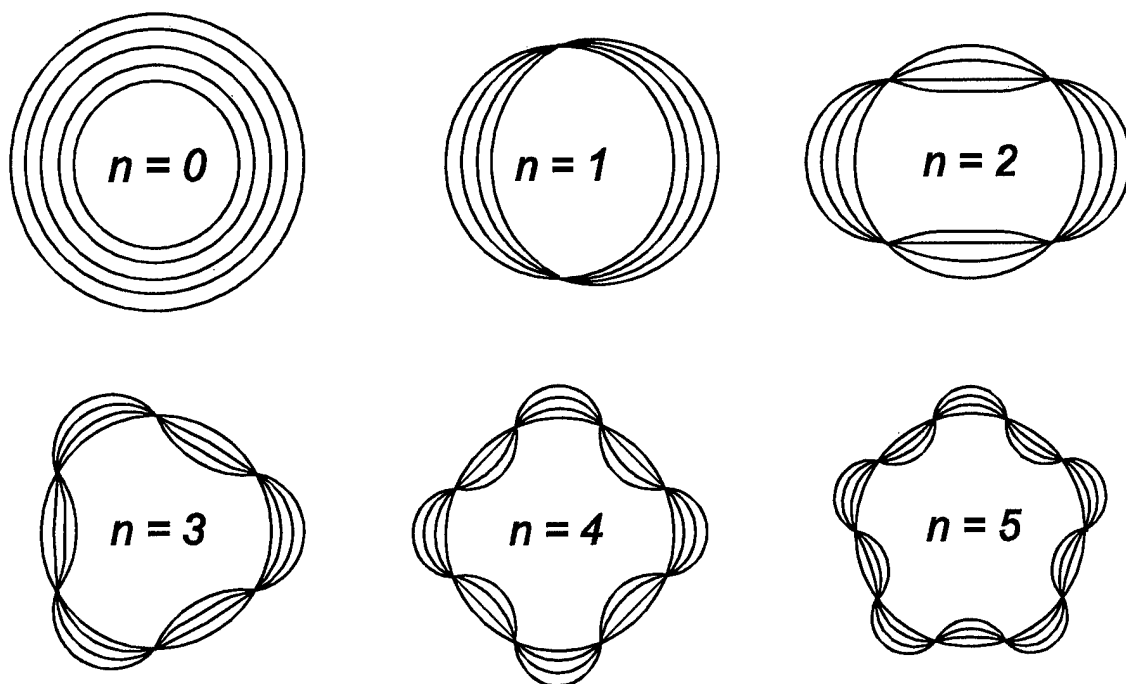
FIGURE 3-2. Longitudinal or **U** multipole fields of order n, shown as deformations of a spherical surface. Adapted from Greiner and Maruhn (1996).[45]

The form of the scalar potential is the same as for the scalar wave function (Eq. 3.36), and the resulting longitudinal **UVW** multipole field is the following:

$$\mathbf{U}_{nm} = \sqrt{\frac{n}{2n+1}} z_{n-1}(kr) Y_{nm}^{n-1}(\theta,\varphi) + \sqrt{\frac{n+1}{2n+1}} z_{n+1}(kr) Y_{nm}^{n+1}(\theta,\varphi) \tag{3.58}$$

The forms for the electric and magnetic (SE and SM) **UVW** multipole fields are the following:

$$\mathbf{V}_{nm} = i\sqrt{\frac{n+1}{2n+1}} z_{n-1}(kr) Y_{nm}^{n-1}(\theta,\varphi) - i\sqrt{\frac{n}{2n+1}} z_{n+1}(kr) Y_{nm}^{n+1}(\theta,\varphi) \tag{3.59}$$

$$\mathbf{W}_{nm} = z_n(kr) Y_{nm}^{n}(\theta,\varphi) \tag{3.60}$$

The **UVW** multipole fields are identical to the vector multipole fields of Rose[44] and Greiner and Maruhn[45] (Eqs. 40-42), except for a factor of i multiplying the electric multipole field:

$$\mathbf{U}_{nm} = \mathbf{A}_{nm}(r;L) \tag{3.61}$$

$$\mathbf{V}_{nm} = i\mathbf{A}_{nm}(r;E) \tag{3.62}$$

$$\mathbf{W}_{nm} = \mathbf{A}_{nm}(r;M) \tag{3.63}$$

We find that the multipole fields **V** and **W** are also essentially the **N** and **M** wave functions, but now with the same normalization constant:

$$\mathbf{V}_{nm} = \mathbf{N}_{nm} \frac{i}{\sqrt{(n)(n+1)}} (-1)^m \sqrt{\frac{2n+1}{4\pi} \frac{(n-m)!}{(n+m)!}} \tag{3.64}$$

$$\mathbf{W}_{nm} = \mathbf{M}_{nm} \frac{i}{\sqrt{(n)(n+1)}} (-1)^m \sqrt{\frac{2n+1}{4\pi} \frac{(n-m)!}{(n+m)!}} \tag{3.65}$$

The **UVW** multipole fields (Eqs. 3.58-3.60) are therefore valid for electromagnetic waves and consistent with the traditional solution approach for the Navier equation. Because of the relative merits of the vector multipole formalism, the modified vector multipole fields are also more attractive as a set of spherical wave functions than the **LNM** wave functions.

Using Eqs. 3.43-3.44 and Eqs. 3.61-3.63, we find that the **UVW** multipole fields are related to the electric and magnetic fields as follows:

$$\mathbf{E}(r) = k\big[\mathbf{V}(r) + i\mathbf{W}(r)\big] \tag{3.66}$$

$$\mathbf{H}(r) = k\big[\mathbf{V}(r) - i\mathbf{W}(r)\big] \tag{3.67}$$

Because the vector multipole fields were modified to be consistent with the definitions for the shear fields, the **UVW** multipole fields are related to the elastic displacement fields in a more direct and simple manner:

$$\mathbf{u}_L(r) = \mathbf{U}(r) \tag{3.68}$$

$$\mathbf{u}_{SE}(r) = \mathbf{V}(r) \tag{3.69}$$

$$\mathbf{u}_{SM}(r) = \mathbf{W}(r) \tag{3.70}$$

Finally, we note that the **UVW** Navier multipole fields as defined in this monograph differ from the **V, W,** and **X** vector spherical wave functions defined by Hill (which are not presented here due to their lack of general use in the physics literature).[43] It is unfortunate that only a limited supply of appropriate symbols exists for naming functions that have a plurality of definitions and usages in the literature. The accidental re-use of some vector field symbols is unavoidable in such a case.

3.3 Boundary Condition Solutions for Single Sphere Scattering

3.3 (a) Solution Method

With the multipole fields **U, V,** and **W** we can now formulate both the electromagnetic and elastic wave fields in spherical coordinates. For scattering from a single sphere, the wave fields can be divided into an incoming (incident) external field, a refracted internal field, and an outgoing (scattered) external field. The forms of the spherical Bessel functions in **U, V,** and **W** for each of these fields are listed in Table 3-1. Each of the wave fields will also have amplitude coefficients associated with them. These amplitude coefficients are designated in Table 3-2 and shown schematically in Figure 3-3 for elastic waves.

TABLE 3-1. Spherical Bessel functions for wave fields in the single sphere scattering problem.

Region and Wave Type	Spherical Bessel Function
Exterior to sphere; Incident	$h_n^{(2)}(k_{ext}r)$
Interior to sphere; Refracted	$j_n(k_{int}r)$
Exterior to sphere; Scattered	$h_n^{(1)}(k_{ext}r)$

TABLE 3-2. Amplitude coefficients for wave fields in the single sphere scattering problem.

	Incident Field	Refracted Field	Scattered Field
Elastic Waves			
Longitudinal ($\mathbf{u}_L$)	A_{nm}	D_{nm}	G_{nm}
Shear-electric ($\mathbf{u}_{SE}$)	B_{nm}	E_{nm}	H_{nm}
Shear-magnetic ($\mathbf{u}_{SM}$)	C_{nm}	F_{nm}	I_{nm}
Electromagnetic Waves			
Electric multipole (**V**)	a_{nm}	c_{nm}	e_{nm}
Magnetic multipole (**W**)	b_{nm}	d_{nm}	f_{nm}
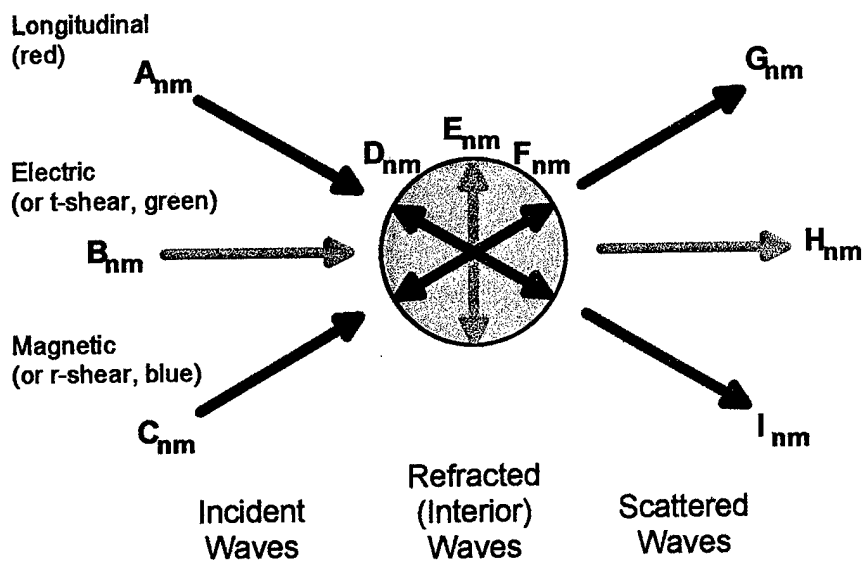
FIGURE 3-3. Diagram of incident, refracted, and scattered elastic waves for single particle scattering, with associated amplitude coefficients.

Given the incident field, the amplitude coefficients of the refracted and scattered fields can be solved by solving the boundary conditions on the surface of the sphere. For electromagnetic waves, the boundary conditions are continuity of the tangential components of **E** and **H**. For elastic waves, the boundary conditions are continuity of the displacements and stresses. The general form of the boundary conditions is therefore

$$\mathbf{F}^{incident} + \mathbf{F}^{scattered} = \mathbf{F}^{refracted} \tag{3.71}$$

where **F** is a general vector multipole field.

These boundary conditions are typically presented in the literature as scalar equations and the solutions given without the intermediate steps. This is misleading, however, since rigorous solution of the boundary condition equations requires that they are solved in <u>vector</u> form. Although this point is not often addressed in the literature, it is important since vague, inexact, and incorrect statements and derivations have been published.[13,23,24]

Mie scattering will be used as an example, although the arguments apply to elastic wave scattering as well. Although the Mie solutions are well-established and unquestionable due to their correctness, the mathematical procedure for arriving at the solutions from the boundary conditions has often been either obscurely or incorrectly published. The widespread use of the **LNM** wave functions has additionally created confusion due to their cumbersome form and orthogonality relationships, and the confusion remains when spherical harmonic functions are also used to solve the Mie scattering problem.

The problem arises over the use of orthogonality to solve the boundary condition equations for spherically-symmetric scattering problems. A simplified version of the mathematics is presented in order to get to the core of the problem. Rendered into scalar components, the boundary condition equations are of the form

$$F_x^{incident} + F_x^{scattered} = F_x^{refracted} \tag{3.72}$$

where F_x denotes the x-th scalar component of the field. The incident, scattered, and refracted (interior) fields are comprised of multipole expansions of spherical wave functions:

$$F_x = \sum_{n=0}^{\infty} \sum_{m=-\infty}^{+\infty} A_{nm} z_n(kr) Y_{nm}(\theta, \varphi) \tag{3.73}$$

Here, A_{nm} is the amplitude coefficient and $z_n(kr)$ represents a spherical Bessel or Hankel function appropriate to whether the wave is traveling toward, away from, or inside the sphere (see Table 3-1). An example of such boundary conditions include the tangential components of the electric and magnetic fields in Mie scattering, here broken down into scalar components as presented in the literature:

$$E_\theta^{incident} + E_\theta^{scattered} = E_\theta^{refracted} \tag{3.74}$$

$$E_\varphi^{incident} + E_\varphi^{scattered} = E_\varphi^{refracted} \tag{3.75}$$

$$H_\theta^{incident} + H_\theta^{scattered} = H_\theta^{refracted} \tag{3.76}$$

$$H_\varphi^{incident} + H_\varphi^{scattered} = H_\varphi^{refracted} \tag{3.77}$$

There is no problem and the solutions are straightforward if all of the fields have spherical harmonic terms of the same multipole order (n,m). In terms of the multipole expansions, the boundary condition equation is

$$\sum_{n=0}^{\infty} \sum_{m=-\infty}^{+\infty} A_{nm} h_n^{(2)}(kr) Y_{nm}(\theta,\varphi) + \sum_{n=0}^{\infty} \sum_{m=-\infty}^{+\infty} C_{nm} h_n^{(1)}(kr) Y_{nm}(\theta,\varphi) =$$
$$\sum_{n=0}^{\infty} \sum_{m=-\infty}^{+\infty} B_{nm} j_n(kr) Y_{nm}(\theta,\varphi) \tag{3.78}$$

To solve this equation, we first multiply all of the terms in the expansions by $Y_{NM}^*(\theta,\varphi)$ and then integrate over θ and φ. The spherical Bessel and Hankel functions are evaluated at the sphere's surface ($r = a$). Integration over the surface of the sphere removes the summations and spherical harmonic terms due to orthogonality:

$$\sum_{n=0}^{\infty} \sum_{m=-n}^{n} A_{nm} \iint d\Omega\, Y_{NM}^*(\theta,\varphi) Y_{nm}(\theta,\varphi) = \sum_{n=0}^{\infty} \sum_{m=-n}^{n} A_{nm} \delta_{Nn} \delta_{Mm} = A_{NM} \tag{3.79}$$

The indices n and m are now N and M, resulting from multiplying the field expansions by $Y_{NM}^*(\theta,\varphi)$ and integrating over θ and φ. This effectively pulls the amplitude coefficients out of the expansions and allows them to be directly related in an equation:

$$\sum_{n=0}^{\infty}\sum_{m=-\infty}^{+\infty}A_{nm}h_n^{(2)}(kr)_{r=a}\iint d\Omega\, Y_{NM}^*(\theta,\varphi)Y_{nm}(\theta,\varphi)+$$

$$\sum_{n=0}^{\infty}\sum_{m=-\infty}^{+\infty}C_{nm}h_n^{(1)}(kr)_{r=a}\iint d\Omega\, Y_{NM}^*(\theta,\varphi)Y_{nm}(\theta,\varphi)-$$

$$\sum_{n=0}^{\infty}\sum_{m=-\infty}^{+\infty}B_{nm}j_n(kr)_{r=a}\iint d\Omega\, Y_{NM}^*(\theta,\varphi)Y_{nm}(\theta,\varphi)=$$

$$A_{NM}h_N^{(2)}(ka)+C_{NM}h_N^{(1)}(ka)-B_{NM}j_N(ka)=0$$

(3.80)

The final equation relating the amplitude coefficients is

$$A_{NM}h_N^{(2)}(ka)+C_{NM}h_N^{(1)}(ka)=B_{NM}j_N(ka)$$

(3.81)

A problem arises, however, when some of the fields have spherical harmonic terms of different (n,m) order than the others. This occurs in both electromagnetic (Mie) scattering and elastic wave scattering. A simplified example is the following:

$$\sum_{n=0}^{\infty}\sum_{m=-\infty}^{+\infty}A_{nm}h_n^{(2)}(kr)Y_{nm}(\theta,\varphi)+\sum_{n=0}^{\infty}\sum_{m=-\infty}^{+\infty}C_{nm}h_n^{(1)}(kr)Y_{n+1,m}(\theta,\varphi)=$$

$$\sum_{n=0}^{\infty}\sum_{m=-\infty}^{+\infty}B_{nm}j_n(kr)Y_{n-1,m}(\theta,\varphi)$$

(3.82)

Note the spherical harmonic terms of order $(n+1,m)$ and $(n-1,m)$ in the field expansions. Multiplying all of the terms in the expansions by $Y_{NM}^*(\theta,\varphi)$ and then integrating over θ and φ does not, however, cause these terms and their associated amplitude coefficients to disappear. Rather, the integrations will be of the form

$$\sum_{n=0}^{\infty}\sum_{m=-n}^{n}A_{nm}\iint d\Omega\, Y_{NM}^*(\theta,\varphi)Y_{n+1,m}(\theta,\varphi)=\sum_{n=0}^{\infty}\sum_{m=-n}^{n}A_{nm}\delta_{N,n+1}\delta_{Mm}$$

$$=\sum_{n=0}^{\infty}\sum_{m=-n}^{n}A_{nm}\delta_{N-1,n}\delta_{Mm}=A_{N-1,M}$$

(3.83)

and

$$\sum_{n=0}^{\infty}\sum_{m=-n}^{n}A_{nm}\iint d\Omega\, Y_{NM}^*(\theta,\varphi)Y_{n-1,m}(\theta,\varphi)=\sum_{n=0}^{\infty}\sum_{m=-n}^{n}A_{nm}\delta_{N,n-1}\delta_{Mm}$$

$$=\sum_{n=0}^{\infty}\sum_{m=-n}^{n}A_{nm}\delta_{N+1,n}\delta_{Mm}=A_{N+1,M}$$

(3.84)

Note that the integrations pull out amplitude coefficients of either lower or higher multipole order, but that they do not force the terms to vanish. Because we are performing an integration within an expansion of many terms, the integral pulls out a coefficient appropriate for the spherical harmonic order it is associated with. In other words, because we have to integrate all of the terms in all of the expansions, we must pull out each of the coefficients independently of the coefficients in the other expansions. We are therefore required to pull out coefficients of different (N,M) order due to the spherical harmonic they are associated with, but not due to the spherical harmonics in the other expansions. The resulting boundary condition equation is therefore

$$\sum_{n=0}^{\infty}\sum_{m=-\infty}^{+\infty} A_{nm} h_n^{(2)}(kr)_{r=a} \iint d\Omega Y_{NM}^*(\theta,\varphi) Y_{nm}(\theta,\varphi) +$$

$$\sum_{n=0}^{\infty}\sum_{m=-\infty}^{+\infty} C_{nm} h_n^{(1)}(kr)_{r=a} \iint d\Omega Y_{NM}^*(\theta,\varphi) Y_{n+1,m}(\theta,\varphi) -$$

$$\sum_{n=0}^{\infty}\sum_{m=-\infty}^{+\infty} B_{nm} j_n(kr)_{r=a} \iint d\Omega Y_{NM}^*(\theta,\varphi) Y_{n-1,m}(\theta,\varphi) =$$

$$A_{NM} h_N^{(2)}(ka) + C_{N-1,M} h_{N-1}^{(1)}(ka) - B_{N+1,M} j_{N+1}(ka) = 0 \qquad (3.85)$$

Note that the delta functions also change the multipole order of the radial functions. The resultant coefficient equation is

$$A_{NM} h_N^{(2)}(ka) + C_{N-1,M} h_{N-1}^{(1)}(ka) = B_{N+1,M} j_{N+1}(ka) \qquad (3.86)$$

This equation relates coefficients of one multipole order (N) with coefficients of higher and lower order ($N+1$ and $N-1$). In other words, the equation mixes coefficients of different moments, resulting in recursive equations for the coefficients. For brevity, the coefficients of higher and lower multipole order will be called *cross-order coefficients*.

The cross-order coefficients in the solutions are problematic since they make the boundary conditions unsolvable. There are now more unknowns than there are equations to solve, and the scattering problem can therefore not be solved in closed form. However, many published presentations of this solution method casually throw away the cross-order coefficients using the orthogonality argument. An example of such a justification is the following:

"The summation sign in these expressions is removed by making use of the orthogonality properties of the trigonometric and Legendre functions. As a result only coefficients of the same order have to be compared."[13]

Such an application of orthogonality is equivalent to what was demonstrated above with the scalar spherical harmonics, and is therefore not a correct approach for dispensing with the cross-coefficient terms. Similar errors have appeared in the solution for elastic waves. Einspruch and Truell, and Einspruch *et al.* err in that they forget they are integrating over an infinite summation of terms in the boundary conditions for elastic wave scattering, but nonetheless arrive at correct solutions by mis-applying the orthogonality conditions for the Legendre functions.[23,24]

The classical solutions for Mie and elastic wave scattering do not contain cross-order coefficients, and can be shown to be numerically correct to the precision of modern computers. Yet, as has been shown, the cross-order coefficients cannot be eliminated with only the use of orthogonality conditions for scalar functions. Since the cross-order terms in Eq. 3.86 must vanish in order to arrive at a solvable scattering problem (*i.e.*, with the same number of equations and unknowns) and in order to be numerically correct, one may argue that the cross-order terms should either cancel each other out or are numerically equivalent to zero. We have found that such a result cannot be demonstrated either analytically or numerically. Since the original approach of applying orthogonality must be kept in order to extract the coefficients from the summations, another mathematical method or procedure must exist to force the cross-order coefficients to vanish.

To eliminate the cross-order terms, the boundary conditions require an extra constraint that is not available with the use of the orthogonality of the scalar components. Fortuitously, the orthogonality of the vector spherical harmonics (Eq. 3.87) provides such an extra constraint (the δ_{Ll}) that critically forces the cross-order terms to vanish.

$$\int_0^{2\pi} d\varphi \int_0^\pi d(\cos\theta) \mathbf{Y}_{NM}^L * (\theta,\varphi) \mathbf{Y}_{nm}^l (\theta,\varphi) = \delta_{Ll}\delta_{Nn}\delta_{Mm} \qquad (3.87)$$

Therefore, by retaining the vector form of the boundary condition equations and applying orthogonality of the vector spherical harmonics, the Mie scattering solutions can be derived in a rigorous and unambiguous manner.

The vector solution method for Mie scattering is summarized here as an example. In vector form, the transverse electric and magnetic field boundary conditions are the following:

$$\mathbf{E}_{inc,transverse} + \mathbf{E}_{sct,transverse} = \mathbf{E}_{ref,transverse} \tag{3.88}$$

$$\mathbf{H}_{inc,transverse} + \mathbf{H}_{sct,transverse} = \mathbf{H}_{ref,transverse} \tag{3.89}$$

To find the vector form of the transverse electric and magnetic fields, without resorting the scalar θ and φ components, we first rewrite $\mathbf{E}$ and $\mathbf{H}$ in terms of our multipole fields $\mathbf{V}$ and $\mathbf{W}$:

$$\mathbf{E}_{inc} = \sum_{n=0}^{\infty} \sum_{m=-n}^{n} k_{ext} \left[a_{nm} \mathbf{V}_{nm}(\mathbf{r}) + ib_{nm} \mathbf{W}_{nm}(\mathbf{r}) \right] \tag{3.90}$$

$$\mathbf{E}_{ref} = \sum_{n=0}^{\infty} \sum_{m=-n}^{n} k_{int} \left[c_{nm} \mathbf{V}_{nm}(\mathbf{r}) + id_{nm} \mathbf{W}_{nm}(\mathbf{r}) \right] \tag{3.91}$$

$$\mathbf{E}_{sct} = \sum_{n=0}^{\infty} \sum_{m=-n}^{n} k_{ext} \left[e_{nm} \mathbf{V}_{nm}(\mathbf{r}) + if_{nm} \mathbf{W}_{nm}(\mathbf{r}) \right] \tag{3.92}$$

$$\mathbf{H}_{inc} = \eta_{ext} \sum_{n=0}^{\infty} \sum_{m=-n}^{n} k_{ext} \left[b_{nm} \mathbf{V}_{nm}(\mathbf{r}) - ia_{nm} \mathbf{W}_{nm}(\mathbf{r}) \right] \tag{3.93}$$

$$\mathbf{H}_{ref} = \eta_{int} \sum_{n=0}^{\infty} \sum_{m=-n}^{n} k_{int} \left[d_{nm} \mathbf{V}_{nm}(\mathbf{r}) - ic_{nm} \mathbf{W}_{nm}(\mathbf{r}) \right] \tag{3.94}$$

$$\mathbf{H}_{sct} = \eta_{ext} \sum_{n=0}^{\infty} \sum_{m=-n}^{n} k_{ext} \left[f_{nm} \mathbf{V}_{nm}(\mathbf{r}) - ie_{nm} \mathbf{W}_{nm}(\mathbf{r}) \right] \tag{3.95}$$

Instead of breaking up the full vector equations into scalar transverse components, we will retain the vector character of the equations and therefore gain advantage of using the additional orthogonality condition attendant with the vector spherical harmonics. Since the magnetic multipole field $\mathbf{W}$ has no radial components, it is already fully transverse. We can find the transverse vector associated with the electric multipole field $\mathbf{V}$ by taking two successive cross-products with a normal radial vector $\mathbf{n}_r$:

$$\mathbf{V}_{nm}(\mathbf{r})_{transverse} = \mathbf{n}_r \times (\mathbf{n}_r \times \mathbf{V}_{nm}(\mathbf{r}))$$

$$= \left[(n+1)\frac{z_n(kr)}{kr} - z_{n+1}(kr) \right](-i)\left\{ \sqrt{\frac{n+1}{2n+1}}\mathbf{Y}_{nm}^{n-1}(\theta,\varphi) + \sqrt{\frac{n}{2n+1}}\mathbf{Y}_{nm}^{n+1}(\theta,\varphi) \right\} \qquad (3.96)$$

The $\mathbf{E}_{transverse}$ and $\mathbf{H}_{transverse}$ fields in the boundary conditions (Eqs. 3.88 and 3.89) are now replaced with the expanded forms of the $\mathbf{V}_{transverse}$ and $\mathbf{W}_{transverse}$ fields containing the spherical Bessel functions and vector spherical harmonics (Eqs. 3.96 and 3.60). After some algebraic manipulations, the orthogonality conditions for the vector spherical harmonics are applied twice to each boundary condition. The first application involves multiplication and integration with $\mathbf{Y}_{NM}^{N-1}*(\theta,\varphi)$, and yields an independent coefficent equation for each of the two boundary conditions:

$$a_{NM}k_{ext}\left[(N+1)\frac{h_N^{(2)}(k_{ext}\alpha)}{k_{ext}\alpha} - h_{N+1}^{(2)}(k_{ext}\alpha) \right] +$$

$$e_{NM}k_{ext}\left[(N+1)\frac{h_N^{(1)}(k_{ext}\alpha)}{k_{ext}\alpha} - h_{N+1}^{(1)}(k_{ext}\alpha) \right] - \qquad (3.97)$$

$$c_{NM}k_{int}\left[(N+1)\frac{j_N(k_{int}\alpha)}{k_{int}\alpha} - j_{N+1}(k_{int}\alpha) \right] = 0$$

$$b_{NM}\eta_{ext}k_{ext}\left[(N+1)\frac{h_N^{(2)}(k_{ext}\alpha)}{k_{ext}r} - h_{N+1}^{(2)}(k_{ext}\alpha) \right] +$$

$$f_{NM}\eta_{ext}k_{ext}\left[(N+1)\frac{h_N^{(1)}(k_{ext}\alpha)}{k_{ext}\alpha} - h_{N+1}^{(1)}(k_{ext}\alpha) \right] - \qquad (3.98)$$

$$d_{NM}\eta_{int}k_{int}\left[(N+1)\frac{j_N(k_{int}\alpha)}{k_{int}\alpha} - j_{N+1}(k_{int}\alpha) \right] = 0$$

The second application involves multiplication and integration with $\mathbf{Y}_{NM}^N*(\theta,\varphi)$, and also yields an independent equation for each of the two boundary conditions:

$$b_{NM}k_{ext}h_N^{(2)}(k_{ext}\alpha) + f_{NM}k_{ext}h_N^{(1)}(k_{ext}\alpha) - d_{NM}k_{int}j_N(k_{int}\alpha) = 0 \qquad (3.99)$$

$$a_{NM}\eta_{ext}k_{ext}h_N^{(2)}(k_{ext}\alpha) + e_{NM}\eta_{ext}k_{ext}h_N^{(1)}(k_{ext}\alpha) - c_{NM}\eta_{int}k_{int}j_N(k_{int}\alpha) = 0 \qquad (3.100)$$

The above four equations are the correct equations for solution of the Mie scattering coefficients. Note that none of these equations contain the cross-ordser coefficient terms which would remain if we

would have used only the scalar equations. The extra constraint provided by the orthogonality of the vector spherical harmonics allows a rigorous method for removing the cross-order terms.

The solution of the Mie scattering problem with the use of pure-orbital vector spherical harmonics is not a common approach, and few references have been found which use this method or show how the orthogonality of the these functions are necessary for solving the boundary conditions. It should be noted that Bohren and Huffman state that the use of the orthogonality of the **LNM** vector wave functions is required to solve the Mie boundary conditions, but do not show the details of the solution.[14] Knopoff also mentions that integration over the vector wave functions **L**, **M**, and **N** is required to solve for the scattering of shear elastic waves by a sphere.[21]

In comparison to the **LNM** vector wave functions, vector wave functions constructed from pure-orbital vector spherical harmonics (such as the **UVW** multipoles) have advantages in providing an elegant and rigorous solution to the Mie boundary conditions. The orthogonality conditions for the vector spherical harmonics are simpler, and the manipulation of the functions are more straightforward. Of additional importance is the fact that the pure-orbital vector spherical harmonics are harmonious with the mathematical descriptions of continuum mechanics, quantum mechanics, and gravitational radiation physics.

3.3 (b) Solutions for Electromagnetic Wave Scattering

The boundary condition solutions for electromagnetic wave scattering from a sphere are given by Eqs. 3.97-3.100. The results for electromagnetic scattering yield four linear equations with four unknowns. In matrix format these equations are

$$
\begin{pmatrix}
\eta_{int}J_{N0} & -\eta_{ext}H_{N0} & 0 & 0 \\
J_{N1} & -H_{N1} & 0 & 0 \\
0 & 0 & J_{N0} & -H_{N0} \\
0 & 0 & \eta_{int}J_{N1} & -\eta_{ext}H_{N1}
\end{pmatrix}
\begin{pmatrix}
c_{NM} \\
e_{NM} \\
d_{NM} \\
f_{NM}
\end{pmatrix}
=
\begin{pmatrix}
a_{NM}\eta_{ext}G_{N0} \\
a_{NM}G_{N1} \\
b_{NM}G_{N0} \\
b_{NM}\eta_{ext}G_{N1}
\end{pmatrix}
\qquad (3.101)
$$

The indices of refraction are η_{int} for inside the sphere and η_{ext} for outside the sphere. The notation shortcuts are the following, where α is the sphere's radius:

$$G_{N0} = k_{ext} h_N^{(2)}(k_{ext}\alpha) \tag{3.102}$$

$$H_{N0} = k_{ext} h_N^{(1)}(k_{ext}\alpha) \tag{3.103}$$

$$J_{N0} = k_{int} j_N(k_{int}\alpha) \tag{3.104}$$

$$G_{N1} = k_{ext}\left[(N+1)\frac{h_N^{(2)}(k_{ext}\alpha)}{k_{ext}\alpha} - h_{N+1}^{(2)}(k_{ext}\alpha)\right] \tag{3.105}$$

$$H_{N1} = k_{ext}\left[(N+1)\frac{h_N^{(1)}(k_{ext}\alpha)}{k_{ext}\alpha} - h_{N+1}^{(1)}(k_{ext}\alpha)\right] \tag{3.106}$$

$$J_{N1} = k_{int}\left[(N+1)\frac{j_N(k_{int}\alpha)}{k_{int}\alpha} - j_{N+1}(k_{int}\alpha)\right] \tag{3.107}$$

Solution of this matrix is readily accomplished, yielding the famous Mie coefficient solutions for the internal refracted fields and external scattered fields:

$$c_{NM} = \frac{a_{NM}\eta_{ext}(H_{N0}G_{N1} - H_{N1}G_{N0})}{\eta_{ext}H_{N0}J_{N1} - \eta_{int}H_{N1}J_{N0}} \tag{3.108}$$

$$e_{NM} = \frac{a_{NM}(\eta_{int}J_{N0}G_{N1} - \eta_{ext}J_{N1}G_{N0})}{\eta_{ext}H_{N0}J_{N1} - \eta_{int}H_{N1}J_{N0}} \tag{3.109}$$

$$d_{NM} = \frac{b_{NM}\eta_{ext}(H_{N0}G_{N1} - H_{N1}G_{N0})}{\eta_{int}H_{N0}J_{N1} - \eta_{ext}H_{N1}J_{N0}} \tag{3.110}$$

$$f_{NM} = \frac{b_{NM}(\eta_{ext}J_{N0}G_{N1} - \eta_{int}J_{N1}G_{N0})}{\eta_{int}H_{N0}J_{N1} - \eta_{ext}H_{N1}J_{N0}} \tag{3.111}$$

3.3 (c) Solutions for Elastic Wave Scattering

Solution of the boundary conditions for elastic wave scattering are more involved, presenting a set of six linear equations for six unknowns. Three of these equations evolve from the continuity of displacement boundary condition, which is a simple equality between the sum of the incident and scattered waves and the sum of the interior refracted waves. Although these equations are solved (incorrectly) in

scalar form in most published articles, they are also readily solvable in vector form, and yield the same three linear equations.

The other three linear equations for elastic wave scattering come from the continuity of the stresses, which is trickier since the stress is a tensor and not a vector. Using the old (incorrect) approach, one can equate the scalar stress components in spherical coordinates, which are complex but available from Graff and others.[188,189] Although the approach is incorrect, it yields the correct three linear equations if cross-order terms are thrown out.

The correct approach would be to derive boundary conditions preserving the vector properties of the displacement. This is difficult since the equation relating stress and displacement is the tensor equation $\sigma_{ij} = C_{ijkl}\varepsilon_{kl}$, where σ_{ij} is the stress tensor, C_{ijkl} is the three-dimensional stiffness tensor, and ε_{kl} is the strain.[190] The strain tensor derives from the displacement by

$$\varepsilon_{ij} = \frac{1}{2}\left(\frac{\partial u_i}{\partial x_j} + \frac{\partial u_j}{\partial x_i}\right) \tag{3.112}$$

Since we are concerned with isotropic solids, the stress-strain relationship reduces to Cauchy's law:

$$\sigma_{ij} = \lambda \varepsilon_{kk}\delta_{ij} + 2\mu\varepsilon_{ij} \tag{3.113}$$

However, we are still confronted with a tensor equation which is difficult to reduce to one or more vector equations (which would be necessary to use the orthogonality of the vector spherical harmonics). One possibility would be to use tensor spherical harmonics to solve the stress boundary conditions, but that would imply a serious overhaul of our spherical wave function forms.

We are confident that a rigorously correct solution method exists for the stress boundary conditions. However, in the interest of time and effort, the linear equations from the scalar stress components were used minus the cross-order terms. The final solution matrix has the following form:

$$\begin{pmatrix} T_1(j) & -T_1(h) & T_2(j) & -T_2(h) & 0 & 0 \\ T_6(j) & -T_6(h) & T_7(j) & -T_7(h) & 0 & 0 \\ T_4(j) & -T_4(h) & T_5(j) & -T_5(h) & 0 & 0 \\ T_9(j) & -T_9(h) & T_{10}(j) & -T_{10}(h) & 0 & 0 \\ 0 & 0 & 0 & 0 & T_3(j) & -T_3(h) \\ 0 & 0 & 0 & 0 & T_8(j) & -T_8(h) \end{pmatrix} \begin{pmatrix} D_{NM} \\ G_{NM} \\ E_{NM} \\ H_{NM} \\ F_{NM} \\ I_{NM} \end{pmatrix} = \begin{pmatrix} A_{NM}T_1(g) + B_{NM}T_2(g) \\ A_{NM}T_6(g) + B_{NM}T_7(g) \\ A_{NM}T_4(g) + B_{NM}T_5(g) \\ A_{NM}T_9(g) + B_{NM}T_{10}(g) \\ C_{NM}T_3(g) \\ C_{NM}T_8(g) \end{pmatrix}$$

(3.114)

Fortunately, the solution matrix separates into two smaller matrices:

$$\begin{pmatrix} T_1(j) & -T_1(h) & T_2(j) & -T_2(h) \\ T_6(j) & -T_6(h) & T_7(j) & -T_7(h) \\ T_4(j) & -T_4(h) & T_5(j) & -T_5(h) \\ T_9(j) & -T_9(h) & T_{10}(j) & -T_{10}(h) \end{pmatrix} \begin{pmatrix} D_{NM} \\ G_{NM} \\ E_{NM} \\ H_{NM} \end{pmatrix} = \begin{pmatrix} A_{NM}T_1(g) + B_{NM}T_2(g) \\ A_{NM}T_6(g) + B_{NM}T_7(g) \\ A_{NM}T_4(g) + B_{NM}T_5(g) \\ A_{NM}T_9(g) + B_{NM}T_{10}(g) \end{pmatrix}$$

(3.115)

and

$$\begin{pmatrix} T_3(j) & -T_3(h) \\ T_8(j) & -T_8(h) \end{pmatrix} \begin{pmatrix} F_{NM} \\ I_{NM} \end{pmatrix} = \begin{pmatrix} C_{NM}T_3(g) \\ C_{NM}T_8(g) \end{pmatrix}$$

(3.116)

The j, h, and g in the T-functions refer to the type of spherical Bessel function that is in the function {$j = j_n(kr)$, $g = h_n^{(2)}(kr)$, $h = h_n^{(1)}(kr)$}. The 2×2 matrix is readily solved with simple algebra. The 4×4 matrix was solved for a generic matrix on Mathematica. The algebraic expressions were then programmed into the VMIST algorithm.

The T-symbols are complex functions of spherical Bessel functions, multipole order N, the wavevectors k_L and k_S, and the sphere radius a:

$$T_1(z) = (N)\frac{z_N(k_L a)}{k_L a} - z_{N+1}(k_L a)$$

(3.117)

$$T_2(z) = (i)\sqrt{(N)(N+1)}\frac{z_N(k_S a)}{k_S a}$$

(3.118)

$$T_3(z) = z_N(k_S a)$$

(3.119)

$$T_4(z) = \frac{z_N(k_L a)}{k_L a}$$

(3.120)

$$T_5(z) = \frac{i}{\sqrt{(N)(N+1)}}\left[(N+1)\frac{z_N(k_S a)}{k_S a} - z_{N+1}(k_S a)\right]$$

(3.121)

$$T_6(z) = k_L\left[-\lambda z_N(k_L a) + 2\mu\left\{\left[\frac{(N-1)(N)}{(k_L a)^2} - \frac{N+1}{N+2}\right]z_N(k_L a) + \frac{z_{N+1}(k_L a)}{k_L a}\right\}\right]$$

(3.122)

$$T_7(z) = 2i\mu k_S\sqrt{(N)(N+1)}\left[(N-1)\frac{z_N(k_S a)}{(k_S a)^2} - \frac{z_{N+1}(k_S a)}{k_S a}\right]$$

(3.123)

$$T_8(z) = \mu k_S\left[(N-1)\frac{z_N(k_S a)}{k_S a} - z_{N+1}(k_S a)\right]$$

(3.124)

$$T_9(z) = 2\mu k_L\left[(N-1)\frac{z_N(k_L a)}{(k_L a)^2} - \frac{z_{N+1}(k_L a)}{k_L a}\right]$$

(3.125)

$$T_{10}(z) = \frac{i\mu k_S}{\sqrt{(N)(N+1)}}\left[\left[\frac{2(N^2-1)}{(k_S a)^2} - \frac{N+1}{N+2}\right]z_N(k_S a) + \frac{z_{N+1}(k_S a)}{k_S a}\right]$$

(3.126)

3.4 Translation of Scattered Fields

3.4 (a) Vector Addition Theorem

A realistic description of multiple scattering at the microscopic level requires that the scattered fields from each particle interact with the other particles (Figure 3-4). Since the coordinates of the wave functions are specific to each particle, the fields scattered from particle α will be in α's coordinate system. However, fields incident to particle β need to be in β's coordinate system in order to calculate the interaction with particle β via the single particle scattering solutions. Therefore, particle α's scattered wave fields need to be transformed into particle β's coordinate system. This is accomplished with the use of translational addition theorems. These theorems are the "main engine" driving the VMIST multiple scattering algorithm.
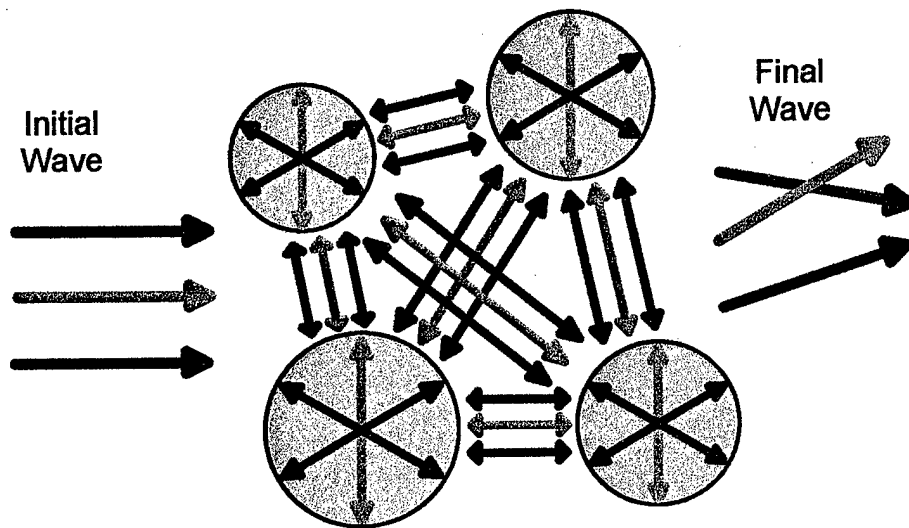
FIGURE 3-4. Diagram of multiple scattering of vector multipole fields, showing how each of the three fields U (red), V (green), and W (blue) require translation from each sphere to every other sphere.

As summarized in Chapter 2, many versions of the translational addition theorems have been derived. Most are mathematically awkward or were derived for specific wave functions such as the LNM vector spherical wave functions. For the VMIST approach, addition theorems for wave functions based on pure-orbital vector spherical harmonics were desired. It was also desired that the addition theorems be in a more elegant form, and use commonly recognized functions and symbols such as Clebsch-Gordan coefficients. Finally, the complex nature of the addition theorems and their importance in the algorithm impelled that they be rederived and tested for correctness and convergence. The addition theorems were therefore rederived using a straightforward integral transform approach which has not been reported previously in the literature.

In Section 3.3 the coefficients for the scattered fields (two for the electromagnetic case, three for the elastic wave case) were solved for a single sphere. In order to compute multiple scattering using these vector fields, we need to translate the fields from the coordinate system of the scattering sphere to those of another sphere located at an arbitrary position. The first scattering sphere will be subsequently referred to as the "transmitting" or α sphere, and the second sphere as the "receiving" or β sphere. The coefficients, coordinates, radius, and elastic properties for each sphere are denoted in Table 3-3.

TABLE 3-3. Coefficients, coordinates, and properties for the transmitting (α) sphere and the receiving (β) sphere.

Region	Outgoing Waves EM	Outgoing Waves Elastic	Incoming Waves EM	Incoming Waves Elastic	Coord	Radius	Properties EM	Properties Elastic	Wave Vectors EM	Wave Vectors Elastic
Sphere α	e_{nm}^α f_{nm}^α	G_{nm}^α H_{nm}^α I_{nm}^α			r_α θ_α φ_α	a_α	η^α	λ^α μ^α	k^α	k_L^α k_S^α
Sphere β			a_{vw}^β b_{vw}^β	A_{vw}^β B_{vw}^β C_{vw}^β	r_β θ_β φ_β	a_β	η^β	λ^β μ^β	k^β	k_L^β k_S^β
Matrix							η^{ext}	λ^{ext} μ^{ext}	k^{ext}	k_L^{ext} k_S^{ext}

The global position vectors for the two spheres are $\mathbf{R}_\alpha$ and $\mathbf{R}_\beta$. The position of sphere α with respect to sphere β is therefore $\mathbf{R}_{\alpha\beta} = \mathbf{R}_\alpha - \mathbf{R}_\beta$. Figure 3-5 displays these position vectors. The coordinate systems for the α and β spheres are local coordinate systems, and are denoted in the above table and shown in Figure 3-6 along with the global coordinates of spheres α and β.
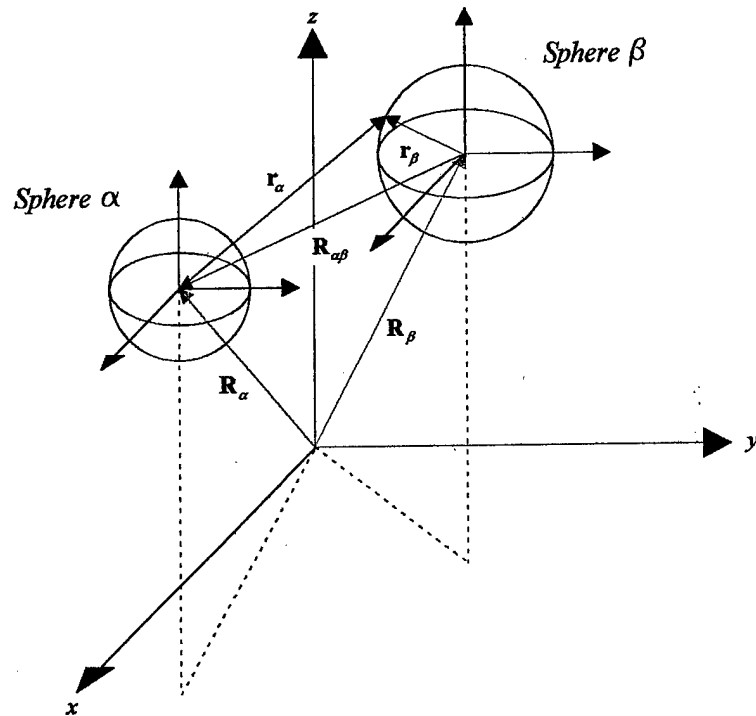
FIGURE 3-5. Relative and global position vectors for spheres α and β.
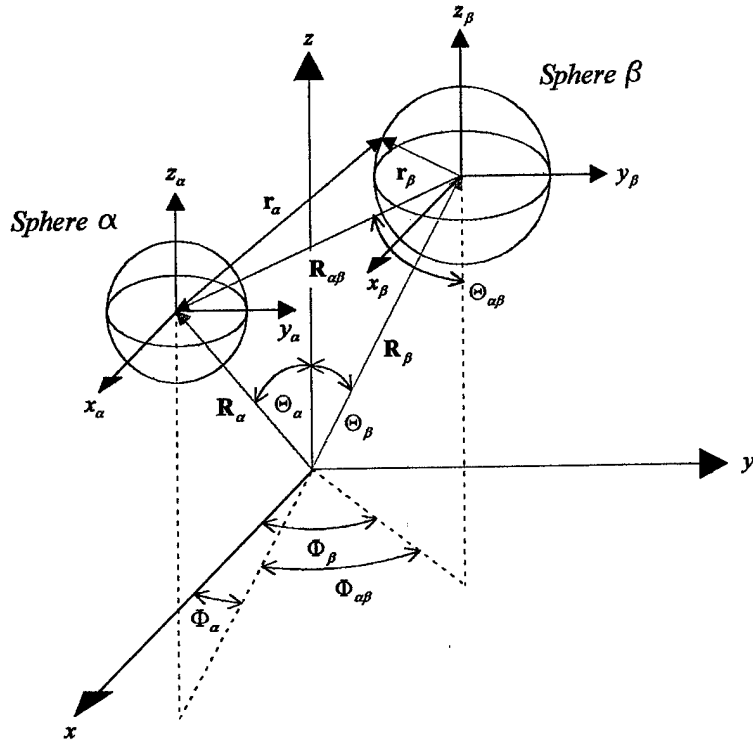
FIGURE 3-6. Local and global coordinates for spheres α and β.

To solve for the scattered field coefficients of sphere β we need to find the incident field coefficients for sphere β. The incident waves for β, however, are the scattered waves from α. We therefore need to translate the multipole fields from the α coordinate system into the β coordinate system. First we note that the scattered α fields contain vector multipole terms of the following forms:

$$h_{n-1}^{(1)}(kr_\alpha)\mathbf{Y}_{nm}^{n-1}(\theta_\alpha,\varphi_\alpha) \tag{3.127}$$

$$h_{n+1}^{(1)}(kr_\alpha)\mathbf{Y}_{nm}^{n+1}(\theta_\alpha,\varphi_\alpha) \tag{3.128}$$

$$h_n^{(1)}(kr_\alpha)\mathbf{Y}_{nm}^{n}(\theta_\alpha,\varphi_\alpha) \tag{3.129}$$

We now assume the addition theorem for these terms will have the following form:

$$h_l^{(1)}(kr_\alpha)\mathbf{Y}_{nm}^{l}(\theta_\alpha,\varphi_\alpha) = \sum_{\nu=0}^{\infty}\sum_{\lambda=\nu-1}^{\nu+1}\sum_{\mu=-\nu}^{+\nu}\Pi_{\lambda,\nu,\mu}^{l,n,m}(\mathbf{R}_{\alpha\beta})\mathbf{Y}_{\nu\mu}^{\lambda}(\theta_\beta,\varphi_\beta) \tag{3.130}$$

The expansion coefficients $\Pi_{\lambda,\nu,\mu}^{l,n,m}(\mathbf{R}_{\alpha\beta})$ are functions only of the relative position vector $\mathbf{R}_{\alpha\beta}$, and can be calculated in the same manner as one would calculate the coefficients for a Fourier series. The coefficients are calculated from the following integral:

$$\Pi_{\lambda,\nu,\mu}^{l,n,m}(\mathbf{R}_{\alpha\beta}) = \int_{0}^{2\pi}d\varphi_{\beta}\int_{-1}^{+1}d(\cos\theta_{\beta})h_{l}^{(1)}(kr_{\alpha})\left\{\mathbf{Y}_{nm}^{l}(\theta_{\alpha},\varphi_{\alpha})\cdot\mathbf{Y}_{\nu\mu}^{\lambda}*(\theta_{\beta},\varphi_{\beta})\right\} \tag{3.131}$$

The values of the scattered α/incident β multipole fields are only relevant at the surface of sphere β, therefore we integrate over the surface of sphere β with θ_{β} and φ_{β} as our variables of integration.

To evaluate this integral we first expand the dot product between the two vector spherical harmonics by rewriting the complex conjugate of a vector spherical harmonic as given by Greiner and Maruhn:[45]

$$\mathbf{Y}_{nm}^{l}*(\theta,\varphi) = (-1)^{m+n+l+1}\mathbf{Y}_{n,-m}^{l}(\theta,\varphi) \tag{3.132}$$

We then expand the vector spherical harmonics into their scalar components using helicity basis vectors and the compact notation of Clebsch-Gordan coefficients as defined by Varshalovich et al.:[47]

$$\mathbf{Y}_{nm}^{l}(\theta,\varphi) = C_{l,m+1,1,-1}^{n,m}Y_{l,m+1}\mathbf{e}_{-1} + C_{l,m,1,0}^{n,m}Y_{l,m}\mathbf{e}_{0} + C_{l,m-1,1,1}^{n,m}Y_{l,m-1}\mathbf{e}_{+1} \tag{3.133}$$

The scalar components of the two vector spherical harmonics are then multiplied together based on their helicity basis vectors. This involves computing the dot product of the helicity basis vectors, which does not yield the same result as one would expect from our experience with cartesian basis vectors. Whereas $\mathbf{e}_{+1}\cdot\mathbf{e}_{+1} = \mathbf{e}_{-1}\cdot\mathbf{e}_{-1} = 0$, we find that $\mathbf{e}_{+1}\cdot\mathbf{e}_{+1}* = \mathbf{e}_{-1}\cdot\mathbf{e}_{-1}* = 1$. However, $\mathbf{e}_{0}\cdot\mathbf{e}_{0} = \mathbf{e}_{0}\cdot\mathbf{e}_{0}* = 1$. The dot product between two vector spherical harmonics is therefore not as simple as separately multiplying the $\mathbf{e}_{+1}$, $\mathbf{e}_{0}$, and $\mathbf{e}_{-1}$ components. Rather, the $\mathbf{e}_{+1}$ components multiply with the $\mathbf{e}_{-1}$ components. The $\mathbf{e}_{0}$ components can still be separately multiplied, however. The vector spherical harmonic dot product in our integral therefore becomes the following:

$$
\mathbf{Y}_{nm}^{l}(\theta_\alpha,\varphi_\alpha) \cdot \mathbf{Y}_{\nu\mu}^{\lambda}{}^{*}(\theta_\beta,\varphi_\beta) = (-1)^{\nu+\lambda+1}
$$

$$
\times
\begin{bmatrix}
C_{l,m+1,1,-1}^{n,m}C_{\lambda,-\mu-1,1,1}^{\nu,-\mu}Y_{l,m+1}(\theta_\alpha,\varphi_\alpha)Y_{\lambda,\mu+1}{}^{*}(\theta_\beta,\varphi_\beta) + \\
C_{l,m,1,0}^{n,m}C_{\lambda,-\mu,1,0}^{\nu,-\mu}Y_{l,m}(\theta_\alpha,\varphi_\alpha)Y_{\lambda,\mu}{}^{*}(\theta_\beta,\varphi_\beta) + \\
C_{l,m-1,1,1}^{n,m}C_{\lambda,-\mu+1,1,-1}^{\nu,-\mu}Y_{l,m-1}(\theta_\alpha,\varphi_\alpha)Y_{\lambda,\mu-1}{}^{*}(\theta_\beta,\varphi_\beta)
\end{bmatrix}
\tag{3.134}
$$

We now use two expansion identities from Varshalovich et al. to finish the integration.[47] The first

is the expansion of spherical waves in terms of bipolar spherical harmonics of rank L, valid for $r_1 < r_2$:

$$
z_L(kr)Y_{LM}(\theta,\varphi) = \sqrt{\frac{4\pi}{2L+1}}\sum_{l_1,l_2=0}^{\infty} i^{l_1-l_2-L}\sqrt{(2l_1+1)(2l_2+1)}
$$

$$
\times C_{l_1,0,l_2,0}^{L,0}\, j_{l_1}(kr_1)z_{l_2}(kr_2)\left\{Y_{l_1}(\Omega_1)\otimes Y_{l_2}(\Omega_2)\right\}_{LM}
\tag{3.135}
$$

The second is the expansion for the bipolar spherical harmonics themselves:

$$
\left\{Y_{l_1}(\theta_1,\varphi_1)\otimes Y_{l_2}(\theta_2,\varphi_2)\right\}_{LM} = \sum_{m_1,m_2=0}^{\infty} C_{l_1,m_1,l_2,m_2}^{L,M} Y_{l_1 m_1}(\theta_1,\varphi_1)Y_{l_2 m_2}(\theta_2,\varphi_2)
\tag{3.136}
$$

Substituting Eq. 3.136 into Eq. 3.135, the spherical wave expansion becomes

$$
z_L(kr)Y_{LM}(\theta,\varphi) = \sqrt{\frac{4\pi}{2L+1}}\sum_{l_1,l_2=0}^{\infty} i^{l_1-l_2-L}\sqrt{(2l_1+1)(2l_2+1)}
$$

$$
\times C_{l_1,0,l_2,0}^{L,0}\, j_{l_1}(kr_1)z_{l_2}(kr_2)\sum_{m_1,m_2=0}^{\infty} C_{l_1,m_1,l_2,m_2}^{L,M} Y_{l_1 m_1}(\theta_1,\varphi_1)Y_{l_2 m_2}(\theta_2,\varphi_2)
\tag{3.137}
$$

Note that this is just the translational addition theorem for the scalar wave function

$z_L(kr)Y_{LM}(\theta,\varphi)$. We now rewrite this theorem in terms of our coordinate systems (Figures 3-5 and 3-

6). Since $\mathbf{r} = \mathbf{r}_1 - \mathbf{r}_2$ and the vector from the α-sphere terminates on the surface of the β-sphere ($\mathbf{r}_\alpha = \mathbf{a}_\beta -$

$\mathbf{R}_{\alpha\beta}$), we have the following correspondences between the particle coordinate systems and the notation in

Varshalovich et al.:[47]

$$
\begin{array}{lll}
r = r_\alpha & \theta = \theta_\alpha & \varphi = \varphi_\alpha \\
r_1 = a_\beta & \theta_1 = \theta_\beta & \varphi_1 = \varphi_\beta \\
r_2 = R_{\alpha\beta} & \theta_2 = \Theta_{\alpha\beta} & \varphi_2 = \Phi_{\alpha\beta}
\end{array}
\tag{3.138}
$$

Note that the condition $r_1 < r_2$ is satisfied as long as the two spheres do not interpenetrate. Our spherical

wave expansion can therefore be written as

$$h_l^{(1)}(kr_\alpha)Y_{l,m}(\theta_\alpha,\varphi_\alpha) = \sqrt{\frac{4\pi}{2l+1}}\sum_{l_1,l_2=0}^{\infty}i^{l_1-l_2-l}\sqrt{(2l_1+1)(2l_2+1)}\times C_{l_1,0,l_2,0}^{l,0}j_{l_1}(ka_\beta)h_{l_2}^{(1)}(kR_{\alpha\beta})$$

$$\times\sum_{m_1,m_2=0}^{\infty}C_{l_1,m_1,l_2,m_2}^{l,m}Y_{l_1m_1}(\theta_\beta,\varphi_\beta)Y_{l_2m_2}(\Theta_{\alpha\beta},\Phi_{\alpha\beta})$$

$$(3.139)$$

We now combine the spherical wave expansion with the dot product expansion:

$$h_l^{(1)}(kr_\alpha)\mathbf{Y}_{nm}^l(\theta_\alpha,\varphi_\alpha)\cdot\mathbf{Y}_{\nu\mu}^\lambda*(\theta_\beta,\varphi_\beta)=$$

$$(-1)^{\nu+\lambda+1}\sqrt{\frac{4\pi}{2l+1}}\times\sum_{l_1,l_2=0}^{\infty}i^{l_1-l_2-l}\sqrt{(2l_1+1)(2l_2+1)}\times C_{l_1,0,l_2,0}^{l,0}j_{l_1}(ka_\beta)h_{l_2}^{(1)}(kR_{\alpha\beta})$$

$$\times\sum_{m_1,m_2=0}^{\infty}\begin{bmatrix}C_{l,m+1,1,-1}^{n,m}C_{\lambda,-\mu-1,1,1}^{\nu,-\mu}C_{l_1,m_1,l_2,m_2}^{l,m+1}Y_{\lambda,\mu+1}*(\theta_\beta,\varphi_\beta)Y_{l_1m_1}(\theta_\beta,\varphi_\beta)Y_{l_2m_2}(\Theta_{\alpha\beta},\Phi_{\alpha\beta})\\ +C_{l,m,1,0}^{n,m}C_{\lambda,-\mu,1,0}^{\nu,-\mu}C_{l_1,m_1,l_2,m_2}^{l,m}Y_{\lambda,\mu}*(\theta_\beta,\varphi_\beta)Y_{l_1m_1}(\theta_\beta,\varphi_\beta)Y_{l_2m_2}(\Theta_{\alpha\beta},\Phi_{\alpha\beta})\\ +C_{l,m-1,1,1}^{n,m}C_{\lambda,-\mu+1,1,-1}^{\nu,-\mu}C_{l_1,m_1,l_2,m_2}^{l,m-1}Y_{\lambda,\mu-1}*(\theta_\beta,\varphi_\beta)Y_{l_1m_1}(\theta_\beta,\varphi_\beta)Y_{l_2m_2}(\Theta_{\alpha\beta},\Phi_{\alpha\beta})\end{bmatrix}$$

$$(3.140)$$

The above expression is now integrated over the surface of sphere β (θ_β and φ_β). Orthogonality dictates that $l_1 = \lambda$, $m_1 = \mu + 1$, $m_1 = \mu$, and $m_1 = \mu - 1$, respectively, eliminating the summations over l_1 and m_1. The l_2 and m_2 indices persist, and are renamed p and q for simplicity:

$$\Pi_{\lambda,\nu,\mu}^{l,n,m}(\mathbf{R}_{\alpha\beta}) = \int_0^{2\pi}d\varphi_\beta\int_{-1}^1 d(\cos\theta_\beta)h_l^{(1)}(kr_\alpha)\{\mathbf{Y}_{nm}^l(\theta_\alpha,\varphi_\alpha)\cdot\mathbf{Y}_{\nu\mu}^\lambda*(\theta_\beta,\varphi_\beta)\}=$$

$$(-1)^{\nu+\lambda+1}\sqrt{\frac{4\pi}{2l+1}}\times\sum_{p=0}^{\infty}i^{\lambda-l-p}\sqrt{(2\lambda+1)(2p+1)}\times C_{\lambda,0,p,0}^{l,0}j_\lambda(ka_\beta)h_p^{(1)}(kR_{\alpha\beta})$$

$$\times\sum_{q=0}^{\infty}\begin{bmatrix}C_{l,m+1,1,-1}^{n,m}C_{\lambda,-\mu-1,1,1}^{\nu,-\mu}C_{\lambda,\mu+1,p,q}^{l,m+1}\\ +C_{l,m,1,0}^{n,m}C_{\lambda,-\mu,1,0}^{\nu,-\mu}C_{\lambda,\mu,p,q}^{l,m}\\ +C_{l,m-1,1,1}^{n,m}C_{\lambda,-\mu+1,1,-1}^{\nu,-\mu}C_{\lambda,\mu-1,p,q}^{l,m-1}\end{bmatrix}\times Y_{pq}(\Theta_{\alpha\beta},\Phi_{\alpha\beta})$$

$$(3.141)$$

We can adjust the indices on the Clebsch-Gordan coefficients in our addition theorem using the following relationship:

$$C_{l_1,m_1,l_2,m_2}^{L,M} = (-1)^{l_1+l_2-L}C_{l_1,-m_1,l_2,-m_2}^{L,-M}$$

$$(3.142)$$

Furthermore, the Clebsch-Gordan coefficients impose conditions on the values for q, specifically $q = m - \mu$, thus eliminating one summation. There are no restrictions on the index p that would remove the summation over p, so it remains. However, since by the vector addition rules the last Clebsch-Gordan coefficient term implies $\lambda + \mathbf{p} = \mathbf{1}$, therefore $\mathbf{p} = \mathbf{1} - \lambda$, we can deduce that $p \leq l + \lambda$ and that the lower limit on p is $|l - \lambda|$. These simplifications result in the following for the addition theorem:

$$
\Pi_{\lambda,\nu,\mu}^{l,n,m}(\mathbf{R}_{\alpha\beta}) = j_\lambda(ka_\beta) \sum_{p=|l-\lambda|}^{l+\lambda} (i)^{\lambda-l-p} h_p^{(1)}(kR_{\alpha\beta}) Y_{p,m-\mu}(\Theta_{\alpha\beta},\Phi_{\alpha\beta}) \sqrt{\frac{4\pi(2\lambda+1)(2p+1)}{2l+1}}
$$

$$
\times C_{\lambda,0,p,0}^{l,0} \begin{bmatrix} C_{l,m+1,1,-1}^{n,m} C_{\lambda,\mu+1,1,-1}^{\nu,\mu} C_{\lambda,\mu+1,p,m-\mu}^{l,m+1} + \\ C_{l,m,1,0}^{n,m} C_{\lambda,\mu,1,0}^{\nu,\mu} C_{\lambda,\mu,p,m-\mu}^{l,m} + \\ C_{l,m-1,1,1}^{n,m} C_{\lambda,\mu-1,1,1}^{\nu,\mu} C_{\lambda,\mu-1,p,m-\mu}^{l,m-1} \end{bmatrix}
$$

$$(3.143)$$

One final simplification is to incorporate a summation over τ to simplify the Clebsch-Gordan coefficient sums in the bracket:

$$
\Pi_{\lambda,\nu,\mu}^{l,n,m}(\mathbf{R}_{\alpha\beta}) = j_\lambda(ka_\beta) \sum_{p=|l-\lambda|}^{l+\lambda} (i)^{\lambda-l-p} h_p^{(1)}(kR_{\alpha\beta}) Y_{p,m-\mu}(\Theta_{\alpha\beta},\Phi_{\alpha\beta}) \sqrt{\frac{4\pi(2\lambda+1)(2p+1)}{2l+1}}
$$

$$
\times C_{\lambda,0,p,0}^{l,0} \sum_{\tau=-1}^{1} C_{l,m-\tau,1,\tau}^{n,m} C_{\lambda,\mu-\tau,1,\tau}^{\nu,\mu} C_{\lambda,\mu-\tau,p,m-\mu}^{l,m-\tau}
$$

$$(3.144)$$

This results in a very compact form for the translational addition theorem for vector spherical wave functions.

The Clebsch-Gordan coefficients can be evaluated using many expressions. A representation in the form of algebraic sums is given by Wigner:[47]

$$
C_{a,\alpha,b,\beta}^{c,\gamma} = \delta_{\gamma,\alpha+\beta}\Delta(abc)\sqrt{\frac{(c+\gamma)!(c-\gamma)!(2c+1)}{(a+\alpha)!(a-\alpha)!(b+\beta)!(b-\beta)!}}
$$
$$
\times \sum_z \frac{(-1)^{b+\beta+z}(c+b+\alpha-z)!(a-\alpha+z)!}{z!(c-a+b-z)!(c+\gamma-z)!(a-b-\gamma+z)!}
$$

$$(3.145)$$

where

$$\Delta(abc) = \sqrt{\frac{(a+b-c)!(a-b+c)!(-a+b+c)!}{(a+b+c+1)!}} \qquad (3.146)$$

This was the expression used to compute the Clebsch-Gordan coefficients in the VMIST algorithm.

3.4 (b) Scalar Addition Theorem

Although the scalar addition theorem cannot be used to translate vector fields, it can be useful for translating potentials. It can therefore be used to translate the potential for the longitudinal field in elastic wave scattering. The scalar addition theorem has been published extensively, and is of the form

$$h_n^{(1)}(kr_\alpha)Y_{n,m}(\theta_\alpha,\varphi_\alpha) = \sum_{v=0}^{\infty}\sum_{\mu=-v}^{v} Z_{v,\mu}^{n,m} j_v(ka_\beta)Y_{v\mu}(\theta_\beta,\varphi_\beta) \qquad (3.147)$$

with

$$Z_{v,\mu}^{n,m} = \sqrt{4\pi}\sum_{p=0}^{\infty} i^{v-p-n} h_p^{(1)}(kR_{\alpha\beta})Y_{p,m-\mu}(\Theta_{\alpha\beta},\Phi_{\alpha\beta})$$
$$\times \sqrt{\frac{(2v+1)(2p+1)}{(2n+1)}} C_{v,0,p,0}^{n,0} C_{v,\mu,p,m-\mu}^{n,m} \qquad (3.148)$$

3.4 (c) Direct Translation of Vector Fields

The vector translation theorem (Eqs. 3.130 and 3.144) allows us to translate individual terms in the UVW multipole functions, but are not sufficient for translating the elastic or electromagnetic fields themselves. Further expressions therefore needed to be derived to translate the entire field expressions as given by Eqs. 3.58-3.60.

In the course of this research it was found that there were two methods for translating the vector fields from sphere α to sphere β. First, the vector fields can be translated directly using the vector addition theorem (Eq. 3.144). Second, since the fields can be derived from scalar and vector potentials, the potentials of the fields can be translated using a combination of the scalar (Eqs. 3.147, 3.148) and vector (Eqs. 3.130, 3.144) addition theorems. Although the first approach is straightforward and therefore attractive, the second approach should be more computationally efficient since the scalar addition theorem is less complex and takes less time to calculate.

Both the direct translation method and potential translation method were developed and tested in this work for two reasons. First, development of both methods helped to identify and resolve problems in the theory. Since each method is developed from a different starting point in the theory, they result in mathematically different expressions. Additionally, the longitudinal field is translated using the vector addition theorem in the direct approach, but with the scalar addition theorem in the potential approach. However, the numerical results should be the same. Having both methods therefore worked as a check for the theory—if the numerical results did not agree then there was an error either in the wave function definitions or in the addition theorems. Second, the computational speed of each method could be tested and compared to verify that the potential method was indeed more efficient.

Although the incoming spherical wavefields will, in general, be comprised of terms of the form

$$h_l^{(2)}(kr_\alpha)\mathbf{Y}_{nm}^l(\theta_\alpha,\varphi_\alpha)$$

(3.149)

expansions of the incoming spherical wavefields can also be comprised of terms of the form

$$j_l(kr_\alpha)\mathbf{Y}_{nm}^l(\theta_\alpha,\varphi_\alpha)$$

(3.150)

where the spherical Bessel function $j_l\,(kr)$ replaces the Hankel function of the the second kind $h_l^{(2)}(kr)$. This is the case for the vector plane wave expansion (see Section 3.5). Similarly, the addition theorems restrict the form of the radial function to a spherical Bessel function, and not a Hankel function of the second kind. Recall that our vector addition theorem is

$$h_l^{(1)}(kr_\alpha)\mathbf{Y}_{nm}^l(\theta_\alpha,\varphi_\alpha) = \sum_{\nu=0}^{\infty}\sum_{\lambda=\nu-1}^{\nu+1}\sum_{\mu=-\nu}^{+\nu}\Pi_{\lambda,\nu,\mu}^{l,n,m}(\mathbf{R}_{\alpha\beta})\mathbf{Y}_{\nu\mu}^\lambda(\theta_\beta,\varphi_\beta)$$

(3.151)

where

$$\Pi_{\lambda,\nu,\mu}^{l,n,m}(\mathbf{R}_{\alpha\beta}) = j_\lambda(ka_\beta)\sum_{p=|l-\lambda|}^{l+\lambda}(i)^{\lambda-l-p}h_p^{(1)}(kR_{\alpha\beta})Y_{p,m-\mu}(\Theta_{\alpha\beta},\Phi_{\alpha\beta})\sqrt{\frac{4\pi(2\lambda+1)(2p+1)}{2l+1}}$$
$$\times C_{\lambda,0,p,0}^{l,0}\sum_{\tau=-1}^{1}C_{l,m-\tau,1,\tau}^{n,m}C_{\lambda,\mu-\tau,1,\tau}^{\nu,\mu}C_{\lambda,\mu-\tau,p,m-\mu}^{l,m-\tau}$$

(3.152)

To obtain **UVW** multipole fields from the addition theorems, we must express the addition

theorems in terms of spherical wave functions of order λ. To do this we pull the $j_\lambda(ka_\beta)$ term out of the

translation coefficient and define a new translation coefficient $Z_{\lambda,\nu,\mu}^{l,n,m}(\mathbf{R}_{\alpha\beta})$:

$$h_l^{(1)}(kr_\alpha)\mathbf{Y}_{nm}^l(\theta_\alpha,\varphi_\alpha) = \sum_{\nu=0}^{\infty}\sum_{\lambda=\nu-1}^{\nu+1}\sum_{\mu=-\nu}^{+\nu}Z_{\lambda,\nu,\mu}^{l,n,m}(\mathbf{R}_{\alpha\beta})j_\lambda(ka_\beta)\mathbf{Y}_{\nu\mu}^{\lambda}(\theta_\beta,\varphi_\beta) \qquad (3.153)$$

Note that a_β is just r_β evaluated at the surface of the receiving sphere. The new translation coefficient

$Z_{\lambda,\nu,\mu}^{l,n,m}(\mathbf{R}_{\alpha\beta})$ is just

$$Z_{\lambda,\nu,\mu}^{l,n,m}(\mathbf{R}_{\alpha\beta}) = \sum_{p=|l-\lambda|}^{l+\lambda}(i)^{\lambda-l-p}h_p^{(1)}(kR_{\alpha\beta})Y_{p,m-\mu}(\Theta_{\alpha\beta},\Phi_{\alpha\beta})\sqrt{\frac{4\pi(2\lambda+1)(2p+1)}{2l+1}}$$

$$\times C_{\lambda,0,p,0}^{l,0}\sum_{\tau=-1}^{1}C_{l,m-\tau,1,\tau}^{n,m}C_{\lambda,\mu-\tau,1,\tau}^{\nu,\mu}C_{\lambda,\mu-\tau,p,m-\mu}^{l,m-\tau}$$

$$(3.154)$$

We are now in a position to compute how the longitudinal field **U** translates from one sphere to

another. The outgoing wavefield from the transmitting sphere is

$$\mathbf{U}_{nm}(r_\alpha) = G_{nm}\left[\sqrt{\frac{n}{2n+1}}h_{n-1}^{(1)}(kr_\alpha)\mathbf{Y}_{nm}^{n-1}(\theta_\alpha,\varphi_\alpha)+\sqrt{\frac{n+1}{2n+1}}h_{n+1}^{(1)}(kr_\alpha)\mathbf{Y}_{nm}^{n+1}(\theta_\alpha,\varphi_\alpha)\right] \qquad (3.155)$$

and the incoming wavefield to the receiving sphere is

$$\mathbf{U}_{\nu\mu}(r_\beta) = A_{\nu\mu}\left[\sqrt{\frac{\nu}{2\nu+1}}j_{\nu-1}(ka_\beta)\mathbf{Y}_{\nu\mu}^{\nu-1}(\theta_\beta,\varphi_\beta)+\sqrt{\frac{\nu+1}{2\nu+1}}j_{\nu+1}(ka_\beta)\mathbf{Y}_{\nu\mu}^{\nu+1}(\theta_\beta,\varphi_\beta)\right] \qquad (3.156)$$

Expanding the $h_l^{(1)}(kr_\alpha)\mathbf{Y}_{nm}^l(\theta_\alpha,\varphi_\alpha)$ terms in the outgoing field (Eq. 3.155) with the addition theorem

produces six terms. We regroup the translated terms and equate them to the incoming field (Eq. 3.156)

according to their vector spherical harmonic components. After some lengthy algebra we arrive at the

following three simultaneous equations:

$$A_{\nu\mu}^{nm} = G_{nm}\sqrt{\frac{2\nu+1}{\nu}}\left[\sqrt{\frac{n}{2n+1}}Z_{\nu-1,\nu,\mu}^{n-1,n,m}+\sqrt{\frac{n+1}{2n+1}}Z_{\nu-1,\nu,\mu}^{n+1,n,m}\right] \qquad (3.157)$$

$$\sqrt{\frac{n}{2n+1}}Z^{n-1,n,m}_{v,v,\mu} + \sqrt{\frac{n+1}{2n+1}}Z^{n+1,n,m}_{v,v,\mu} = 0 \qquad (3.158)$$

$$A^{nm}_{v\mu} = G_{nm}\sqrt{\frac{2v+1}{v+1}}\left[\sqrt{\frac{n}{2n+1}}Z^{n-1,n,m}_{v+1,v,\mu} + \sqrt{\frac{n+1}{2n+1}}Z^{n+1,n,m}_{v+1,v,\mu}\right] \qquad (3.159)$$

Note that there are two equations for the incident wavefield coefficient $A^{nm}_{v\mu}$ in terms of

translation coefficients and the scattered wavefield coefficient G_{nm}. We therefore have two solutions for

translation of the longitudinal field. Numerical testing has verified that these two equations are equal. The

following condition can therefore be derived for the translation coefficients (along with Eq. 3.158, which is

a second condition on the translation coefficients):

$$\frac{1}{\sqrt{v}}\left[\sqrt{n}\cdot Z^{n-1,n,m}_{v-1,v,\mu} + \sqrt{n+1}\cdot Z^{n+1,n,m}_{v-1,v,\mu}\right] = \frac{1}{\sqrt{v+1}}\left[\sqrt{n}\cdot Z^{n-1,n,m}_{v+1,v,\mu} + \sqrt{n+1}\cdot Z^{n+1,n,m}_{v+1,v,\mu}\right] \qquad (3.160)$$

We note that the above conditions can be used to build recursion relations for the vector addition theorem.

Using the same approach for the electric (**V**) and magnetic (**W**) multipole fields, we will derive the

incoming wavefield coefficients from the translation expansions of the outgoing coefficients. The outgoing

electric and magnetic (or SE and SM) wavefields from the transmitting sphere are

$$\mathbf{V}_{nm}(r_\alpha) = iH_{nm}\left[\sqrt{\frac{n+1}{2n+1}}h^{(1)}_{n-1}(kr_\alpha)\mathbf{Y}^{n-1}_{nm}(\theta_\alpha,\varphi_\alpha) - \sqrt{\frac{n}{2n+1}}h^{(1)}_{n+1}(kr_\alpha)\mathbf{Y}^{n+1}_{nm}(\theta_\alpha,\varphi_\alpha)\right] \qquad (3.161)$$

$$\mathbf{W}_{nm}(r_\alpha) = I_{nm}h^{(1)}_{n}(kr_\alpha)\mathbf{Y}^{n}_{nm}(\theta_\alpha,\varphi_\alpha) \qquad (3.162)$$

The corresponding incoming wavefields to the receiving sphere are

$$\mathbf{V}_{v\mu}(r_\beta) = iB_{v\mu}\left[\sqrt{\frac{v+1}{2v+1}}j_{v-1}(ka_\beta)\mathbf{Y}^{v-1}_{v\mu}(\theta_\beta,\varphi_\beta) - \sqrt{\frac{v}{2v+1}}j_{v+1}(ka_\beta)\mathbf{Y}^{v+1}_{v\mu}(\theta_\beta,\varphi_\beta)\right] \qquad (3.163)$$

$$\mathbf{W}_{v\mu}(r_\beta) = C_{v\mu}j_{v}(ka_\beta)\mathbf{Y}^{v}_{v\mu}(\theta_\beta,\varphi_\beta) \qquad (3.164)$$

Similar to expansion of the longitudinal field, expanding the outgoing electric and magnetic fields

with the addition theorem produces nine terms. Again we regroup the translated terms and equate them to

the incoming fields (Eqs. 3.163, 3.164) according to their vector spherical harmonic components. Again,

after the necessary algebra, we arrive at the following three simultaneous equations for the incident

wavefield coefficients $B_{\nu\mu}$ and $C_{\nu\mu}$:

$$B_{\nu\mu}^{nm} = \sqrt{\frac{2\nu+1}{\nu+1}}\left[H_{nm}\sqrt{\frac{n+1}{2n+1}}Z_{\nu-1,\nu,\mu}^{n-1,n,m} - iI_{nm}Z_{\nu-1,\nu,\mu}^{n,n,m} - H_{nm}\sqrt{\frac{n}{2n+1}}Z_{\nu-1,\nu,\mu}^{n+1,n,m} \right] \quad (3.165)$$

$$C_{\nu\mu}^{nm} = iH_{nm}\sqrt{\frac{n+1}{2n+1}}Z_{\nu,\nu,\mu}^{n-1,n,m} + I_{nm}Z_{\nu,\nu,\mu}^{n,n,m} - iH_{nm}\sqrt{\frac{n}{2n+1}}Z_{\nu,\nu,\mu}^{n+1,n,m} \quad (3.166)$$

$$B_{\nu\mu}^{nm} = -\sqrt{\frac{2\nu+1}{\nu}}\left[H_{nm}\sqrt{\frac{n+1}{2n+1}}Z_{\nu+1,\nu,\mu}^{n-1,n,m} - iI_{nm}Z_{\nu+1,\nu,\mu}^{n,n,m} - H_{nm}\sqrt{\frac{n}{2n+1}}Z_{\nu+1,\nu,\mu}^{n+1,n,m} \right] \quad (3.167)$$

There is only one equation for the $C_{\nu\mu}^{nm}$ coefficient (Eq. 3.166). Again, the two equations for the

$B_{\nu\mu}^{nm}$ coefficient have been shown to be equivalent with numerical testing, and therefore require the

following condition to hold true:

$$\sqrt{\nu}\left[H_{nm}\sqrt{\frac{n+1}{2n+1}}Z_{\nu-1,\nu,\mu}^{n-1,n,m} - iI_{nm}Z_{\nu-1,\nu,\mu}^{n,n,m} - H_{nm}\sqrt{\frac{n}{2n+1}}Z_{\nu-1,\nu,\mu}^{n+1,n,m} \right] =$$
$$-\sqrt{\nu+1}\left[H_{nm}\sqrt{\frac{n+1}{2n+1}}Z_{\nu+1,\nu,\mu}^{n-1,n,m} - iI_{nm}Z_{\nu+1,\nu,\mu}^{n,n,m} - H_{nm}\sqrt{\frac{n}{2n+1}}Z_{\nu+1,\nu,\mu}^{n+1,n,m} \right] \quad (3.168)$$

Since the coefficients H_{nm} and I_{nm} are independent, the condition in Eq. 3.168 is actually two conditions that

again may be useful for recursion formulas:

$$\frac{1}{\sqrt{\nu+1}}\left[\sqrt{n+1}\cdot Z_{\nu-1,\nu,\mu}^{n-1,n,m} - \sqrt{n}\cdot Z_{\nu-1,\nu,\mu}^{n+1,n,m} \right] = -\frac{1}{\sqrt{\nu}}\left[\sqrt{n+1}\cdot Z_{\nu+1,\nu,\mu}^{n-1,n,m} - \sqrt{n}\cdot Z_{\nu+1,\nu,\mu}^{n+1,n,m} \right] \quad (3.169)$$

$$\sqrt{\nu}\cdot Z_{\nu-1,\nu,\mu}^{n,n,m} + \sqrt{\nu+1}\cdot Z_{\nu+1,\nu,\mu}^{n,n,m} = 0 \quad (3.170)$$

In the more traditional S and T translation coefficient notation (Eqs. 3.53, 3.54), we have the

following for the direct electric-to-electric field (E→E) translation:

$$S_{\nu\mu(E\to E)}^{nm} = \sqrt{\frac{2\nu+1}{\nu+1}}\left(\sqrt{\frac{n+1}{2n+1}}Z_{\nu-1,\nu,\mu}^{n-1,n,m} - \sqrt{\frac{n}{2n+1}}Z_{\nu-1,\nu,\mu}^{n+1,n,m} \right) \quad (3.171)$$

or

$$S_{v\mu(E \to E)}^{nm} = -\sqrt{\frac{2v+1}{v}}\left(\sqrt{\frac{n+1}{2n+1}}Z_{v+1,v,\mu}^{n-1,n,m} - \sqrt{\frac{n}{2n+1}}Z_{v+1,v,\mu}^{n+1,n,m}\right) \tag{3.172}$$

For the direct magnetic-to-magnetic field (M→M) translation, we have the following:

$$S_{v\mu(M \to M)}^{nm} = Z_{v,v,\mu}^{n,n,m} \tag{3.173}$$

For the indirect magnetic-to-electric field (M→E) translation, we have

$$T_{v\mu(M \to E)}^{nm} = -i\sqrt{\frac{2v+1}{v+1}}Z_{v-1,v,\mu}^{n,n,m} \tag{3.174}$$

or

$$T_{v\mu(M \to E)}^{nm} = i\sqrt{\frac{2v+1}{v}}Z_{v+1,v,\mu}^{n,n,m} \tag{3.175}$$

Finally, for the indirect electric-to-magnetic field (E→M) translation, we have

$$T_{v\mu(E \to M)}^{nm} = i\sqrt{\frac{n+1}{2n+1}}Z_{v,v,\mu}^{n-1,n,m} - i\sqrt{\frac{n}{2n+1}}Z_{v,v,\mu}^{n+1,n,m} \tag{3.176}$$

Due to the symmetry of our addition theorems, Eq. 3.171, 3.172, and 3.173 are equivalent. Eqs. 3.174, 3.175, and 3.176 are also equal to each other. Again, these equivalencies will allow us to construct recursion relations for the vector addition theorem if found useful (*e.g.*, more computationally efficient).

3.4 (d) Translation of Vector Fields using Potentials

Since the electromagnetic and elastic wave fields can be derived from potentials, these vector fields can also be translated via their potentials. To do this we first express the (vector fields + amplitude coefficients) as (potential fields + amplitude coefficients). The potential fields are then translated into the new coordinate system. Equating the translated outgoing potential fields with the incoming potential fields allows the addition theorem relationships to be derived for the amplitude coefficients. The potential method for translating the vector fields is better than the vector method for one reason: computation of the scalar addition theorem for the longitudinal waves is more efficient than computation using the vector addition theorem.

We first start with the longitudinal field **U**. Recall that the vector fields for longitudinal waves can be expressed as the gradient of a scalar potential $\Phi_{nm} = G_{nm}h_n^{(1)}(kr_\alpha)Y_{nm}(\theta_\alpha,\varphi_\alpha)$:

$$\mathbf{U}_{nm} = \frac{1}{k}\nabla\Phi_{nm} = G_{nm}\left[\begin{array}{c} \sqrt{\dfrac{n}{2n+1}}h_{n-1}^{(1)}(kr_\alpha)\mathbf{Y}_{nm}^{n-1}(\theta_\alpha,\varphi_\alpha) \\ +\sqrt{\dfrac{n+1}{2n+1}}h_{n+1}^{(1)}(kr_\alpha)\mathbf{Y}_{nm}^{n+1}(\theta_\alpha,\varphi_\alpha) \end{array}\right] \tag{3.177}$$

We expand the scalar potential and derive the translated vector field by taking the gradient of the translated potential in the β coordinate system. Since the scalar addition theorem is of the form

$$h_n^{(1)}(kr_\alpha)Y_{n,m}(\theta_\alpha,\varphi_\alpha) = \sum_{\nu=0}^{\infty}\sum_{\mu=-\nu}^{\nu}Z_{\nu,\mu}^{n,m}j_\nu(ka_\beta)Y_{\nu\mu}(\theta_\beta,\varphi_\beta) \tag{3.178}$$

the outgoing wave field potential is therefore expressed as

$$\Phi_{nm}^{\alpha} = G_{nm}h_n^{(1)}(kr_\alpha)Y_{n,m}(\theta_\alpha,\varphi_\alpha) = G_{nm}\sum_{\nu=0}^{\infty}\sum_{\mu=-\nu}^{\nu}Z_{\nu,\mu}^{n,m}j_\nu(ka_\beta)Y_{\nu\mu}(\theta_\beta,\varphi_\beta) \tag{3.179}$$

Summing over n and m yields the total outgoing wave field potential:

$$\Phi^{\alpha} = \sum_{n=0}^{\infty}\sum_{m=-n}^{n}G_{nm}\sum_{\nu=0}^{\infty}\sum_{\mu=-\nu}^{\nu}Z_{\nu,\mu}^{n,m}j_\nu(ka_\beta)Y_{\nu\mu}(\theta_\beta,\varphi_\beta) \tag{3.180}$$

The incoming wave field potential for the β particle is of the following form:

$$\Phi_{\nu\mu}^{\beta} = A_{\nu\mu}j_\nu(kr_\beta)Y_{\nu\mu}(\theta_\beta,\varphi_\beta) \tag{3.181}$$

Each $A_{\nu\mu}$ coefficient will have n,m sub-coefficients ($A_{\nu\mu}^{nm}$) contributed from the scattered field of the transmitting sphere α:

$$\Phi_{\nu\mu}^{\beta} = \sum_{n=0}^{\infty}\sum_{m=-n}^{n}A_{\nu\mu}^{nm}j_\nu(kr_\beta)Y_{\nu\mu}(\theta_\beta,\varphi_\beta) \tag{3.182}$$

Finally, we sum over ν and μ to get the total incoming wave field potential:

$$\Phi^{\beta} = \sum_{n=0}^{\infty}\sum_{m=-n}^{n}\sum_{\nu=0}^{\infty}\sum_{\mu=-\nu}^{\nu}A_{\nu\mu}^{nm}j_\nu(kr_\beta)Y_{\nu\mu}(\theta_\beta,\varphi_\beta) \tag{3.183}$$

Equating Φ^α and Φ^β at the surface of sphere β yields the following translation equation for the wave field coefficients:

$$\sum_{n=0}^{\infty}\sum_{m=-n}^{n}\sum_{\nu=0}^{\infty}\sum_{\mu=-\nu}^{\nu}G_{nm}Z_{\nu,\mu}^{n,m}j_\nu(ka_\beta)Y_{\nu\mu}(\theta_\beta,\varphi_\beta) = \sum_{n=0}^{\infty}\sum_{m=-n}^{n}\sum_{\nu=0}^{\infty}\sum_{\mu=-\nu}^{\nu}A_{\nu\mu}^{nm}j_\nu(ka_\beta)Y_{\nu\mu}(\theta_\beta,\varphi_\beta) \qquad (3.184)$$

From inspection the $A_{\nu\mu}^{nm}$ sub-coefficients can be solved for:

$$A_{\nu\mu}^{nm} = G_{nm}Z_{\nu,\mu}^{n,m} \qquad (3.185)$$

Summing the $A_{\nu\mu}^{nm}$ sub-coefficients over n and m yields the $A_{\nu\mu}$ coefficients:

$$A_{\nu\mu} = \sum_{n=0}^{\infty}\sum_{m=-n}^{n}A_{\nu\mu}^{nm} \qquad (3.186)$$

The coefficients for the electric and magnetic multipole fields can be translated in a similar manner. Recall that the vector fields for the electric (SE) and magnetic (SM) waves can be expressed respectively as the curl and curl-curl of a vector potential $\mathbf{\Psi} = \sum_{n=0}^{\infty}\sum_{m=-n}^{+n}z_n(kr)\mathbf{Y}_{nm}^n(\theta,\varphi)$:

$$\mathbf{V}_{nm} = \frac{1}{k}\nabla\times\mathbf{\Psi}_{nm}^E = H_{nm}\left[\begin{array}{c} i\sqrt{\dfrac{n+1}{2n+1}}h_{n-1}^{(1)}(kr_\alpha)\mathbf{Y}_{nm}^{n-1}(\theta_\alpha,\varphi_\alpha) \\[2ex] -i\sqrt{\dfrac{n}{2n+1}}h_{n+1}^{(1)}(kr_\alpha)\mathbf{Y}_{nm}^{n+1}(\theta_\alpha,\varphi_\alpha) \end{array}\right] \qquad (3.187)$$

$$\mathbf{W}_{nm} = \frac{1}{k^2}\nabla\times(\nabla\times\mathbf{\Psi}_{nm}^M) = I_{nm}h_n^{(1)}(kr_\alpha)\mathbf{Y}_{nm}^n(\theta_\alpha,\varphi_\alpha) \qquad (3.188)$$

We now use the vector addition theorem. Note, however, the vector potential has only one vector spherical harmonic with $l = n$, therefore simplifying the expansions. The outgoing wave field potentials are

$$\mathbf{\Psi}_{nm}^E = H_{nm}h_n^{(1)}(kr_\alpha)\mathbf{Y}_{nm}^n(\theta_\alpha,\varphi_\alpha) = H_{nm}\sum_{\nu=0}^{\infty}\sum_{\lambda=\nu-1}^{\nu+1}\sum_{\mu=-\nu}^{+\nu}Z_{\lambda,\nu,\mu}^{n,n,m}(\mathbf{R}_{\alpha\beta})j_\lambda(ka_\beta)\mathbf{Y}_{\nu\mu}^\lambda(\theta_\beta,\varphi_\beta) \qquad (3.189)$$

$$\mathbf{\Psi}_{nm}^M = I_{nm}h_n^{(1)}(kr_\alpha)\mathbf{Y}_{nm}^n(\theta_\alpha,\varphi_\alpha) = I_{nm}\sum_{\nu=0}^{\infty}\sum_{\lambda=\nu-1}^{\nu+1}\sum_{\mu=-\nu}^{+\nu}Z_{\lambda,\nu,\mu}^{n,n,m}(\mathbf{R}_{\alpha\beta})j_\lambda(ka_\beta)\mathbf{Y}_{\nu\mu}^\lambda(\theta_\beta,\varphi_\beta) \qquad (3.190)$$

Again we sum over n and m to produce the total outgoing wave field potential:

$$\Psi^E = \sum_{n=0}^{\infty} \sum_{m=-n}^{n} H_{nm} \sum_{v=0}^{\infty} \sum_{\lambda=v-1}^{v+1} \sum_{\mu=-v}^{+v} Z_{\lambda,v,\mu}^{n,n,m}(\mathbf{R}_{\alpha\beta}) j_\lambda(ka_\beta) \mathbf{Y}_{v\mu}^\lambda(\theta_\beta, \varphi_\beta) \tag{3.191}$$

$$\Psi^M = \sum_{n=0}^{\infty} \sum_{m=-n}^{n} I_{nm} \sum_{v=0}^{\infty} \sum_{\lambda=v-1}^{v+1} \sum_{\mu=-v}^{+v} Z_{\lambda,v,\mu}^{n,n,m}(\mathbf{R}_{\alpha\beta}) j_\lambda(ka_\beta) \mathbf{Y}_{v\mu}^\lambda(\theta_\beta, \varphi_\beta) \tag{3.192}$$

Note that Eqs. 3.189-3.192 have $\lambda = v+1$, $\lambda = v$, and $\lambda = v-1$ expansion coefficients. The $\lambda = v$ coefficients represent direct translations of the electric and magnetic fields. That is, the electric potential translates to an electric potential (electric→electric), and the magnetic potential translates to a magnetic potential (magnetic→magnetic). The $\lambda = v+1$ and $\lambda = v-1$ coefficients represent indirect or "conversion" translations, where the electric field translates to a magnetic field (electric→magnetic), and the magnetic field translates to an electric field (magnetic→electric). This comes about due to the form of the vector field solutions when the curl (or curl-curl) is taken of the $\mathbf{Y}_{v\mu}^{v+1}$ and $\mathbf{Y}_{v\mu}^{v-1}$ vector spherical harmonic terms.

The $\lambda = v$ condition results in incoming wave field potentials of the form

$$\Psi_{v\mu}^E = B_{v\mu} j_v(kr_\beta) \mathbf{Y}_{v\mu}^v(\theta_\beta, \varphi_\beta) \tag{3.193}$$

$$\Psi_{v\mu}^M = C_{v\mu} j_v(kr_\beta) \mathbf{Y}_{v\mu}^v(\theta_\beta, \varphi_\beta) \tag{3.194}$$

Since these vector potentials are of the same form as the original, untranslated vector potentials, they will produce the analogous fields (electric → electric and magnetic → magnetic) when the curl and curl-curl operations are performed on them. The addition theorem translation coefficient is simplified in this case to $Z_{v,v,\mu}^{n,n,m}(\mathbf{R}_{\alpha\beta})$. As in the longitudinal wave field case, we split the $B_{v\mu}$ and $C_{v\mu}$ coefficients into $B_{v\mu}^{nm}$ and $C_{v\mu}^{nm}$ sub-coefficients for the incoming wave field potential:

$$\Psi_{vw}^E = \sum_{n=0}^{\infty} \sum_{m=-n}^{n} B_{v\mu}^{nm} j_v(kr_\beta) \mathbf{Y}_{v\mu}^v(\theta_\beta, \varphi_\beta) \tag{3.195}$$

$$\Psi_{vw}^M = \sum_{n=0}^{\infty} \sum_{m=-n}^{n} C_{v\mu}^{nm} j_v(kr_\beta) \mathbf{Y}_{v\mu}^v(\theta_\beta, \varphi_\beta) \tag{3.196}$$

Finally, we sum over v and μ to arrive at the total incoming wave field potential:

$$\Psi^E = \sum_{n=0}^{\infty} \sum_{m=-n}^{n} \sum_{v=0}^{\infty} \sum_{\mu=-v}^{v} B_{v\mu}^{nm} j_v(kr_\beta) \mathbf{Y}_{v\mu}^v(\theta_\beta, \varphi_\beta) \tag{3.197}$$

$$\Psi^M = \sum_{n=0}^{\infty} \sum_{m=-n}^{n} \sum_{v=0}^{\infty} \sum_{\mu=-v}^{v} C_{v\mu}^{nm} j_v(kr_\beta) \mathbf{Y}_{v\mu}^v(\theta_\beta, \varphi_\beta) \tag{3.198}$$

We now equate the outgoing wave field potentials (from sphere α) to the incoming wave field potentials (to sphere β) at the surface of sphere β to arrive at the following translation equations for the wave field coefficients:

$$B_{v\mu(E \to E)}^{nm} = H_{nm} Z_{v,v,\mu}^{n,n,m} \tag{3.199} \quad ; \quad C_{v\mu(M \to M)}^{nm} = I_{nm} Z_{v,v,\mu}^{n,n,m} \tag{3.200}$$

This result is equivalent to the direct translation result in Eq. 3.173. As used before, the (E→E) and (M→M) subscripts denote that these sub-coefficients come from a direct translation of the vector potential. Again, summing over n and m yields the $B_{v\mu}$ and $C_{v\mu}$ coefficients:

$$B_{v\mu(E \to E)} = \sum_{n=0}^{\infty} \sum_{m=-n}^{n} B_{v\mu(E \to E)}^{nm} \tag{3.201} \qquad C_{v\mu(M \to M)} = \sum_{n=0}^{\infty} \sum_{m=-n}^{n} C_{v\mu(M \to M)}^{nm} \tag{3.202}$$

There will also be sub-coefficients that will come from a conversion translation of the vector potential, denoted with (E→M) and (M→E) subscripts. The $\lambda = v-1$ and $\lambda = v+1$ conditions result in incoming wave field potentials of the form

$$\Psi_{v\mu(v-1)}^E = B_{v\mu(v-1)} j_{v-1}(kr_\beta) \mathbf{Y}_{v\mu}^{v-1}(\theta_\beta, \varphi_\beta) \tag{3.203}$$

$$\Psi_{v\mu(v+1)}^E = B_{v\mu(v+1)} j_{v+1}(kr_\beta) \mathbf{Y}_{v\mu}^{v+1}(\theta_\beta, \varphi_\beta) \tag{3.204}$$

$$\Psi_{v\mu(v-1)}^M = C_{v\mu(v-1)} j_{v-1}(kr_\beta) \mathbf{Y}_{v\mu}^{v-1}(\theta_\beta, \varphi_\beta) \tag{3.205}$$

$$\Psi_{v\mu(v+1)}^M = C_{v\mu(v+1)} j_{v+1}(kr_\beta) \mathbf{Y}_{v\mu}^{v+1}(\theta_\beta, \varphi_\beta) \tag{3.206}$$

Since these vector potentials are different from the original, untranslated vector potentials, they will produce different fields (electric→magnetic and magnetic→electric) when the curl and curl-curl operations are performed on them, respectively. For the v-1 component we get

$$\frac{1}{k}\nabla \times j_{\nu-1}(kr_\beta)\mathbf{Y}_{\nu\mu}^{\nu-1}(\theta_\beta,\varphi_\beta) = -i\sqrt{\frac{\nu+1}{2\nu+1}}j_\nu(kr_\beta)\mathbf{Y}_{\nu\mu}^\nu(\theta_\beta,\varphi_\beta) \tag{3.207}$$

$$\frac{1}{k^2}\nabla \times \left[\nabla \times j_{\nu-1}(kr_\beta)\mathbf{Y}_{\nu\mu}^{\nu-1}(\theta_\beta,\varphi_\beta)\right] =$$
$$\sqrt{\frac{\nu+1}{2\nu+1}}\left[\sqrt{\frac{\nu+1}{2\nu+1}}j_{\nu-1}(kr_\beta)\mathbf{Y}_{\nu\mu}^{\nu-1}(\theta_\beta,\varphi_\beta) - \sqrt{\frac{\nu}{2\nu+1}}j_{\nu+1}(kr_\beta)\mathbf{Y}_{\nu\mu}^{\nu+1}(\theta_\beta,\varphi_\beta)\right] \tag{3.208}$$

Note that the curl of the ν-1 component yields a multipole field of the magnetic form, whereas the curl-curl of the ν-1 component yields a multipole field of the electric form.

For the ν+1 component we get

$$\frac{1}{k}\nabla \times j_{\nu+1}(kr_\beta)\mathbf{Y}_{\nu\mu}^{\nu+1}(\theta_\beta,\varphi_\beta) = i\sqrt{\frac{\nu}{2\nu+1}}j_\nu(kr_\beta)\mathbf{Y}_{\nu\mu}^\nu(\theta_\beta,\varphi_\beta) \tag{3.209}$$

$$\frac{1}{k^2}\nabla \times \left[\nabla \times j_{\nu+1}(kr_\beta)\mathbf{Y}_{\nu\mu}^{\nu+1}(\theta_\beta,\varphi_\beta)\right] =$$
$$-\sqrt{\frac{\nu}{2\nu+1}}\left[\sqrt{\frac{\nu+1}{2\nu+1}}j_{\nu-1}(kr_\beta)\mathbf{Y}_{\nu\mu}^{\nu-1}(\theta_\beta,\varphi_\beta) - \sqrt{\frac{\nu}{2\nu+1}}j_{\nu+1}(kr_\beta)\mathbf{Y}_{\nu\mu}^{\nu+1}(\theta_\beta,\varphi_\beta)\right] \tag{3.210}$$

Similar to the ν-1 component, the curl of the ν+1 component again yields a multipole field of the magnetic form, whereas the curl-curl of the ν+1 component again yields a multipole field of the electric form.

We now look at the individual potentials. The incoming magnetic wave field evolves from the outgoing electric potential (E→M):

$$\frac{1}{k}\nabla \times \mathbf{\Psi}_{(E\to M)}^E =$$
$$\sum_{n=0}^\infty \sum_{m=-n}^n H_{nm} \sum_{\nu=0}^\infty \sum_{\mu=-\nu}^\nu \left[\sqrt{\nu}\cdot Z_{\nu+1,\nu,\mu}^{n,n,m} - \sqrt{\nu+1}\cdot Z_{\nu-1,\nu,\mu}^{n,n,m}\right]\frac{i}{\sqrt{2\nu+1}}j_\nu(ka_\beta)\mathbf{Y}_{\nu\mu}^\nu(\theta_\beta,\varphi_\beta) \tag{3.211}$$

We now define a new magnetic field sub-coefficient $C_{\nu\mu(E\to M)}^{nm}$:

$$C_{\nu\mu(E\to M)}^{nm} = H_{nm}\frac{i}{\sqrt{2\nu+1}}\left[\sqrt{\nu}\cdot Z_{\nu+1,\nu,\mu}^{n,n,m} - \sqrt{\nu+1}\cdot Z_{\nu-1,\nu,\mu}^{n,n,m}\right] \tag{3.212}$$

Similarly, the incoming electric field evolves from the outgoing magnetic potential (M→E):

$$\frac{1}{k^2}\nabla\times\left[\nabla\times\mathbf{\Psi}^M_{(M\to E)}\right]=\sum_{n=0}^{\infty}\sum_{m=-n}^{n}I_{nm}\sum_{v=0}^{\infty}\sum_{\mu=-v}^{v}\left[\sqrt{v}\cdot Z^{n,n,m}_{v+1,v,\mu}-\sqrt{v+1}\cdot Z^{n,n,m}_{v-1,v,\mu}\right]$$

$$\times\frac{i}{\sqrt{2v+1}}\left[i\sqrt{\frac{v+1}{2v+1}}j_{v-1}(ka_\beta)\mathbf{Y}^{v-1}_{v\mu}(\theta_\beta,\varphi_\beta)-i\sqrt{\frac{v}{2v+1}}j_{v+1}(ka_\beta)\mathbf{Y}^{v+1}_{v\mu}(\theta_\beta,\varphi_\beta)\right] \quad (3.213)$$

The new electric field sub-coefficient $B^{nm}_{v\mu(M\to E)}$ is similar to the magnetic field sub-coefficient:

$$B^{nm}_{v\mu(M\to E)}=I_{nm}\frac{i}{\sqrt{2v+1}}\left[\sqrt{v}\cdot Z^{n,n,m}_{v+1,v,\mu}-\sqrt{v+1}\cdot Z^{n,n,m}_{v-1,v,\mu}\right] \quad (3.214)$$

To summarize our electric and magnetic field sub-coefficients, we have:

$$B^{nm}_{v\mu(E\to E)}=H_{nm}Z^{n,n,m}_{v,v,\mu} \quad (3.215) \qquad C^{nm}_{v\mu(M\to M)}=I_{nm}Z^{n,n,m}_{v,v,\mu} \quad (3.216)$$

$$B^{nm}_{v\mu(M\to E)}=I_{nm}\frac{i}{\sqrt{2v+1}}\left[\sqrt{v}\cdot Z^{n,n,m}_{v+1,v,\mu}-\sqrt{v+1}\cdot Z^{n,n,m}_{v-1,v,\mu}\right] \quad (3.217)$$

$$C^{nm}_{v\mu(E\to M)}=H_{nm}\frac{i}{\sqrt{2v+1}}\left[\sqrt{v}\cdot Z^{n,n,m}_{v+1,v,\mu}-\sqrt{v+1}\cdot Z^{n,n,m}_{v-1,v,\mu}\right] \quad (3.218)$$

Again, we put them into the traditional S and T translation coefficient notation of Eqs. 3.53, 3.54:

$$S^{nm}_{v\mu}=Z^{n,n,m}_{v,v,\mu} \quad (3.219)$$

$$T^{nm}_{v\mu}=\frac{i}{\sqrt{2v+1}}\left[\sqrt{v}\cdot Z^{n,n,m}_{v+1,v,\mu}-\sqrt{v+1}\cdot Z^{n,n,m}_{v-1,v,\mu}\right] \quad (3.220)$$

3.5 Multiple Scattering Computations

The single sphere scattering solutions (Section 3.3) and translation addition theorems (Section 3.4) provide the algorithmic core of the VMIST program. However, to simulate the multiple scattering *in toto* for a particle ensemble and calculate the macroscopic field properties (amplitude and direction as a function of position and frequency), the computations must be performed in a specific sequence of steps. The sequence of steps in the VMIST computation are the following, and are also displayed as a flow diagram in Figure 3-7:

1. Input maximum multipole order *nmax* to compute, maximum number of iterations *imax* to compute if program does not converge, and content of initial plane wave (only for elastic waves; ratio of longitudinal to shear component).

2. Set up frequency loop to scan frequency range for frequency-domain computations, or image grid for spatial-domain computations.

3. Irradiate all of the particles in the ensemble with polarized, phase-corrected plane waves propagating in z-direction.

4. Calculate the scattered wave fields for each particle due to the plane waves (first-order scattering) using the single sphere scattering algorithm.

5. Compute the translation coefficients for all possible particle pairs in the ensemble using the translation addition theorem algorithms.

6. Start iterations—Translate the scattered waves for all particles and sum the translated fields incident on each particle.

7. Calculate the scattered wave fields for each sphere due to the translated waves (second and higher-order scattering) using the single sphere scattering algorithm.

8. Compare new scattered wave field coefficients (new iterated values) with old (previous iterated values) for convergence.

9. If wave field coefficients have not converged to the user-specified criteria, loop back to step 6 and continue computation.

10. If wavefield coefficients have converged to the user-specified criteria, convert wavefields to cartesian coordinates and evaluate fields at evaluation or grid point.

11. Loop back to step 2 for frequency-domain computations, step 10 for spatial domain computations.

12. Output individual wavefield amplitudes— longitudinal, electric (SE), and magnetic (SM)—for the specified point (frequency domain) or image grid (spatial domain).
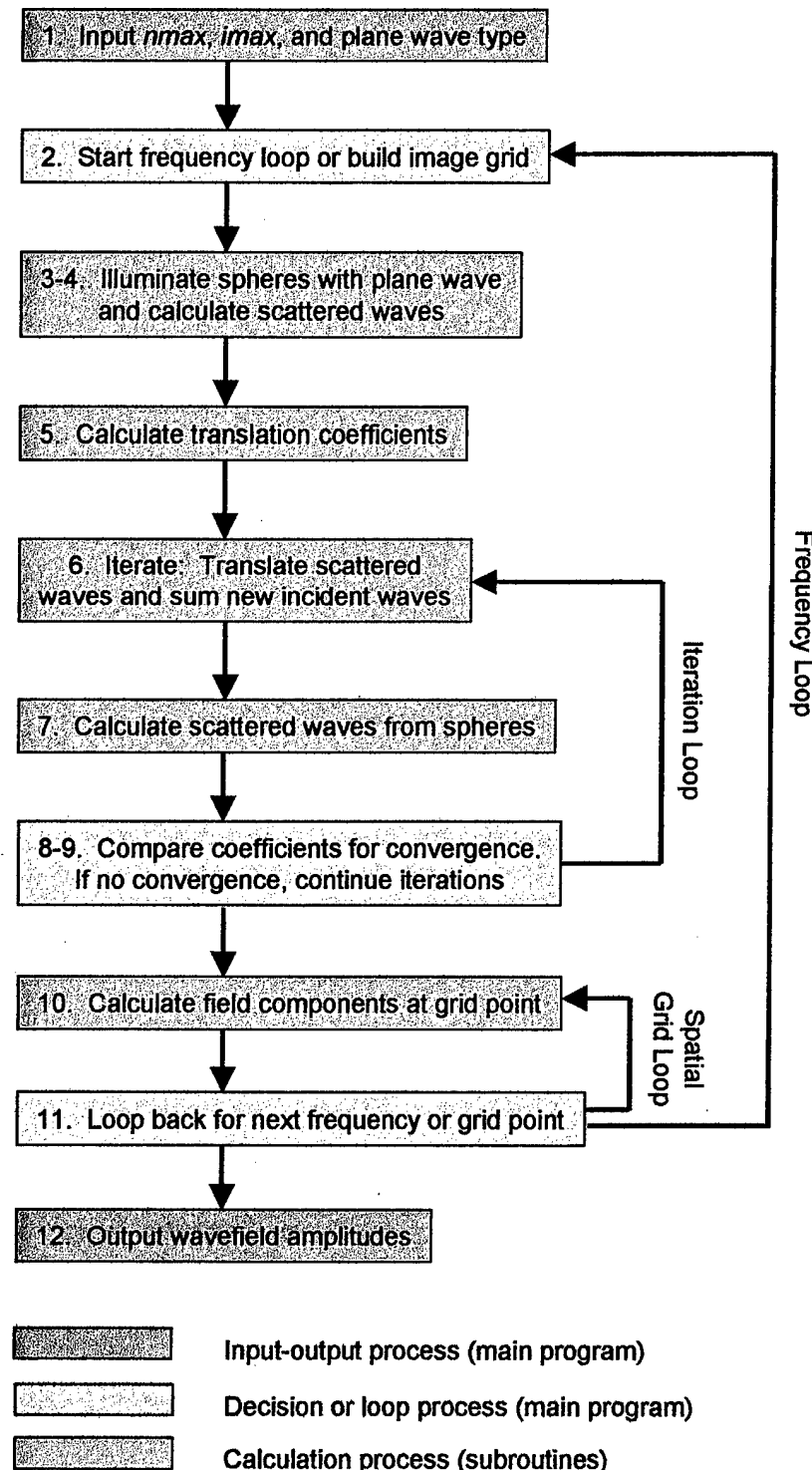
FIGURE 3-7. Flow diagram of computation steps performed in the VMIST algorithm.

The plane wave, scattered wave, and addition theorem expansions are computed to a maximum multipole order n_{max} specified by the user. The value n_{max} truncates these normally infinite expansions, and thereby introduces error into the models. Selection of appropriate n_{max} values for the calculations is therefore critical since the selection will always be a compromise between computation time and accuracy. Although higher n_{max} values provide greater accuracy, they do so at the price of increasing the computation time in an exponential manner. Because of the importance of n_{max} in the simulations, this parameter was examined in detail with respect to convergence, accuracy, and total computation time for the models.

The plane wave expansion for the elastic longitudinal wave can be derived from the plane wave expansion of the scalar potential given by Stratton and Jackson.[9,41] The coefficients used in the VMIST code for constructing a longitudinal plane wave propagating in the z-direction were the following:

$$\mathbf{e}_z e^{ikz} = \sum_{n=0}^{\infty} i^{n-1} \sqrt{4\pi(2n+1)} \mathbf{U}_{n,0} \tag{3.221}$$

Various plane wave expansions have been presented for vector wave fields, and although they are similar in form they do not agree as far as the correct combination of coefficients and vector fields.[9,41,45] Trial-and-error was therefore used with the VMIST code to construct plane wave expansions that produced an electric (shear-electric) field polarized in the x-direction, and a magnetic (shear-magnetic) field polarized in the y-direction. Subsequently, it was found that the trial-and-error results for the longitudinal plane wave expansion was in agreement with Stratton. The trial-and-error expansions for the electric and magnetic multipole fields were in partial agreement with Stratton and Jackson, but differed from the forms given by Greiner and Maruhn.[9,41,45]

The final form of the plane wave expansion for electromagnetic waves propagating in the z-direction was the following:

$$e_x e^{ikz} = \sum_n i^n \sqrt{4\pi(2n+1)} \left[\mathbf{W}_{n,+1} + \mathbf{V}_{n,+1} - \mathbf{W}_{n,-1} - \mathbf{V}_{n,-1} \right] \tag{3.222}$$

$$e_y e^{ikz} = (-i) \sum_n i^n \sqrt{4\pi(2n+1)} \left[\mathbf{W}_{n,+1} + \mathbf{V}_{n,+1} + \mathbf{W}_{n,-1} + \mathbf{V}_{n,-1} \right] \tag{3.223}$$

The final form of the plane wave expansion for shear elastic waves propagating in the z-direction was the following:

$$e_x e^{ikz} = \sum_n i^n \sqrt{4\pi(2n+1)} \left[\mathbf{V}_{n,+1} - \mathbf{V}_{n,-1} \right] \tag{3.224}$$

$$e_y e^{ikz} = (-i) \sum_n i^n \sqrt{4\pi(2n+1)} \left[\mathbf{W}_{n,+1} - \mathbf{W}_{n,-1} \right] \tag{3.225}$$

The plane wave expansions describe waves with a fixed phase with regards to the $z = 0$ plane. Using the plane wave expansions as incident coefficients for each particle is therefore problematic, since the incident coefficients are in terms of the particle's local coordinate system, but their global position with respect to the z-axis determines what the plane wave phase is when it hits the particle. In other words, using the plane wave coefficients as is for the incident coefficients effectively puts all of the particles on the $z = 0$ plane for the initial scattering event. This is not a correct way to model multiple scattering since we have to be concerned with phase interactions and interference effects. Although the phases are automatically taken care of in the translation of the spherical wave fields, they have to be accounted for in the initial plane wave. This is readily accomplished by multiplying the expansion coefficients by a phase factor of $e^{ikR(z)}$, where $R(z)$ is the distance of the particle from the $z = 0$ plane (*i.e.*, its global z coordinate).

After VMIST computes the initial scattering of the plane waves by the particles, the program then computes the translational expansion coefficients all possible particle pairs. Since the coefficients are a function of the wave vector k in the spherical Bessel functions, they have to be recomputed for each frequency step in a frequency-domain computation. This makes the frequency domain computations much more time-consuming than the spatial domain computations, where the frequency is fixed but the fields are evaluated at several points in an image grid.

Once the translation coefficients are computed the iterations begin (Figure 3-8). During an iteration step, the outgoing scattered wavefields from each particle are translated into incident wavefields for all of the other particles. For a particle ensemble of N particles, there will be 2(N-1) or 3(N-1) (electromagnetic or elastic fields, respectively) new incident wave field coefficients for each particle. These new incident coefficients are summed and added to the old coefficients. Each i-th iteration represents an i+1 multiple scattering order (first-order scattering being the initial plane wave scattering), and each new contribution to the field coefficients gets smaller and smaller until the field coefficients for all of the particles converge to a stable value.
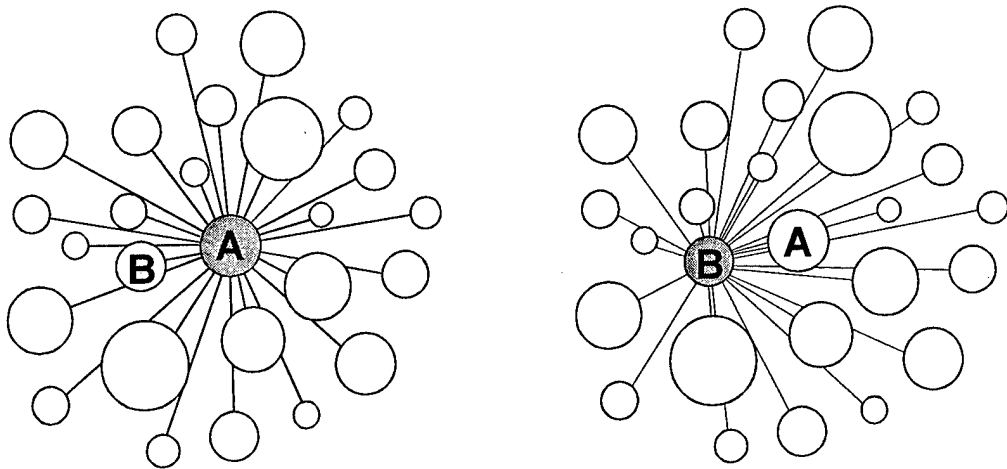
FIGURE 3-8. Illustration showing how each particle interacts with (N-1) particles in an N-particle dispersion, resulting in N(N-1) total interactions. The interactions are iterated through all of the particles, firsat A, then B, etc.—until all interactions have been accounted for. The iterations then continue with A again, B, etc. until the scattered field amplitudes from all particles converge.

Convergence is measured by comparing the sum total of all of the field coefficients between two successive iteration steps. If the relative difference between the the two coefficient sums is less than the specified convergence criteria (for example, a change of less than 10^{-6}), then the iteration procedure stops. The coefficients are then used to compute the fields at an evaluation point. The fields for each particle are converted into cartesian coordinates and evaluated at the evaluation point using the position vector between the particle and the point. The fields for all of the particles are summed at the evaluation point to yield the total vector field strength. The longitudinal, shear-electric (electric), and shear-magnetic (magnetic) fields are kept separate, however, to ascertain the contribution of each to the total field at that point.

If a frequency-domain analysis (spectrum) is desired, only a single evaluation is used, but the the entire computation—from initial plane wave to final evaluation of converged coefficients—must be repeated for each frequency step. As previously mentioned, this is a rather time-consuming process. If a spatial-domain analyis (image) is desired, then a planar grid of evaluation points are used. The fields are evaluated at each of the grid points to construct an image of the wavefield amplitudes and directions on the

image plane. The cartesian expansions of the **UVW** multipole fields are rather long and therefore not presented here.

The VMIST algorithms were written, debugged, and compiled in Fortran 90. The translational addition theorem tests and VMIST simulations were performed on a personal desktop computer with 256 MB RAM and an AMD Athalon XP 2000+ processor running at 1.679 GHz.

CHAPTER 4

RESULTS: TRANSLATIONAL ADDITION THEOREMS

4.1 Mathematical Review and Comparisons

Convergence tests were performed for the vector addition theorem derived in Section 3.4 (a) and the scalar addition theorem presented in Section 3.4 (b) For review, the vector addition theorem derived for pure-orbital vector spherical harmonics using an integral transform method is the following:

$$h_l^{(1)}(kr_\alpha)\mathbf{Y}_{nm}^l(\theta_\alpha,\varphi_\alpha) = \sum_{\nu=0}^{\infty}\sum_{\lambda=\nu-1}^{\nu+1}\sum_{\mu=-\nu}^{+\nu}Z_{\lambda,\nu,\mu}^{l,n,m}(\mathbf{R}_{\alpha\beta})j_\lambda(ka_\beta)\mathbf{Y}_{\nu\mu}^\lambda(\theta_\beta,\varphi_\beta) \tag{4.1}$$

where

$$Z_{\lambda,\nu,\mu}^{l,n,m}(\mathbf{R}_{\alpha\beta}) = \sum_{p=|l-\lambda|}^{l+\lambda}(i)^{\lambda-l-p}h_p^{(1)}(kR_{\alpha\beta})Y_{p,m-\mu}(\Theta_{\alpha\beta},\Phi_{\alpha\beta})\sqrt{\frac{4\pi(2\lambda+1)(2p+1)}{2l+1}}$$

$$\times C_{\lambda,0,p,0}^{l,0}\sum_{\tau=-1}^{1}C_{l,m-\tau,1,\tau}^{n,m}C_{\lambda,\mu-\tau,1,\tau}^{\nu,\mu}C_{\lambda,\mu-\tau,p,m-\mu}^{l,m-\tau}$$

$$\tag{4.2}$$

This theorem will henceforth be called the pure-orbital addition theorem, since it is formulated for the translation of vector multipoles containing pure-orbital vector spherical harmonics. Using the "direct" and "indirect" translation coefficient notation of $S_{\nu\mu}^{nm}$ and $T_{\nu\mu}^{nm}$ respectively, we have

$$S_{\nu\mu}^{nm} = Z_{\nu,\nu,\mu}^{n,n,m} \tag{4.3}$$

$$T_{\nu\mu}^{nm} = \frac{i}{\sqrt{2\nu+1}}\left[\sqrt{\nu}\cdot Z_{\nu+1,\nu,\mu}^{n,n,m} - \sqrt{\nu+1}\cdot Z_{\nu-1,\nu,\mu}^{n,n,m}\right] \tag{4.4}$$

Eqs. 4.2-4.4 comprise the set of pure-orbital addition theorems for translating vector spherical wave functions from one coordinate system to another.

The scalar addition theorem, adapted from Varshalovich et al., is the following:

$$h_n^{(1)}(kr_\alpha)Y_{n,m}(\theta_\alpha,\varphi_\alpha) = \sum_{\nu=0}^{\infty}\sum_{\mu=-\nu}^{\nu}Z_{\nu,\mu}^{n,m}j_\nu(ka_\beta)Y_{\nu\mu}(\theta_\beta,\varphi_\beta) \tag{4.5}$$

where

$$Z_{v,\mu}^{n,m} = \sqrt{4\pi} \sum_{p=0}^{\infty} \left\{ i^{v-p-n} h_p^{(1)}(kR_{\alpha\beta}) Y_{p,m-\mu}(\Theta_{\alpha\beta}, \Phi_{\alpha\beta}) \sqrt{\frac{(2v+1)(2p+1)}{(2n+1)}} C_{v,0,p,0}^{n,0} C_{v,\mu,p,m-\mu}^{n,m} \right\}$$

(4.4)

Testing of the pure-orbital addition theorems was necessary to evaluate their convergence (how fast do they converge?) and correctness (do they converge to the actual translated field values?). Also, since alternate expressions for the addition theorems have been published, a comparison between the pure-orbital theorems derived in this work and those derived by others would be a useful and interesting exercise. Such a comparison has not been previously reported in the open literature despite the variety of expressions that have been put forward for the addition theorems.

Two sets of scalar and vector addition theorems were selected for comparison. The first set were by Cruzan.[55] Cruzan's theorems are essentially the "gold standard" for addition theorems due to the number of times they have been cited and used. Many recursion formulas have also been derived to more efficiently compute Cruzans's addition theorems.[61-64, 91]

The Cruzan vector addition theorems are also significantly mathematically different from those derived in this work. For a fairer comparison and easier programming, the Cruzan theorems were adjusted by converting Wigner 3j coefficients to Clebsch-Gordan coefficients, converting Legendre polynomials and trigonometric functions to spherical harmonic notation, and normalizing to convert from **N** and **M** spherical wave functions to **V** and **W** spherical wave functions. After these changes, the Cruzan vector addition theorems are still mathematically distinct from this work's theorems:

$$S_{v\mu}^{nm}(\mathbf{R}_{\alpha\beta}) = \sqrt{4\pi} \sum_{p} \left\{ \begin{array}{l} z_p(kR_{\alpha\beta}) Y_{p,m-\mu}(\Theta_{\alpha\beta}, \Phi_{\alpha\beta}) C_{v,0,p,0}^{n,0} C_{v,\mu,p,m-\mu}^{n,m} \\ \times a(n,v,p) \sqrt{\dfrac{(v)(v+1)(2p+1)}{(n)(n+1)(2v+1)(2n+1)}} \end{array} \right\}$$

(4.7)

$$T_{v\mu}^{nm}(\mathbf{R}_{\alpha\beta}) = \sqrt{4\pi} \sum_{p} \left\{ \begin{array}{l} z_p(kR_{\alpha\beta}) Y_{p,m-\mu}(\Theta_{\alpha\beta}, \Phi_{\alpha\beta}) C_{v,0,p-1,0}^{n,0} C_{v,\mu,p,m-\mu}^{n,m} \\ \times b(n,v,p) \sqrt{\dfrac{(v)(v+1)(2p+1)}{(n)(n+1)(2v+1)(2n+1)}} \end{array} \right\}$$

(4.8)

where

$$a(n,v,p) = i^{v+p-n} \frac{1}{2v(v+1)} \begin{bmatrix} 2v(v+1)(2v+1) \\ +(v+1)(n-v+p+1)(n+v-p) \\ -v(v-n+p+1)(n+v+p+2) \end{bmatrix} \qquad (4.9)$$

$$b(n,v,p) = i^{v+p-n} \frac{(2v+1)}{2v(v+1)} \begin{bmatrix} (n+v+p+1)(v-n+p) \\ \times(n-v+p)(n+v-p+1) \end{bmatrix}^{1/2} \qquad (4.10)$$

After the required conversions, the Cruzan scalar addition theorem is the same as Eq. 4.4. A minor difference is that Cruzan's coordinate system is inverted, with the displacement vector $\mathbf{R}_{\alpha\beta}$ pointing in the opposite direction (from sphere α to sphere β, instead from sphere β to sphere α as in this work). This only leads to a change in the sign of p in the exponent of the factor $i^{\lambda-p-n}$ in Eq. 4.4, and similarly for the i^{v+p-n} factor in Eqs. 4.9 and 4.10.

The second set of addition theorems were from Liu *et al.*[69] Their theorems were selected for the following reasons:

1. Liu *et al.* is a recent publication, and therefore should reflect the latest and most accurate information.

2. Since Liu *et al.* apply the addition theorems to elastic wave scattering, they present both scalar and vector addition theorems. Most other papers present only the scalar theorem for acoustic (longitudinal wave only) scattering, or only the vector theorems for electromagnetic scattering.

3. The theorems presented by Liu *et al.* are close in form to the pure-orbital addition theorems, with Clebsch-Gordan coefficients and spherical harmonic notation. However, they still differ in content from this work's theorems.

Liu *et al.* use vector wave functions $\mathbf{J}_{nm1}$, $\mathbf{J}_{nm2}$, and $\mathbf{J}_{nm3}$ which are close in form to the $\mathbf{L}$, $\mathbf{M}$, and $\mathbf{N}$ wave functions, and therefore related to the $\mathbf{U}$, $\mathbf{V}$, and $\mathbf{W}$ vector multipole fields, except for a factor of $-i$ for the transverse functions:

$$\mathbf{J}_{nm1}(\mathbf{r}) = \frac{1}{k}\nabla\left[z_n(kr)Y_{nm}(\theta,\varphi)\right]$$

$$= \frac{1}{k}\mathbf{L}_{nm}(-1)^m\sqrt{\frac{2n+1}{4\pi}\frac{(n-m)!}{(n+m)!}} = \mathbf{U}_{nm}(r) \tag{4.11}$$

$$\mathbf{J}_{nm2}(\mathbf{r}) = \frac{1}{\sqrt{n(n+1)}}\nabla\times\left[\mathbf{r}z_n(kr)Y_{nm}(\theta,\varphi)\right]$$

$$= \frac{1}{\sqrt{n(n+1)}}\mathbf{M}_{nm}(-1)^m\sqrt{\frac{2n+1}{4\pi}\frac{(n-m)!}{(n+m)!}} = -i\mathbf{W}_{nm}(\mathbf{r}) \tag{4.12}$$

$$\mathbf{J}_{nm3}(\mathbf{r}) = \frac{1}{k_S\sqrt{n(n+1)}}\nabla\times\nabla\times\left[\mathbf{r}z_n(kr)Y_{nm}(\theta,\varphi)\right]$$

$$= \frac{1}{\sqrt{n(n+1)}}\mathbf{N}_{nm}(-1)^m\sqrt{\frac{2n+1}{4\pi}\frac{(n-m)!}{(n+m)!}} = -i\mathbf{V}_{nm}(\mathbf{r}) \tag{4.13}$$

Liu *et al.* call their addition theorems *structure constants*, and denote them with capital G's. The Liu *et al.* scalar addition theorem is

$$G_{\nu,\mu,L}^{n,m,L}(\mathbf{R}_{\alpha\beta}) = 4\pi\sum_p i^{\nu+p-n}C_{\nu,\mu,p,m-\mu}^{n,m}h_p(k_L R_{\alpha\beta})Y_{p,m-\mu}(\Theta_{\alpha\beta},\Phi_{\alpha\beta}) \tag{4.14}$$

Again, inversion of the coordinate system leads to a change in the sign of p in the factor $i^{\nu+p-n}$. However, Eq. 4.14 differs from Eq. 4.4 by the absence of the factor

$$\sqrt{\frac{(2\nu+1)(2p+1)}{(2n+1)}}C_{\nu,0,p,0}^{n,0} \tag{4.15}$$

which is a significant departure from our scalar addition theorem.

The vector addition theorems in Liu *et al.* were originally presented by Wang *et al.*[65] Their "direct" translation coefficient or structure factor is

$$G_{\nu,\mu,E/M}^{n,m,E/M}(\mathbf{R}_{\alpha\beta}) = 4\pi\sum_p i^{\nu+p-n}h_p(k_S R_{\alpha\beta})Y_{p,m-\mu}(\Theta_{\alpha\beta},\Phi_{\alpha\beta})$$

$$\times\sum_{\tau=-1}^{1}C_{n,m-\tau,1,\tau}^{n,m}C_{\nu,\mu-\tau,1,\tau}^{\nu,\mu}C_{\nu,\mu-\tau,p,m-\mu}^{n,m-\tau} \tag{4.16}$$

Their "indirect" translation coefficient or structure factor is

$$G_{v,\mu,M/E}^{n,m,E/M}(\mathbf{R}_{\alpha\beta}) = -i\sqrt{\frac{2v+1}{v+1}}4\pi\sum_{p} i^{v-1+p-n} h_p(k_S R_{\alpha\beta}) Y_{p,m-\mu}(\Theta_{\alpha\beta},\Phi_{\alpha\beta})$$

$$\times \sum_{\tau=-1}^{1} C_{n,m-\tau,1,\tau}^{n,m} C_{v-1,\mu-\tau,1,\tau}^{v,\mu} C_{v-1,\mu-\tau,p,m-\mu}^{n,m-\tau}$$

(4.17)

As with the Cruzan addition theorems, the Liu *et al.* structure constants also differ by a sign

change in p for the factor i^{v+p-n}, again attributable to a coordinate inversion. However, the differences

between the Liu *et al.* structure constants and the pure-orbital vector addition theorems are significant:

1. A factor of $\sqrt{\frac{(2\lambda+1)(2p+1)}{2l+1}} \times C_{\lambda,0,p,0}^{l,0}$ in the pure-orbital addition theorems is absent from

    Liu *et al.*'s structure constants.

2. Liu *et al.*'s "indirect" structure constant only has a $\lambda = v\text{-}1$ expansion term, whereas the "indirect"

    pure-orbital translation coefficient of Eq. 4.6 has both $\lambda = v\text{-}1$ and $\lambda = v\text{+}1$ expansion terms.

3. Liu *et al.*'s "indirect" structure constant also differs from the $\lambda = v\text{-}1$ term of the "indirect" pure-

    orbital translation coefficient by a factor of $\left(\frac{2\lambda+1}{2l+1}\right)$.

Although the published addition theorems differ from the pure-orbital addition theorems in

analytic form, do they differ numerically when put to the test? The following sections desribe how the

comparison tests were performed and the results.

4.2 Numerical Test Methods

The numerical tests were performed by creating a longitudinal (**U**) field, electric (**V**) field, and

magnetic (**W**) field each with a ($n=2$, $m=1$) quadrupole moment. The fields were translated from the origin

(sphere α) to an evaluation point on the surface of a test sphere (sphere β) using the addition theorems and

translation coefficients for the fields. The radius, distance, and angular orientation of the test sphere with

respect to the origin were varied in the tests, as was the position of the evaluation point. These variations

were incorporated to determine the convergence and accuracy of the addition theorems for a variety of

geometries. Five surface position-radius-distance-orientation variations were tested, and are summarized in Table 4-1. A radius for sphere α (the origin of the translated fields) did not have to be specified since it does not contribute to the translation coefficient computations.

The position of sphere β and of the evaluation point on sphere β's surface were varied to cover different quadrants with respect to the origin and sphere β's coordinate system respectively. The positions by quadrant are listed in Table 4-2. Table 4-3 shows how each of the parameters in Table 4-1 were varied to provide an unbiased sampling of the performance of the addition theorems. Figure 4-1 displays the relative distances of sphere β and the positions of the evaluation points per test (angular orientation is not shown).

TABLE 4-1. Parameters for five test conditions for the addition theorem comparison tests with sphere β as the test sphere.

Test	Sphere β distance $R_{\alpha\beta}$	Sphere β radius r_β	$R_{\alpha\beta}/r_\beta$	Sphere β position (angular orientation with respect to origin)		Evaluation point position with respect to sphere β coordinates	
				$\Theta_{\alpha\beta}$	$\Phi_{\alpha\beta}$	θ_β	φ_β
1	3.4 cm	0.5 cm	6.8	37°	53°	151°	233°
2	1.4	0.5	2.8	146	115	163	320
3	3.4	0.1	34	71	304	44	9
4	14.0	0.5	28	146	115	163	320
5	3.4	1.0	3.4	71	304	44	9

TABLE 4-2. Position of sphere β and evaluation point by quadrant.

Test	Quadrant position of sphere β with respect to origin	Quadrant position of evaluation point with respect to Sphere β
1	+x, +y, +z quadrant	–x, -y, -z quadrant
2	-x, +y, -z quadrant	+x, -y, -z
3	+x, -y, +z quadrant	+x, +y, +z
4	-x, +y, -z quadrant	+x, -y, -z
5	+x, -y, +z quadrant	+x, +y, +z

TABLE 4-3. Varied parameters by test.

Test	Distance $R_{\alpha\beta}$ varied	Radius r_β varied	$\Theta_{\alpha\beta}, \Phi_{\alpha\beta}$ varied	$\theta_\beta, \varphi_\beta$ varied
1				
2	x 0.412 from test 1	same as 1	yes	yes
3	same as 1	x 0.200 from test 1	yes	yes
4	x 10 from test 2	same as 1	same as 2	same as 2
5	same as 1	x 10 from test 3	same as 3	same as 3
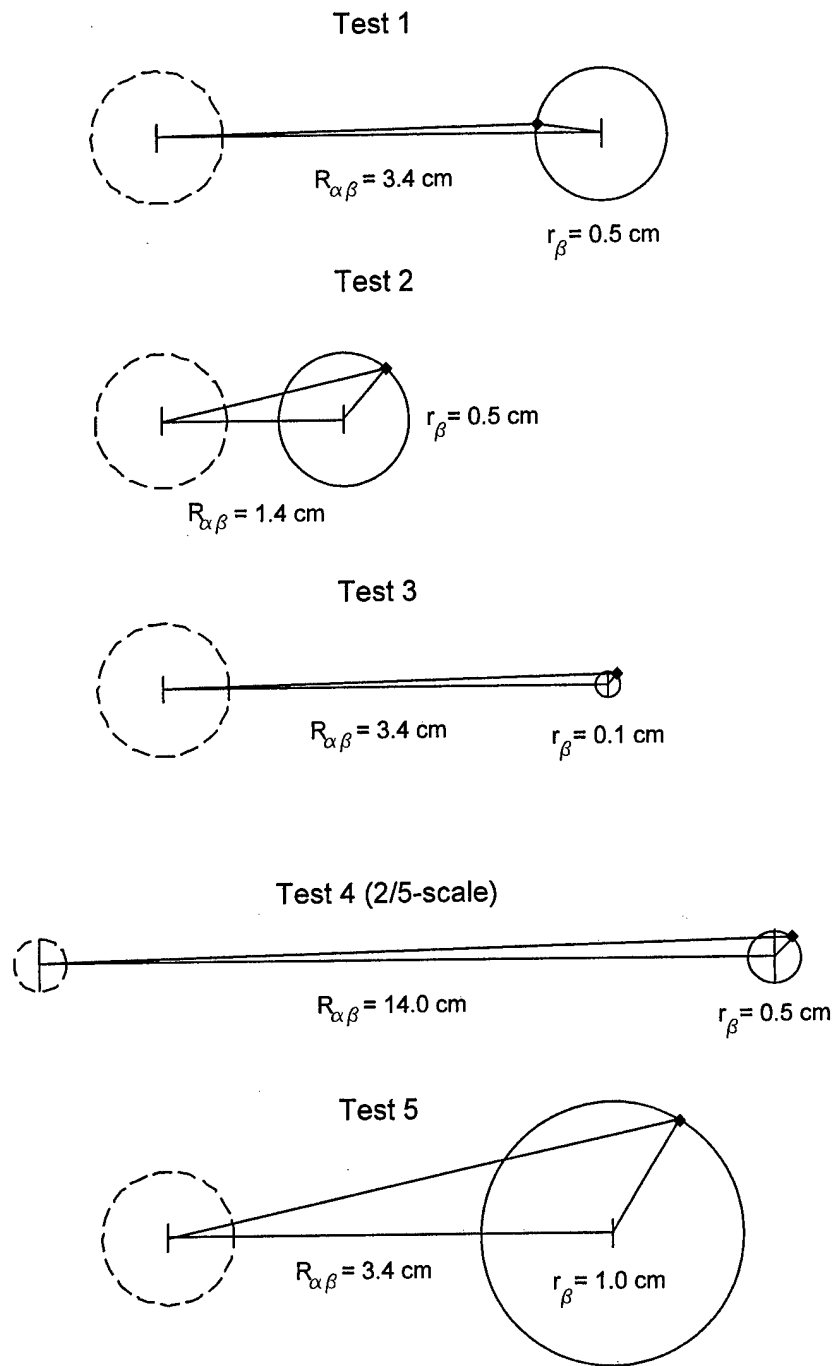
FIGURE 4-1. Distances and radii of sphere β (solid circle) from sphere α (dashed circle), and the relative positions of evaluation points on sphere β's surface (small filled diamonds) for each addition theorem comparison test.

The fields were translated out to the evaluation points using the pure-orbital, Cruzan, and Liu *et al.* addition theorems as discussed in the previous section.[55,69] The maximum mulipole order, n_{max}, that the expansions were computed to was also continuously varied from $n_{max} = 2$ to $n_{max} = 16$. There were therefore 15 simulations ran for each of the three addition theorem versions and for each of the five test positions as descibed in Table 4-1.

The cartesian components of the fields were evaluated directly at the point on the sphere where they were translated, first for the direct, untranslated (2,1) quadrupole field emanating from the origin, second from the fields translated to sphere β's surface. This allowed direct comparison of the translated fields with the untranslated fields as a function of frequency and field component (x, y, or z of the longitudinal, electric, or magnetic fields). The deviation of the translated fields from the untranslated fields was quantified by calculating the difference between the magnitudes of the fields (by summing the squares of the cartesian components and taking the square root) and by averaging over the frequency band. The results were then plotted as convergence curves as a function of n_{max}.

The comparison tests were performed in the frequency domain. The range of parameters and how they translate to elastic and electromagnetic wavelengths for the comparison tests are listed in Table 4-4. The longitudinal and shear wavespeeds were based on solid ice as the matrix, since ice has elastic wave properties intermediate between those of a "soft" solid such as plastic and a "hard" solid such as steel.[191] The corresponding electromagnetic frequency range is based on the shear elastic wavelength, since the shear multipole fields correspond to the electromagnetic multipole fields.

TABLE 4-4. Range of frequency-dependent parameters for the addition theorem comparison tests.

Parameter	Start	End
frequency	10 kHz	1 MHz
wavelength, longitudinal	39.8 cm	0.398 cm
wavelength, shear	19.9 cm	0.199 cm
k, longitudinal	0.15787 cm^{-1}	15.787 cm^{-1}
k, shear	0.31574 cm^{-1}	31.574 cm^{-1}
kr (r = 0.5), longitudinal	0.0789	7.89
kr (r = 0.5), shear	0.158	15.8
equivalent EM wavelengths	20 cm (1.5 GHz)	0.20 cm (150 GHz)

Computation time was also measured for each of the theorems and as a function of n_{max} and test geometries. The next section discusses the convergence results from the comparsion tests.

4.3 Numerical Test Results

4.3 (a) Convergence Results

Convergence of the addition theorems was quantified by calculating the magnitude of the difference vector between each of the untranslated U, V, and W multipole fields and the corresponding translated fields (Figure 4-2). By using the magnitude of the difference vector, instead of the difference between the two vector magnitudes, the comparisons can account for variations in angle as well as magnitude between the translated and untranslated fields. The difference vector magnitudes were then averaged over the frequency range and plotted as a function of n_{max}.
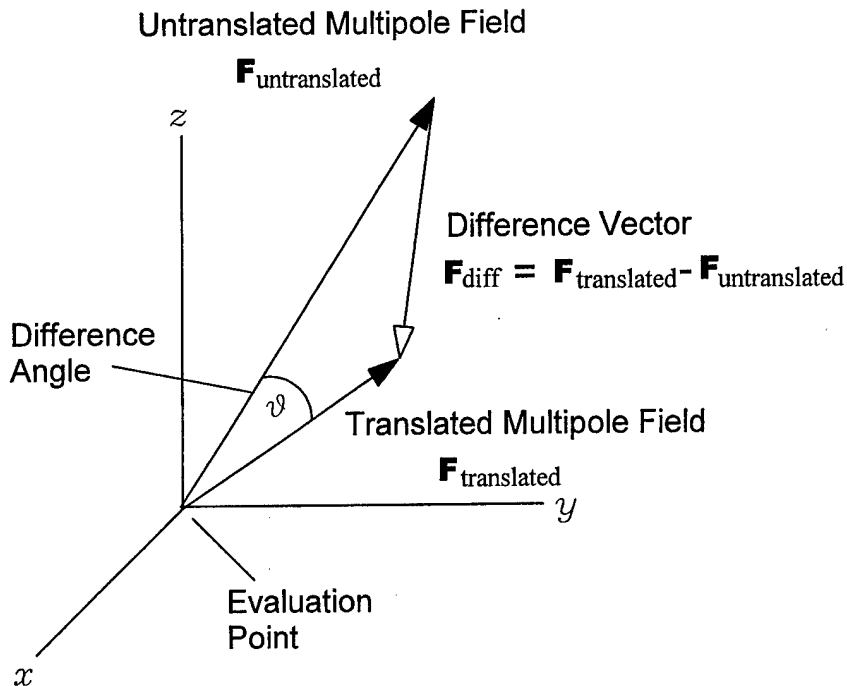
FIGURE 4-2. Diagram of difference vector between untranslated and translated field component F (representative of either U, V, or W). The magnitude of this vector was used to quantify the convergence and accuracy of the addition theorem results.

One of the first results to be noted was that the theorems by Cruzan produced numerically identical results to the pure-orbital theorems. The only difference between the two sets of theorems was the time required to compute the results. Table 4-5 displays the time required to compute the translated fields for $n_{max} = 16$.

TABLE 4-5. Computation time in hours to translate the **UVW** multipolde fields for each test configuration.

Test	Addition Theorems		
	Pure-Orbital	Cruzan	Liu *et al.*
1	11.09	6.85	7.28
2	10.06	6.15	6.55
3	10.93	6.79	7.28
4	16.95	11.09	11.60
5	11.03	6.80	7.29

As can be seen from the Table 4-5, the theorems of Cruzan were fastest, with the theorems of Liu *et al.* second, and the pure-orbital theorems the slowest. These results can be attributed to the fact that both the theorems of Cruzan and Liu *et al.* have fewer Clebsch-Gordan coefficients in the expressions. The computation of the Clebsch-Gordan coefficients are most likely less computationally efficient, and therefore take longer. The theorems of Cruzan substitute algebraic expressions for some of the Clebsch-Gordan coefficients, whereas Liu *et al.* just leave them out of the equations with no apparent substitution. The algebraic expressions of Cruzan are faster than calculating the equivalent Clebsch-Gordan coefficients. However, although the omission of Clebsch-Gordan terms in the expressions of Liu *et al.* also increase computational speed, it is difficult to imagine how their theorems and the pure-orbital (or Cruzan's) theorems can demonstrate the same accuracy.

Another observation from Table 4-5 is that the computation time is directly related to $R_{\alpha\beta}$, the distance between sphere β and sphere α. The only function in the addition theorems which contains $R_{\alpha\beta}$ explicitly is the spherical Hankel function $h_p^{(1)}(kR_{\alpha\beta})$. Therefore, it appears that calculation of the spherical Hankel function is a major contributor to the computation efficiency in addition to the Clebsch-Gordan coefficients.

The computation time for the addition theorems as a function of n_{max} assumes a power-law form. Modeling the power law as

$$Time = c \cdot (n_{max})^K \tag{4.19}$$

the constant c and exponent K can be determined from the data using least squares fitting. Table 4-6 shows the results of this fitting, and Figure 4-3 displays this power-law behavior. The power-law results indicate that, for each test, all three theorems scale to n_{max} by approximately the same power-law exponent. However, the linear constant can vary by as much as 2x between the theorems. So, although the theorems differ in computational speed, they differ linearly with n_{max} and not exponentially.

TABLE 4-6. Results of least-squares fit to computation time vs. n_{max}.

Test	Constant c ($\times 10^{-6}$)			Exponent K		
	Pure-Orbital	Cruzan	Liu *et al.*	Pure-Orbital	Cruzan	Liu *et al.*
1	1.28	0.631	0.713	5.76	5.84	5.82
2	0.537	0.228	0.288	6.04	6.17	6.11
3	1.42	0.625	0.735	5.72	5.84	5.81
4	10.4	7.76	6.71	5.16	5.11	5.18
5	0.822	0.609	0.695	5.92	5.85	5.83
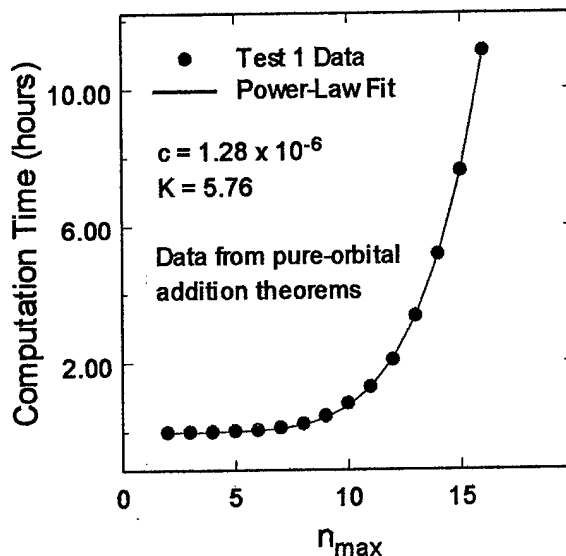
FIGURE 4-3. Power-law behavior of computational time as a function of n_{max}.

Figures 4-4 to 4-9 display the convergence results for the theorems of Cruzan (and therefore the pure-orbital theorems as well) and Liu *et al*. Due to the wide range of error (magnitude of difference vector), the vertical scale for each of the plots is logarithmic.
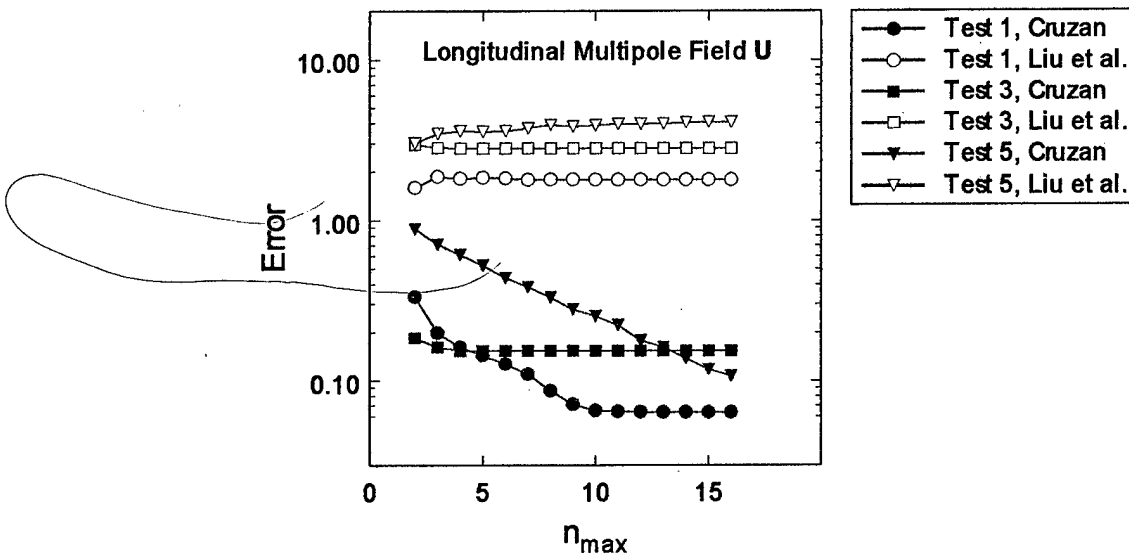
FIGURE 4-4. Convergence of longitudinal multipole field U for Tests 1, 3, and 5 for the Cruzan/pure-orbital and Liu *et al.* theorems.
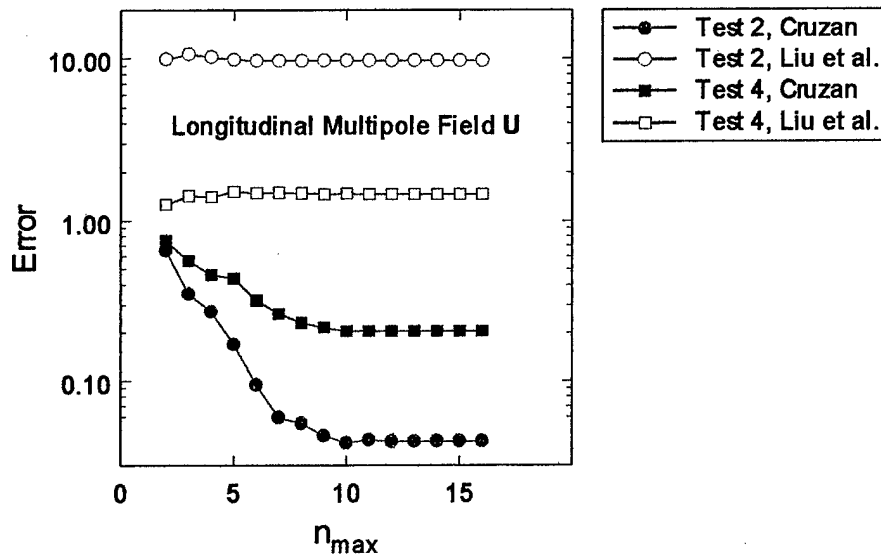
FIGURE 4-5. Convergence of longitudinal multipole field U for Tests 2 and 4 for the Cruzan/pure-orbital and Liu *et al.* theorems.
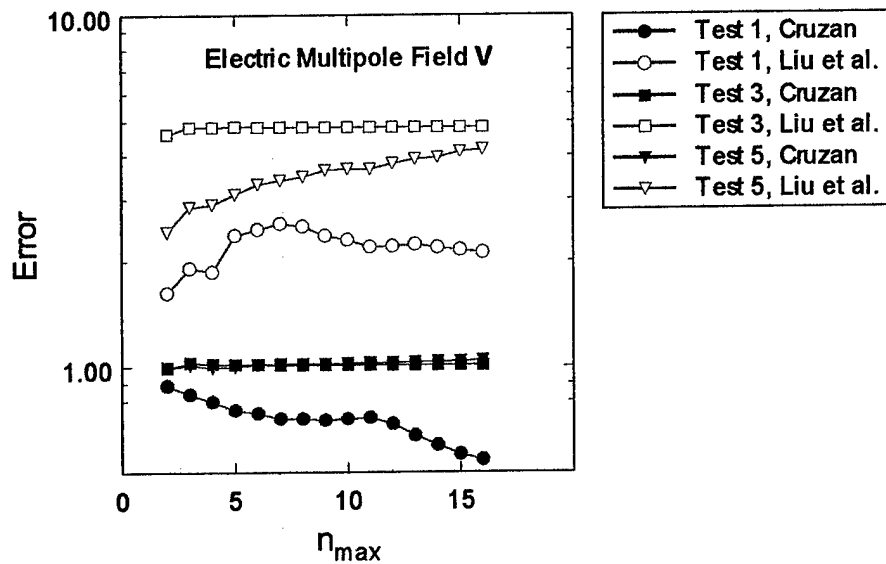
FIGURE 4-6. Convergence of electric multipole field **V** for Tests 1, 3, and 5 for the Cruzan/pure-orbital and Liu *et al.* theorems.
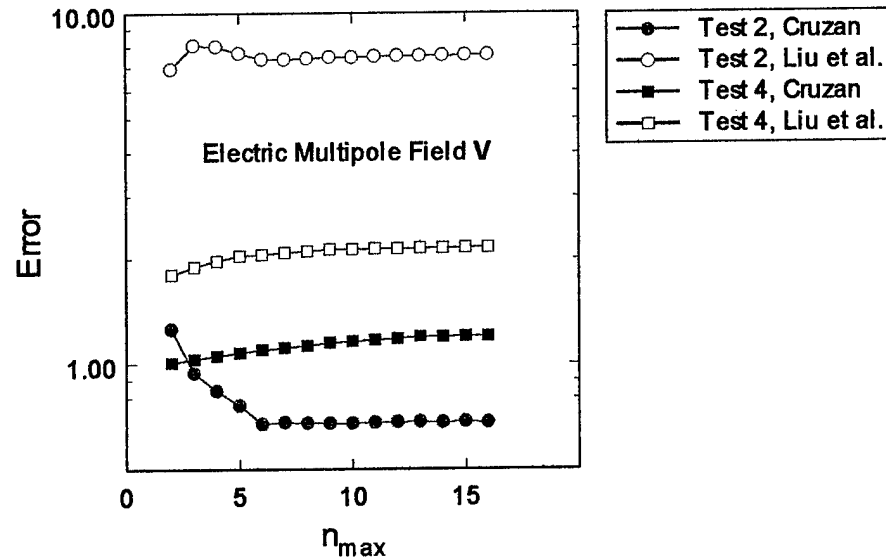
FIGURE 4-7. Convergence of electric multipole field **V** for Tests 2 and 4 for the Cruzan/pure-orbital and Liu *et al.* theorems.
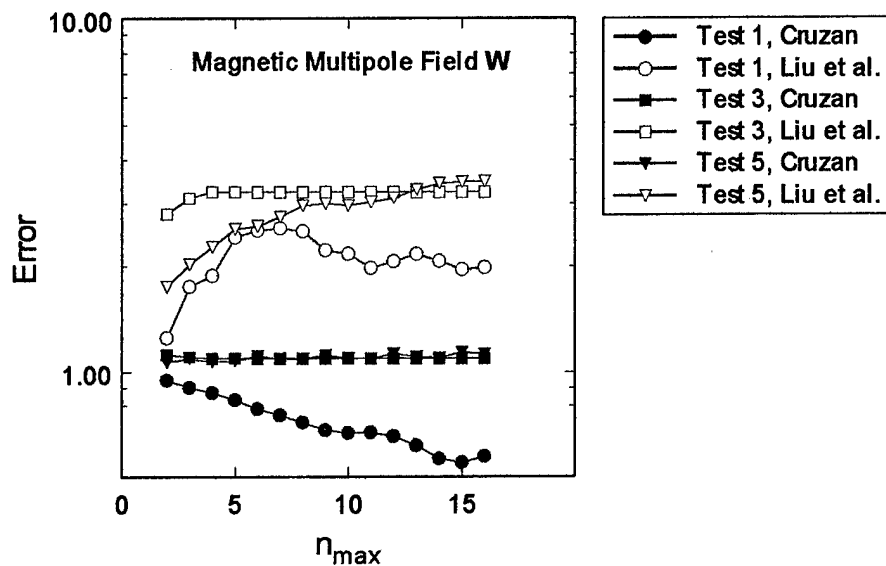
FIGURE 4-8. Convergence of magnetic multipole field **W** for Tests 1, 3, and 5 for the Cruzan/pure-orbital and Liu *et al.* theorems.
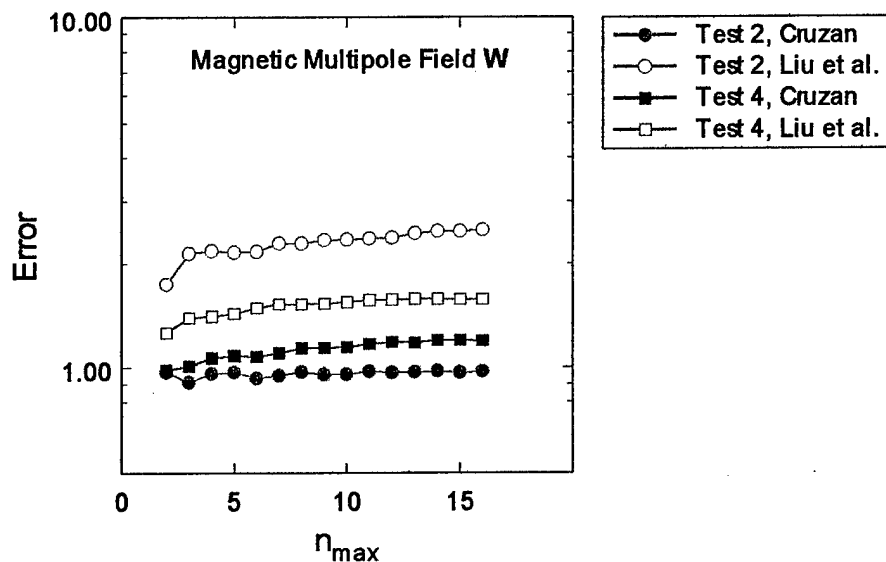
FIGURE 4-9. Convergence of magnetic multipole field **W** for Tests 2 and 4 for the Cruzan/pure-orbital and Liu *et al.* theorems.

As can be seen from Figures 4-4 to 4-9, the theorems of Liu *et al.* either diverge or show no change in convergence. The errors (difference vector magnitudes) are also consistently higher for the Liu *et al.* theorems, often by an order of magnitude or more.

The Cruzan/pure-orbital theorems show convergence for about half of the tests. The best convergence trends are for the longitudinal multipole field U for Tests 1, 2, and 5. The electric (V) and magnetic (W) multipole fields display less convergence in their trends. The worst convergence trends are seen for the magnetic multipole field W, where only Test 1 shows any convergence behavior.

Although the Cruzan/pure-orbital theorems show greater convergence over the range of tested configurations, it is still disconcerting to note the poor convergence for some of the test geometries and multipole fields. Although the testing was only conducted to $n_{max} = 16$ due to time and computational capabilities, it appears from many of the convergence trends that further testing to higher n_{max} would not improve the results significantly. The next section will examine the accuracy of the translation operation associated with these convergence trends.

4.3 (b) Accuracy Results

The accuracy of the addition theorems was first qualitatively judged by comparing the frequency spectra of the untranslated field with the translated fields at various n_{max} values. The accuracy was also quantitatively assessed as a function of frequency (kd) by using the magnitude of the difference vector as described in the previous section.

Figures 4-10 and 4-11 show the spectra of the y-components of the longitudinal and electric multipole fields respectively (U_y and V_y) for Test 1 of the Cruzan/pure-orbital theorems. The magnetic multipole field results are similar to those of the electric multipole field, Figure 4-11. The figures show fairly good accuracy as far as periodicity and amplitude as a function of frequency. Excellent agreement is seen at specific frequencies as well, such as at $kd = 30$ for the longitudinal field and $kd = 100$ for the electric field. The x- and z-components of the fields display generally the same periodicity and amplitudes, but less precise accuracy.
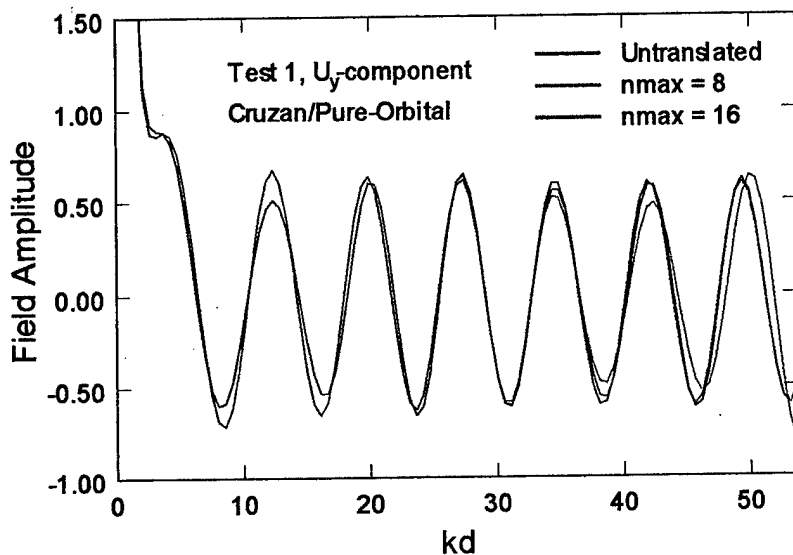
FIGURE 4-10. Spectra of the y-components of the longitudinal multipole field U for Test 1, using the Cruzan/pure-orbital theorems.
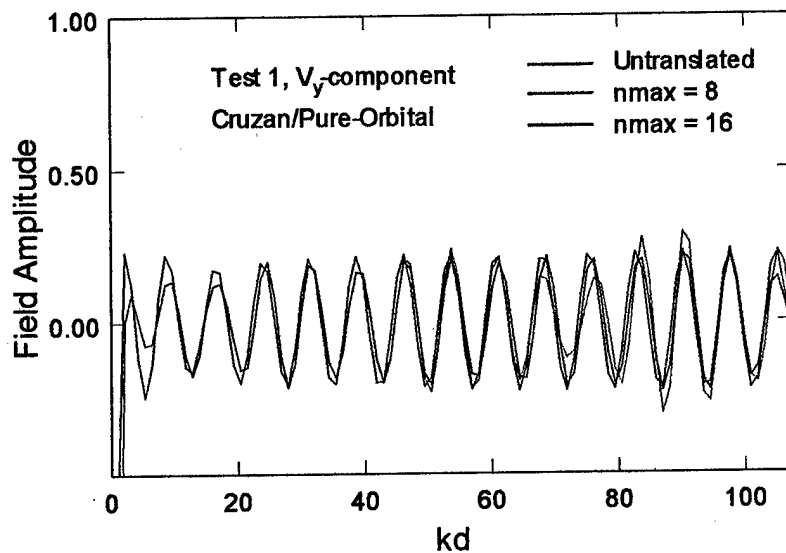
FIGURE 4-11. Spectra of the y-components of the electric multipole field V for Test 1, using the Cruzan/pure-orbital theorems.

The results from the other tests are less promising, however. Figures 4-12 and 4-13 display the

frequency (kd) spectra of the y-components of the longitudinal and electric multipole fields respectively

(U_y and V_y) for Test 2 of the Cruzan/pure-orbital theorems. Again, the magnetic multipole field results are similar to those of the electric multipole field, Figure 4-13. The results are still good for the longitudinal field, but very poor for both the electric and magnetic fields. Again, specific frequencies show excellent aggreement for the longitudinal field, particularly at low frequency ($kd < 2$) and $kd = 13$. The electric field shows agreement between the translated and untranslated field only at low frequency ($kd < 1$). No agreement is observed at any frequency for the magnetic field. The results become even poorer for Tests 3, 4, and 5.
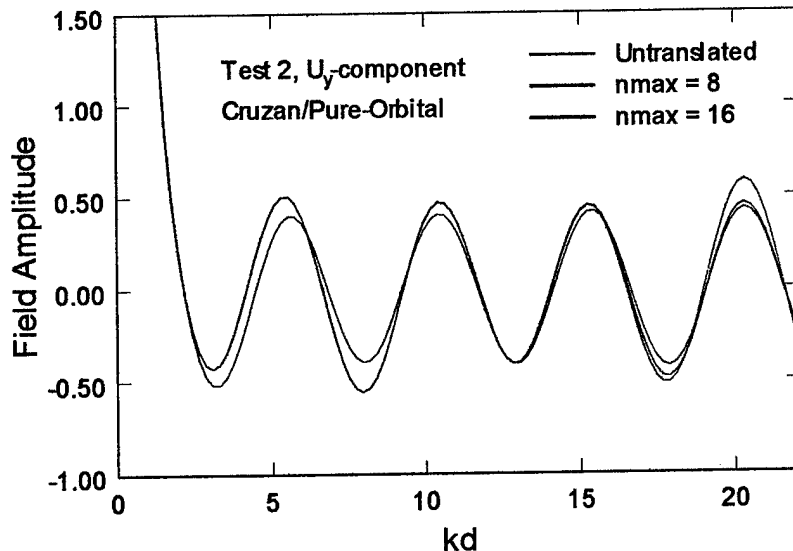
FIGURE 4-12. Spectra of the y-components of the longitudinal multipole field U for Test 2, using the Cruzan/pure-orbital theorems.
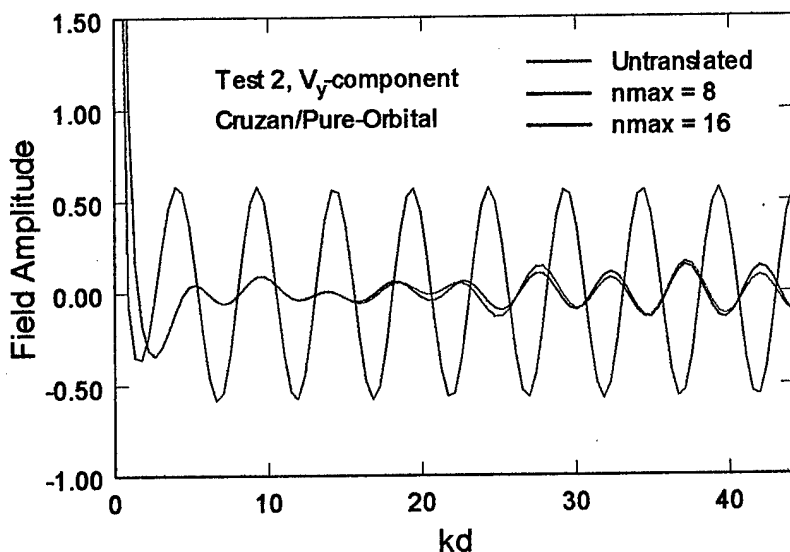
FIGURE 4-13. Spectra of the y-components of the electric multipole field V for Test 2, using the Cruzan/pure-orbital theorems.

The results from the Liu *et al.* theorems do not show any agreement for any of the fields (U, V, or W) or field components (x, y, or z). Figures 4-14 and 4-15 display the frequency spectra of the y-components of the longitudinal and electric multipole fields respectively (U_y and V_y) for Test 1 of the Liu *et al.* theorems. As with the Cruzan/pure-orbital theorem results, the magnetic multipole field results are similar to those of the electric multipole field, Figure 4-15. The results for the five test geometries show that the Liu *et al.* forms of the translational addition theorems are not accurate at any frequency at *nmax* = 16.
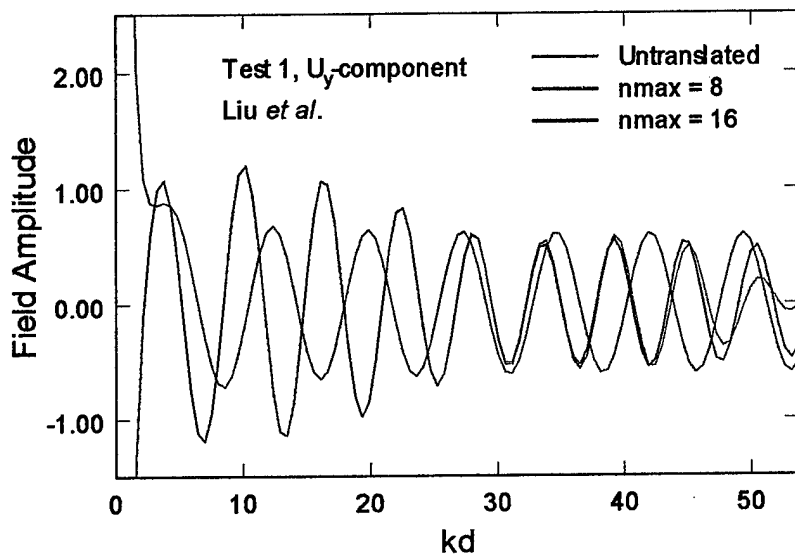
FIGURE 4-14. Spectra of the y-components of the longitudinal multipole field U for Test 1, using the Liu et al. theorems.
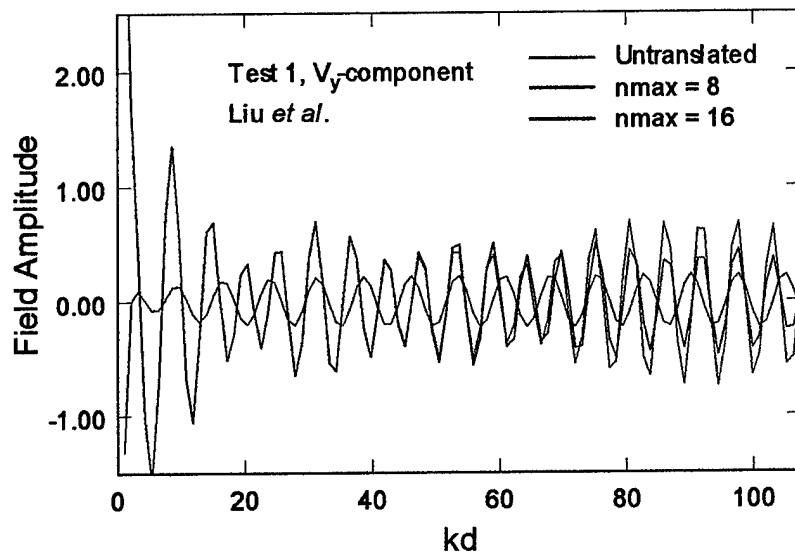
FIGURE 4-15. Spectra of the y-components of the electric multipole field V for Test 1, using the Liu et al. theorems.

To quantitatively measure the degree of accuracy, the magnitude of the difference vector between the untranslated and translated fields (Figure 4-2) was computed as a function of frequency (kd). In order to compare various multipole fields and test geometries, the magnitude of the difference vector needs to be

normalized to yield a percent deviation. The most straightforward normalization would be to divide the difference vector magnitude with the untranslated vector magnitude at each frequency step. This, however, grossly overestimates the deviation at frequencies the untranslated vector magnitude approaches zero. Likewise, at frequencies where the untranslated vector magnitude is large the deviation is underestimated. To achieve a more even normalization, the difference vector magnitude was divided by the frequency-averaged untranslated vector magnitude for each frequency step.

The results for the longitudinal and electric multipole fields are displayed in Figures 4-16 and 4-17, respectively, for the Cruzan/pure-orbital theorems, Test 1. The deviations for the magnetic multipole field are similar to those for the electric multipole field in Figure 4-17. The vertical scale on the plot shows the magnitude of the difference vector with respect to the frequency-averaged untranslated field vector, and is given in units of percent.
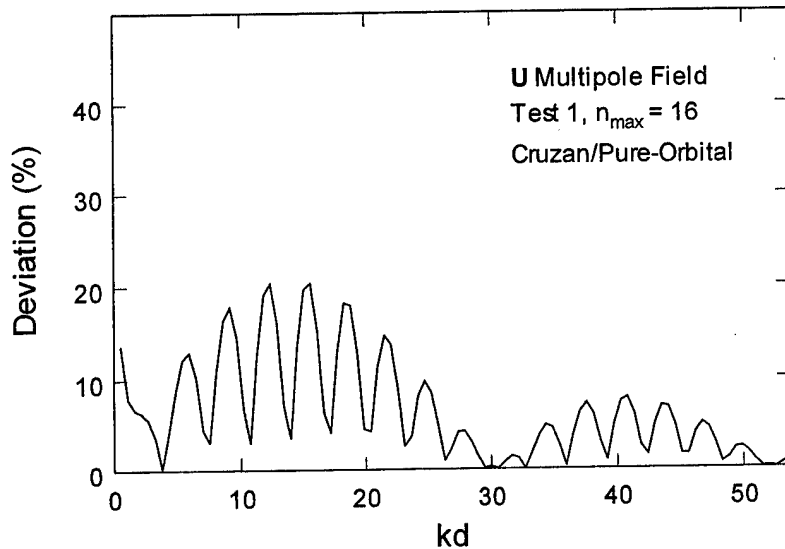
FIGURE 4-16. Percent deviation of translated longitudinal multipole field U from untranslated field, for the Cruzan/pure-orbital theorems, Test 1.
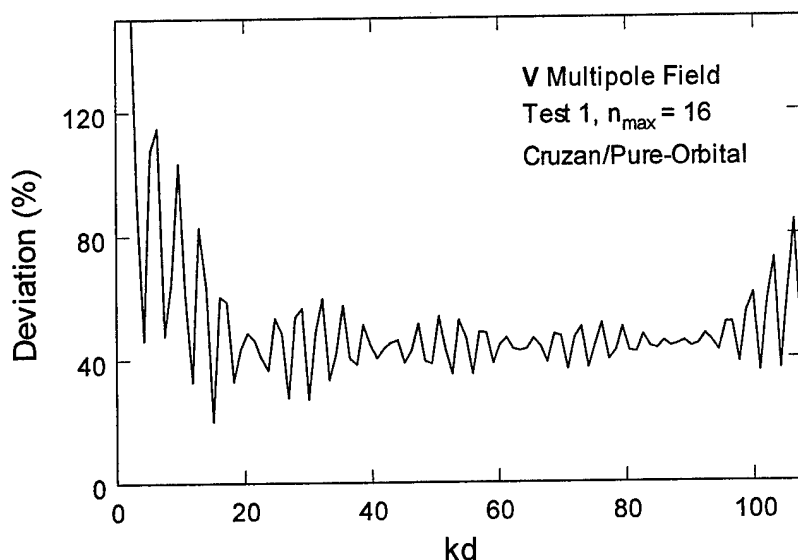
FIGURE 4-17. Percent deviation of translated electric multipole field **V** from untranslated field, for the Cruzan/pure-orbital theorems, Test 1.

Note that the magnitude of the difference vector goes to zero for particular frequency bands of the longitudinal field, but increases up to 20% for other frequency bands. The bands of zero magnitude represent spectral regions where the addition theorem is in very good agreement with the untranslated field. The bands of high magnitude represent regions where the addition theorem fails to reproduce the untranslated field.

The magnitude of the difference vector for the electric and magnetic multipole fields never does go to zero. The minimum magnitude at $n_{max} = 16$ is approximately 20% for the both multipole fields, and ranges up to 500% in the low frequency range.

The difference vector magnitudes for the other tests show the same type of behavior as for Test 1, but with smaller ranges of deviation for the electric and magnetic multipole fields. Figures 4-18 and 4-19 show the longitudinal and electric multipole field deviations as a function of frequency for Test 2. Note that the longitudinal multipole field again displays narrow frequency bands of good agreement (deviation $\approx$ 0%) and broader frequency bands of poorer agreement (deviation 5-15%). The electric and magnetic multipole fields have overall higher deviations, but within a tighter range across the spectrum.
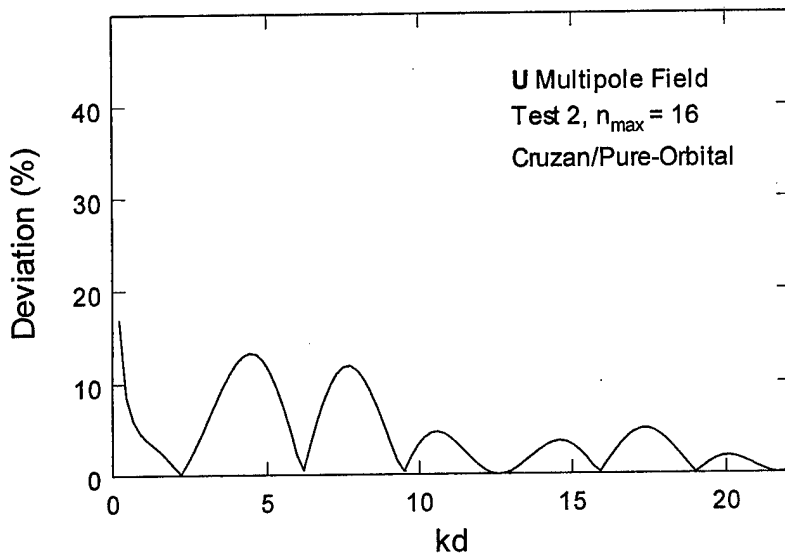
FIGURE 4-18. Percent deviation of translated longitudinal multipole field U from untranslated field, for the Cruzan/pure-orbital theorems, Test 2.
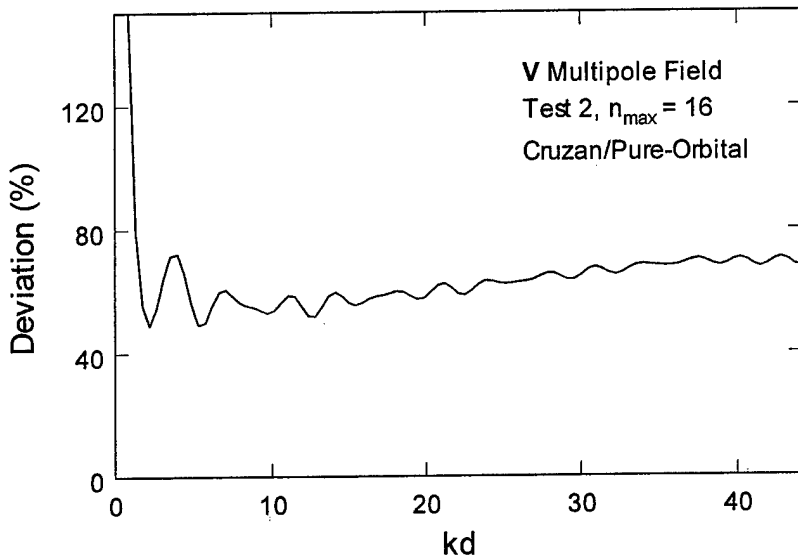
FIGURE 4-19. Percent deviation of translated electric multipole field V from untranslated field, for the Cruzan/pure-orbital theorems, Test 2.

As expected, the deviations for the multipole fields from the Liu *et al.* theorems are extremely high. The results for the longitudinal and electric multipole fields are displayed in Figures 4-20 and 4-21, respectively, for the Liu *et al.* theorems, Test 1.
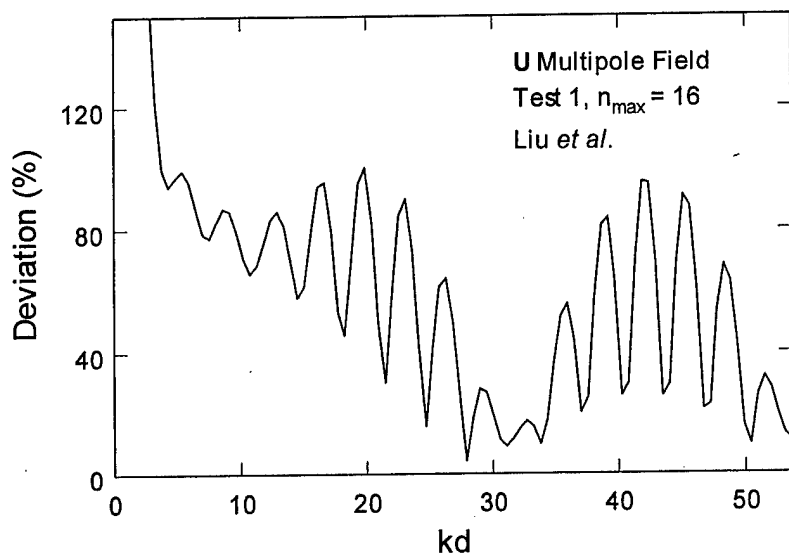
FIGURE 4-20. Percent deviation of translated longitudinal multipole field **U** from untranslated field, for the Liu *et al.* theorems, Test 1.
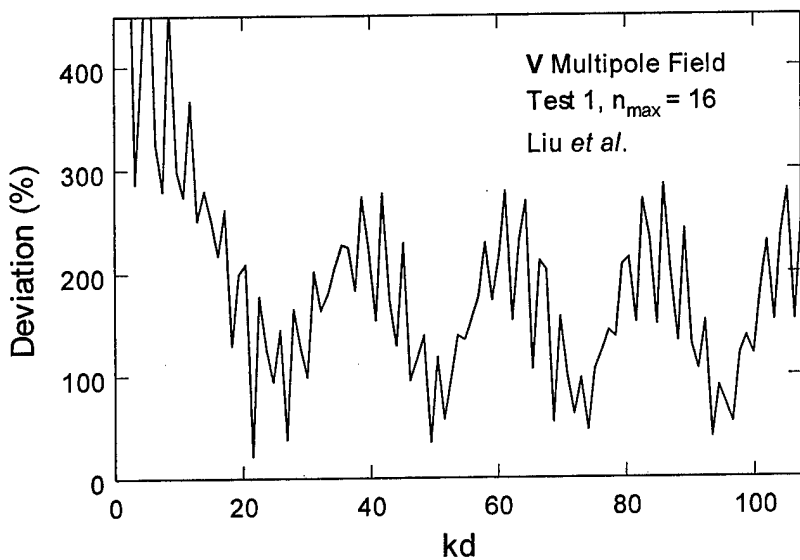
FIGURE 4-21. Percent deviation of translated electric multipole field **V** from untranslated field, for the Liu *et al.* theorems, Test 1.

Table 4-7 lists the deviations for each test and multipole field at n_{max} = 16 for the Cruzan/pure-

orbital and Liu *et al.* theorems. The deviations are also averaged over all five tests.

TABLE 4-7. Average deviation of translated field from frequency-averaged untranslated field for each multipole field and test.

Test	U (% dev)	V (% dev)	W (% dev)
Cruzan/Pure-Orbital Theorems			
1	6.38	54.2	57.3
2	4.25	68.0	97.5
3	15.4	101	109
4	20.5	120	120
5	10.7	104	113
Averaged over tests	11.4	89.4	99.4
Liu et al. Theorems			
1	179	211	198
2	972	759	249
3	280	483	325
4	147	215	158
5	408	418	347
Averaged over tests	397	417	255

The conclusions from Table 4-7 are dismal. Using the Cruzan/pure-orbital scalar addition theorem, the translated longitudinal multipole field will deviate on average about 11.4%. The results are worse for the vector addition theorem and translation coefficients for the electric and magnetic multipole fields. On average, the translated electric and magnetic multipole fields will deviate 90-100%. As bad as these results are, the addition theorems from Liu et al. are much worse, with average deviations in the translated fields ranging from 255% to 417%.

Further analysis of the addition theorem test results indicates that the error in the translated multipole fields arises equally from deviations in the amplitude of the vector field and deviations in the orientation (difference angle) of the vector field. Deviations in the amplitude can vary up to 400%, while deviations in orientation (vector angle) can vary up to a full 180° (for the Cruzan/pure-orbital theorems). Interestingly, the translated longitudinal fields have greater amplitude deviations, while the translated electric and magnetic fields have greater angular deviations.

Although numerical testing of the addition theorems was not exhaustive (more sphere geometries and multipole moments could have been tested) the results are consistent for the five tests. The results of the numerical testing can be summarized as follows:

1. Although the theorems of Cruzan differ mathematically—principally in formalism—from the pure-orbital theorems derived in this work, they are numerically equivalent and superior with regards to computational speed.

2. Although the theorems of Liu *et al.* use the same formalism as the pure-orbital theorems, they differ mathematically. Since the pure-orbital theorems were rigorously derived, it can be concluded that errors exist in the Liu *et al.* theorems.

3. Numerical testing verifies that the theorems of Liu *et al.* do not even approximately translate the three multipole fields for the five geometries tested. It can therefore be concluded that, in comparison to the Cruzan/pure-orbital theorems, the Liu *et al.* theorems are in error.

4. For specific sphere geometries (*e.g.*, Test 1), the Cruzan/pure-orbital theorems approximate the translated fields as a function of frequency. However, for most frequencies and scattering geometries, the theorems miscalculate the translated fields with errors up to several hundred percent.

The results are fairly stark: For current practical applications, translational addition theorems are neither efficient or accurate for the modeling of multiple scattering over a range of frequencies and particle configurations. A remaining question arises of why this is the case. The addition theorems have been rigorously derived by Cruzan. This work rederived the addition theorems through an independent method (integral transform) and formalism (**UVW** multipole fields vs. **LNM** spherical wave functions), and arrived at expressions that are numerically identical to Cruzan's. Since no approximations were made in either derivation, the addition theorems must be considered as exact expressions. Yet the numerical tests show far from accurate results for n_{max} up to 16.

The most probable answer is that the addition theorems are just not accurate unless the expansions are carried out to high multipole orders, possibly on the order of $n_{max} = 50\text{-}500$. Since the computations take so long for even small values of n_{max}, we cannot determine whether this is true or not with current computer hardware. However, we can look at other multipole expansions and their convergence behavior.

4.3 (c) Plane Wave Expansion Tests

For a comparison to the addition theorem expansions, the plane wave expansions in Eqs. 3.221, 3.224, and 3.225 were numerically tested in the same frequency range and with the same material properties as were the addition theorems. The evaluation point for the plane wave expansions was placed on the z-axis at 3.4 cm from the origin. This was the same distance as sphere β in Test 1 of the addition theorem tests. To determine convergence and accuracy, the plane wave expansions were compared to the exact plane wave expression ($\cos(kd)$) as a function of frequency (kd) and n_{max}. Due to the simplicity of the expansions, the computations were fast (from a few seconds to several minutes). However, beyond n_{max} = 84 the test program failed due to internal errors.

Figures 4-22 and 4-23 show the convergence behavior of the plane wave expansions for the UVW vector multipole fields. Figure 4-22 displays the convergence from n_{max} = 2 to n_{max} = 16, whereas Figure 4-23 displays the convergence from n_{max} = 10 to n_{max} = 80. For comparison, the convergence of the Cruzan/pure-orbital addition theorems in Test 1 are shown in Figure 4-24 with the same linear scale.
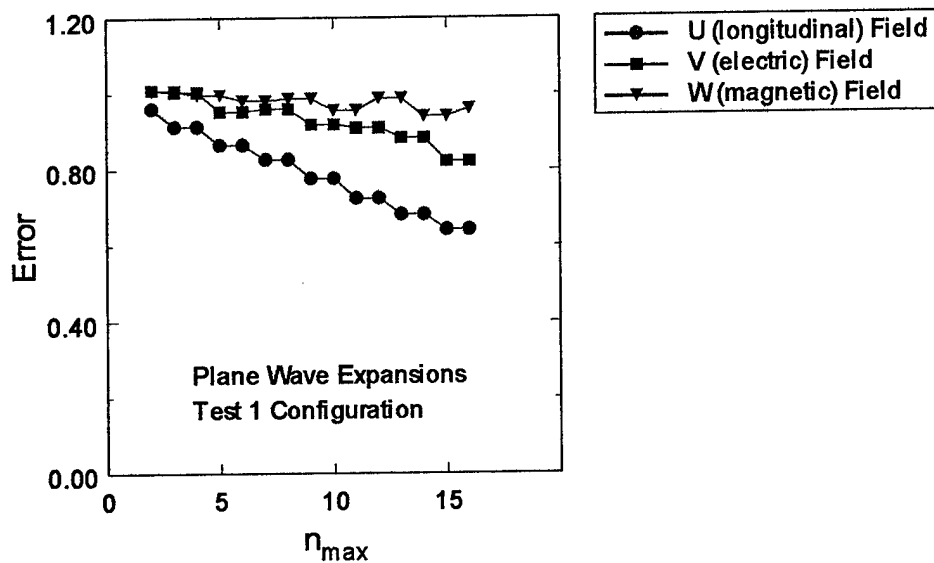
FIGURE 4-22. Convergence for the plane wave expansion of the UVW vector multipole fields, from n_{max} = 2 to n_{max} = 16.
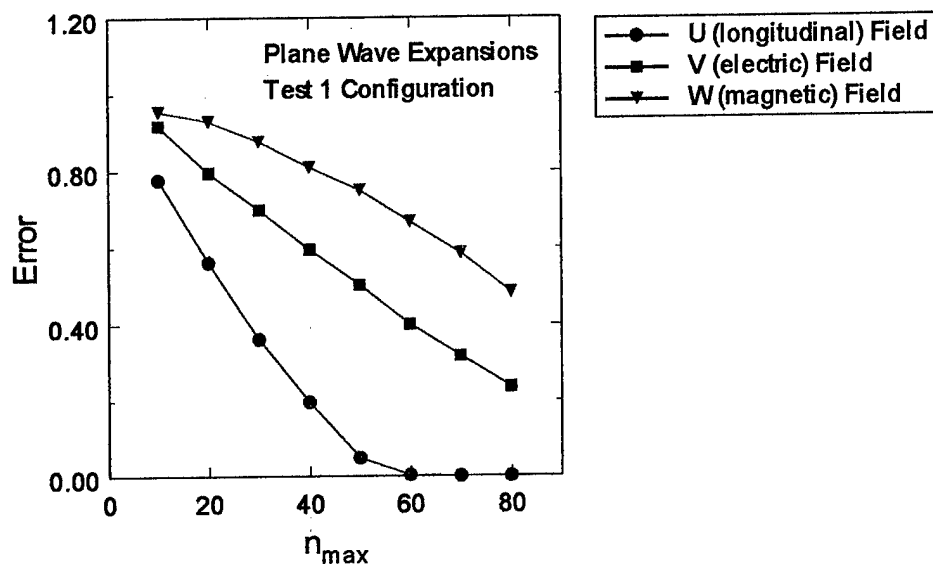
FIGURE 4-23. Convergence for the plane wave expansion of the UVW vector multipole fields, from n_{max} = 10 to n_{max} = 80.
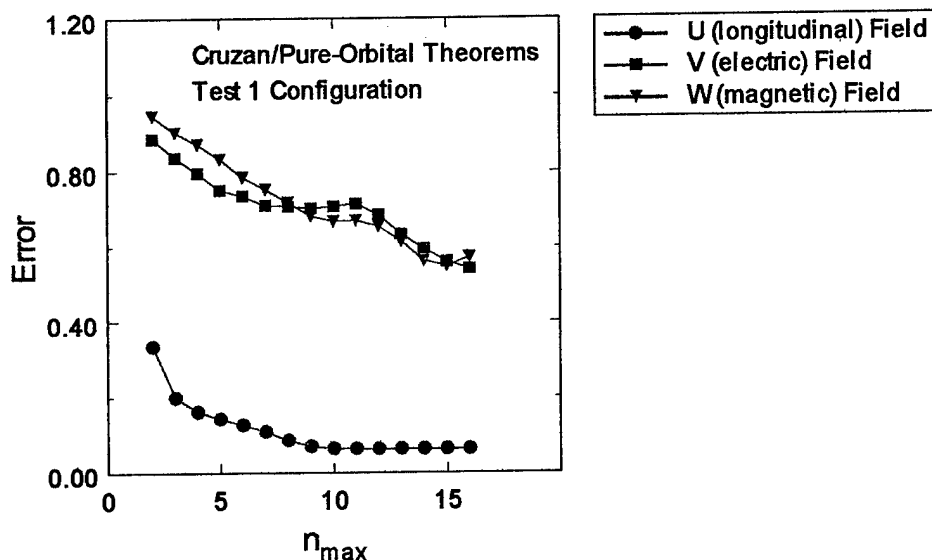
FIGURE 4-24. Convergence for the Cruzan/pure-orbital addition theorem, Test 1, from n_{max} = 2 to n_{max} = 16.

Comparison of the addition theorem convergence curves with the plane wave expansion convergence curves demonstrates that the slow convergence of the addition theorems is not unusual, but may be a general feature of multipole expansions. In fact, the addition theorems appear to converge faster

than plane wave expansions. Figures 4-25 and 4-26 display the spectra (field amplitudes as a function of

frequency) for the plane wave expansions of the longitudinal multipole field U and magnetic multipole

field W. Spectra for n_{max} = 16 and n_{max} = 84 are shown and compared with the exact value for the plane

wave ($\cos(kd)$).
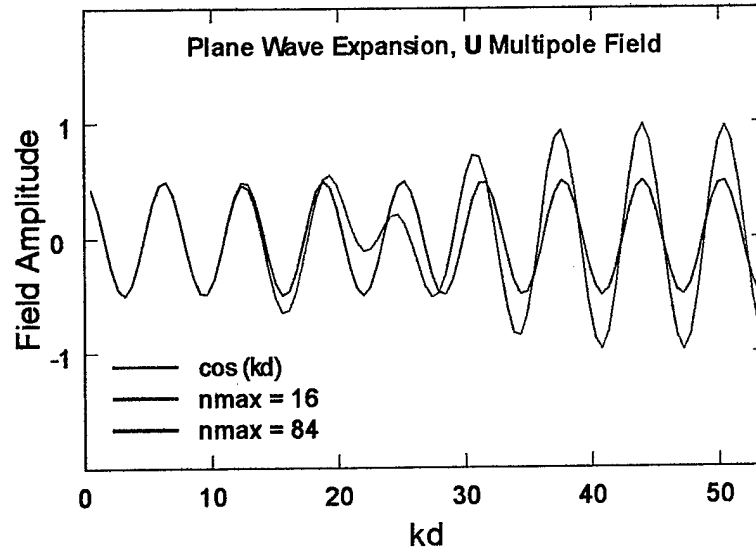
FIGURE 4-25. Spectra of the plane wave expansion of the longitudinal multipole field U. Expansion at n_{max} = 84 overlays $\cos(kd)$ to within resolution of plot.
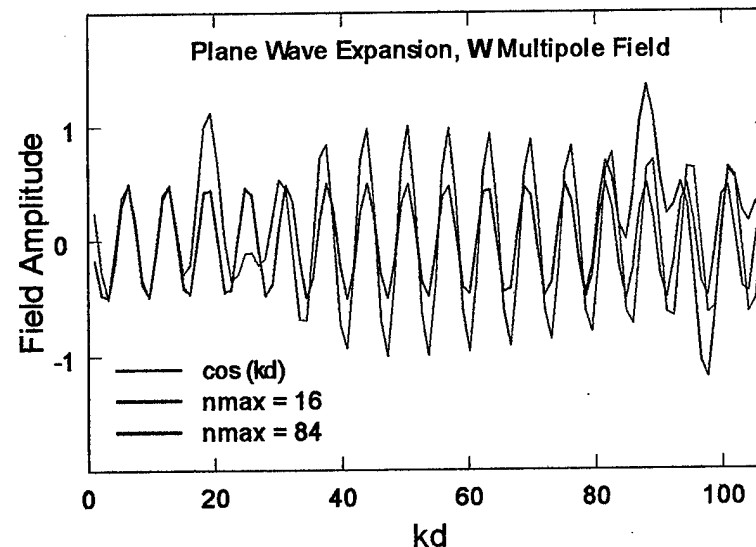
FIGURE 4-26. Spectra of the plane wave expansion of the longitudinal multipole field W.

At n_{max} = 16, the longitudinal multipole field converges at low frequency (< 0.2 MHz), but deviatesat higher frequencies. At n_{max} = 60, the longitudinal multipole field (Figure 4-23) converges to the exact values ($\cos(kd)$) for the entire frequency range, and completely ovelays the $\cos(kd)$ curve in Figure 4-25. The magnetic multipole field (Figure 4-26) shows large deviations at n_{max} = 16, but converges for n_{max} = 84 to the $\cos(kd)$ curve at low and mid frequencies (kd < 80).

Figures 4-27 and 4-28 display the percent deviation of the plane wave expansion field amplitudes from the exact plane wave amplitude averaged over the frequency range ($\frac{1}{v_{max}} \sum_{v=0}^{v_{max}} \cos[k(v) \cdot d]$). Again the longitudinal and magnetic multipole fields are shown for n_{max} = 16, 50, and 84.
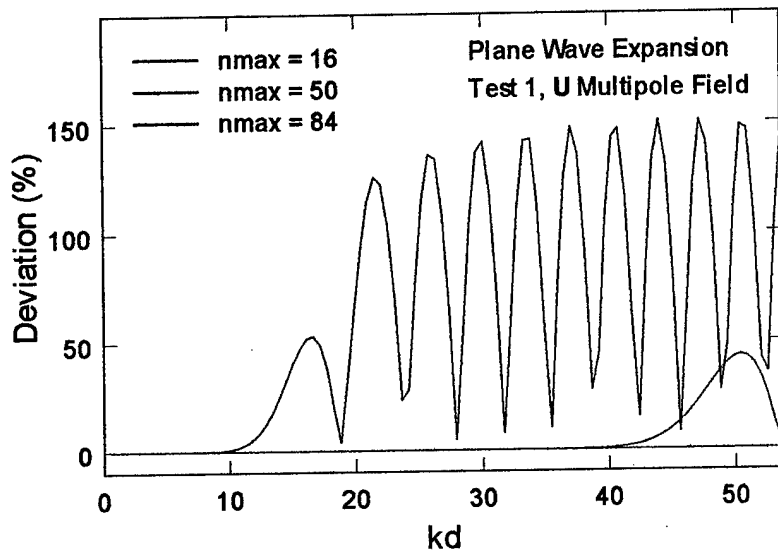
FIGURE 4-27. Percent deviation of the plane wave expansion of the longitudinal multipole field U from the exact value $\cos(kd)$ averaged over frequency band.
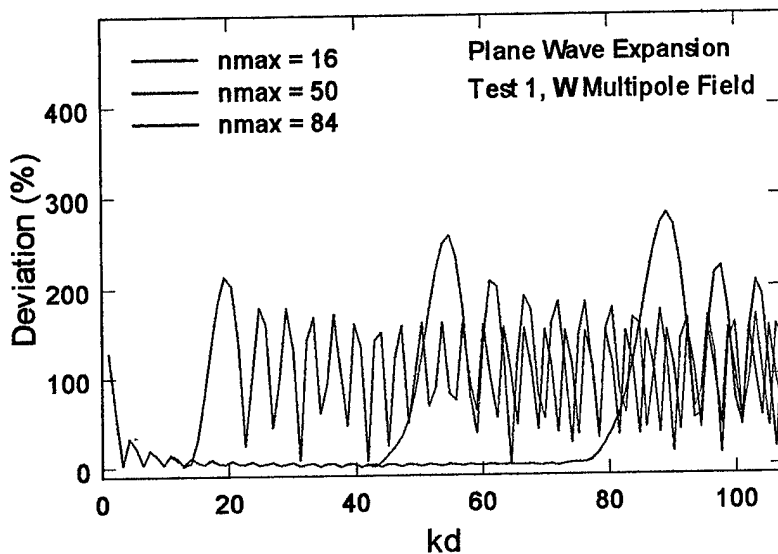
FIGURE 4-28. Percent deviation of the plane wave expansion of the magnetic multipole field **W** from the exact value $\cos(kd)$ averaged over frequency band.

Figures 4-27 and 4-28 clearly show how the plane wave expansions converge at low frequencies first and the progression of the convergence to higher frequencies. Table 4-8 tabulates the average percent deviation of the plane wave expansions for n_{max} = 16, 50, and 84, showing the improvement in convergence with higher n_{max}. Table 4-8 also shows the percent deviation results from two other test geometries (distances). Table 4-9 compares the average deviations from the plane wave expansions with those from the addition theorem tests (Cruzan/pure-orbital theorems) for n_{max} = 16.

TABLE 4-8. Average deviation of plane-wave expansion from the exact value $\cos(kd)$ for each multipole field and three n_{max} values.

Plane Wave Expansions			
n_{max}	U (% dev)	V (% dev)	W (% dev)
Test 1: $d = 3.4$ cm			
16	64.2	82.2	96.0
50	4.85	50.5	75.1
84	7.85×10^{-5}	20.2	44.4
Test 2: $d = 1.4$ cm			
16	23.1	66.1	99.4
50	6.94×10^{-5}	11.7	11.7
84	6.94×10^{-5}	11.7	11.7
Test 4: $d = 14.0$ cm			
16	91.7	97.3	97.7
50	73.2	85.8	98.6
84	54.1	79.6	87.9

TABLE 4-9. Comparison of deviations between plane-wave expansions and addition theorems for $n_{max} = 16$.

Test	U (% dev)	V (% dev)	W (% dev)
Plane Wave Expansions ($n_{max} = 16$)			
1	64.2	82.2	96.0
2	23.1	66.1	89.2
4	91.7	97.3	97.7
Average	59.7	81.9	94.3
Cruzan/Pure-Orbital Addition Theorems ($n_{max} = 16$)			
1	6.38	54.2	57.3
2	4.25	68.0	97.5
4	20.5	120	120
Average	10.4	80.7	91.6

The results from numerical testing of the plane wave expansions tells us that we should not be too surprised that the addition theorems do not converge at $n_{max} = 16$. Tables 4-8 and 4-9 indicate that the plane wave expansions and addition theorems have similar convergence behavior. Similarities include the following:

1. For both plane wave and addition theorem expansions, the longitudinal multipole field converges faster than either the electric or magnetic multipole fields.

2. Although the longitudinal multipole field converges faster for the addition theorems, the electric and magnetic multipole fields show about the same convergence results (deviations) at $n_{max} = 16$ for both plane wave and addition theorem expansions.

3. The convergence for the plane wave expansions, and to some extent the addition theorems, is proportional to the distance of the evaluation point or target sphere. (Test 4, which is the farthest at 14.0 cm, displayed the slowest convergence for both plane waves and addition theorems.)

4.3 (d) Discussion

The results indicate that the addition theorems converge too slowly for practical application to multiple scattering algorithms. This slow convergence is not due to algorithmic errors, but is inherent in the general nature of vector multipole expansions. It should be noted that part of the slow convergence for the addition theorems in this work is due to the fact that the computations are performed for 100 separate frequency steps in order to determine their behavior as a function of frequency. Most published work using addition theorems confine their simulations to one of a few frequencies, and are therefore able to compute the results up to 100x faster.

Although many researches resort to recurrence relations to compute the addition theorems and subsequent field translations much more quickly, their computations severely underestimate n_{max}. Borghese et al. only went to $n_{max} = 3$ with their vector field translations.[96] Fuller justifies this by noting that the wave frequency, sphere sizes, and sphere separations were in the Rayleigh region of scattering ($kd < 1$).[94] Similarly, Mackowski claimed convergence of electromagnetic field translations for $n_{max} = 2$-10 for $kd = 0.1$, $n_{max} = 3$-6 for $kd = 1$, and $n_{max} = 14$ for $kd = 10$.[100] Gumerov and Duraiswami also indicate that the addition theorem expansions for the longitudinal field can be truncated at $n_{max} \approx 10$ for $kd \leq 10$.[119] In comparison, none of the addition theorems in the numerical tests of this work converge by $n_{max} = 16$ for the $kd < 1$ region, as shown by Figures 4-16 through 4-21.

Why is there a such a large discrepancy between the published results and the results of this work? A closer look at the published results reveals four reasons:

1. The criteria for convergence in the published results appears to be a relative flattening of the translated field values as a function of n_{max}.[94,96,100] Figures 4-4 through 4-9 show that several of the translated field values do flatten in the $n_{max} = 2$-16 range. However, this flattening does not correspond to a convergence to what the values should be (the untranslated field), as shown in

Figures 4-10 through 4-13, and Figures 4-16 through 4-19. Rather, the flattening is most likely a transient plateau region, much like that for the electric multipole field in Figure 4-24.

2. None of the published results found to date compare the addition theorem results themselves to the actual, untranslated field results. Rather, the addition theorems are used to calculate the sphere-to-sphere scattering coefficients, and the scattering results are used to determine convergence. This is not a good test for the accuracy and convergence of the addition theorems, as it can be shown that the scattering solutions can plateau (flatten) at low n_{max}, although the addition theorems are grossly inaccurate at those n_{max} values. Again, there is a confusion between convergence and a transient plateau region, which leads to accuracy errors.

3. Several of the published results are for spheres in a geometric configuration which may bias the convergence (for example, along the x, y, or z axis).[70,100] In comparison, the configurations for this work's numerical tests were chosen at random and represent arbitrary distances and orientations.

4. Only a few of the published results found to date look at convergence of the addition theorems across a sufficiently wide and detailed frequency (or kd) range.[70,71] Rather, only a few values for kd are selected and analyzed. As noted, the longitudinal multipole field converges to the actual (untranslated) values at certain frequency values, but widely diverges at others.

Some of the most detailed studies of the addition theorems are by Liang and Lo, and Bruncing and Lo.[70,71] Although they did not directly evaluate the addition theorems, but rather looked at two-sphere scattering solutions, they did evaluate their results across a broad range of frequencies (kd) or sphere spacings. They also compared their results to ray-optics solutions and experimental measurements. Although the addition theorem approach predicted the overall characteristics of the scattering, discrepancies are present between the addition theorem approach, ray-optics solutions, and experimental data.

It should be noted that single sphere scattering can provide a very good approximation of the general scattering characteristics for a collection of spheres. Therefore, testing the addition theorems by

using multiple sphere scattering may not be a good approach since the single sphere scattering contribution is not separated out in the solutions. This is probably the primary reason why approaches which use addition theorems continue to be researched and published with little acknowledgement of their poor accuracy and convergence. The single scatterer contribution overwhelms any errors introduced by the addition theorem translations.

From the results of the numerical testing of the translational addition theorems derived in this work, the following conclusions and recommendations are made:

1. The convergence and accuracy of the addition theorems vary as a function of frequency, distance, target (β) sphere size, and orientation. Therefore, all of these parameters must be considered in determining convergence and accuracy.

2. The convergence and accuracy of the addition theorems vary differently for each of the three multipole fields.

3. Convergence and accuracy are not equivalent for the addition theorem expansions. Although the translated vector field amplitudes may flatten with n_{max}, implying convergence, in the cases studied the amplitudes still deviated considerably (up to several hundred percent) from the actual vector field. The flattening is therefore probably a plateau region, and not a true convergence.

4. Convergence of multiple scattering solutions is not a test for convergence of translational addition theorems.

5. Initial plane wave expansions must also be given due consideration with respect to convergence.

The convergence and accuracy problems presented by the use of addition theorem expansions will probably only be remedied by either finding mathematical methods to accelerate the addition theorem convergence or foregoing addition theorem expansions altogether in the multiple scattering theory. Chapter 8 presents a few ideas of how this may be achieved.

CHAPTER 5

RESULTS: SCATTERING MODELS FOR MULTIPLE SPHERES

Although numerical testing showed that the translational addition theorems had significant convergence and accuracy limitations, scattering models were nonetheless constructed and tested with the theorems to demonstrate the general concept of the approach. Additionally, previous work has shown that such an approach produces results that are close to expected and experimental values.[70-72,88-100] We were therefore curious as to how such results could be obtained in light of the deficiencies of the addition theorems.

Three types of scattering models were developed and tested. These models were the following:

1. Elastic wave scattering in the spatial domain, yielding scattered wavefield images.

2. Elastic wave scattering in the frequency domain, yielding scattered wavefield spectra.

3. Electromagnetic scattering in the frequency domain, yielding scattered wavefield spectra.

The spatial domain models represent a "virtual microscope" where the computer model creates images of the fields and their cartesian components at the microscopic or particle size level. Likewise, the frequency domain models create a "virtual spectrometer" where the behavior of the fields as a function of frequency are examined. The results of these models for various particle configurations will now be presented.

5.1 Elastic Wave Scattering in the Spatial Domain

Spatial domain models for elastic wave scattering were constructed according to the flow diagram in Figure 3-7. Each of the fields (longitudinal, shear-electric, and shear-magnetic) and their cartesian components were evaluated at points comprising a square lattice of user-selected size and resolution. This grid constituted the image plane of the model with each point as a pixel. The multiple scattering models, employing wavefield translations and iteration, were compared to single scatterer models, where the initial plane waves are scattered only once by each particle and the scattered fields superimposed at the evaluation points.

The simplest particle configuration to look at is a pair of identical spheres aligned along the direction of the plane wave propagation. For the following figures, the two spheres were quartz particles

(rocks) in ice, with diameters of 1.0 cm and separated by 2.0 cm center-to-center. The acoustic properties of ice and quartz were sufficiently different to clearly show scattering phenomena such as reflection, but not too different to preclude some types of wave propagation (refraction through the particle, for instance). The acoustic properties were obtained from Ensminger.[191]

Figures 5-1 through 5-4 show scattered wavefield images of the two-particle configuration with an elastic wave frequency of 0.5 MHz. (Note that these images could also correspond to other particle size/frequency range combinations, such as 0.5 cm/1.0 MHz, 0.1 cm/5.0 MHz, and so forth.) Various wavefields and components are presented to show how the models reproduce physical phenomena such as focusing and mode conversion. To highlight the scattering behavior and any differences between the multiple and single scatterer models, only the scattered wavefields are imaged without the superposition of the incident plane wave.

Figures 5-1 and 5-2 display the wavefield images arising from the interaction of a purely longitudinal plane wave (propagating from the left or –z direction) with the two quartz spheres. Figure 5-1 shows the z-component of the longitudinal field, illustrating the focusing of the longitudinal wave by the two spheres. The multiple scattering model (left image) and single scattering model (right image) are plotted to the same color scale, and show subtle differences in scattered field intensity. The overall patterns of the scattered fields, however, are the same.
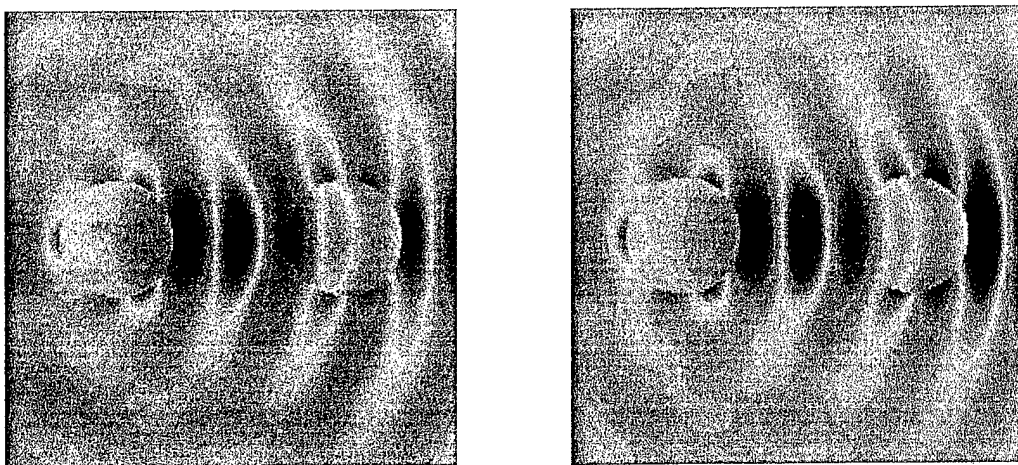
FIGURE 5-1. Color plots from the multiple scattering model (left) and single scattering model (right) of the scattered longitudinal wave z-component arising from an incident longitudinal wave.
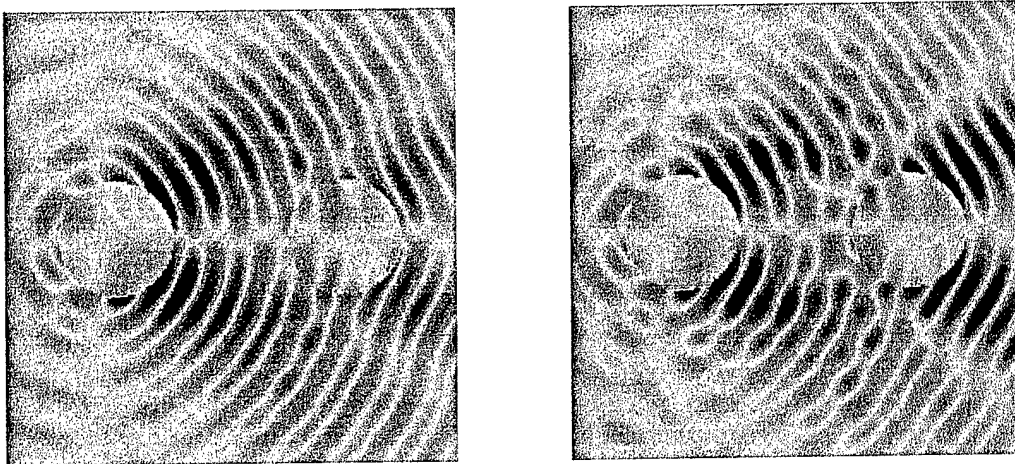
FIGURE 5-2. Color plots from the multiple scattering model (left) and single scattering model (right) of the scattered shear-electric wave y-component arising from mode conversion from an incident longitudinal wave.

Figure 5-2 shows the y-component of the shear-electric field arising from mode conversion of the pure longitudinal incident plane wave from the two quartz spheres. Again, the wavefield patterns appear nearly identical, but the amplitudes vary to some extent. Figures 5-1 and 5-2 also faithfully reproduce other features of elastic wave scattering such as the forward scattering of the longitudinal wave and the more sideward scattering of the shear wave.

Figures 5-3 and 5-4 display wavefield images arising from the interaction of a mixed incident plane wave (50% longitudinal, 50% shear) with the two quartz spheres. Figure 5-3 again shows the z-component of the longitudinal field, illustrating the focusing of the longitudinal wave by the two spheres. However, for this case, the wavefields from the multiple scattering model and single scattering model differ in both intensity and pattern. The asymmetry displayed in the multiple scattering image arises from translation of the asymmetric shear-magnetic field which changes it to a shear-electric field. The translated field is subsequently mode converted to a longitudinal field upon rescattering. This feature is absent from the single scattering image since the shear-magnetic field can only be converted into another field by translation. The shear-magnetic field is decoupled from the shear-electric and longitudinal fields in the single particle scattering solutions.
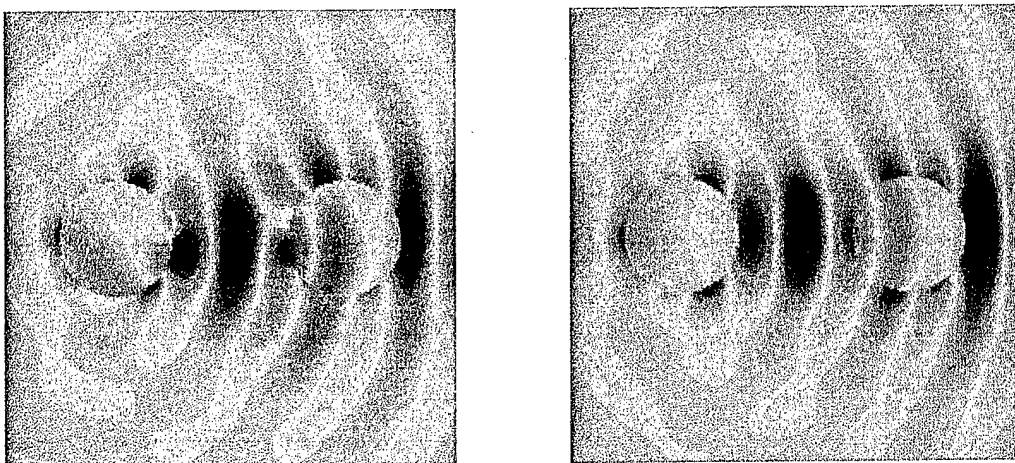
FIGURE 5-3. Color plots from the multiple scattering model (left) and single scattering model (right) of the scattered longitudinal wave z-component arising from an incident mixed longitudinal-shear wave.
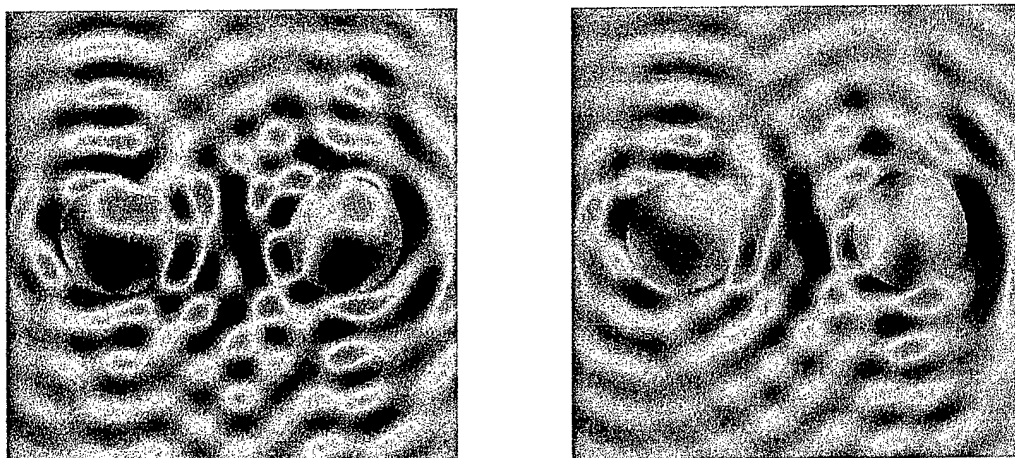
FIGURE 5-4. Color plots from the multiple scattering model (left) and single scattering model (right) of the scattered displacement wave z-component (longitudinal + shear) arising from an incident mixed longitudinal-shear wave.

Figure 5-4 displays the z-component of the entire displacement field (longitudinal + shear waves), with the more isotropic scattering of the shear waves dominating. Here, both the multiple scattering and single scattering models show asymmetric field patterns due to the inclusion of the shear-magnetic waves in the total displacement field. Variations in intensity between the two models are again evident.

The results from the two-particle simulations reproduced expected behavior for both single and multiple scattering. Processes such as refraction (focusing) and mode conversion of longitudinal to shear-electric waves were demonstrated, as well as mode conversion of shear-magnetic waves to shear-electric and longitudinal waves due to translation and multiple scattering. These results verified that the models were performing as intended and producing physically realistic effects. Additionally, the similarity between the single scattering and multiple scattering results was surprising.

The spatial domain elastic wave models were further tested with simulations of two-dimensional configurations of 16 particles (Figure 5-5). The first particle configuration was a 4x4 square lattice of quartz particles of 1.0-cm diameter and spaced every 2.0 cm (Figure 5-5, left). The second particle configuration consisted of a random dispersion of quartz particles with diameters varying from 0.8 to 1.4 cm (Figure 5-5, right). The 16-particle configurations were tested at various frequencies, and results are shown for 0.1 MHz. A mixed (50% longitudinal + 50% shear) plane wave was used in the simulations, and was superimposed on the scattered wavefields to give a truer representation of the elastic fields in the material system.
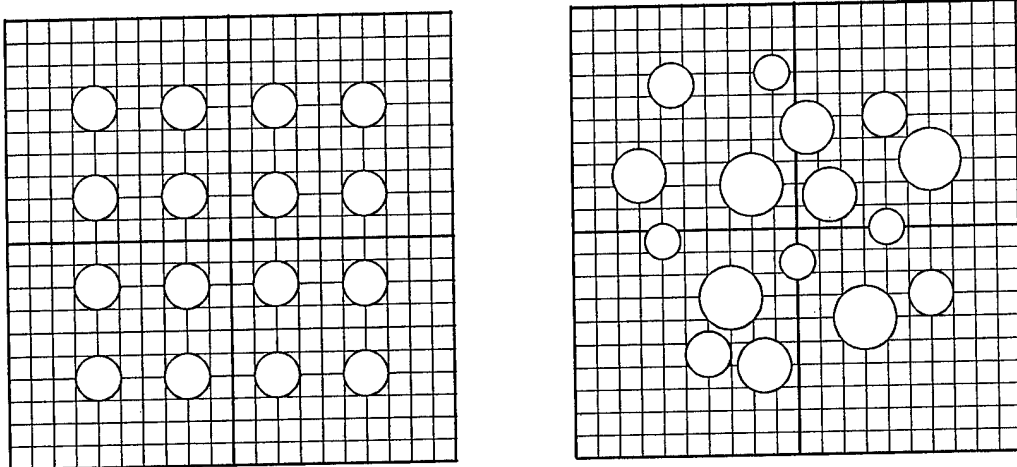
FIGURE 5-5. Two-dimensional, 16-particle configurations for spatial domain simulations, ordered lattice structure (left) and random structure (right).

Figure 5-6 shows the z-component of the longitudinal fields from the ordered (left image) and random (right image) particle configurations. Both images are plotted to the same color scale. It is readily apparent that the higher elastic wave velocities of the particles shortens the field wavelengths inside the particles. This wavelength squeezing inside the particles is also accompanied with an increase in field amplitude within the particles. Additionally, the random particle configuration displays higher localized wavefield concentrations than the ordered configuration. The higher amplitudes are only associated with some particles, however, and other particles in the random configuration show lower amplitudes than present in the matrix.

Figure 5-7 displays the x-component of the shear-electric fields in the ordered (left) and random (right) particle configurations. Again, both images are plotted to the same color scale, and the particles for both ordered and random arrangements show wavefield amplitude enhancements. As with the longitudinal wave, specific particles within the random configuration significantly concentrate the wavefield energy more than others.
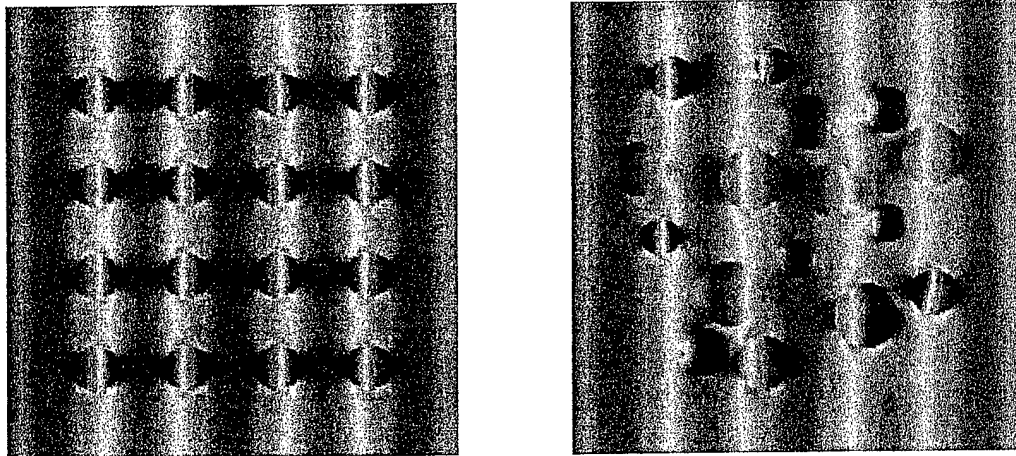
FIGURE 5-6. Color plots of the total longitudinal wave z-component from an ordered (left) and random (right) configuration of 16 quartz particles in ice, with an incident mixed longitudinal-shear wave.
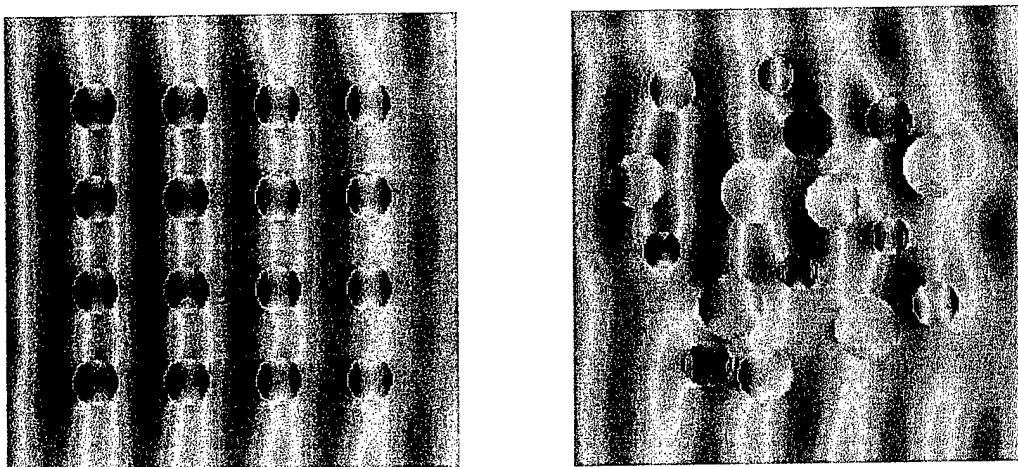
FIGURE 5-7. Color plots of the total shear-electric wave x-component from an ordered (left) and random (right) configuration of 16 quartz particles in ice, with an incident mixed longitudinal-shear wave.

An unexpected observation from Figure 5-7 is that the shear-electric wave appears to be attenuating as it progress through the ordered lattice from left to right. This result probably arises from mode conversion of the shear-electric fields to longitudinal fields. However, multiple scattering effects must also be responsible for this attenuation since mode conversion from single particle scattering would be uniform throughout the particle configuration, and would therefore results in a uniform (non-attenuating) shear-electric wave. It is interesting to also note that such an attenuation is not observed for the longitudinal wave in Figure 5-6. It is also not apparent in the random dispersion, so may be associated with a type of band-gap phenomenon for ordered lattices.

Finally, Figure 5-8 displays the z-component of the total displacement field (longitudinal + shear waves) for the two particle configurations. As with Figures 5-6 and 5-7, the particles in the random dispersion show significant concentrations of field energy. The nonuniformity of the random particle configuration also gives rise to localized areas of higher wavefield amplitudes in the matrix.
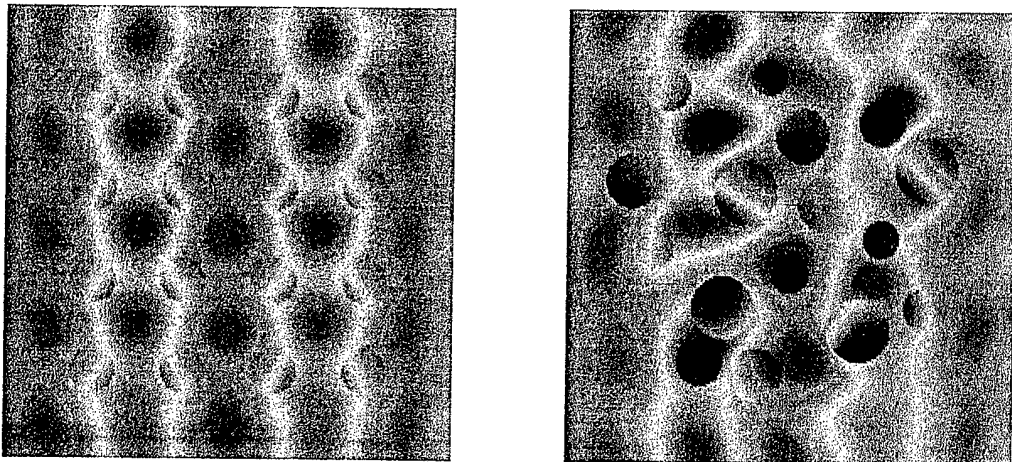
FIGURE 5-8. Color plots of the total displacement in the z-direction for an ordered (left) and random (right) configuration of 16 quartz particles in ice, with an incident mixed longitudinal-shear wave.

The results from the 16-particle simulations show that random particle dispersions may produce higher field concentrations both within and outside the particles due to the nonuniform structure and resultant scattering interactions. An additional result is that the scattering interactions by themselves can lead to attenuation mechanisms not associated with the inherent absorption properties of the materials comprising the matrix or particles. Such attenuation may be related to band-gap phenomena for ordered particle arrays.

5.2 Elastic Wave Scattering in the Frequency Domain

5.2 (a) Results for Small Dispersions

Frequency domain models for elastic wave scattering were constructed according to the flow diagram in Figure 3-7. Each of the fields (longitudinal, shear-electric, and shear-magnetic) and their cartesian components were evaluated at a single point located a fixed distance from the particle configuration. This distance was set equal to the longest wavelength evaluated—the longitudinal wavelength at the lowest frequency. Placing the evaluation point here eliminated interference effects between the wavelength of the scattered waves and the free propagation length.

The scattering computations were performed for 100 equally-spaced frequencies. The frequency stepsize was 0.01 MHz and the range was 0.01 to 1.00 MHz. The frequency was converted to the

dimensionless parameter kd in the spectra, where k is the wavevector of the longitudinal or shear wave, and d is the average particle diameter. The kd parameter is more physically insightful since the wavelengths of the longitudinal and shear waves differ for the same frequency due to the differences in wave velocities.

As with the spatial domain models, multiple scattering simulations were compared to single scatterer simulations to determine the influence of the multiple scattering interactions. Comparisons were also drawn between ordered and random particle configurations. The materials were again ice for the matrix and quartz for the particles. These materials were found to be a good compromise for providing particles with neither too low or too high of contrast with the matrix. These materials were additionally a fair approximation for many industrially useful metals, ceramics, and hard plastics.

Both two- and three-dimensional particle configurations were simulated. The two-dimensional dispersions included 16-particle configurations similar to those already examined with the spatial domain methods. Figure 5-9 shows an ordered lattice of 16 particles already used in the spatial domain simulations (left), and a random arrangement similar to the one previously studied but with uniform particle sizes (right). For both configurations the particle diameters were 1.0 cm. The lattice particles were separated by 2.0 cm center-to-center.
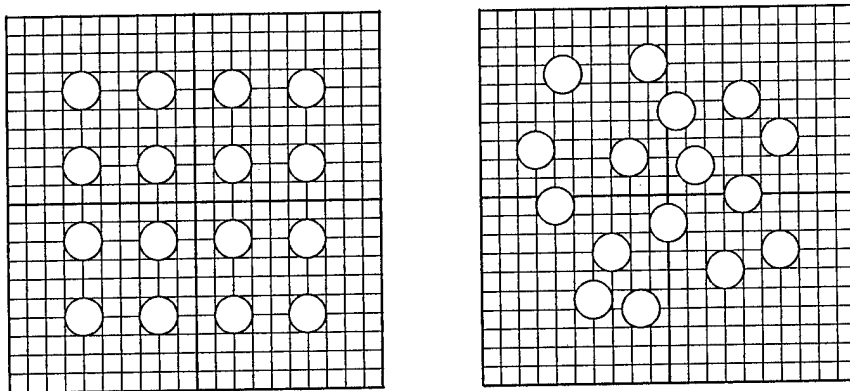
FIGURE 5-9. Two-dimensional, 16-particle configurations for frequency domain simulations, ordered lattice structure (left) and random structure (right).

Particle sizes were varied for the particle configurations in Figure 5-9 to test this variable. Two-dimensional square lattices containing 12, 8, and 4 particles were also tested. The three-dimensional particle configurations included 8 particles positioned at the corners of a cube (Figure 5-10, left) and 8 particles with random positions (Figure 5-10, right). The particles in both configurations had 1.0-cm diameters. The cubically-ordered particles were separated by 2.0 cm center-to-center.
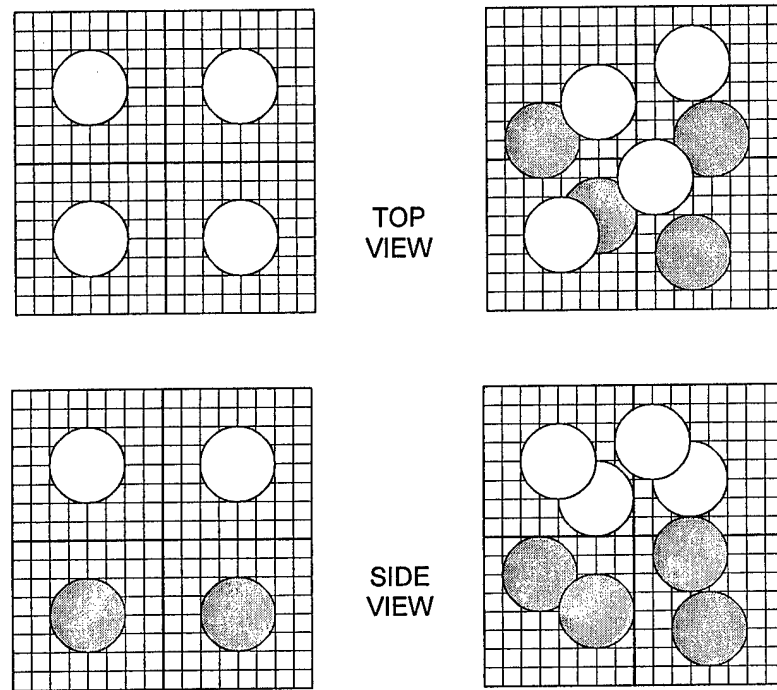
FIGURE 5-10. Three-dimensional, 8-particle configuration for frequency domain simulations with cubic (left) and random (right) structures.

Figures 5-11, 5-12, and 5-13 display the spectra for the longitudinal, shear-electric, and shear-magnetic fields respectively for the 16-particle square lattice configuration. The spectra contain gaps where the computations failed to converge within a preset (250) iteration limit. It is believed that setting a higher iteration limit would not have yielded convergence since the wavefield coefficients showed no convergence behavior within the 250 iterations. Where the computations did converge they converged rapidly, usually within less than 30 iterations. The spectra for the longitudinal and shear-electric fields particularly display significant changes with increasing n_{max}. Due to the length of time for performing the computations (about 10 hours for $n_{max} = 5$), computations for $n_{max} > 5$ would have been impractical, Convergence across the spectra range could not therefore be achieved, but is apparent for the $kd \leq 6$ region.
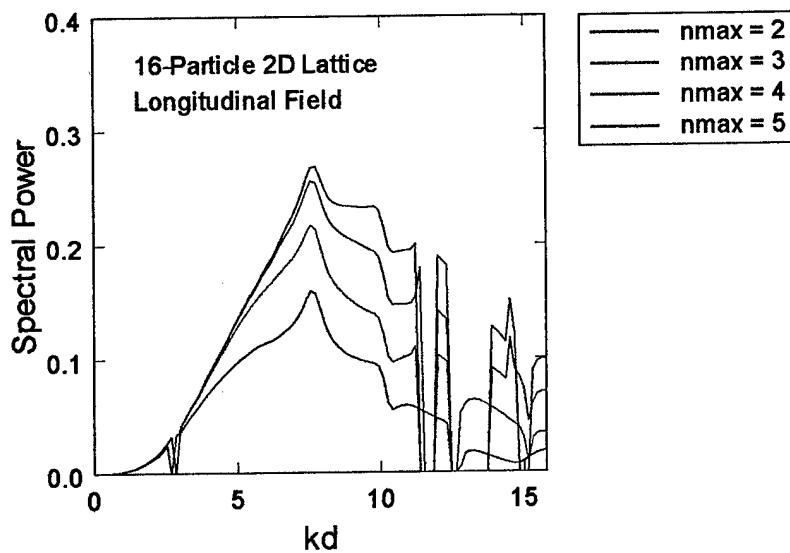
FIGURE 5-11. Power spectrum for longitudinal wave propagating through a 16-particle, two-dimensional square lattice of 1.0-cm quartz particles in an ice matrix.
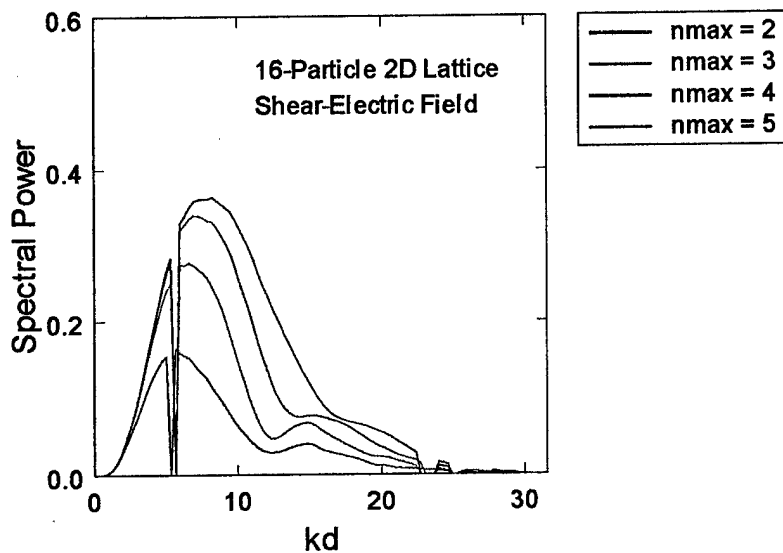
FIGURE 5-12. Power spectra for shear-electric waves propagating through a 16-particle, two-dimensional square lattice of 1.0-cm quartz particles in an ice matrix.
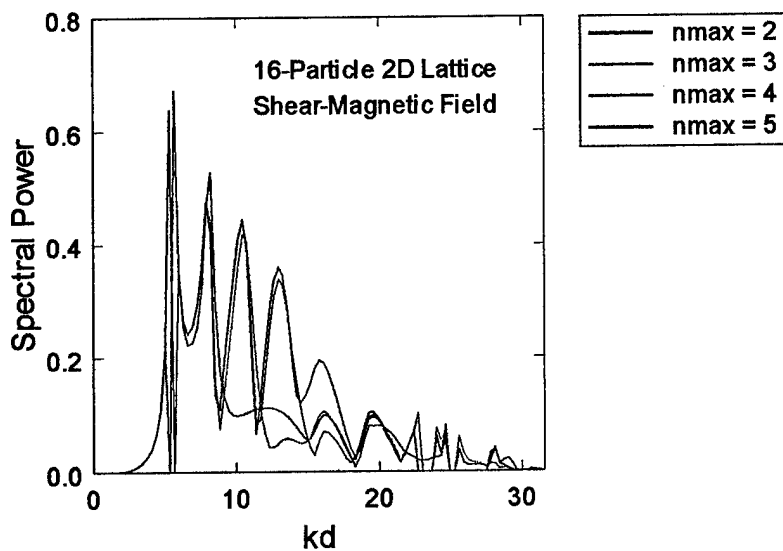
FIGURE 5-13. Power spectra for shear-magnetic waves propagating through a 16-particle, two-dimensional square lattice of 1.0-cm quartz particles in an ice matrix.

Figures 5-14, 5-15, and 5-16 display the spectra for the longitudinal, shear-electric, and shear-magnetic fields respectively for the 8-particle cubic configuration. Again the spectra contain significant gaps where the computations failed to converge within a preset (250) iteration limit. The computations for

the 8-particle 3D configurations could be carried out to higher n_{max}, however, since the number of particles were less than for the 16-particle 2D configurations. It is readily seen that the spectra converge in the $kd \le$ 10 region at $n_{max} = 7$.
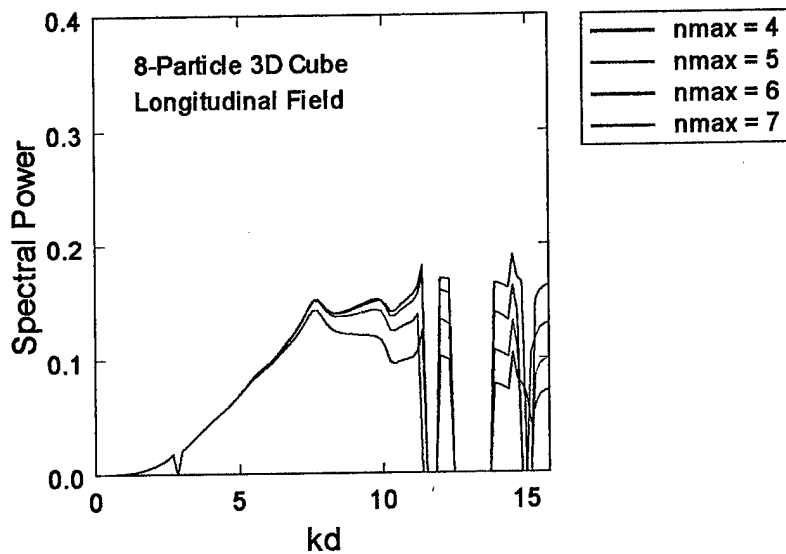
FIGURE 5-14. Power spectrum for longitudinal wave propagating through an 8-particle, three-dimensional cube of 1.0-cm quartz particles in an ice matrix.
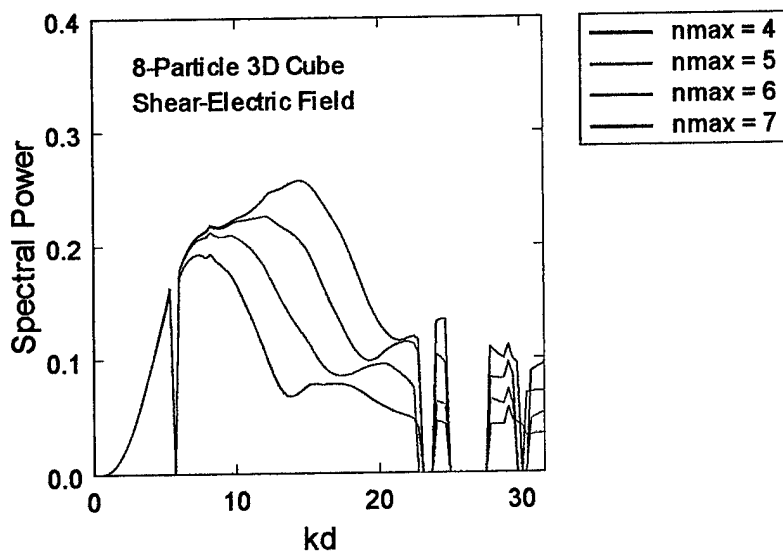
FIGURE 5-15. Power spectrum for shear-electric wave propagating through an 8-particle, three-dimensional cube of 1.0-cm quartz particles in an ice matrix.

1.2

8-Particle 3D Cube
Shear-Magnetic Field

	nmax = 4
	nmax = 5
	nmax = 6
	nmax = 7

Spectral Power

0.8

0.4

0.0

0   10   20   30

kd
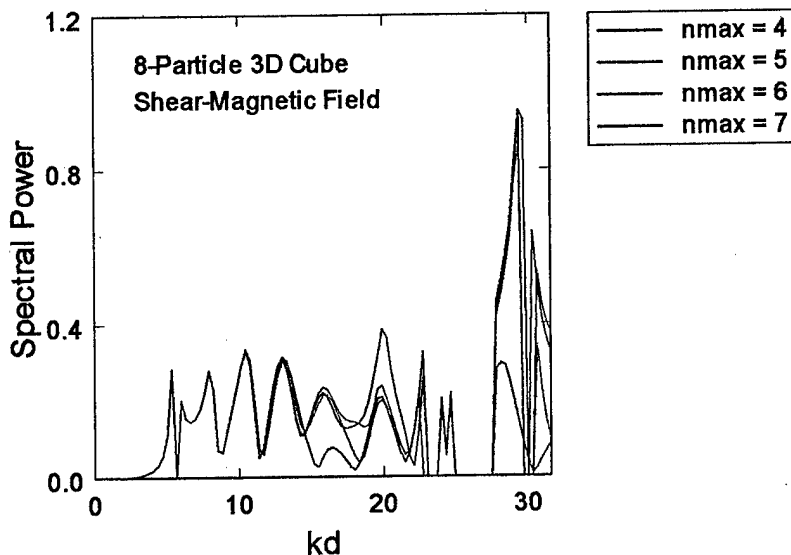
FIGURE 5-16. Power spectrum for shear-magnetic wave propagating through an 8-particle, three-dimensional cube of 1.0-cm quartz particles in an ice matrix.

The spectra in Figures 5-11 through 5-16 indicate that the longitudinal, shear-electric, and shear-magnetic fields produce different and distinctive spectra. The shear-electric field appears to peak at higher kd values than the longitudinal field, and displays broader features. The longitudinal spectra contains sharp features superimposed on broad peaks, for example at $kd = 7.5$. Most interesting, however, is the high resolution structure in the shear-magnetic spectra, displaying many more peaks than either longitudinal or shear-electric spectra.

5.2 (b) Comparison of Ordered vs. Random Structures

Figures 5-17 and 5-18 compare the longitudinal and shear-electric spectra of the 16-particle square lattice configuration with the 16-particle random configuration. Although small, overall amplitude changes are seen, the general characteristics of the spectra are the same. Similar results are observed for the 8-particle cube and random configurations (Figures 5-19 and 5-20). The similarity between the spectra is probably due to single-particle scattering dominating the characteristics of the spectra. The particle configurations tested may additionally be too small to show any significant order-disorder differences.
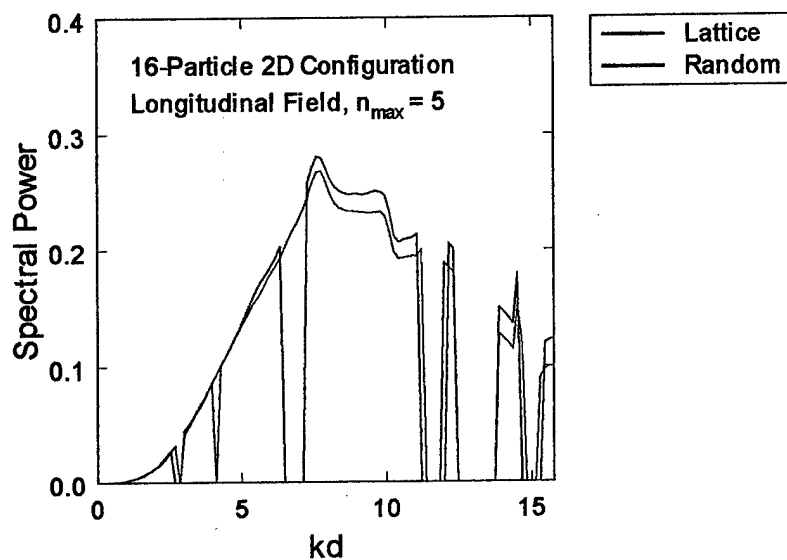
FIGURE 5-17. Power spectra for longitudinal waves comparing 16-particle ordered and random configurations of 1.0-cm quartz particles in an ice matrix.
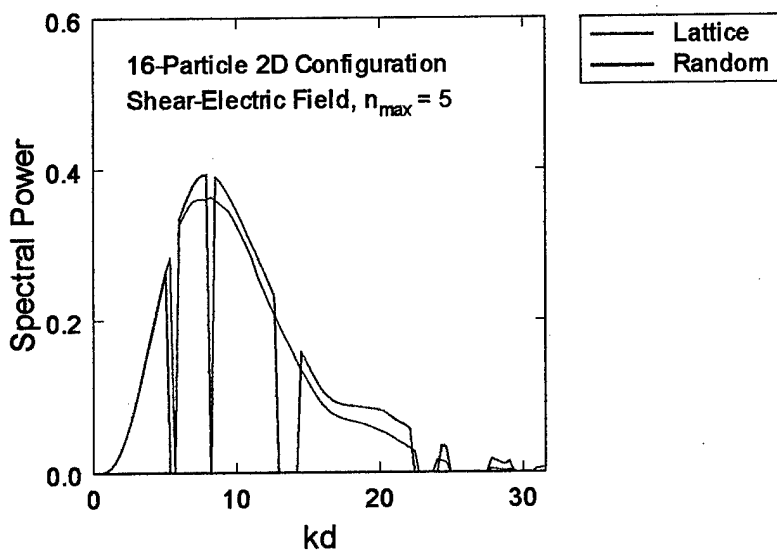
FIGURE 5-18. Power spectra for shear-electric waves comparing 16-particle ordered and random configurations of 1.0-cm quartz particles in an ice matrix.
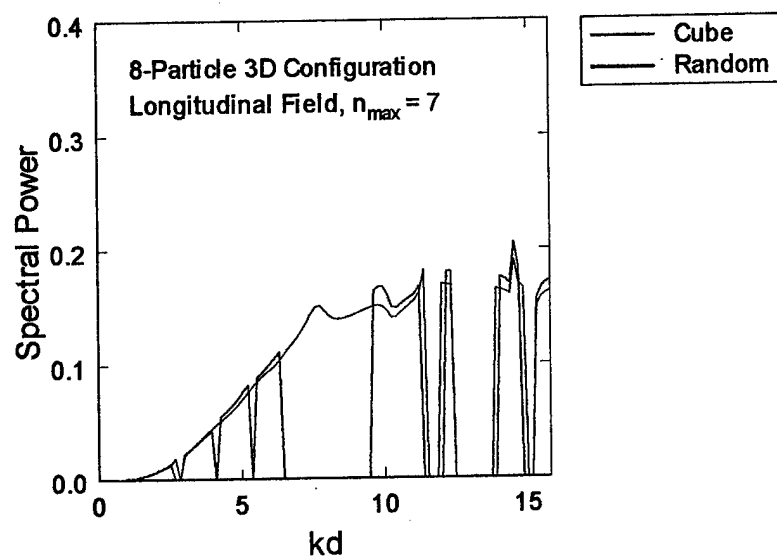
FIGURE 5-19. Power spectra for longitudinal waves comparing 8-particle cubic and random configurations of 1.0-cm quartz particles in an ice matrix.
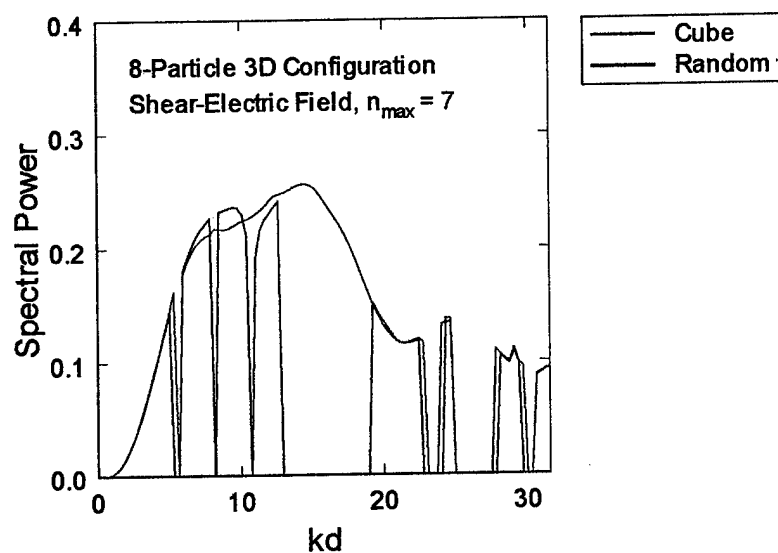
FIGURE 5-20. Power spectra for shear-electric waves comparing 8-particle cubic and random configurations of 1.0-cm quartz particles in an ice matrix.

5.2 (c) Comparison of Multiple vs. Single Scattering Computations

In addition to the multiple scattering computations, single scattering computations were performed to determine whether single scattering was the predominant contributing factor to the spectra as suggested by the ordered structure-random structure comparisons above. For the single scattering simulations, the incident plane wave is scattered only once by each particle and the resultant scattered waves are added at the evaluation point. Figures 5-21 through 5-24 compares spectra from multiple and single scattering computations. Again, the longitudinal and shear-electric fields are shown for the 16-particle 2D square lattice and 8-particle 3D cube.
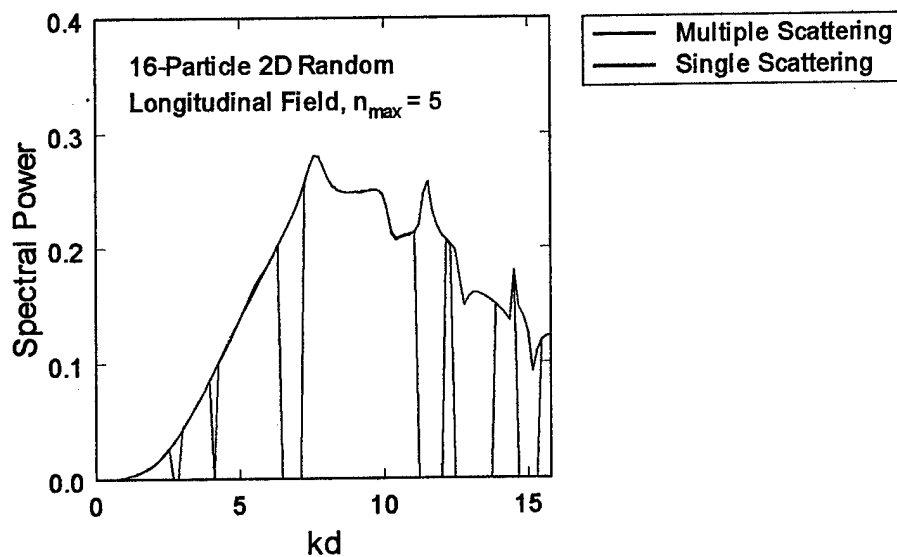
FIGURE 5-21. Power spectra for longitudinal waves comparing multiple vs. single scatterer computations for the 16-particle random configuration of 1.0-cm particles.
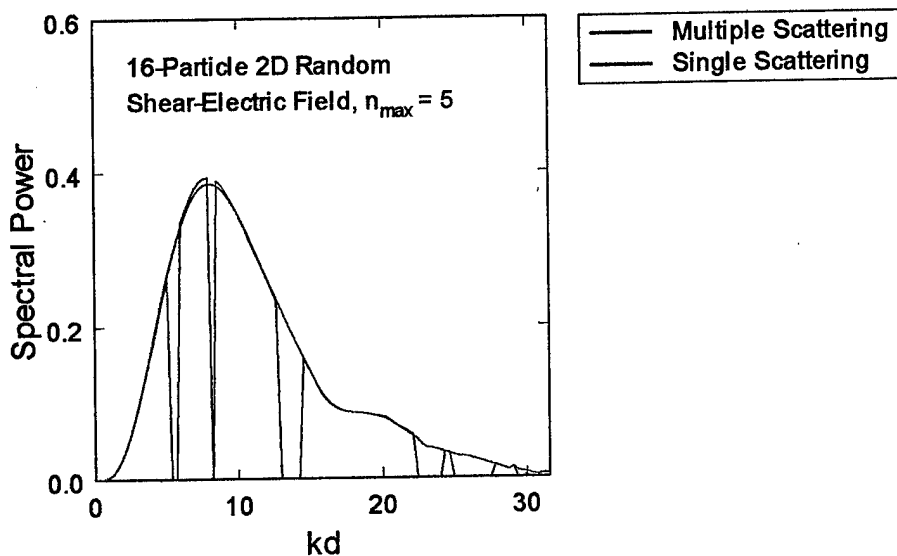
FIGURE 5-22. Power spectra for shear-electric waves comparing multiple vs. single scatterer computations for the 16-particle random configuration of 1.0-cm particles.
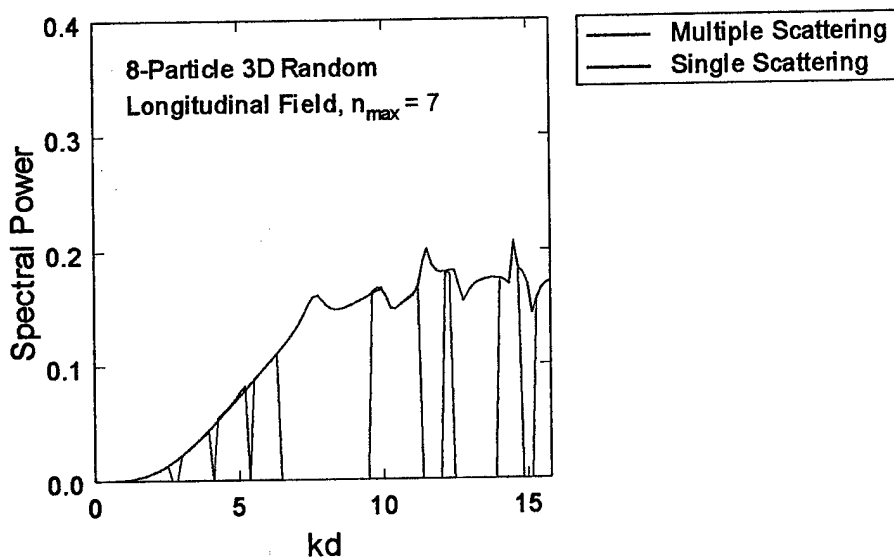
FIGURE 5-23. Power spectra for longitudinal waves comparing multiple vs. single scatterer computations for the 8-particle random configuration of 1.0-cm particles.
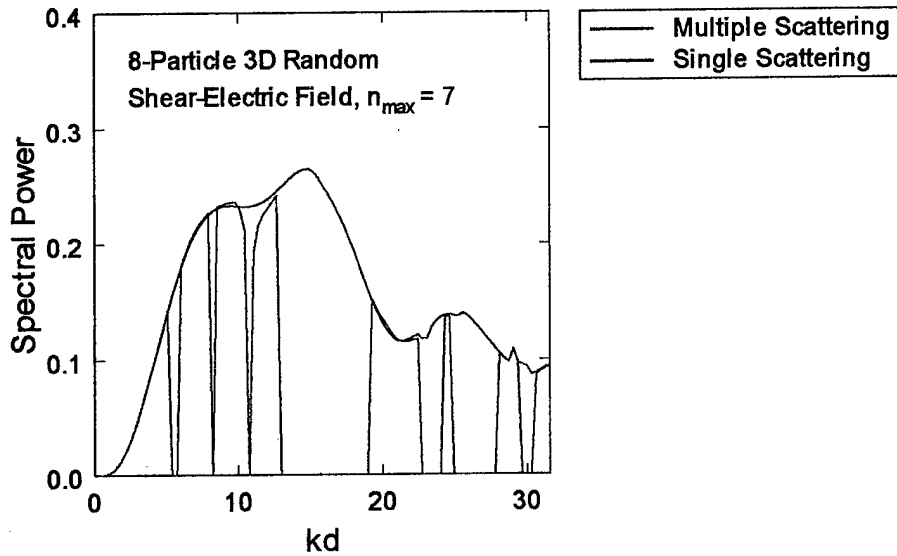
FIGURE 5-24. Power spectra for shear-electric waves comparing multiple vs. single scatterer computations for the 8-particle random configuration of 1.0-cm particles.

The results from the multiple vs. single scattering comparisons indicate that, except for the regions of nonconvergence in the multiple scattering, the spectra are virtually identical. This clearly demonstrates that single particle scattering overwhelmingly dominates the spectral characteristics for these particle configurations, material properties, spectral region, and n_{max} values. Since convergence of the spectra is observed for low kd ($kd \leq 6$ at $n_{max} = 5$ and $kd \leq 10$ at $n_{max} = 7$), we can conclude that convergence of the computations is not a factor in the predominance of the single particle scattering. The primary effect of the multiple scattering is to produce bands in the spectra where the solutions do not converge.

5.2 (d) Convergence and Efficiency of Computations

The appearance of bands representing nonconvergent solutions in the spectral simulations is problematic. Initially, the width of the bands increase with increasing n_{max}, indicating that the percent of nonconvergent solutions is increasing. This is counter-intuitive since higher n_{max} should yield more accurate solutions to the scattering. Further simulations with the 4-particle 2D square configuration shows, however, that the nonconvergence bands peak at $n_{max} = 5$ and then either plateau or start to decrease slightly with higher n_{max} values (Figure 5-25). It is possible that if the simulations were continued to higher n_{max}

values (currently not practical due to the slow speed of the computations), that the nonconvergence bands would continue to decrease and eventually disappear.

Another interesting feature of the nonconvergence bands is that they appear independent of particle number in the configuration, but are dependent on structure and particle size. Tables 5-1 and 5-2 list the percent spectral coverage of the nonconvergence bands as a functions of particle configuration and n_{max}. Both the 16-particle 2D lattice and 8-particle 3D cube have identical nonconvergence coverage (percent) values. The random analogs to these structures show higher nonconvergence coverage values, as does the 16-particle lattice with larger (d = 1.5 cm) particles. Table 5-2, however, shows that there is almost no dependence of the nonconvergence bands on the particle number in the configuration.
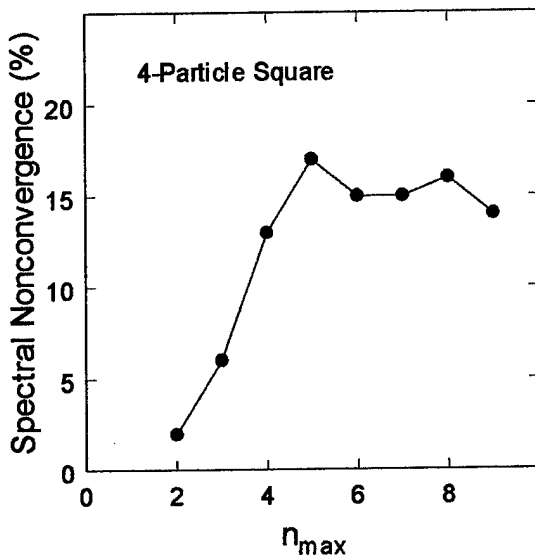
FIGURE 5-25. Percent of iterative computations not converging across spectral range.

TABLE 5-1. Percent of iterative computations not converging across spectral range (d is particle diameters in cm).

n_{max}	16-particle 2D lattice d = 1.0	16-particle 2D random d = 1.0	16-particle 2D lattice d = 1.5	16-particle 2D random d = 0.8-1.4	8-particle 3D cube d = 1.0	8-particle 3D random d = 1.0
2	3	6	8	4	3	6
3	7	12	13	6	7	13
4	13	19	25	19	13	19
5	17	28	36	39	17	32
6					15	37
7					15	42

TABLE 5-2. Percent of iterative computations not converging across spectral range (particle diameters are a constant 1.0 cm).

n_{max}	16-particle 2D lattice	12-particle 2D lattice	8-particle 2D lattice	4-particle 2D lattice
2	3	3	3	2
3	7	7	7	6
4	13	13	13	13
5	17	17	17	17

It is difficult to draw definitive conclusions from this data, other than the nonconvergence of the multiple scattering computions is

1. frequency dependent

2. structure dependent (random structures yield higher nonconvergence)

3. dependent on particle size

4. independent of particle number

It is possible that the dependence on particle size is actually a dependence on particle-particle separation, since larger particles are closer together in a lattice with fixed particle spacings. This dependence will be explored more in depth in the next section.

The convergence behavior of the single-scattering interactions was also investigated. Additional single-scatterer simulations were performed for the 8-particle 3D random configuration in order to determine the convergence behavior of the fields across the spectral range tested. Since the single-scatterer computations were extremely rapid due to not having to calculate the multiple scattering interactions, the simulations were ran to higher n_{max} values than possible with the multiple scattering computations. Figure

5-26 displays the results of these simulations, and shows plots of the convergence frequency as a function of n_{max}. The convergence frequency was defined to be the highest frequency at which the field did not vary by more than 1% from the comparison. The comparison was chosen to be the spectral results for $n_{max} = 20$, since at that n_{max} value all the fields converged to within 1% across the entire spectral range.

Figure 5-26 indicates that the longitudinal and shear-electric fields converge at the same rate, and that the shear-magnetic field converges faster. The convergence behavior for all three fields is fairly uniform. The results demonstrate that convergence is strongly frequency dependent. They also suggest that since the single particle scattering does not converge for the entire frequency range until $n_{max} = 19$ (mainly for the shear-electric field—the others converge faster), that the multiple scattering computations should also be ideally performed at $n_{max} = 19$.
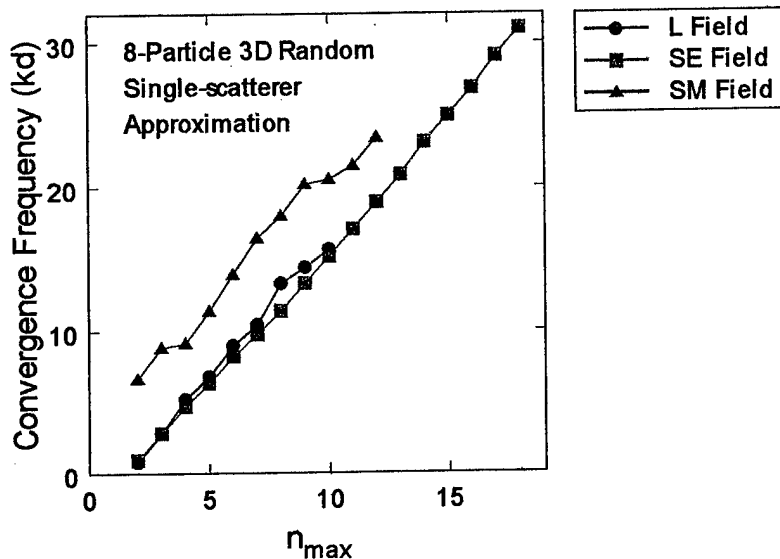
FIGURE 5-26. Convergence frequency vs. n_{max}, showing frequency at which 99% convergence is achieved with respect to $n_{max} = 20$.

Running the preceding simulations at $n_{max} = 19$ would unfortunately take much too long for practical considerations. Table 5-3 lists the computation times for the various particle configurations and how they vary with respect to n_{max} when modeled with a power law. The power law fit was extremely good for the time-n_{max} relationship, and the results definitively show that computation time time scales as the 4th power of n_{max} for 2D particle configurations, and as the 4.6 power of n_{max} for 3D particle configurations. From these results we can calculate that even for the 4-particle 2D square dispersion, performing a frequency-domain simulation at $n_{max} = 19$ would take 74 hours. For the 16-particle square lattice, the $n_{max} = 19$ computations would require 2215 hours or approximately 92 days.

TABLE 5-3. Computation time for various particle configurations as a function of n_{max} modeled with the power law $T = g * (n_{\max})^{K}$.

Particle Configuration	T for $n_{max} = 5$ (hours)	K	g
Two-dimensional			
16-particle lattice, d = 1.0	10.22	3.98	0.017
16-particle random, d = 1.0	10.41	4.16	0.013
16-particle lattice, d = 1.5	10.78	4.04	0.016
16-particle random, d = 0.8-1.4	10.60	4.23	0.012
12-particle lattice, d = 1.0	5.15	4.04	7.73×10^{-3}
8-particle lattice, d = 1.0	2.10	4.07	3.00×10^{-3}
4-particle lattice, d = 1.0	0.35	3.99	5.69×10^{-4}
Three-dimensional			
8-particle cube, d = 1.0	1.77	4.61	1.02×10^{-3}
8-particle random, d = 1.0	1.71	4.66	9.12×10^{-4}

With regards to the number of particles (p) in the dispersion, multiple scattering computations are expected to scale as p^2. This is easy to see since there are $p(p-1)$ non-redundant interactions, and therefore $p(p-1)$ translation coefficients to compute. To check this assumption, Table 5-4 lists the results of modeling the computation time as a power law function of p.

TABLE 5-4. Computation time for two-dimensional square lattice particle configuration as a function of the number of particles p, modeled with the power law $T = h * (p)^{J}$.

n_{max}	J	h
2	2.47	3.93×10^{-4}
3	2.40	1.84×10^{-3}
4	2.38	5.60×10^{-3}
5	2.34	0.016

Two observations may be noted from Table 5-4. First, J is not 2 as would be expected for the multiple scattering computations scaling to the square of the particle number p. This is due to other computations performed by the program, such as the single particle scattering calculations and such. These "overhead" computations are more apparent due to the small number of particles we are simulating. Second, J is decreasing with increasing n_{max}. It is probably a reasonable assumption that as n_{max} gets very large that J will asymptotically approach 2. Again, this is due to the multiple scattering computations overshadowing the background "overhead" computations as n_{max} increases.

5.2 (e) Results for 91-Particle bcc Dispersion

A larger particle configuration was tested to determine if multiple scattering would have a more pronounced effect with a larger number of particles. The particle configuration was a 91-particle lattice in the the shape of a cube and with a body-centered cubic (bcc) structure (Figure 5-27, left). Since the computation time for multiple scattering roughly scales as p^2, accounting for all of the multiple scattering interactions would have been impractical. Instead, a nearest-neighbor approximation was used, where multiple scattering contributions were calculated for only the nearest 14 neighbors to any particle (Figure 5-27, right). The translational symmetry of the bcc structure was also used to advantage. Since the translational addition coefficients would be the same for each of the nearest neighbors, independent of which particle the fields were being translated to, only 14 sets of translation coefficients required computation.
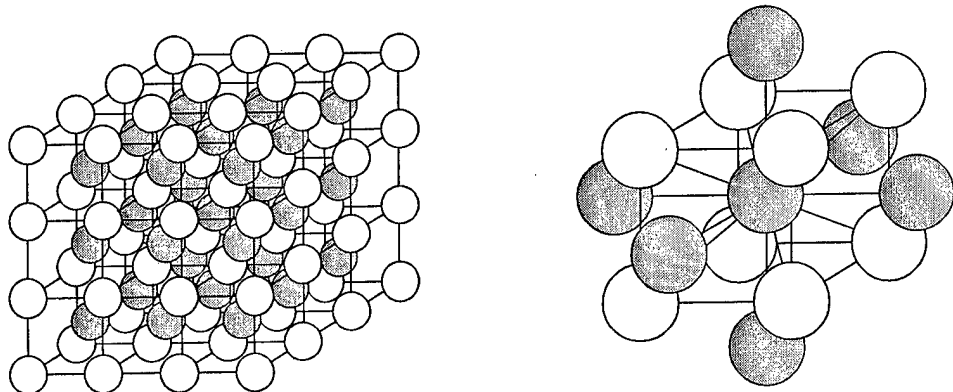
FIGURE 5-27. Body-centered cubic 91-particle configuration (left) and the 14 nearest neighbors (right) used to compute the multiple scattering interactions.

The particles were again 1.0-cm diameter quartz spheres in an ice matrix. Simulations were ran

for three different particle-particle separations (lattice constants c) to produce particle volume fractions of

10% ($c = 2.188$ cm), 25% ($c = 1.612$ cm), and 40% ($c = 1.378$ cm). Figure 5-28 displays the percent

spectral nonconvergence for the three particle separations at various n_{max} values. Nonconvergence clearly

increases as the particle separation decreases. The nonconvergence of the 10% volume fraction lattice is

similar to that of the 2D square lattice configurations with 1.0-cm particle diameters. Likewise, the

nonconvergence of the 25% and 40% lattices are similar to those of the random 2D configurations and 2D

configurations with larger particle diameters.
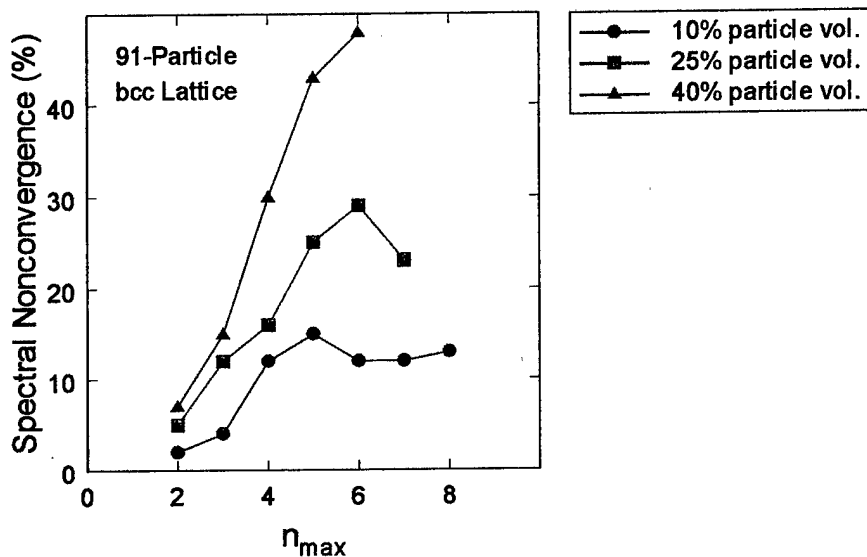
FIGURE 5-28. Percent of iterative computations not converging across spectral range for three 91-particle body-centered cubic configurations with particle volume fractions of 10%, 25%, and 40%.

Figures 5-29 and 5-30 display longitudinal and shear-electric field spectra for the 91-particle bcc

configurations. The spectra are very similar to those of the 8-particle 3D cube (Figures 5-14 and 5-15), but

are significantly more marred with spectral bands of nonconvergent solutions.
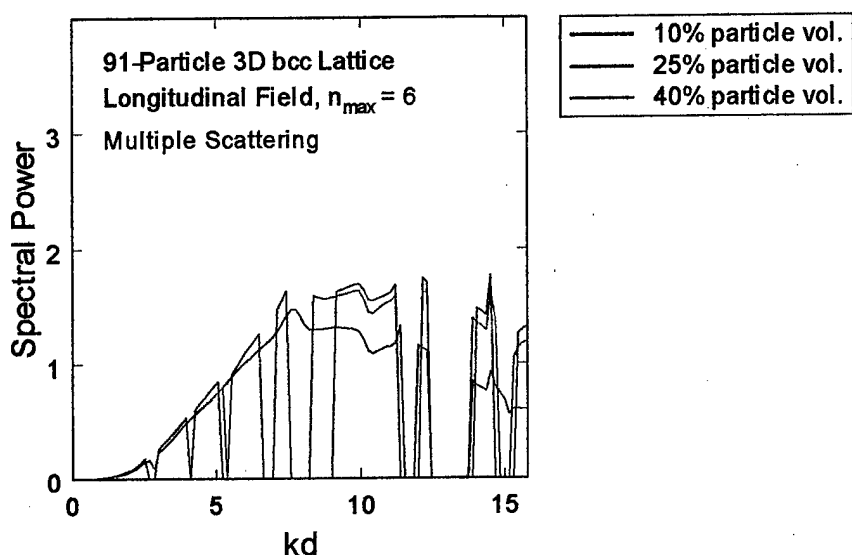
FIGURE 5-29. Power spectrum for longitudinal wave propagating through a 91-particle bcc-ordered lattice of 1.0-cm quartz particles in an ice matrix and for three different lattice constants (particle volume fractions).
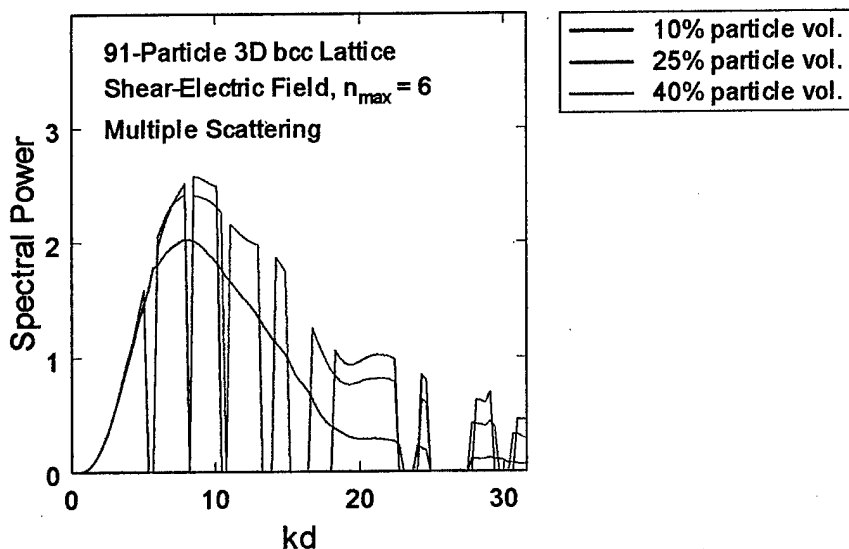
FIGURE 5-30. Power spectrum for shear-electric wave propagating through a 91-particle bcc-ordered lattice of 1.0-cm quartz particles in an ice matrix and for three different lattice constants (particle volume fractions).

Figures 5-31 and 5-32 display single-particle scattering simulations of the 91-particle bcc lattice. Comparison with Figures 5-29 and 5-30 again shows that the single particle scattering dominates the behavior of the waves, even for the relatively close pack of 40%.
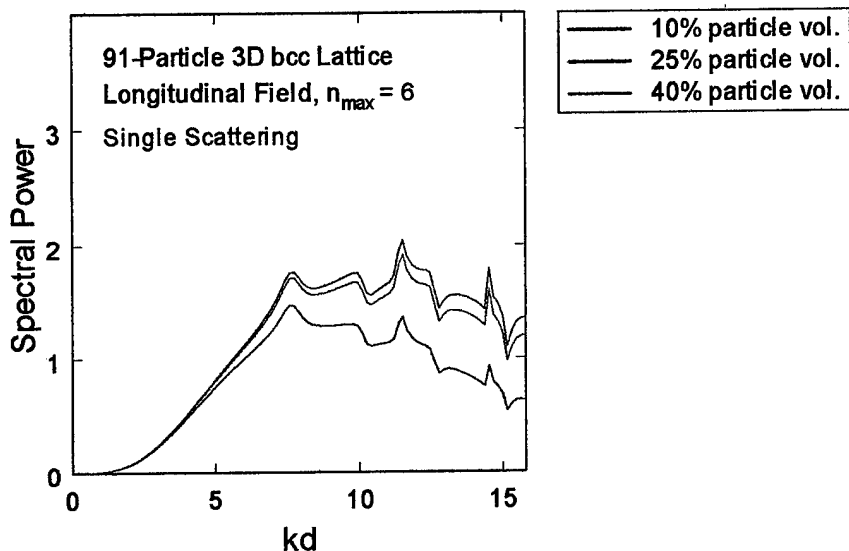
FIGURE 5-31. Power spectrum for longitudinal wave propagating through a 91-particle bcc-ordered lattice of 1.0-cm quartz particles in an ice matrix and for three different lattice constants (particle volume fractions).
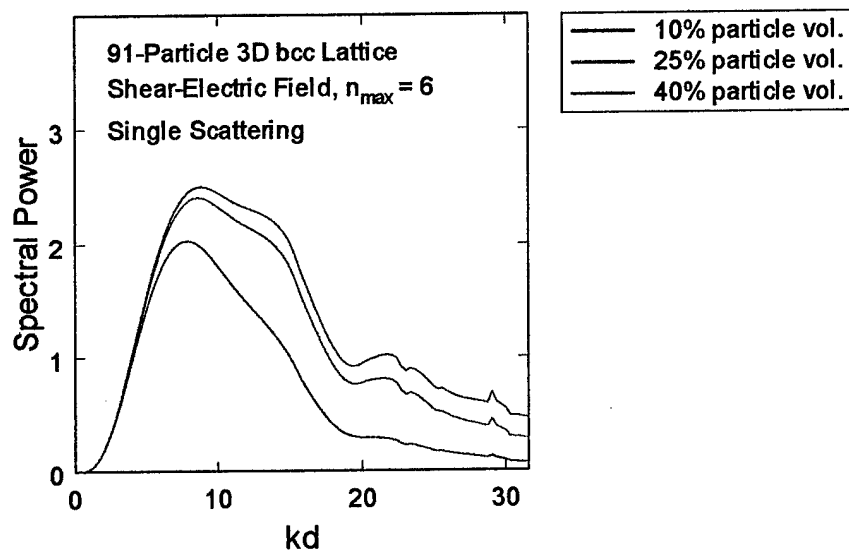
FIGURE 5-32. Power spectrum for shear-electric wave propagating through a 91-particle bcc-ordered lattice of 1.0-cm quartz particles in an ice matrix and for three different lattice constants (particle volume fractions).

The high degree of nonconvergence for the lattices with 25% and 40% particle volumes strongly indicates that particle-particle separation is a primary factor for convergence of the multiple scattering calculations. Additional simulations were performed with the 91-particle bcc lattice with the particle properties changed to those of plexiglass. This provided a particle-matrix combination with low contrast in acoustic properties. These simulations produced spectra with 100% convergent solutions. The results suggest that the factors that increase the degree of multiple scattering—small particle-particle separations and high acoustic property contrasts—also lead to nonconverging solutions for multiple bands of frequencies.

Finally, the close resemblance between spectra from multiple scattering computations and spectra from single scattering computations suggests one or both of the following conclusions:

1. Single-particle scattering dominates the scattering behavior of particle configurations with up to 40% particle volume fractions;

2. The multiple scattering computations do not contribute significantly to the final scattering solutions for n_{max} values below those required for convergence of the translational addition theorems.

As shown in Chapter 4, convergence of the translation coefficients for all three multipole fields cannot be achieved for $n_{max} \leq 16$, and would most likely require n_{max} values in the range of 50-100 (based on plane wave convergence results). With the inefficiency of the current computation method it is not possible to perform multiple scattering simulations at such n_{max} values.

5.3 Preliminary Ultrasonic Scattering Model for a Composite Material

The frequency domain elastic wave scattering model was applied to the simulation of a particulate composite material to investigate the feasibility of using such models for industrial applications such as nondestructive evaluation. A polymer rubber filled with inorganic particles was selected as the test material. Such materials find uses as tires, thermal insulation, and solid propellants. The density and elastic properties of sodium chloride (salt) were used as a generic model for the inorganic solid filler.[192] The rubber also had generic properties typical of lightly cross-linked, highly attenuating polymers with

longitudinal wave velocity and density close to that of water ($c_L = 1.45 \times 10^5$ cm/s, $\rho = 1.0$ g/cm^3).[193,194]

Using a Poisson's ratio of 0.49, which is typical for rubber materials, a shear wave velocity of $c_S = 2.0 \times 10^4$ cm/s was derived for use in the computations.

The particles were 200-μm spheres with volume packing fractions of 10%, 30%, and 50%. The particle microgeometries were both ordered (body-centered cubic) and random. The random particle configurations were provided by ATK-Thiokol Propulsion using a proprietary particle packing code. The random particle microstructures provided by ATK-Thiokol Propulsion were spherical conglomerations comprised of 12,820 particles (Figure 5-33). Equivalent particle conglomerations were constructed with a crystalline bcc structure to test the effects of order and multiple scattering (Figure 5-34). Disks of uniform size were cut from the spherical packs to eliminate sample size effects (since the diameter of the conglomerate sphere varied with volume packing fraction). The excised disks had a 5.0 mm diameter and 2.5 mm thickness.
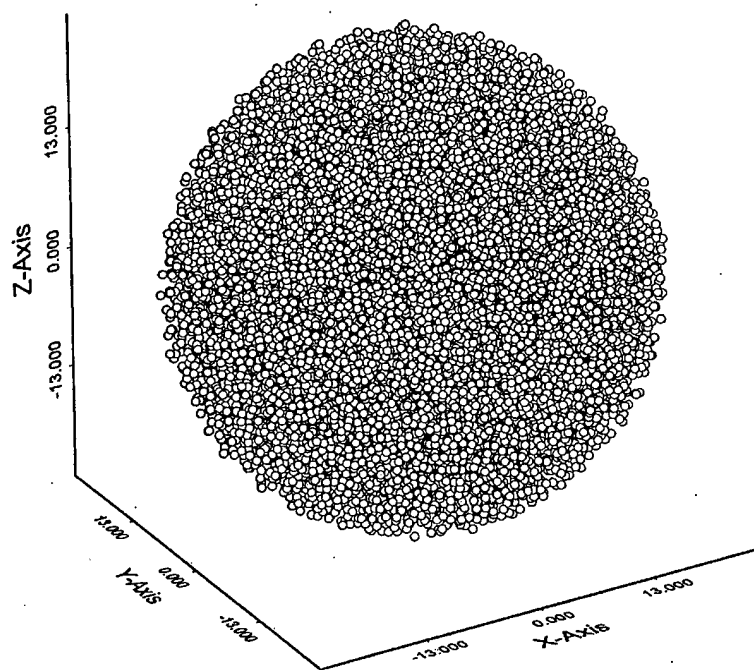
FIGURE 5-33. Spherical collection of 12,820 particles with a random microstructure.
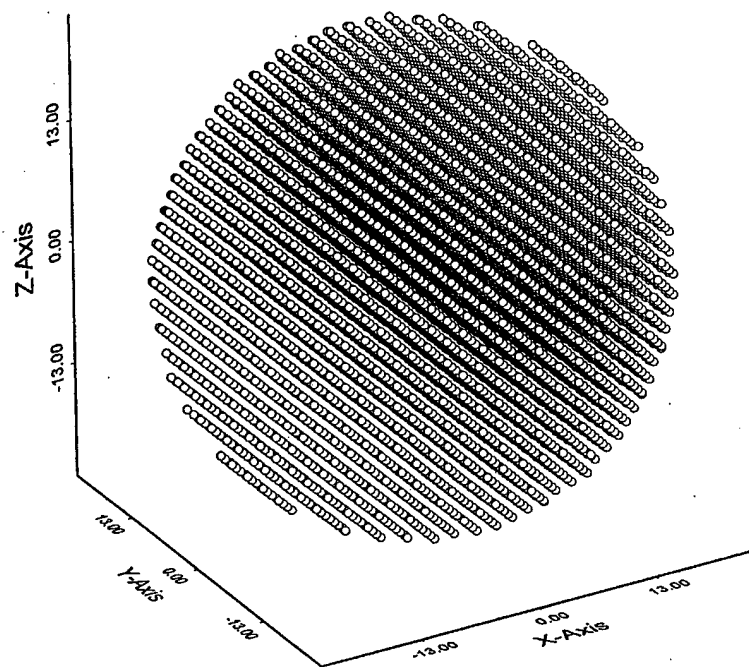
FIGURE 5-34. Spherical collection of 12,820 particles with an ordered bcc microstructure.
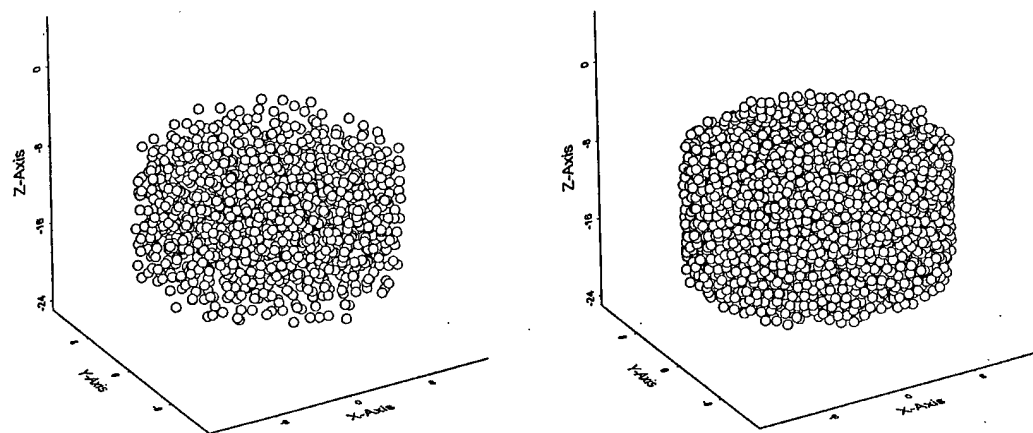
FIGURE 5-35. Disk-shaped collections of 1191 particles (10% packing fraction, left) and 5885 particles (50% packing fraction, right) with random microstructures.
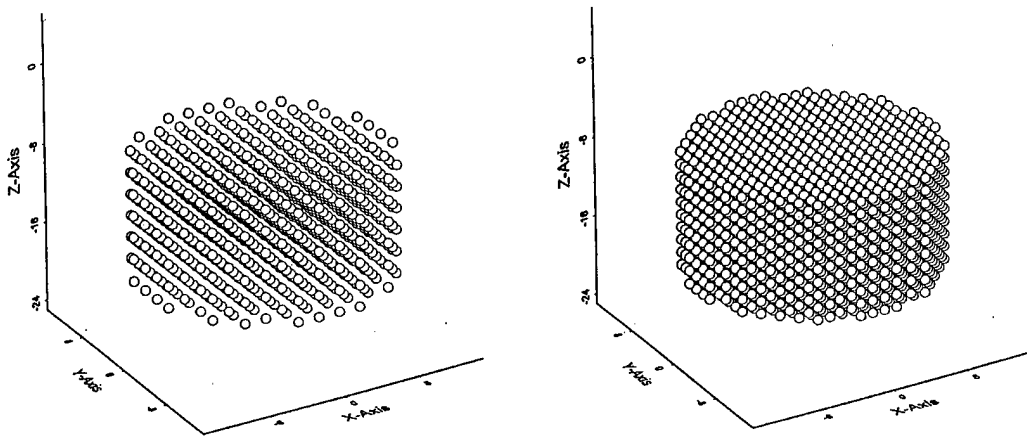
FIGURE 5-36. Disk-shaped collections of 1177 particles (10% packing fraction, left) and 5637 particles (50% packing fraction, right) with ordered bcc microstructures.

Multiple scattering simulations were found to be much too time intensive and inefficient to be performed on the random particle packs. Multiple scattering simulations were possible with the ordered particle packs, however, using the translational symmetry of the bcc cubic crystal and the nearest neighbor approximation. Single scattering computations were also ran for comparison. As an example of the difference in computation times between multiple and single scatterer simulations, the computation time for the multiple scatterer simulation was 33.11 hours whereas for the single scatterer simulation was 0.35 hours (5637-particle pack, $n_{max} = 4$). Although higher n_{max} values are desirable for convergence, the long computation time limited the n_{max} to 4 or less.

Figures 5-37 and 5-38 display comparisons between spectra from multiple and single scattering computations. The spectra are plotted as functions of actual frequencies (0-2.0 MHz) that are used in ultrasonic inspection and evaluation of materials. Equivalent kd values (where d is the particle diameter) for 2.0 MHz are 1.73 for the longitudinal field and 12.6 for the shear fields.
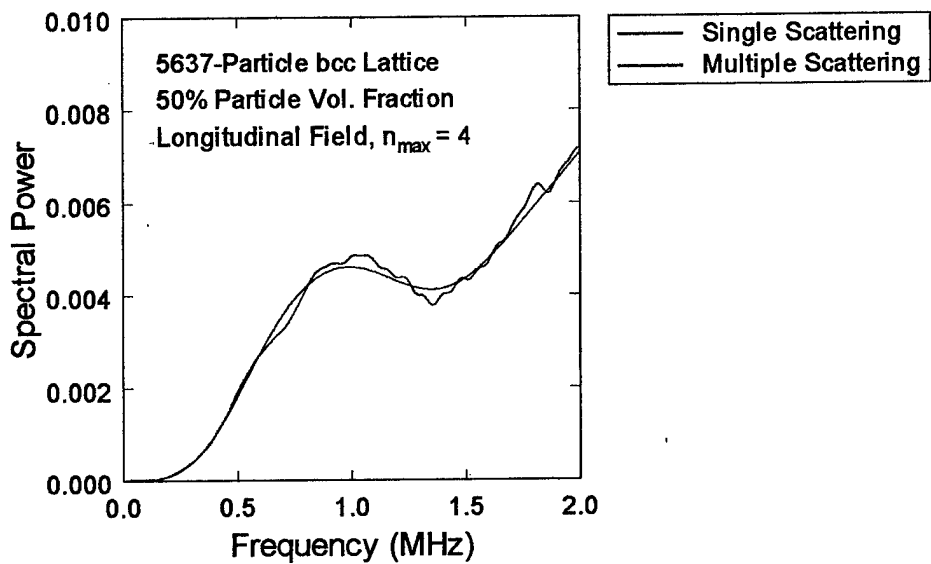
FIGURE 5-37. Comparison of longitudinal field power spectra for multiple vs. single scattering computations for a bcc crystal with 50% volume packing fraction.
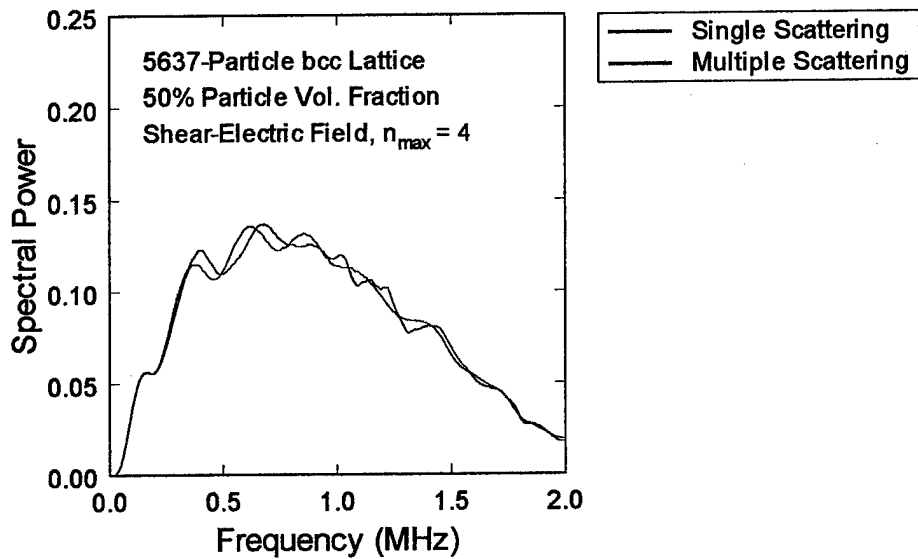
FIGURE 5-38. Comparison of shear-electric field power spectra for multiple vs. single scattering computations for a bcc crystal with 50% volume packing fraction.

The spectra in Figures 5-37 and 5-38 show that the single scatterer approximation captures the general features of the ultrasonic spectra reasonably well. Although there are some differences in fine detail, the match is good, especially at low frequencies (< 0.5 MHz). Of most importance is that the single scatterer approximation shortens the computation time by about 100x, and works just as fast for random as well as ordered particle packings.

To test the n_{max} criterium necessary for convergence of the single scattering computations, scattering computations were performed for a single 200-μm NaCl sphere in the rubber matrix and ran to high n_{max} values. Figure 5-39 shows the results of this test. The main conclusion is that single sphere scattering converges by $n_{max} = 6$ for ultrasonic frequencies of practical use in these materials—0-1.0 MHz. Extending the n_{max} value to 7 widens the spectral region of convergence to 0-1.5 MHz.
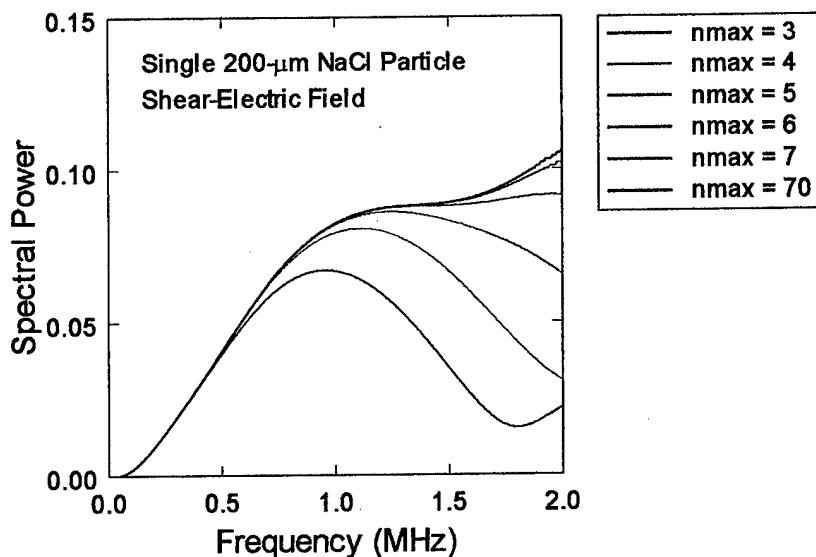
FIGURE 5-39. Shear-electric field power spectra for scattering from a single 200-μm NaCl sphere in a rubber matrix, showing convergence behavior for various n_{max} values.

For the small particle configurations looked at in Section 5-2, the fields were evaluated at a single point located a large distance from the pack equal to the longest wavelength associated with the lowest frequency. This was done to eliminate phase interference effects in the spectra due to the interplay between the field wavelength and evaluation point distance. For the larger particle packs of the particle-filled rubber simulations, placing the evaluation point a distance from the particle pack introduced additional spurious effects in the spectra due to the overall shape of the conglomeration (*i.e.*, the particle pack shape *in toto*— disk, sphere, etc.—introduces a unique scattering signature onto the spectra).

To eliminate this shape effect the evaluation point was placed close (1.25 mm) to the disk's circular face. Although this eliminated the particle pack shape effects, it reintroduced field wavelength-evaluation distance interference effects. These interference effects manifested themselves as a periodic waviness in the spectra analogous to interference fringes. To reduce this effect, the fields were evaluated over several spatially separated points. Figure 5-40 shows spectra from a single point, from a cross-shaped configuration of 9 points, and from a square grid of 25 points. Each of the evaluation point configurations was 1.25 mm from the disk.
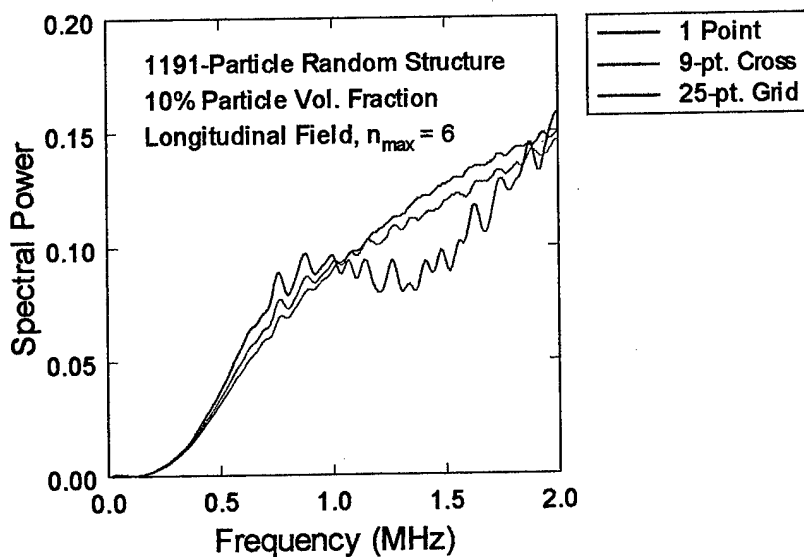
FIGURE 5-40. Comparison of longitudinal field power spectra evaluated at a point, at a cross comprised of 9 points, and at a square grid comprised of 25 points.

As can be seen in Figure 5-40, evaluating all of the fields at a single point produces too much position-dependent structure in the spectrum. The use of multiple evaluation points, however, clearly resolves the interference effects in the spectra and removes the position bias associated with using a single evaluation point. Interestingly, the 9-point cross configuration is almost as good at removing the interference effects as the 25-point square grid. This is probably due to the cross being able to span the same spatial distance as the grid but without requiring as many points. Although the 25-point grid was very good at averaging out the position-dependent spectral structure, it proved to be too time-consuming to implement. Instead, the 9-point cross proved to be a good compromise between computation time and position bias.

The testing of a simulated particle-filled rubber provided insight into the most efficient and accurate method for modeling its ultrasonic properties. For particle packs up to 50% particle volume fraction the single scatterer approximations works just as well as the current multiple scattering computations. Additionally, the single scattering calculations converge at low n_{max} (≈ 7) for most of the frequency range for practical ultrasonic measurements. Finally, evaluating the fields at a single point introduces position-dependent interference effects that can be reduced by evaluating the fields over a grid or cross configuration of points.

5.4 Electromagnetic Wave Scattering in the Frequency Domain

Frequency domain models for electromagnetic wave scattering were constructed by appropriately modifying the scattering equations and material properties in the elastic wave models. Instead of calculating three fields (longitudinal, shear-electric, and shear-magnetic) as in the elastic wave model, only two fields (electric and magnetic) require computation in the electromagnetic case. For material properties, the Lame elastic constants are replaced with the dielectric permittivity and magnetic susceptibility. These properties, as well as particle size, were varied to simulate a variety of particulate systems. All of the simulations were of the 91-particle bcc configuration pictured in Figure 5-27 or of larger bcc lattices. Spectra were computed for both the individual field components and for the total energy of the wave (the amplitude of the Poynting vector).

Like the elastic wave simulations, multiple scattering computations for electromagnetic waves were nearly identical to single scattering computations. Unlike the elastic wave simulations, however, very few convergence problems were encountered. Most of the calculations converged within 10 iterations for the frequency ranges and n_{max} values tested. Nonconvergence was observed for only close particle packings (50-60% particle volume), high n_{max} (≥ 8), and high electromagnetic property contrasts (for example, water droplets in air). However, the nonconvergence covered only a small percent of the spectral frequencies (about 1%) as compared to the elastic wave simulations.

A striking feature of the electromagnetic wave simulations was the appearance of band gaps in the spectra. The frequency position of these band gaps was a function of the bcc lattice constant and not of the particle diameter, indicating that they were photonic band gaps arising from interference and localization effects in the lattice.

Figure 5-41 is the total energy spectrum of 1.0-μm diameter quartz spheres in an ice matrix, plotted with respect to wavelength. The frequency range tested was in the optical (infrared and visible) region of the electromagnetic spectrum, and varied from 10-1000 THz (0.3-30 μm wavelength in air). The optical properties were obtained from two well-known physics textbooks.[196,197] The six plots represent 91-particle bcc lattices with various particle volume fractions. The lattice constants for each of the particle volume fractions are listed in Table 5-5.

TABLE 5-5. Lattice constants for each of the particle volume fractions in the 91-particle bcc lattice simulations.

Particle Volume Fraction (%)	Lattice Constant (μm)
10	2.188
20	1.736
30	1.517
40	1.378
50	1.279
60	1.204
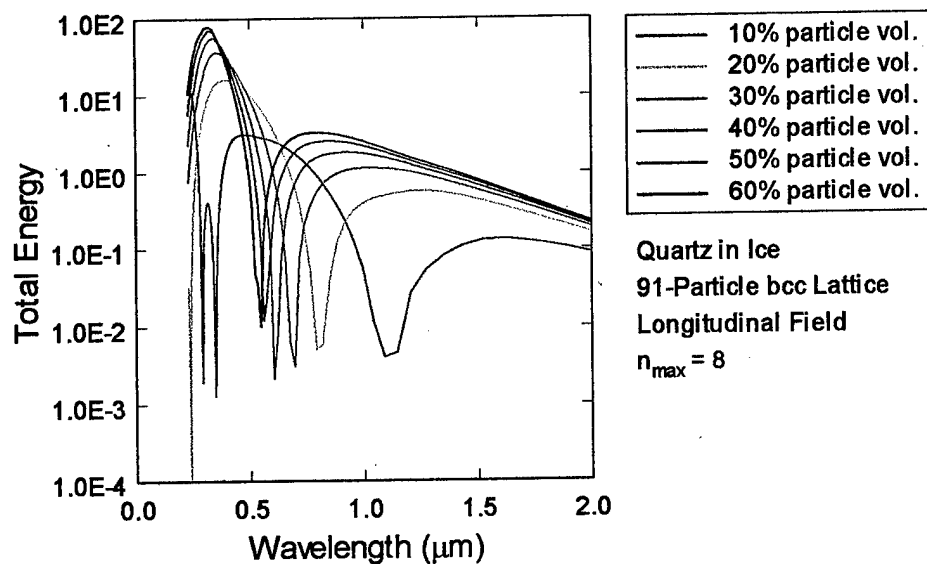
FIGURE 5-41. Simulated total energy spectrum vs. wavelength of microwaves passing through a 91-particle bcc lattice of 1.0-μm quartz particles in ice.

It is clear from Figure 5-41 that the position of the band gap regions vary with particle volume fraction and therefore with lattice constant. Replotting the quartz-ice spectrum as a function of ka, where k is the wavevector and a is the lattice constant, reveals a direct relationship between the band gaps and lattice constants (Figure 5-42). The band gap at $ka = 14$ is particularly consistent for the six particle configurations (lattice constants), and it appears that a band gap at approximately $ka = 47$ is also a general feature of the spectra as well. The $ka = 14$ band gap is close to the value of 4.5π, indicating that this band gap is occurring where the wavelength is equal to 0.44 times the lattice constant. Experimental data from bcc colloidal crystals show strong band gaps near wavelengths of 0.7, 0.8, and 0.88 a.[198] The colloidal crystals, however, had a very low particle volume fraction of 1.3%, and photonic band gaps have been shown to have a very strong dependence on the ratio between particle radius and lattice constant (r/a).[199] For two-dimensional lattices of dielectric columns, as r/a increases the wavelength of photonic band gap decreases, which is consistent with our simulation results and the experimental results.
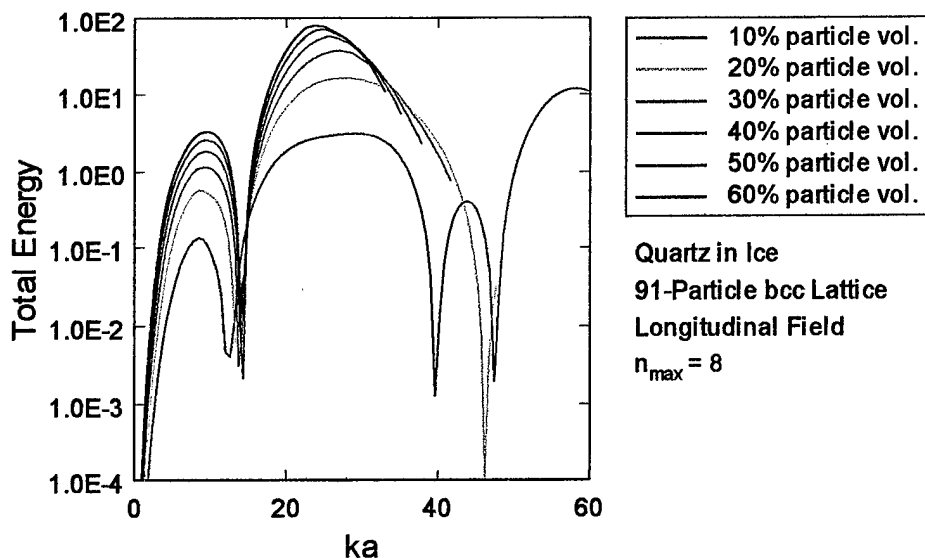
FIGURE 5-42. Simulated total energy spectrum vs. parameter ka of microwaves passing through a 91-particle bcc lattic of 1.0-μm quartz particles in ice.

Although the quartz-in-ice simulations are at optical frequencies and micrometer scales, they could be readily rescaled to microwave frequencies (1-100 GHz) and centimeter scales (1.0-cm diameter particles). Figures 5-41 and 5-42 would therefore be applicable to these longer wavelengths and larger particle sizes if the optical properties of ice and quartz were assumed to be constant into the microwave bands. Unfortunately this is not a good assumption. The electromagnetic properties of water and ice change appreciably with frequency, and therefore have to be accurately modeled in order to obtain reliable results for microwaves.

Since the microwave properties of quartz were difficult to find, water droplets in air were modeled to test the electromagnetic simulations at microwave frequencies. The particles were 1.0-cm diameter water droplets arranged in a 91-partcile bcc lattice. Although a random lattice would have been more appropriate for modeling atmospheric precipitation such as rain, the bcc lattice was convenient due to the translational order and nearest neighbor approximation providing a considerable reduction in computation time. The frequency range of the simulations was 1-100 GHz. The microwave properties of the water droplets were modeled as a function of frequency using the Cole-Cole equation.[200]

Figures 5-43 and 5-44 display the computed spectra for water drop configurations at various particle concentrations. Due to the difference in electromagnetic properties, the spectra do not look like those of the quartz-ice configurations in Figures 5-41 and 5-42, but rather exhibit much more fine structure and sharp peaks. The existence of photonic band gaps is also less certain for the results in Figures 5-43 and 5-44. It is possible that some band gap structures may exist in the ka =4-14 region in Figure 5-44, but they are not consistent with particle concentration (lattice constant) as in Figure 5-42.
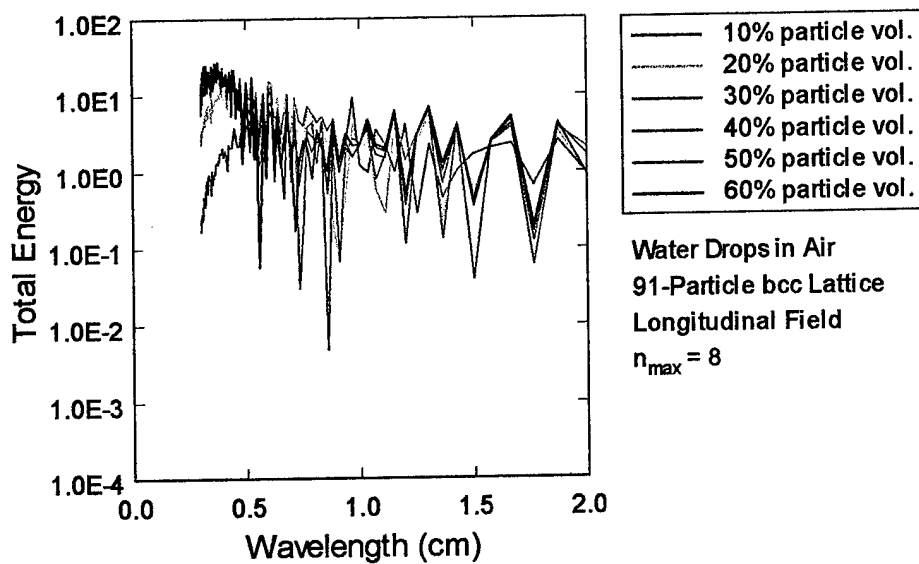
FIGURE 5-43. Simulated total energy spectrum vs. wavelength of microwaves passing through a 91-particle bcc lattic of 1.0-μm water particles in air.
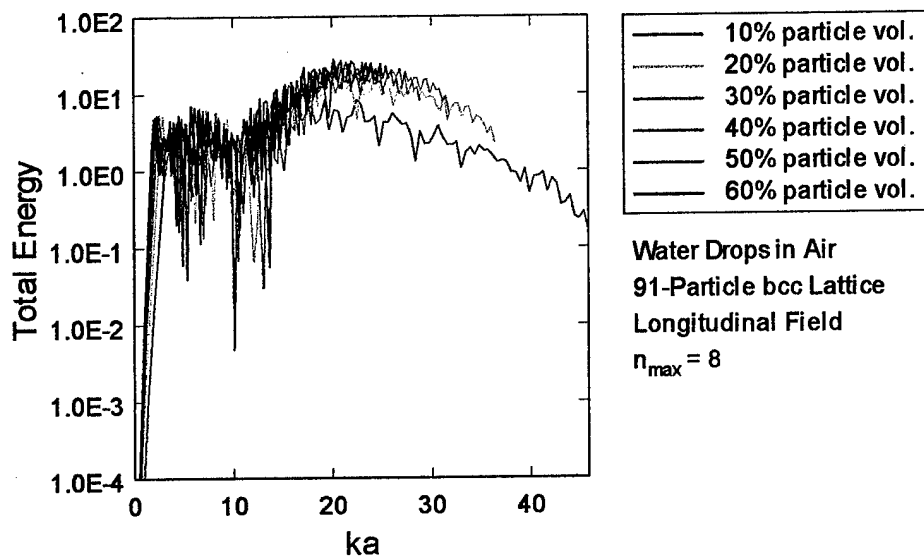
FIGURE 5-44. Simulated total energy spectrum vs. parameter *ka* of microwaves passing through a 91-particle bcc lattic of 1.0-μm water particles in air.

The excellent convergence and prediction of photonic band gap structures by the electromagnetic simulations are encouraging. However, it must still be realized that the simulations are essentially operating in the single scattering approximation since the multiple scattering calculations do not differ significantly from the single scattering calculations. The insufficiency of convergence for the translation coefficients remains a major problem, as does the sluggishness and inefficiency of the computations.

CHAPTER 6

DISCUSSION

6.1 Prediction of Real Wave Propagation Behavior

One method for determining the fidelity and accuracy of scattering models is to determine if they can predict physically realistic phenomena. Although not quantitative, such an approach can provide information on the model's qualitative correctness (*i.e.*, are the basic equations and algorithmic approach of the model sound?).

The results of the elastic and electromagnetic scattering computations exhibit such real world phenomena. The spatial domain images for elastic wave scattering reveal focusing effects for longitudinal waves (Figures 5-1 and 5-3), mode conversion and a higher degree of sideward scattering for shear waves (Figure 5-2), changes in the field wavelength as it passes through media of different elastic properties (Figures 5-6 and 5-7), and amplification of fields in localized regions of disorder (Figures 5-6 and 5-7). Such effects are based on common acoustic (or wave propagation) principles, and their prediction by the elastic wave models is reassuring evidence that the models are functioning in a qualitatively correct manner.

Of even greater interest is the appearance of photonic band gaps in frequency domain spectra of the electromagnetic scattering models. Photonic crystals, also called photonic band gap materials, have been identified and studied only in the last 15 years. They are inhomogeneous materials comprised of an ordered lattice of microscopic particles, inclusions, or columns embedded in an optical medium. The ordering of the inhomogeneities gives photonic crystals amazing properties such as perfect reflectivity, suppression of spontaneous emission, photon localization, and the ability to guide and channel the path of light. These properties arise from band gaps which forbid the propagation of light at certain wavelengths. These photonic band gaps are analogous to the electronic band gaps in semiconductors and lie in the infrared and visible parts of the spectrum.

The electromagnetic scattering models predicted band gaps for crystalline bcc particle configurations. The band gaps were direct functions of the crystal's lattice constant, indicating that they

arise from the crystalline arrangement of the particles (Figure 5-42). Although the band gap positions predicted by the scattering models do not match those found experimentally in colloidal crystals, the differences in particle concentration between the simulated and experimental photonic crystals can account for this discrepancy.

The ability of the multipole-based scattering models to predict both conventional wave propagation phenomena (focusing, mode conversion, *etc.*) and exotic wave propagation phenomena (localization, photonic band gaps, *etc.*) is solid evidence that the models are working correctly at a qualitative level. The models, however, appear to have deficiencies which prevent them from operating at a quantitative level. These deficiencies will now be explored in the following section.

6.2 Deviations from Real Wave Propagation Behavior

6.2 (a) Additive Effect of Scattering from Increasing Numbers of Particles

The VMIST algorithms employ the principle of superposition to derive the total wave field after interacting with the particle dispersion. The incident plane wave and scattered wave fields from all of the particles are added linearly to arrive at the final field amplitude. Linear superposition predicts that both constructive and destructive interference would alter the wave fields in a physically realistic manner to produce results which would be consistent with natural laws such as conservation of energy. Therefore, the incident plane wave was not artificially attenuated in any fashion by the algorithm when it interacted with each of the particles, regardless of how far into the dispersion the particle was. Again, the principle of superposition and the multiple scattering interactions should take care of the amplitudes in a physically meaningful manner.

The results of the scattering simulations demonstrated that the VMIST models were not working in a quantitatively correct manner to enable superposition to function properly. For example, Figure 6-1 displays the maximum spectral amplitude as a function of particle number for the composite simulations of 200-μm NaCl particles in a rubber matrix. Since the size of the disk-shaped sample remained constant, the particle numbers varied due to changes in the particle volume fraction (10%, 30%, and 50%). Figure 6-1 clearly shows that the wave field amplitudes increase linearly with particle number. This result is strongly

counter-intuitive since back and side scattering from the particles should lead to an overall decrease in field amplitude with increasing particle number.

It is evident from Figure 6-1 that the forward scattering is additive as a function of particle number. On introspection this result should be obvious with the use of a single-scatterer approximation. Since the incident waves are not attenuated or modified in the simulations (except for phase), all of the particles see the same incident wave field where the amplitude is only controlled by the phase of the incident wave at the particle position. For long wavelengths as in the composite simulations, all of the particles therefore have approximately the same forward scattering amplitudes. Since these forward scattering contributions are added linearly, as the number of particles increases, so does the amount of contribution to the fields from forward scattering in a direct linear fashion. This is why the single-scatterer approximation fails for dispersions with even modest (>15%) particle volume fractions.[1,2]
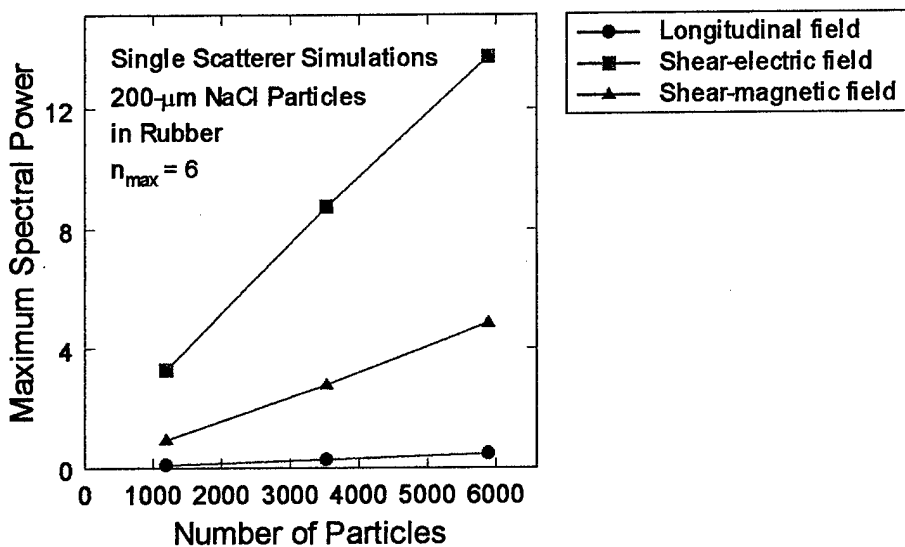
Figure 6-1. Maximum spectral power as a function of particle number for composite material simulations.

Similar additive effects are seen for the multiple scattering computations (*e.g.*, Figures 5-29 and 5-30), indicating that the VMIST algorithm is not calculating a large enough multiple scattering contribution to destructively interfere with the incident and singly-scattered waves. Note that an incorrect computation of the phase of the multiply-scattered fields would have an equivalent or greater effect as an incorrect computation of amplitude. The evidence strongly suggests that the vector multipole based iterative scattering method cannot sufficiently simulate multiple scattering in particulate dispersions for reasonable computation times (*i.e.*, low n_{max} values). The next section provides further evidence for this conclusion and an explanation why the VMIST models are not performing at a quantitative level.

6.2 (b) Similarity between Single and Multiple Scattering Models

One of the more surprising and perplexing results from the scattering simulations was that there was no significant difference between computations employing a single scatterer approximation and full multiple scattering. This result held for small (4-particle), large (91-particle), and very large (5,637-particle) simulations, and was also independent of particle concentration (tested for particle volume fractions up to 60%).

One explanation for these results is that the multiple scattering contributions are naturally much smaller than the single scattering contributions. This is probably true for dilute packings, but cannot be valid for dense packings where wave propagation should assume diffusive characteristics. A more probable explanation is that the multiple scattering contributions are very small since the simulations are running with insufficient n_{max} values for convergence of the addition theorems. This explanation would hold even if the translated field amplitudes were of the same order of magnitude as the convergent values since the phase of the translated fields (*i.e.*, direction) is just as influential in wave interference and superposition effects.

Interestingly, the similarity between the single and multiple scattering computations may be attributable to the same lack of multiply-scattered waves that causes an unnatural additive effect on the scattering (Section 6.2 (a)). Without the destructive interference of multiple scattering, each particle experiences the same incident wave (varied only by phase). The strongest fields, aside from the incident wave, are therefore the first, singly-scattered waves. Due to the lack of destructive interference by multiple

scattering, these fields themselves are not diminished as they propagate through the particle dispersion. The secondary multiple scattered waves will always be significantly smaller than the incident and singly-scattered waves since the incident and singly-scattered waves are not significantly attenuated by interference as they progress through the dispersion.

As a result of the under-evaluation of the multiple scattering contributions, the particle dispersion behaves as a dilute medium in the computations, independent of particle concentration. The original incident and singly-scattered waves pass through the dispersion without attenuation. In an actual densely-packed particle dispersion, the incident waves are quickly converted to scattered waves in the first few particle layers. The only waves reaching the interior particles are those which have been scattered from other particles. By the time the waves pass completely through the disperion they have scattered multiple times from many particles, and little trace of the original plane wave or singly-scattered wave is present.

Little research or discussion has been found in the literature that quantitatively evaluates the single vs. multiple scattering contibutions in multipole-based multiple scattering computations. It is evident, however, that under-evaluation of multiple scattering leads to nonphysical wave propagation behavior. Resolution of this problem is therefore of highest priority in further development of multiple scattering models.

6.3 Computational Inefficiencies

Computational inefficiencies arise from two sources in the multiple scattering computations. The first is just the laborious calculations required to compute such functions as spherical Bessel functions, spherical harmonics, and Clebsch-Gordan coefficients, and then assembling these basic functions into more complex ones such as vector multipole expansions and translational addition theorem coefficients. Many shortcuts have been published for computing these functions faster and more efficiently, mostly with better and more refined recursion formulas. A careful investigation and implementation of these methods in the VMIST algorithm would be of obvious benefit.

The second source for the computational inefficiencies reside in the convergence behavior of many of VMIST's components and the entire algorithm as a whole. The need for convergence forces us to

higher n_{max} values, thus increasing the computation time dramatically since the computation time scales as n_{max} to the 4th power and greater (Table 5-3). Aside from the convergence issues associated with computing basic functions from recursion formulas (such as spherical Bessel functions), there are four primary convergences that affect the performance of VMIST. These are the following:

1. Convergence of the translational addition theorems
2. Convergence of the plane wave expansions
3. Convergence of the single-sphere scattering solutions
4. Convergence of the multiple scattering iterations

Since the convergence of the multiple scattering iterations is the most obvious convergence criteria (since lack of convergence here means the lack of a solution), it is discussed first.

The multiple scattering computations arrive at a solution when the iterations over the scattered field amplitudes converge. As the results of Section 5-2 show, for large particles (1 cm) compared with the shortest wavelength in the matrix (0.2 cm for shear waves at 1 MHz), the elastic wave computations do not converge within certain spectral bands. These bands grow as n_{max} increases, then appear to plateau and even start decreasing. For frequencies not within these bands, the iterations converge fairly fast (< 30 iterations for elastic waves; < 10 iterations for electromagnetic waves).

The origin of the nonconvergence is not known, but one speculation is that the nonconvergent frequencies correspond to resonances either associated with the particle sizes or the particle-particle separations (since changing both alters the degree of nonconvergence in the spectra). The resonances could also arise from mode couplings between the longitudinal and shear modes. As mode conversion at the particle's surface converts longitudinal and shear-electric waves back and forth, translation of the shear fields convert shear-electric and shear-magnetic waves back and forth as well. It is easy to imagine resonant instabilities being set up in such a situation.

(Note that in the electromagnetic models the electric and magnetic fields do not couple by scattering, only by translation. There is no longitudinal mode to give rise to mode conversion from scattering. Not surprisingly, the electromagnetic models do not display iterative nonconvergence except for extreme conditions suchas dense particle packings and highly contrasting material properties.)

Other possible explanations for the nonconvergences are that the computations are unstable in some other fashion, or that the translation coefficients behave anomalously in these frequency regions. More testing is required to resolve the source of the nonconvergences.

The composite material simulations (Section 5-3) did not exhibit nonconvergent behavior, possibly due to the small size of the particles (200 μm) compared with the shortest wavelength in the matrix (100 μm for shear waves at 2 MHz). The excellent convergence behavior of the computations could also be attributable to the large disparity between the longitudinal and shear velocities in the matrix (1450 m/s vs. 200 m/s). This difference could reduce any resonant coupling between the shear and longitudinal modes and thereby preventing instabilities.

A remarkable feature of the multiple scattering computations is the ability of the iterations to converge at all. As we have seen in Chapter 4, the translational addition theorems do not converge at the n_{max} values we are forced to work with. The plane wave expansions are mostly nonconvergent for these n_{max} values as well, as are the single sphere scattering solutions (Figures 5-31, 5-32, and 5-39). In spite of this, the scattered wavefield coefficients converge readily in the iterative process for the majority of frequencies.

These differences in convergence behaviors between the various parts of the algorithm can be misleading. For example, the convergence of the iterative process has been taken by other researchers as an indication that the translational addition theorem coefficients have converged as well. Recently, other researchers have looked at the convergence issues separately. However, it is clear that the ability of the scattering algorithm to converge although individual components of the algorithm—specifically the translation coefficients and plane waves—are not near convergence is a two-edged sword that has lead to a significant underestimation of the convergence problem.

The lack of convergence for the translational addition theorems for modestly high n_{max} values (~16), and indications that convergence may not even be achievable for exceptionally high n_{max} values (~80), is of utmost concern for the multiple scattering computations. The accuracy of even modest multiple scattering computations is dubious without accurate (*i.e.*, converged) translation coefficients. Resolving

the translational addition theorem convergence problem will be perhaps the most challenging task in furthering and improving the VMIST approach.

CHAPTER 7

APPLICATIONS

The applications of wave propagation in particulate media are legion. From the dancing of starlight among interstellar dust grains to the probing of ultrasound in the human body, the mathematical description for the interaction of waves with an ensemble of particles is the same. Therefore, computational models developed for solving the general case of vector wave scattering in a particle-filled medium will have a very wide use and appeal.

Table 7-1 presents examples of particulate systems classified by the state of matter for the matrix and particles. These systems embody a variety of interests, including

- scientific (basic understanding of matter, energy, and the universe)

- economic (materials evaluation, geophysical exploration, weather radar)

- defense (ocean acoustics, radar surveillance)

- environmental (remote sensing, atmospheric scattering)

- human health (medical imaging and diagnostics, food quality and safety)

TABLE 7-1. A sampling of particulate systems that exhibit multiple scattering of elastic or electromagnetic waves.

Matrix Particles	Gas	Liquid	Solid
Gas	Turbulent eddies Thermal "bubbles" Plasma structures	Liquid foams Bubbly liquids Ocean bubbles	Solid foams Photonic crystals Porous rocks
Liquid	Mists Clouds Rain	Emulsions Immiscible melts Ocean inhomogeneities	Biological tissue Semisolids Fluid-bearing rocks
Solid	Smoke Dusts Snow and ice	Suspensions Slurries Ocean plankton	Composites Precipitates/inclusions Rocks

Table 7-2 lists some of the fields of study applicable to the particulate systems listed in Table 7-1 and categorized by matrix state. These fields encompass a wide breadth of disciplines and interests.

In its present form VMIST can be applied to many of the physical systems listed in Table 7.1. In particular, VMIST is currently structured to model solid particles in a solid matrix for elastic waves, and dielectric particles in a dielectric matrix for electromagnetic waves. Although the VMIST algorithm would have to be modified for other forms of matter, the changes would not be extensive or difficult. For example, the current VMIST simulations encounter problems for elastic waves in fluids (gases and solids) since the shear velocity in these materials is zero. This corresponds to an infinite wave vector k_S. Although this is physically realistic, since it mathematically forces the spherical Bessel and Hankel functions to go to zero in the field coefficient solutions, the VMIST code cannot handle an infinite value for k_S. Instead, the boundary condition solutions in the code must be changed by omitting those terms which contain k_S (in fact, all computations involving k_S must be modified or omitted). Similar modifications would be necessary for electromagnetic scattering of conductive or magnetic materials.

Table 7-3 lists specific applications for particulate scattering models, corresponding experimental or measurement methods for the material systems, and references for these applications. The references listed are intended only to be representative, not exhaustive, of the extensive knowledge base that exists on the applications of electromagnetic and elastic wave scattering.

TABLE 7-2. Applicable fields of study.

Matrix	Gas	Liquid	Solid
Field of study	Meteorology Climatology Planetology Astrophysics	Chemistry Chemical processing Food science Oceanography	Materials science Medicine Biophysics Geophysics

TABLE 7-3. Specific applications of particulate scattering models that could benefit from the VMIST approach.

Field	Application	Measurement Method	References
Nondestructive Evaluation	Particulate composites (particle-filled plastics and rubber, concrete, ceramics)	Ultrasound Microwaves Eddy current methods	201-206
	Detection and quantification of porosity, voids, and inclusions in materials	Ultrasound Microwaves Eddy current methods	207-214
	Process control of suspensions (paints, precipitates, etc.)	Ultrasound Optical scattering	215-229
Materials Engineering and Design	Photonic and acoustic band gap materials	Microwaves Infrared and visible light Ultrasound	69, 199, 230-245
	Composites, nanocomposites, and metal foams	Ultrasound Microwaves Diffuse visible and IR scattering	201-206, 246-249
	Multiphase suspensions (colloidal systems, electrorheological materials, liquid crystals, etc.)	Coupled electromagnetic, acoustic, and mechanical fields	215-229
Agriculture, Forestry, and Natural Resources	Milk, oils, processed foods, and other suspensions	Ultrasound Optical scattering	186, 187, 250, 251
	Fruits, vegetables, and meat	Ultrasound and acoustics	186, 252, 253
	Soil characterization	Acoustics Microwaves	254
	Remote sensing of forest, crop, and vegetation health	Optical scattering	255-260
	Fish schools	Sonar	186, 187
Biophysics and Medical Physics	Cell, tissue, and organ characterization Blood and contrast agent scattering	Ultrasound Optical tomography Diffuse visible and IR scattering	261-274
Geophysics	Rocks and geologic formations Marine sediments Soils	Seismic and sonar exploration Subsurface radar EM and resistivity tomography	142-144, 275-289
Oceanography	Ocean acoustics Plankton research	Sonar Surface optical scattering	176, 177, 290-309
Meteorology	Cloud, fog, and precipitation scattering Dust and aerosol scattering	Microwave radar IR, visible, and UV scattering	310-316
Astrophysics	Dusty plasmas Interstellar dust clouds Planetary atmospheres	Electromagnetic radiation	317-327

CHAPTER 8

FUTURE DIRECTIONS

8.1 Efficiency Improvements

A major conclusion of this research is that the use of addition theorems for the translation of vector spherical wave functions is too inefficient (or inaccurate) for the practical modeling of multiple scattering with the use of current desktop computers. One method for avoiding the use of addition theorems has already been investigated in a preliminary fashion. This is the single scatterer approximation, and it appears to be valid for scattering in particle dispersions as long as the material property contrast between particle and matrix is not too great, the particle volume fraction is low, or the number of particles is small. However, the single scatterer approximation is not a general approach, and cannot be used for closely-packed, strongly-scattering particulate media.

The nearest-neighbor approximation addresses the addition theorem efficiency problem by minimizing the computation of translation coefficients. This approximation is not an effective efficiency measure, however, for resolution of the slow addition theorem convergence since the computation time scales only as the particle number squared (p^2), but as the fourth (or greater) power of the maximum multipole order ($n_{max}^{\geq 4}$). Since the convergence of the addition theorems will, at the least, require n_{max} values a magnitude larger than currently practical, the computation time will increase by 10^4-10^5 times. A nearest neighbor approximation will at most provide a 10^2 decrease in compution time for a 10^3 particle dispersion (using the 10 nearest neighbors to each particle). For ordered particle arrays, translational symmetry can provide another 10-fold decrease in time, but still leaves n_{max} the dominant parameter controlling the computation speed.

Other approaches have also been considered for either reducing or completely avoiding the addition theorem computations. These include

- Asymptotic approaches for close particle pairs

- Long wavelength approximation

- Simplification of addition theorem translations using coordinate rotations

- Convergence acceleration methods

- Statistical wave propagation methods

Asymptotic expressions have been developed for particulate mechanics models.[328] They improve the efficiency of the multiple scattering computations by modeling the interactions between closely-spaced particle pairs with the use of a parabolic boundary approximation (Figure 8-1). Although this method has been successfully employed for static elastic fields in particulate media, and could therefore also be used for electrostatic and magnetostatic fields, the application of these approximations to dynamic fields (wave scattering) is not straightforward.
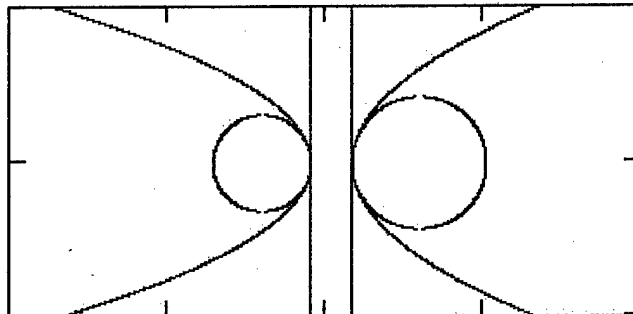
FIGURE 8-1. Asymptotic solutions using flat and parabolic surfaces as 0th and 1st order approximations to spherical interactions.

In the long wavelength approximation, both elastic and electromagnetic waves would be treated as static fields. As the testing in this research indicates, both the scalar and vector addition theorems are more accurate and quickly computed for low frequencies (long wavelengths). At the static limit where the frequency drops to zero and the wavelength increases to infinity (*i.e.*, $k \to 0$), the spherical Bessel and Neumann functions become simple power-law functions of r:[50]

$$j_n(kr) \approx \frac{1}{(2n+1)!!}(kr)^n \tag{8.1}$$

$$y_n(kr) \approx -(2n+1)!! \frac{1}{(kr)^{n+1}} \tag{8.2}$$

Eqs. 8.1 and 8.2 transform the addition theorems from a wave function form containing spherical Bessel functions (remember that the spherical Hankel functions are just a combination of $j_n(kr)$ and $y_n(kr)$) to a static field form containing powers of r. This simplification significantly increases the computational speed and accuracy of the boundary condition solutions and addition theorems, as evidenced by the use of this method for the modeling of static elastic fields in patrticulate media containing 10^4-10^5 particles.[329] The method eliminates the computation of spherical Bessel functions and the inaccuracies of using the wave function form of the addition theorems. However, we again loose the generality that was one of the goals of this research by going to a long-wavelength approximation.

Finally, it has been shown that the addition theorems can be modestly simplified by restricting the translations to along the z-axis.[70] This would moderately improve the computational efficiency, and possibly accuracy, of the addition theorems. However, for random particle packings where the majority of particles are not ordered along parallel axes, extra calculations would be necessary to rotate the multipole fields for each particle pair using Wigner-D functions.[47] It is currently not known whether the improvement in addition theorem computation would make up for these extra calculations. Mathematical methods for accelerating the convergence of the addition theorems, such as transforming the summations into integrals and solving, may also be a possibility.

Other methods that are of interest for future research and that avoid the use of addition theorem expansions include path integral and Monte Carlo random walk methods for modeling wave diffusion. In

the random walk method, the multipole single scatterer solutions determine the scattering angle and amplitude probabilities. They have been successfully employed in light scattering and radiative transfer models for clouds.[330]

8.2 Fidelity Improvements

Fidelity improvements would comprise modeling the microstructure of particulate materials more realistically. These improvements include more faithful models of random particle arrangements, material properties, particle shapes, and particle structure.

Algorithms and statistical methods for constructing three-dimensional particle packs for close-packed particulates with uniform particle sizes have been developed in the ceramics and composites communities.[331-339] However, such models are often not applicable to particulates with large particle size distributions. Careful design of particle packing models are crucial, however, to avoid introducing periodicities or artificial structures not seen in truly random, real-world particulates. Such care is necessary for predicting the properties of such materials.[340] One such particle packing approach builds the particle microstructure using a Monte Carlo "particle-dropping" method.[341] To model particle sizes that may differ by up to 100x, the approach uses a "concentric can" model that builds the microstructure with large particles first by filling the large can, and then successively with smaller particles by filling the smaller cans. This eliminates the need to model the large number of small particles that fill in the interstices between the large particles.

A different approach to specifying the particle pack microstructure is to reconstruct it from observations of real materials.[342-344] Such an approach would provide microstructural models based on images acquired from two-dimensional slices of the material of interest, and would also be a good check for particle packing programs as described above. Particle packing programs are still necessary, however, since the reconstructions are computationally intensive, imperfect, and cannot provide microstructures for a wide range of materials without representative samples and testing.

More accurate and extended models also need to be developed for material properties not addressed by the present work. These properties include conductive particles for electromagnetic scattering, and viscoelastic properties for elastic wave scattering. Both would entail the use of complex wave vectors, with a complex permittivity for electromagnetic scattering, and complex Lamé constants for elastic wave scattering. Foreseeing this need, the VMIST programs were written to accommodate complex variables in the scattering computations.

To represent true particle shapes we need to model nonspherical particle shapes. The first approximation to nonsperical particles is the spheroid (Figure 8-2). A spheroid is capable of modeling both highly-elongated, needle-like particles (prolate spheroids) and highly-flattened, pancake-like particles (oblate spheroids). This would allow the modeling of many particle types such as the long needle-like crystals of many minerals or compounds, or the flat flake-like crystals of clays or snowflakes.

An advantage of using spheroidal particle models is that the Helmholtz wave equation is separable in spheroidal coordinate systems.[345-349] (The Helmholtz equation is also separable in cylindrical and ellipsoidal coordinate systems as well.[346]) It is therefore possible to construct solutions for scattering from spheroidal particles. As in the spherical particle case, such solutions consist of expansions of spherical harmonics (spheroidal angular functions) and spherical Bessel functions (spheroidal radial functions). Although more complex, these functions offer complete solutions to the scattering problem.
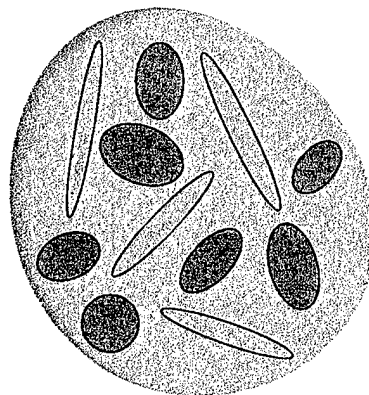
FIGURE 8-2. Dispersion of long, needle-shaped and flat, plate-shaped spheroidal particles.

A sizable number of references have covered electromagnetic scattering from spheroids, with a large emphasis on light scattering.[350-378] Spheroidal models have been used for various particulate media including biological cells, soils, atmospheric dust, clouds, and interstellar grains. Electromagnetic scattering from collections of spheroidal particles has also been modeled, necessitating the derivation of both translational and rotational addition theorems for spheroidal wave functions.[379-387] The scattering of elastic waves from spheroids has been researched less, but the literature includes scattering from spheroidal cavities and rigid particles.[388-393]

Spheroidal particle and void representations would be very useful for a number of modeling applications. For example, the open-cell structure of a metal foam or porous rock, Figure 8-3 (a),could be simulated using a network of spheroids, Figure 8-3 (b). Specific rock pore models would include those for rocks with flat, layered structure such as shale or slate, Figure 8-4 (a), or for rocks with equiaxial grains such as sandstone, Figure 8-4 (b). Spheroids would also be very useful for modeling plant and animal cells with either columnar (elongated) or squamous (flattened) shapes.

(a)   (b)
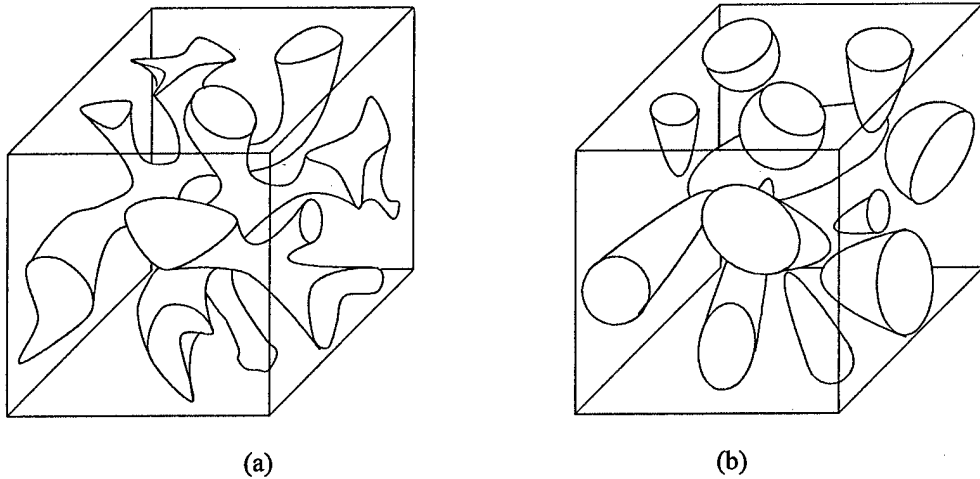
FIGURE 8-3. Open-cell porous microstructure for rocks and metal foams (a), and scattering model representation using spheroids for the pore spaces(b).
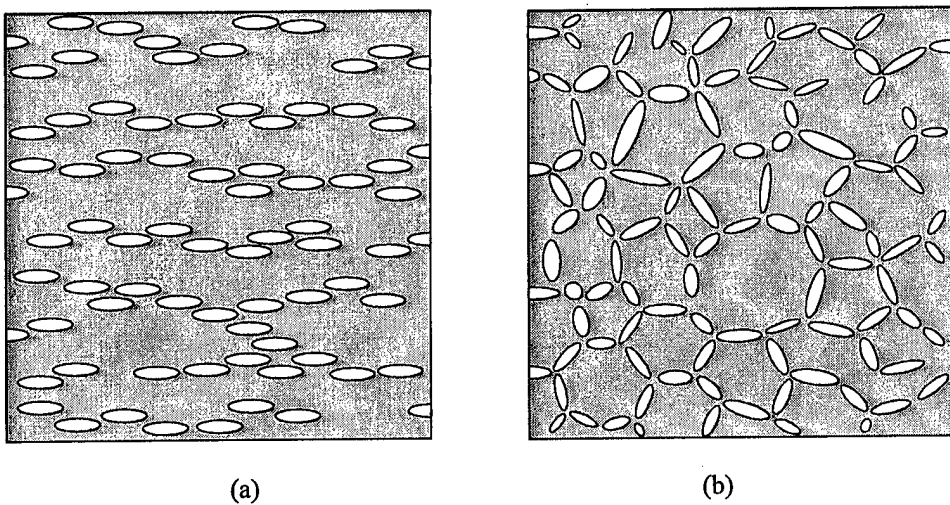
FIGURE 8-4. Porous rock representations using spheroids for the pore spaces, (a) for shales and slates, and (b) for sandstones.

The next level of increasing nonsphericity would be the modeling of ellipsoidal particles with the use of ellipsoidal wave functions. Expressing the Helmholtz equation in ellipsoidal coordinates yields the ellipsoidal wave equation , also called the Lamé wave equation. This is the most general equation that can be derived from the Helmholtz equation in confocal coordinates and that can be solved by separation of variables. The solutions are ellipsoidal (or Lamé) wave functions, and are also referred to as ellipsoidal harmonics.[42] Although enticing because of their generality, ellipsoidal wave functions are very complex and difficult to work with or evaluate analytically. Only a few hardy pioneers have had the fortitude to research and apply ellipsoidal wave functions in scattering and electromagnetic problems.[394-400]

The modeling of particles of arbitrary, nonsymmetric shape is particularly challenging, but has been achieved with a variety of methods. Perturbation approaches have been developed which treat nonsphericity as a perturbation from spherical particles, and scattering solutions have been derived.[401-405] Elliptic cylinders have been used for particle shapes since the Helmholtz equation is also separable in elliptic cylindrical coordinates.[406] Particle symmetries have also been investigated, as well as modeling the shape of a particle as a spherical harmonic expansion superimposed on a sphere (for example, a cuboid would be comprised of spherical harmonic terms $Y_{4,4}(\theta,\varphi)$, $Y_{8,8}(\theta,\varphi)$ and so on).[407-409] Figure 8-5 shows in two dimensions how such successive multipole terms can be used to construct a cubic particle.

Accurate modeling of irregularly-shaped particles is important since it has been shown that light scattering from simple shapes (spheres, spheroids, and cylinders) can deviate significantly from that of hexagonal ice crystals, particle clusters, and other atmospheric aerosols.[410]

Since the Helmholtz equation is separable in cylindrical coordinates, multipole methods have been employed in the modeling of fiber-reinforced composites.[411-415] These methods have only addressed unidirectional composites, however, where all of the fibers are parallel. Translation of the fields between parallel fibers is relatively straightforward with the use of addition theorems for regular (cylindrical) Bessel functions. Additionally, the parallel fiber model reduces to a two-dimensional problem. Most manufactured fiber composites, unfortunately, are not unidirectional but rather have cross-ply and three-dimensional weave structures (Figure 8-6). Modeling such microstructures with multipoles would require a mathematical method for translating fields between nonparallel fibers (Figure 8-7). Surprisingly, literature searches for a translational + rotational addition theorem that would translate fields between skewed cylinders have not yielded any results to date.

1 Multipole Term   5 Multipole Terms   20 Multipole Terms
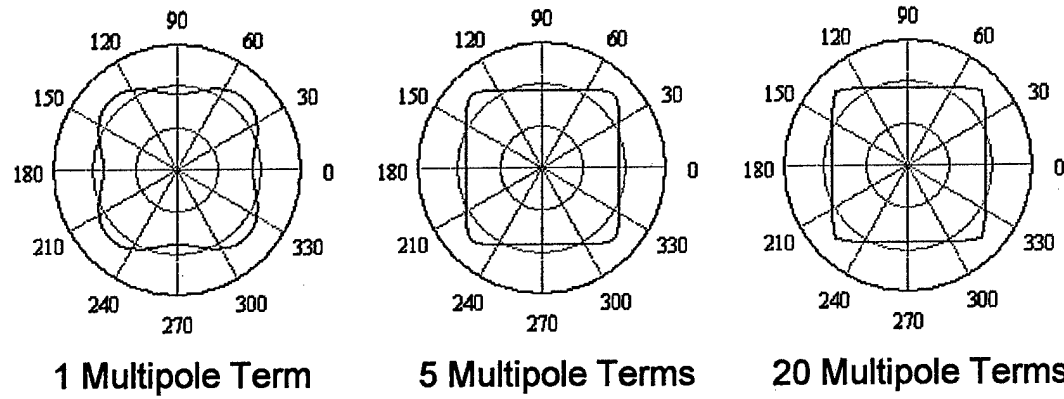
FIGURE 8-5. Construction of a cubic particle (red line) from a spherical harmonic multipole expansion of $Y_{n \times 4, n \times 4}(\theta, \varphi)$ terms.
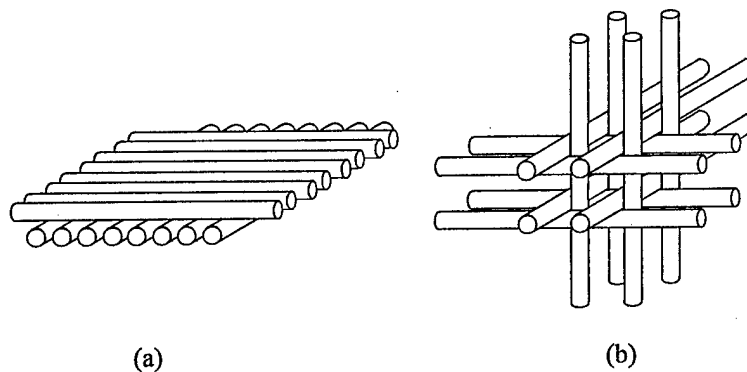
FIGURE 8-6. Idealized microstructures for cross-ply (a) and 3-D weave (b) fiber-reinforced composites.
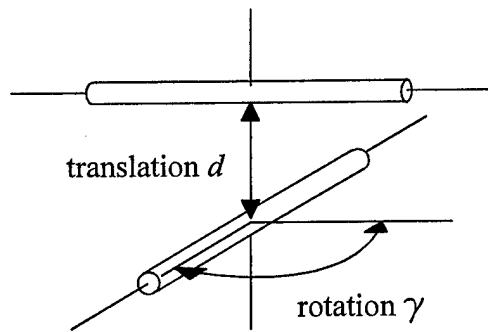
FIGURE 8-7. Nonparallel fiber geometry requiring translation and rotation of multipole fields from one fiber to another.

The final level of fidelity that can be addressed by scattering models is the representation of particles with an inhomogeneous internal structure. This includes layered and multilayered particles, particles with anisotropic or heterogeneous properties, and particles with internal inclusions.[416-435] Again, as with spheroidal scattering, most of the research has been performed for light scattering.[416-432] One paper, however, looks at the scattering of elastic waves from a partially-filled cavity.[433] Quite recently, simulations of light scattering from layered particles has focused on the photonic band gap nature of the scattering.[434,435]

8.3 A Unified Approach to Multipole Fields in Particulate Media

As mentioned in Section 8.1, in the long wavelength limit ($k \rightarrow 0$) both the elastic wave and electromagnetic scattering models become models for the static properties of the medium. These static models are of great interest since the understanding and prediction of electrical and mechanical properties in particulate materials has direct application to material strength, durability, performance, service life, and failure. Also, in concert with the wave scattering models, they would provide a more complete and unified description of particulate material properties and behavior.

Models for electrical conduction in collections of spheres have a venerable history, starting with Maxwell and Rayleigh in the 19th century, and developed further by McPhedran and McKenzie and others in the later half of the 20th century.[436-442] The principal method employed for solving the electrical conduction problem involves multipole expansions of the potential in a lattice of particles. The periodicity of the lattice allows solution of the problem analytically.

The same multipole expansions of the potentials can also be used to model the electrostatic fields in particulate media.[443-446] For random media, Davis rederived the translational addition theorem for static scalar fields using an integral method, and employed an iterative solution for the electrostatic field that was used as the blueprint for the scattering models in this work.[443] With extension to static vector fields, the multipole method has also been applied to elastostatic fields.[328,329,447] The use of elastostatic models for composites and other particulate materials are of keen interest to engineers who want ot predict the mechanical properties of these materials as a function of microstructure.

Models for thermal properties and heat conduction in particulate media have also been developed using multipole approaches.[448,449] Again, these approaches start from the lattice approximation, but could also be generalized to random dispersions of particles.

Although it has been show that the translational addition theorems converge too slowly and are too computationally inefficient for current wave scattering models, addition theorems for static models do not share this fate since the spherical Bessel functions in the wave models are replaced with power-law and inverse-power-law functions of r. These functions do not have the convergence problems that the spherical Bessel functions do, and convergence of the addition theorems are both quicker and more computationally

efficient.[329] Extending the VMIST wave scattering models to static fields would therefore be a straightforward exercise, and may allow the computation of both low-frequency waves and static fields in a unified approach.

Additionally, the ability to model material properties on a continuum from static behavior to dynamic behavior would have substantial technical benefit. Often, the wave propagation properties of a material differ from its static properties, which is a problem for nondestructive characterization methods which seek to determine a material's physical state and properties from the wave properties. A continuum model, however, would allow such a determiniation by providing the "missing link" between static material properties (*e.g.*, mechanical) with dynamic material properties (*e.g.*, ultrasonic).

Finally, the VMIST approach could be expanded to encompass tensor as well as vector and scalar fields. One application of tensor fields has already been mentioned in Section 3.3 with regards to stress and strain fields. Tensor fields might be more appropriate descriptions for stress and strain in anisotropic materials, and expansions of tensor spherical harmonics have already been used to describe crystal orientation effects in seismic wave propagation through rocks.[450] The other physical application of tensor fields is gravitational radiation. Again, tensor spherical harmonics have been formulated for gravity waves.[46,451] Although one is hard put to imagine a multiple scattering scenario for gravity waves, one possible application of a gravity wave scattering or interaction model is in the design of novel gravitational radiation detectors that convert gravity waves to acoustic vibrations in solid materials.[452]

CHAPTER 9

CONCLUSIONS

The goal of this dissertation was to develop and test *ab initio* computational models for the multiple scattering of elastic and electromagnetic waves in particulate media. The purposes for such models would be to (1) determine how the structure of a particle-filled medium influences the propagation and scattering of elastic and electromagnetic waves; (2) predict the structure and properties of a particle-filled medium from the measured wave properties; and (3) design particle-filled materials with new or enhanced properties for technological applications. This work was limited to the development of forward models—models that describe the interaction of waves in a given particle-filled microstructure. However, having the capability to predict how waves interact in a particle-filled medium (the forward model) is the first step in developing models that can predict the properties and structure of a medium from the measured wave properties (the inverse model).

The approach for developing the computational models was comprised of the following steps:

1. Recast the fundamental Maxwell and Navier equations as vector Helmholtz equations and define vector multipole functions appropriate for solution of both equations in a spherical coordinate system.

2. Solve the equations for single particle scattering using boundary conditions and orthogonality of the vector multipoles.

3. Derive translational addition theorems that allow the scattered wave fields from one particle to be recast in the coordinate system of a second particle. This allows the waves to be translated from one particle to another, which is necessary for a first-principles computation of multiple scattering.

4. Design an algorithm to account for all particle-particle interactions in the computations by iterating through the particle configuration.

5. Test the derived translational addition theorems for computational efficiency, accuracy, and convergence, and compare to previously published theorems in the literature.

6. Test the multiple scattering simulations with a variety of particle numbers and configurations, and identify areas for improvement in the models.

7. Compare multiple scattering simulation results with those using single scatterer and nearest neighbor approximations.

The original and significant contributions of the presented work consist of (1) review and reformulation of current theory to achieve greater consistency, elegance, and accuracy; (2) extension of current capabilities to create scattering models with increased generality and greater utility; and (3) quantitative testing of the multiple scattering theory and identification of deficiencies.

The mathematical foundations and theory for the iterative solution of multiple scattering in a particle-filled medium were investigated, and many areas for improvement were discovered. First, several different forms of vector spherical wave functions have been employed in the past to solve spherically-symmetric scattering problems. This work has shown that the choice of vector spherical wave functions is important in simplifying the problem and in deriving the correct form of the translational addition theorems. To address this issue, modified vector wave functions were presented, compared to those previously used, and implemented in this work.

Second, the solution of the boundary conditions for the scattering from a single sphere has often been given cursory treatment in the literature, and yet contains pitfalls and apparent inconsistencies if not properly addressed, specifically in the application of orthogonality to simplify the equations. This issue was resolved by showing how the boundary condition solutions can be elegantly solved in vector form with the use of the orthogonality of the pure-orbital vector spherical harmonics.

Recasting the equations with spherical wave functions built from pure-orbital vector spherical harmonics provided several advantages, both in the solution of the boundary condition equations and in the derivation of the translational addition theorems. The pure-orbitial vector spherical harmonics provide a set of vector spherical wave functions that simplify both single sphere scattering and multiple scattering with addition theorems. It was shown that the boundary conditions for electromagnetic scattering can be readily solved by retaining the vector form of the equations, and by applying orthogonality of the vector spherical harmonics. This same method also works for the displacement boundary conditions for acoustic scattering,

but cannot resolve the stress boundary conditions which are tensor equations of second and fourth-rank tensors.

Third, various forms of translational addition theorems have been published with differing computational results. Some of these theorems produce poor results and their correctness is suspect. Such results can introduce significant error into multiple scattering solutions. To resolve this issue, the addition theorems were rederived in pure-orbital vector spherical harmonic form with an integral approach. A test procedure was also devised to assess the accuracy and convergence of the translation coefficients independent of either single or multiple scattering convergence.

The results confirmed that the pure-orbital addition theorems were numerically equivalent to the most well-known theorems in the literature. The results also showed, however, that some published theorems are incorrect and do not converge. The convergence of the translation coefficients was shown to behave similarly to that of the plane wave expansions, and has therefore been severely underestimated in previous articles. The convergence of the theorems for some geometries was also shown to exhibit extensive flat or plateau-like regions across wide n_{max} values. These plateau regions can give false impressions of convergence when encountered in multiple scattering computations, and may contribute to inaccuracies in the model results.

Using the above mathematical tools, elastic and electromagnetic wave scattering models were constructed to simulate the scattered wavefields as a function of both frequency and spatial distribution from an ensemble of particles. Numerous simulations were generated for particle configurations ranging from 4 to 5,000 particles, and with both ordered and disordered arrangements. The results correctly predicted many physical phenomena including focusing effects, shear wave scattering behavior, wavelength changes in various materials, and the formation of photonic band gaps. The models can therefore be considered valid at a qualititative level

The computations performed in this work were not quantitatively accurate, however. The lack of addition theorem convergence was shown to produce physically unrealistic results. Specifically, the multiple scattering contributions were much smaller than the single scattering contributions, even for dense dispersions of up to 60% particle volume. The inability to accurately calculate the multiple scattering

contribution also resulted in an unrealistic increase in forward scattering with particle number. Without sufficient multiple scattering to destructively interfere with the incident and singly scattered waves, the amplitudes of the transmitted waves increased linearly with particle number and therefore violated conservation of energy.

The testing performed with both the translational addition theorems and scattering models have revealed that nonconvergence of the addition theorems is the most critical problem for the multiple scattering simulations. This problem has not been identified or addressed in the published literature due to the lack of real testing for the translational addition theorems independent of scattering, and due to their plateau-like convergence behavior for wide n_{max} ranges and various geometries.

In addition to the lack of convergence for the translational addition theorems at computationally practical values for n_{max}, the primary computational problems encountered in the development and testing of the particulate media scattering models were the overall slowness and inefficiency of the computations, and the rapid scaling of computation time with particle number and n_{max}. These problems remain unresolved, and yet their solutions are critical for the successful development of multipole-based multiple scattering models.

REFERENCES

1. L. W. Anson and R. C. Chivers, "Ultrasonic velocity in suspensions of solids in solids—a comparison of theory and experiment," J. Phys. D: Appl. Phys. 26 (10), 1506-1575 (1993).

2. F. V. Meulen, G. Feuillard, O. B. Matar, F. Levassort, and M. Lethiecq, "Theoretical and experimental study of the influence of the particle size distribution on acoustic wave properties of strongly inhomogeneous media," J. Acoust. Soc. Am. 110 (5), 2301-2307 (2001).

3. D. M. Ceperley, "Microscopic simulations in physics," Rev. Mod. Phys. 71 (2), S438-S443 (1999).

4. L. Lorenz, "Sur la lumière réfléchie et réfractée par une sphère transparente," Vidensk. Selsk. Skrifter 6, 1-62 (1890).

5. J. J. Thomson, "On the scattering of electromagnetic waves by metallic spheres," Recent Researches in Electricity and Magnetism, (University Press, Oxford, England, 1893), pp. 437-451.

6. G. Mie, "Beiträge zur Optik trüber Medien, speziell kolloidaler Metallösungen," Annalen der Physik 25 (3), 377-445 (1908).

7. P. Debye, "Der Lichtdruck auf Kugeln von beliebigem Material," Annalen der Physik 30, 57-136 (1909).

8. J. A. Stratton and L. J. Chu, "Steady-State Solutions of Electromagnetic Field Problems. II. Forced Oscillations of a Conducting Sphere," J. Appl. Phys. 12, 236-240 (1941).

9. J. A. Stratton, Electromagnetic Theory, (McGraw-Hill, New York, 1941), pp. 563-573.

10. H. C. van de Hulst, Light Scattering by Small Particles, (John Wiley and Sons, Inc., New York, 1957; Dover, New York, 1981).

11. D. L. Sengupta, Electromagnetic and Acoustic Scattering by Simple Shapes, edited by J. Bowman, T. B. A. Senior, P. L. E. Uslenghi (North-Holland, Amsterdam, 1969), pp. 353-415.

12. M. Kerker, The Scattering of Light and Other Electromagnetic Radiation, (Academic Press, New York, 1969), pp. 39-54.

13. L. P. Bayvel and A. R. Jones, Electromagnetic Scattering and Its Applications, (Applied Science Publishers, London, 1981), pp. 1-73.

14. C. F. Bohren and D. R. Huffman, Absorption and Scattering of Light by Small Particles, (John Wiley & Sons, Inc., New York, 1983; Wiley Professional Paperback Edition, 1998).

15. N. A. Logan, "Early History of the Mie Solution," J. Opt. Soc. Am. 52, 342-343 (1962).

16. N. A. Logan, "Survey of Some Early Studies of the Scattering of Plane Waves by a Sphere," Proc. IEEE 53, 773-785 (1965).

17. A. Clebsch, "Ueber die Reflexion an einer Kugelfläche," J. für Math. 61, 195-262 (1863).

18. John William Strut, Baron Rayleigh, The Theory of Sound, Volume Two, (Macmillan, London, 1894; Dover, New York, 1945; first published in 1877) p. 236-284.

19. J. J. Faran, Jr., "Sound Scattering by Solid Cylinders and Spheres," J. Acoust. Soc. Am. 23 (4), 405-418 (1951).

20. C. F. Ying and R. Truell, "Scattering of a Plane Longitudinal Wave by a Spherical Obstacle in an Isotropically Elastic Solid," J. Appl. Phys. 27 (9), 1086-1097 (1956).

21. L. Knopoff, "Scattering of Shear Waves by Spherical Obstacles," Geophysics 24 (2), 209-219 (1959).

22. L. Knopoff, "Scattering of Compression Waves by Spherical Obstacles," Geophysics, 24 (1), 30-39 (1959).

23. N. G. Einspruch and R. Truell, "Scattering of a Plane Longitudinal Wave by a Spherical Fluid Obstacle in an Elastic Medium," J. Acoust. Soc. Am. 32 (2), 214-220 (1960).

24. N. G. Einspruch, E. J. Witterholt, and R. Truell, "Scattering of a Plane Transverse Wave by a Spherical Obstacle in an Elastic Medium," J. Appl. Phys. 31 (5), 806-818 (1960).

25. Y-H. Pao and C. C. Mow, "Scattering of Plane Compressional Waves by a Spherical Obstacle," J. of Appl. Phys. 34 (3), 493-499 (1963).

26. C. C. Mow, "Transient Response of a Rigid Spherical Inclusion in an Elastic Medium," Journal of Applied Mechanics 32, 637-642 (1965).

27. G. Johnson and R. Truell, "Numerical Computations of Elastic Scattering Cross Sections," J. Appl. Phys. 36 (11), 3466-3475 (1965).

28. C. C. Mow, "On the Transient Motion of a Rigid Spherical Inclusion in an Elastic Medium and its Inverse Problem," Journal of Applied Mechanics 33, 807-813 (1966).

29. D. L. Jain and R. P. Kanwal, "Scattering of P and S Waves by Spherical Inclusions and Cavities," J. Sound Vib. 57 (2), 171-202 (1978).

30. M. K. Hinders, "Plane-Elastic-Wave Scattering from an Elastic Sphere," Nuovo Cimento B 106B (7), 799-817 (1991).

31. S. D. Bogan, T. M. Fang, and M. K. Hinders, "Spherical-Wave Scattering from an Elastic Sphere," Nuovo Cimento B 107B (10), 1215-1217 (1992).

32. D. W. Kraft and M. C. Franzblau, "Scattering of Elastic Waves from a Spherical Cavity in a Solid Medium," J. Appl. Phys. 42 (8), 3019-3024 (1971).

33. R. J. McBride and D. W. Kraft, "Scattering of a transverse elastic wave by an elastic sphere in a solid medium," J. Appl. Phys. 43 (12), 4853-4861 (1972).

34. B. R. Tittmann, E. R. Cohen, and J. M. Richardson, "Scattering of longitudinal waves incident on a spherical cavity in a solid," J. Acoust. Soc. Am. 63 (1), 68-74 (1978).

35. G. C. Gaunard and H. Überall, "Theory of resonant scattering from spherical cavities in elastic and viscoelastic media," J. Acoust. Soc. Am. 63 (6), 1699-1712 (1978).

36. D. Brill, G. C. Gaunard, and H. Überall, "Resonance theory of elastic shear-wave scattering from spherical fluid obstacles in solids," J. Acoust. Soc. Am. 67 (2), 414-424 (1980).

37. L. Flax and H. Überall, "Resonant scattering of elastic waves from spherical solid inclusions," J. Acoust. Soc. Am. <u>67</u> (5), 1432-1442 (1980).

38. D. Brill and G. C. Gaunard, "Resonance theory of elastic waves ultrasonically scattered from an elastic sphere," J. Acoust. Soc. Am. <u>81</u> (1), 1-21 (1987).

39. K. L. Williams and P. L. Marston, "Mixed-mode acoustical glory scattering from a large elastic sphere: Model and experimental verification," J. Acoust. Soc. Am. <u>76</u> (5), 1555-1563 (1984).

40. P. M. Morse and H. Feshbach, <u>Methods of Mathematical Physics</u>, (McGraw-Hill Book Company, Inc., New York, 1953).

41. J. D. Jackson, <u>Classical Electrodynamics</u>, 2nd ed., (John Wiley and Sons, New York, 1975).

42. E. W. Weisstein, <u>CRC Concise Encyclopedia of Mathematics</u>, (Chapman & Hall/CRC, Boca Raton, 1999).

43. E. H. Hill, "The Theory of Vector Spherical Harmonics," Amer. J. Phys. <u>22</u>, 211-214 (1954).

44. M. E. Rose, Elementary Theory of Angular Momentum, (John Wiley and Sons, New York, 1957).

45. W. Greiner and J. A. Maruhn, <u>Nuclear Models</u>, (Springer-Verlag, Berlin, 1996).

46. K. S. Thorne, "Multipole Expansions of Gravitational Radiation," Rev. Mod. Phys. <u>52</u> (2—Part I), 299-339 (1980).

47. D. A. Varshalovich, A. N. Moskalev, and V. K. Khersonskii, <u>Quantum Theory of Angular Momentum</u>, (World Scientific, Singapore, 1988).

48. A. R. Edmonds, <u>Angular Momentum in Quantum Mechanics</u>, (Princeton University Press, Princeton, New Jersey, 1957).

49. G. B. Arfken and H. J. Weber, <u>Mathematical Methods for Physicists</u>, 4th ed., (Academic Press, San Diego, 1995).

50. M. Abramowitz and I. A. Stegun, <u>Handbook of Mathematical Tables</u>, (Dover, New York, 1965; 9th Dover edition, 1972)

51. E. Gillman and H. R. Fiebig, "Accurate recursive generation of spherical Bessel and Neumann functions for a large range of indices," Computers in Physics <u>2</u> (1), 62-72 (1988).

52. B. Friedman and J. Russek, "Addition theorems for spherical waves," Q. Appl. Math. <u>12</u>, 13-23 (1954).

53. M. E. Rose, "The electrostatic interaction of two arbitrary charge distributions," Journal of Mathematics and Physics 37, 215-222 (1958).

54. S. Stein, "Addition theorems for spherical wave functions," Q. Appl. Math. <u>19</u>, 15-24 (1961).

55. O. R. Cruzan, "Translational addition theorems for spherical vector wave functions," Q. Appl. Math. <u>20</u> (1), 33-40 (1962).

56. R. A. Sack, "Three-dimensional addition theorem for arbitrary functions involving expansions in spherical harmonics," J. Math. Phys. <u>5</u>, 252-259 (1964).

57. M. Danos and L. C. Maximon, "Multipole matrix elements of the translation operator," J. Math. Phys. 6 (5), 766-778 (1965).

58. L. Aardoom, "Some transformation properties for the coefficients in a spherical harmonics expansion of the earth's gravitational potential," Tellus 4, 572-584 (1969).

59. R. J. Tough, "The transformation properties of vector multipole fields under a translation of coordinate origin," J. Phys. A: Math. Gen. 10, 1079-1087 (1977).

60. R. C. Wittmann, "Spherical Wave Operators and the Translation Formulas," IEEE Transactions on Antennas and Propagation 36 (8), 1078-1087 (1988).

61. W. C. Chew, "Recurrence relations for three-dimnesional scalar vector addition theorem," J. Electromagn. Waves Appl. 6 (2), 133-142 (1992).

62. W. C. Chew, Y. M. Wang, and L. Gürel, "Recursive algorithm for wave-scattering solutions using windowed addition theorem," J. Electromagn. Waves Appl. 6 (11), 1537-1560 (1992).

63. W. C. Chew and Y. M. Wang, "Efficient ways to compute the vector addition theorem," J. Electromagn. Waves Appl. 7 (5), 651-665 (1993).

64. Y. M. Wang and W. C. Chew, "A recursive T-matrix approach for the solution of electromagnetic scattering by many spheres," IEEE Transactions on Antennas and Propagation 41 (12), 1633-1639 (1993).

65. X. Wang, X.-G. Zhang, Q. Yu, and B. N. Harmon, "Multiple-scattering theory for electromagnetic waves," Phys. Rev. B 47 (8), 4161-4167 (1993).

66. M. A. Epton and B. Dembart, "Multipole translation theory for the three-dimensional Laplace and Helmholtz equations," SIAM J. Sci. Comp. 16 (4), 865-897 (1995).

67. M. van Gelderen, "The shift operators and translations of spherical harmonics," DEOS Progress Letter 98.1, 57-67 (1998).

68. N. A. Gumerov and R. Duraiswami, "Fast, exact, and stable computation of multipole translation and rotation coefficients for the 3-D Helmholtz equation," Institute for Advanced Computer Studies Technical Report UMIACS-TR-# 2001-44, University of Maryland, College Park, Maryland (2001).

69. Z. Liu, C. T. Chan, P. Sheng, A. L. Goertzen, and J. H. Page, "Elastic wave scattering by periodic structures of spherical objects: Theory and experiment," Phys. Rev. B 62 (4), 2446-2457 (2000).

70. C. Liang and Y. T. Lo, "Scattering by two spheres," Radio Science 2 (12), 1481-1495 (1967).

71. J. H. Bruning and Y. T. Lo, "Multiple scattering of EM waves by spheres. Part I—Multipole expansion and ray-optical solutions," IEEE Transactions on Antennas and Propagation AP-19 (3), 378-390 (1971).

72. J. H. Bruning and Y. T. Lo, "Multiple scattering of EM waves by spheres. Part II—Numerical and experimental results," IEEE Transactions on Antennas and Propagation AP-19 (3), 391-400 (1971).

73. R. New and T. J. Eisler, "Acoustic radiation from multiple spheres," Journal of Sound and Vibration 22 (1), 1-17 (1972).

74. M. Razavy, "Scattering by two impenetrable spheres," Can. J. Phys. 51, 1850-1860 (1973).

75. A. C. Ludwig, "Scattering by two and three spheres computed by the generalized multipole technique," IEEE Transactions on Antennas and Propagation 39 (5), 703-705 (1991).

76. J.-P. Sessarego and J. Sageloli, "Étude théorique et expérimentale de la diffusion acoustique par deux coques sphériques élastiques," Acustica 79, 14-21 (1993).

77. P. J. Flatau, K. A. Fuller, and D. W. Mackowski, "Scattering by two spheres in contact: comparisons between discrete-dipole approximation and modal analysis," Applied Optics 32 (18), 3302-3305 (1993).

78. M. I. Mishchenko and D. W. Mackowski, "Light scattering by randomly oriented bispheres," Optics Letters 19 (20), 1604-1606 (1994).

79. A. Folacci, J.-L. Rossi, and J.-P. Sessarego, "GTD Analysis of Scattering by Two Elastic Spheres," Acustica 83, 93-104 (1997).

80. C. L. Morfey, J. Garcia-Bonito, and A. T. Peplow, "Acoustic radiation from a pair of spheres," Acustica 84, 701-711 (1998).

81. G. Kapodistrias and P. H. Dahl, "Effects of interaction between two bubble scatterers," J. Acoust. Soc. Am. 107 (6), 3006-3017 (2000).

82. G. C. Gaunaurd and H. Huang, "Acoustic scattering by a spherical body near a plane boundary," J. Acoust. Soc. Am. 96 (4), 2526-2536 (1994).

83. G. C. Gaunaurd and H. Huang, "Sound scattering by bubble clouds near the sea surface," J. Acoust. Soc. Am. 107 (1), 95-102 (2000).

84. G. Kapodistrias and P. H. Dahl, "On scattering from a bubble located near a flat air-water interface: Laboratory measurements and modeling," J. Acoust. Soc. Am. 110 (3), 1271-1281 (2001).

85. P. Denti, F. Borghese, R. Saija, E. Fucile, and O. I. Sindoni, "Optical properties of aggregated spheres in the vicinity of a plane surface," J. Opt. Soc. Am. A 16 (1), 167-175 (1999).

86. J. H. Kim, S. H. Ehrman, G. W. Mulholland, and T. A. Germer, "Polarized light scattering from metallic particles on silicon wafers," in Optical Metrology Roadmap for the Semiconductor, Optical, and Data Storage Industries, edited by A. Duparré and B. Singh, Proc. SPIE 4449, 281-290 (2001).

87. U. Comberg and T. Wriedt, "Comparison of scattering calculations for aggregated particles based on different models," Journal of Quantitative Spectroscopy and Radiative Transfer 63, 149-162 (1999).

88. A-K. Hamid, I. R. Ciric, and M. Hamid, "Multiple Scattering by a Linear Array of Conducting Spheres," Can. J. Phys. 68, 1157-1168 (1990).

89. A-K. Hamid, I. R. Ciric, and M. Hamid, "Electromagnetic Scattering by an Arbitrary Configuration of Dielectric Spheres," Can. J. Phys. 68, 1419-1428 (1990).

90. A-K. Hamid, I. R. Ciric, and M. Hamid, "Iterative Solution of the Scattering by an Arbitrary Configuration of Conducting or Dielectric Spheres," IEE Proceedings-H 138 (6), 565-572 (1991).

91. D. W. Mackowski, "Analysis of radiative scattering for multiple sphere configurations," Proc. R. Soc. Lond. A 433, 599-614 (1991)

92. F. de Daran, V. Vignéras-Lefebvre, and J. P. Parneix, "Modeling of electromagnetic waves scattered by a system of spherical particles," IEEE Trans. Magnetics 31 (3), 1598-1600 (1995).

93. K. A. Fuller and G. W. Kattawar, "Consummate solution to the problem of classical electromagnetic scattering by an ensemble of spheres. II. Clusters of arbitrary configuration," Optics Letters 13 (12), 1063-1065 (1988).

94. K. A. Fuller, "Scattering and absorption cross sections of compounded spheres. I. Theory for external aggregation," J. Opt. Soc. Am. A 11 (12), 3251-3260 (1994).

95. F. Borghese, P. Denti, G. Toscano, and O. I. Sindoni, "Electromagnetic scattering by a cluster of spheres," Applied Optics 18 (1), 116-120 (1979).

96. F. Borghese, P. Denti, R. Saija, G. Toscano, and O. I. Sindoni, "Multiple electromagnetic scattering from a cluster of spheres. I. Theory," Aerosol Science and Technology 3 (2), 227-235 (1984).

97. O. I. Sindoni, F. Borghese, P. Denti, R. Saija, and G. Toscano, "Multiple electromagnetic scattering from a cluster of spheres. II. Symmetrization," Aerosol Science and Technology 3 (2), 237-243 (1984).

98. F. Borghese, P. Denti, R. Saija, G. Toscano, and O. I. Sindoni, "Effects of aggregation on the electromagnetic resonance scattering of dielectric spherical objects," Nuovo Cimento D 6D (6), 545-558 (1985).

99. M. Quinten and U. Kreibig, "Absorption and elastic scattering of light by particle aggregates," Applied Optics 32 (30), 6173-6182 (1993).

100. D. W. Mackowski, "Calculation of total cross sections of multiple-sphere clusters," J. Opt. Soc. Am. A 11 (11), 2851-2861 (1994).

101. P. C. Waterman, "New formulation of acoustic scattering," J. Acoust. Soc. Am. 45 (6), 1417-1429 (1969).

102. P. C. Waterman, "Symmetry, untarity, and geometry in electromagnetic scattering," Phys. Rev. D 3 (4), 825-839 (1971).

103. P. C. Waterman, "Matrix theory of elastic wave scattering," J. Acoust. Soc. Am. 60 (3), 567-580 (1976).

104. P. C. Waterman, "Matrix theory of elastic wave scattering. II. A new conservation law," J. Acoust. Soc. Am. 63 (5), 1320-1325 (1978).

105. B. Peterson and S. Ström, "T matrix for electromagnetic scattering from an arbitrary number of scatterers and representation of E(3)*," Phys. Rev. D 8 (10), 3661-3678 (1973).

106. B. Peterson and S. Ström, "Matrix formulation of acoustic scattering from an arbitrary number of scatterers," J. Acoust. Soc. Am. 56 (3), 771-780 (1974).

107. B. Peterson and S. Ström, "T-matrix formulation of electromagnetic scattering from multilayered scatterers," Phys. Rev. D 10 (8), 2670-2684 (1974).

108. Y.-H. Pao, "Betti's identity and transition matrix for elastic waves," J. Acoust. Soc. Am. 64 (1), 302-310 (1978).

109. A. Boström, "Multiple scattering of elastic waves by bounded obstacles," J. Acoust. Soc. Am. 67 (2), 399-413 (1980).

110. A. Boström, "Scattering by a smooth elastic obstacle," J. Acoust. Soc. Am. 67 (6), 1904-1913 (1980).

111. B. Peterson, V. K. Varadan, and V. V. Varadan, "Scattering of elastic waves by a fluid inclusion," J. Acoust. Soc. Am. 73 (5), 1487-1493 (1983).

112. C. Feuillade and M. F. Werby, "Resonances of deformed gas bubbles in liquids," J. Acoust. Soc. Am. 96 (6), 3684-3692 (1994).

113. P. de Vries, D. V. van Coevorden, and A. Lagendijk, "Point scatterers for classical waves," Rev. Mod. Phys. 70 (2), 447-466 (1998).

114. S. Koc and W. C. Chew, "Calculation of acoustical scattering from a cluster of scatterers," J. Acoust. Soc. Am. 103 (2), 721-734 (1998).

115. M. I. Mishchenko, L. D. Travis, and A. Macke, "T-matrix method and its applications," in Light Scattering by Nonspherical Particles, edited by M. I. Mishchenko, J. W. Hovenier, and L. D. Travis (Academic Press, San Diego, CA, 2000), pp. 147-172.

116. K. A. Fuller and D. W. Mackowski, "Electromagnetic scattering by compounded spherical particles," in Light Scattering by Nonspherical Particles, edited by M. I. Mishchenko, J. W. Hovenier, and L. D. Travis (Academic Press, San Diego, CA, 2000), pp. 225-272.

117. N. C. Skaropoulos and H. W. J. Russchenberg, "Light scattering by arbitrarily oriented rotationally symmetric particles," J. Opt. Soc. Am. A 19 (8), 1583-1591 (2002).

118. B. Stout, C. Andraud, D. Prot, J. Lafait, J. C. Auger, and S. Stout, "Complete field descriptions in three-dimensional multiple scattering problems: A transfer matrix approach," J. Opt. A: Pure Appl. Opt. 4, S182-S187 (2002).

119. N. A. Gumerov and R. Duraiswami, "Computation of scattering from N spheres using multipole reexpansion," J. Acoust. Soc. Am. 112 (6), 2688-2701 (2002).

120. L. Greengard and V. Rokhlin, "A fast algorithm for particle simulations," Journal of Computational Physics 73, 325-348 (1987).

121. V. Rokhlin, "Rapid Solution of Integral Equations of Scattering Theory in Two Dimensions," Journal of Computational Physics 86 (2), 414-439 (1990).

122. R. Coifman, V. Rokhlin, and S. Wnadzura, "The Fast Multipole Method for the Wave Equation: A Pedestrian Prescription," IEEE Antennas and Propagation Magazine 35 (3), 7-12 (June 1993).

123. L. Greengard, "Fast Algorithms for Classical Physics," Science 265, 909-914 (1994).

124. S. S. Bindiganavale and J. L. Volakis, "Comparison of Three FMM Techniques for Solving Hybrid FE-BI Systems," IEEE Antennas and Propagation Magazine 39 (4), 47-60 (August 1997).

125. C. V. Hafner, "On the Design of Numerical Methods," IEEE Antennas and Propagation Magazine 35 (4), 13-21 (August 1993).

126. M. G. Imhof, "Multiple multipole expansions for acoustic scattering," J. Acoust. Soc. Am. 97 (2), 754-763 (1995).

127. M. G. Imhof, "Scattering of acoustic and elastic waves using hybrid multiple multipole expansions—Finite element technique," J. Acoust. Soc. Am. 100 (3), 1325-1338 (1996).

128. N. Atalla, G. Winckelmans, and F. Sgard, "A multiple multipole expansion approach for predicting the sound power of vibrating structures," Acustica 85, 47-53 (1999).

129. B. T. Draine, "The discrete dipole approximation for light scattering by irregular targets," in Light Scattering by Nonspherical Particles, edited by M. I. Mishchenko, J. W. Hovenier, and L. D. Travis (Academic Press, San Diego, CA, 2000), pp. 147-172.

130. M. P. Ioannidou, N. C. Skaropoulos, and D. P. Chrissoulidis, "Study of interactive scattering by clusters of spheres," J. Opt. Soc. Am. A 12 (8), 1782-1789 (1995).

131. M. P. Ioannidou and D. P. Chrissoulidis, "Electromagnetic-wave scattering by a sphere with multiple spherical inclusions," J. Opt. Soc. Am. A 19 (3), 505-512 (2002).

132. V. N. Pustovit, J. A. Sotelo, and G. A. Niklasson, "Coupled multipolar interactions in small-particle metallic clusters," J. Opt. Soc. Am. A 19 (3), 513-518 (2002).

133. A. Doicu, G. Göbel, T. Wriedt, and K. Bauckhage, "Influence of agglomerates of conducting spheres on the response of a phase-Doppler anemometer," Part. Part. Syst. Charact. 15, 225-229 (1998).

134. R. Marklein, K. J. Langenberg, R. Bärmann, K. Mayer, and S. Klaholz, "Nondestructive Testing with Ultrasound: Numerical Modeling and Imaging," Acoustical Imaging, Vol. 22, edited by P. Tortoli and L. Masotti, (Plenum Press, New york, 1996), pp. 757-764.

135. F. Ihlenburg, Finite Element Analysis of Acoustic Scattering, (Springer-Verlag, New York, 1998).

136. P. Yang and K. N. Liou, "Finite difference time domain method for light scattering by nonspherical and inhomogeneous particles," in Light Scattering by Nonspherical Particles, edited by M. I. Mishchenko, J. W. Hovenier, and L. D. Travis (Academic Press, San Diego, CA, 2000), pp. 173-221.

137. W. Axmann and P. Kuchment, "An Efficient Finite Element Method for Computing Spectra of Photonic and Acoustic Band-Gap Materials," J. Comput. Phys. 150, 468-481 (1999).

138. A. A. Gusev, H. R. Lusti, "Rational Design of Nanocomposites for Barrier Applications," Adv. Mater. 13 (21), 1641-1643 (2001).

139. A. A. Gusev, "Numerical Identification of the Potential of Whisker and Platelet Filled Polymers," Macromolecules 34 (9), 3081-3093 (2001).

140. O. A. Gusev, P. Richner, M. G. Rozman, A. A. Gusev, "Void-containing materials with tailored Poisson's ratio," J. Appl. Phys. 88 (7), 4013-4016 (2000).

141. J. L. Rose, Ultrasonic Waves in Solid Media, (Cambridge University Press, Cambridge, UK, 1999).

142. P. Mora, "The lattice Boltzmann phononic lattice solid," Journal of Statistical Physics 68 (3-4), 591-609 (1992).

143. L.-J. Huang and P. Mora, "The phononic lattice solid by interpolation for modelling P waves in heterogenous media," Geophys. J. Int. 119, 766-778 (1994).

144. L.-J. Huang, P. Mora, and M. C. Fehler, "Absorbing boundary and free-surface conditions in the phononic lattice solid by interpolation," Geophys. J. Int. 140, 147-157 (2000).

145. Leslie L. Foldy, "The Multiple Scattering of Waves: I. General Theory of Isotropic Scattering by Randomly Distributed Scatterers," Phys. Rev. 67 (3-4), 107-119 (1945).

146. Melvin Lax, "Multiple Scattering of Waves," Rev. Mod. Phys. 23 (4), 287-310 (1951).

147. Melvin Lax, "Multiple Scattering of Waves. II. The Effective Field in Dense Systems," Phys. Rev. 85 (4), 621-629 (1952).

148. P. S. Epstein and R. R. Carhart, "The Absorption of Sound in Suspensions and Emulsions. I. Water Fog in Air," J. Acoust. Soc. Am. 25 (3), 553-565 (1953).

149. P. C. Waterman and R. Truell, "Multiple Scattering of Waves," J. Math. Phys. 2 (4), 512-537 (1961).

150. J. G. Fikioris and P. C. Waterman, "Multiple Scattering of Waves. II. "Hole Corrections" in the Scalar Case," J. Math. Phys. 5 (10), 1413-1420 (1964).

151. J. Devaney, "Multiple scattering theory for discrete, elastic, random media," J. Math. Phys. 21 (11), 2603-2611 (1980).

152. L. Drolen and C. L. Tien, "Independent and Dependent Scattering in Packed-Sphere Systems," J. Thermophysics 1 (1), 63-68 (1987).

153. W. W. Yuen and W. Dunaway, "Effect of multiple scattering on radiation transmission in absorbing-scattering media," J. Thermophysics 1 (1), 77-82 (1987).

154. F. J. Sabina and J. R. Willis, "A simple self-consistent analysis of wave propagation in particulate composites," Wave Motion 10, 127-142 (1988).

155. M. Baird, F. H. Kerr, and D. J. Townend, "Wave propagation in a viscoelastic medium containing fluid-filled microspheres," J. Acoust. Soc. Am. 105 (3), 1527-1538 (1999).

156. I. Beltzer, Acoustics of Solids, (Springer-Verlag, Berlin, 1988).

157. J. M. Ziman, "Wave propagation through an assembly of spheres. I. The Greenian method of the theory of metals," Proc. Phys. Soc. 88, 387-405 (1966).

158. P. Lloyd, "Wave propagation through an assembly of spheres. II. The density of single-particle eigenstates," Proc. Phys. Soc. 90, 207-216 (1967).

159. P. Lloyd, "Wave propagation through an assembly of spheres. III. The density of states in a liquid," Proc. Phys. Soc. 90, 217-231 (1967).

160. P. Lloyd and M. V. Berry, "Wave propagation through an assembly of spheres. IV. Relations between different multiple scattering theories," Proc. Phys. Soc. 91, 678-688 (1967).

161. G. J. Morgan and J. M. Ziman, "Wave propagation through an assembly of spheres. V. The vibrations of a loaded elastic continuum," Proc. Phys. Soc. 91, 689-688 (1967).

162. L. Tsang and J. A. Kong, "Multiple scattering of acoustic waves by random distributions of scatterers with the use of quasicrystalline-coherent potential approximation," J. Appl. Phys. 52 (9), 5448-5458 (1981).

163. D. R. S. Talbot and J. R. Willis, "Variational estimates for dispersions and attenuation of waves in random composites—I. General theory," Int. J. Solids Structures 18 (8), 673-683 (1982).

164. D. R. S. Talbot and J. R. Willis, "Variational estimates for dispersions and attenuation of waves in random composites—II. Isotropic composites," Int. J. Solids Structures 18 (8), 685-698 (1982).

165. R. L. Weaver, "A variational principle for waves in discrete random media," Wave Motion 7, 105-121 (1985).

166. R. L. Weaver, "Diffusivity of ultrasound in polycrystals," J. Mech. Phys. Solids 38 (1), 55-86 (1990).

167. J. A. Turner and R. L. Weaver, "Radiative transfer and multiple scattering of diffuse ultrasound in polycrystalline media," J. Acoust. Soc. Am. 96 (6), 3675-3683 (1994).

168. J. A. Turner and R. L. Weaver, "Ultrasonic radiative transfer in polycrystalline media: Effects of a fluid-solid interface," J. Acoust. Soc. Am. 98 (5-Part 1), 2801-2808 (1995).

169. J. A. Turner and R. L. Weaver, "Time deppendence of multiply scattered diffuse ultrasound in polycrystalline media," J. Acoust. Soc. Am. 97 (5), 2639-2644 (1994).

170. J. A. Turner, "Elastic wave propagation and scattering in heterogeneous, anisotropic media: Textured polycrystalline materials," J. Acoust. Soc. Am. 106 (2), 541-552 (1999).

171. J. A. Turner and P. Anugonda, "Scattering of elastic waves in heterogeneous media with local isotropy," J. Acoust. Soc. Am. 109 (5), 1787-1795 (2001).

172. M. C. W. van Rossum and Th. M. Nieuwenhuizen, "Multiple scattering of classical waves: microscopy, mesoscopy, and diffusion," Rev. Mod. Phys. 71 (1), 313-371 (1999).

173. V. P. Dick and A. P. Ivanov, "Extinction of light in dispersive media with high particle concentrations: applicability limits of the interference approximation," J. Opt. Soc. Am. A 16 (5), 1034-1039 (1999).

174. W. E. Vargus, "Diffuse radiation intensity propagating through a particulate slab," J. Opt. Soc. Am. A 16 (6), 1362-1372 (1999).

175. R. P. Feynman, "Space-Time Approach to Non-Relativistic Quantum Mechanics," Rev. Mod. Phys. 20 (2), 367-387 (1948).

176. S. M. Flatté, R. Dashen, W. H. Munk, K. M. Watson, and F. Zachariasen, Sound Transmission Through a Fluctuating Ocean, (Cambridge University Press, Cambridge, London, 1979).

177. R. Dashen, S. M. Flatté, and S. A. Reynolds, "Path-integral treatment of acoustic mutual coherence functions for rays in a sound channel," J. Acoust. Soc. Am. 77 (5), 1716-1722 (1985).

178. M. I. Charnotskii, J. Gozani, V. I. Tatarskii, and V. U. Zavorotny, "Wave Propagation Theories in Random Media Based on the Path Integral Approach" in Progress in Optics XXXII edited by E. Wolf (Elsevier Science Publishers, 1993), pp. 204-266.

179. Anthony Lomax, "The wavelength-smoothing method for approximating broad-band wave propagation through complicated velocity structures," Geophys. J. Int. 117, 313-334 (1994).

180. Anthony Lomax and Roel Snieder, "Estimation of finite-frequency waveforms through wavelength-dependent averaging of velocity," Geophys. J. Int. 126, 369-381 (1996).

181. Anthony Lomax, "Path-summation waveforms," Geophys. J. Int. 138, 702-716 (1999).

182. M. A. Jensen, "A recursive Green's function technique for acoustic scattering from heterogeneous objects," J. Acoust. Soc. Am. 103 (2), 713-720 (1998).

183. W. Greiner and J. Reinhardt, Quantum Electrodynamics, (Springer-Verlag, Berlin, 1992).

184. D. Colton and R. Kress, Inverse Acoustic and Electromagnetic Scattering Theory, (Springer-Verlag, Berlin, 1992).

185. M. I. Mishchenko, "Vector radiative transfer equation for arbitarily shaped and arbitrarily oriented particles: A microphysical derivation from statistical electromagnetics," Applied Optics 41 (33), 7114-7134 (2002).

186. M. J. W. Povey and D. J. McClements, editors, Developments in Acoustics and Ultrasonics, (Institute of Physics Publishing, Bristol, 1992).

187. M. J. W. Povey, Ultrasonic Techniques for Fluids Characterization, (Academic Press, San Diego, 1997).

188. K. F. Graff, Wave Motion in Elastic Solids, (Oxford University Press, Oxford, UK, 1975; Dover, New York, 1991).

189. W. F. Hughes and E. W. Gaylord, Basic Equations of Engineering Science: Schaum's Outline Series, (McGraw-Hill, New York, 1964).

190. B. M. Lempriere, Ultrasound and Elastic Waves: Frequently Asked Questions, (Academic Press, San Diego, CA, 2002).

191. D. Ensminger, Ultrasonics: Fundamentals, Technology, Applications, 2nd ed. (Marcel Dekker, Inc., New York, 1988).

192. D. G. Raymer, A. Tommasi, and J-M. Kendall, "Predicting the seismic implications of salt anisotropy using numerical simulations of halite deformation," Geophysics 65 (4), 1272-1280 (2000).

193. P. He, "Experimental verification of models for determining dispersion from attenuation," IEEE Trans. Ultrason., Ferroelect., Freq. Contr. 46 (3), 706-714 (1999).

194. P. He, "Direct measurement of ultrasonic dispersion using a broadband transmission technique," Ultrasonics 37, 67-70 (1999).

195. I. L. Davis, Personal Communication, ATK-Thiokol Propulsion.

196. E. Hecht and A. Zajac, Optics, (Addison-Wesley, Reading, Massachusetts, 1974).

197. D. Halliday and R. Resnick, Fundamentals of Physics, 3rd ed. (Wiley, New York, 1988).

198. R. D. Pradhan, J. A. Bloodgood, and G. H. Watson, "Photonic band structure of bcc colloidal crystals," Phys. Rev. B $\underline{55}$ (15), 9503-9507 (1997).

199. J. D. Joannopoulos, R. D. Meade, and J. N. Winn, Photonic Crystals: Molding the Flow of Light, (Princeton University Press, Princeton, New Jersey, 1995).

200. A. Boughriet, Z. Wu, H. McCann, and L. E. Davis, "The measurement of dielectric properties of liquids at microwave frequencies using open-ended coaxial probes," 1st World Congress on Industrial Process Tomography, Buxton, Greater Manchester, April 14-17, 1999, pp. 318-322.

201. P. K. Datta and R. A. Pethrick, "Ultrasonic studies of glass-filled polymer solids," J. Phys. D: Appl. Phys. $\underline{13}$, 153-161 (1980).

202. V. K. Kinra, M. S. Petraitis, and S. K. Datta, "Ultrasonic wave propagation in a random particulate composite," Int. J. Solids Structures $\underline{16}$, 301-312 (1980).

203. V. K. Kinra and A. Anand, "Wave propagation in a random particulate composite at long and short wavelengths," Int. J. Solids Structures $\underline{18}$ (5), 367-380 (1982).

204. C. M. Sayers and R. L. Smith, "Ultrasonic velocity and attenuation in an epoxy matrix containing lead inclusions," J. Phys. D: Appl. Phys. $\underline{16}$, 1189-1194 (1983).

205. S. K. Datta, H. M. Ledbetter, Y. Shindo, and A. H. Shah, "Phase velocity and attenuation of plane elastic waves in a particle-reinforced composite medium," Wave Motion $\underline{10}$, 171-182 (1988).

206. R. E. Challis, A. K. Holmes, J. S. Tebbutt, and R. P. Cocker, "Scattering of ultrasonic compression waves by particulate filler in a cured epoxy continuum," J. Acous. Soc. Am. $\underline{103}$ (3), 1413-1420 (1998).

207. G. C. Knollman, R. H. Martinson, and J. L. Bellin, "Ultrasonic assessment of cumulative internal damage in filled polymers," J. Appl. Phys. $\underline{50}$ (1), 111-120 (1979).

208. G. C. Knollman and R. H. Martinson, "Nonlinear elastic effects in the ultrasonic assessment of cumulative internal damage in filled polymers," J. Appl. Phys. $\underline{50}$ (12), 8034-8037 (1979).

209. G. C. Knollman, R. H. Martinson, and J. L. Bellin, "Ultrasonic assessment of cumulative internal damage in filled polymers (II)," J. Appl. Phys. $\underline{51}$ (6), 3164-3170 (1980).

210. Ultrasonic Methods in Evaluation of Inhomogeneous Materials edited by A. Alippi and W. G. Mayer, (Martinus Nijhoff publishers, Dordrecht, 1987).

211. I. M. Daniel, S. C. Wooh, and I. Komsky, "Quantitative Porosity Characterization of Composite Materials by Means of Ultrasonic Attenuation Measurements," Journal of Nondestructive Evaluation $\underline{11}$ (1), 1-8 (1992).

212. M. Kupkova, "Porosity dependence of material elastic moduli," Journal of Material Science $\underline{28}$, 5265-5268 (1993).

213. K. Choudhury, A. K. De, K. K. Phani, "Ultrasonic detection of changes in the microstructure of glass-ceramics during crystallization," Journal of Materials Science Letters $\underline{13}$, 310-312 (1994).

214. E. Ruffino and P. P. Delsanto, "Scattering of ultrasonic waves by void inclusions," J. Acoust. Soc. Am. $\underline{108}$ (4), 1941-1945 (2000).

215. J. R. Allegra and S. A. Hawley, "Attenuation of Sound in Suspensions and Emulsions: Theory and Experiments," J. Acoust. Soc. Am. 51 (5-Part 2), 1545-1564 (1972).

216. M. C. Davis, "Attenuation of sound in highly concentrated suspensions and emulsions," J. Acoust. Soc. Am. 65 (2), 387-390 (1979).

217. C. M. Sayers, "On the propagation of ultrasound in highly concentrated mixtures and suspensions," J. Phys. D: Appl. Phys. 13, 179-184 (1980).

218. A. H. Harker and J. A. G. Temple, "Velocity and attenuation of ultrasound in suspensions of particles in fluids," J. Phys. D: Appl. Phys. 21, 1576-1588 (1988).

219. D. J. McClements and M. J. W. Povey, "Scattering of ultrasound by emulsions," J. Phys. D: Appl. Phys. 22, 38-47 (1989).

220. D. J. McClements, E. Dickinson, and M. J. W. Povey, "Crystallization in hydrocarbon-in-water emulsions containing a mixture of solid and liquid droplets," Chem. Phys. Lett. 172 (6), 449-452 (1990).

221. D. J. McClements, M. J. W. Povey, and E. Dickinson, "Absorption and velocity dispersion due to crystallization and melting of emulsion droplets," Ultrasonics 31 (6), 433-437 (1993).

222. G. H. Meeten and N. E. Sherman, "Ultrasonic velocity and attenuation of glass ballotini in viscous and viscoelastic fluids," Ultrasonics 31 (3), 193-199 (1993).

223. J. Adach, R. C. Chivers, and L. W. Anson, "Ultrasonic propagation, scattering, and defocusing in suspensions," J. Acoust. Soc. Am. 93 (6), 3208-3219 (1993).

224. P. Bartlett and W. Van Megen, "Physics of Hard-Sphere Colloidal Suspensions," Granular Matter: An Interdisciplinary Approach, edited by A. Mehta (Springer-Verlag, New York, 1994), pp. 195-257.

225. V. A. Hackley and J. Texter, Conference Report: International workshop on ultrasonic and dielectric characterization techniques for suspended Particulates," J. Res. Natl. Inst. Stand. Technol. 103 (2), 217-223 (1998).

226. D. O. Riese and G. H. Wegdam, "Sound propagation in suspensions of colloidal spheres with viscous coupling," Phys. Rev. Lett. 82 (8), 1676-1679 (1999).

227. J. Mobley, K. R. Waters, C. S. Hall, J. N. Marsh, M. S. Hughes, G. H. Brandenburger, and J. G. Miller, "Measurements and predictions of the phase velocity and attenuation coefficient in suspensions of elastic microspheres," J. Acoust. Soc. Am. 106 (2), 652-659 (1999).

228. S. Temkin, "Attenuation and dispersion of sound in dilute suspensions of spherical particles," J. Acoust. Soc. Am. 108 (1), 126-146 (2000).

229. T. J. O'Neill, J. S. Tebbutt, and R. E. Challis, "Convergence criteria for scattering models of ultrasonic wave propagation in suspensions of particles," IEEE Trans. Ultrason., Ferroelect., Freq. Contr. 48 (2), 419-424 (2001).

230. David C. Dobson, "An efficient method for band structure calculations in 2D photonic crystals," J. Comp. Phys., 149, 363-376 (1999).

231. David C. Dobson, Jayadeep Gopalakrishnan, and Joseph E. Pasciak, "An efficient method for band structure calculations in 3D photonic crystals," J. Comp. Phys., 161, 668-679 (2000).

232. E. E. Kriezis, C. J. P. Newton, T. P. Spiller, and S. J. Elston, "Three-dimensional simulations of light propagation in periodic liquid-crystal microstructures," Applied Optics 41 (25), 5346-5356 (2002).

233. A. Sharkawy, S. Shi, and D. W. Prather, "Heterostructure photonic crystals: Theory and applications," Applied Optics 41 (34), 7245-7253 (2002).

234. Z. Ouyang, C. Jin, D. Zhang, B. Cheng, X. Meng, G. Yang, and J. Li, "Photonic bandgaps in two-dimensional short-range periodic structures," J. Opt. A: Pure Appl. Opt. 4, 23-28 (2002).

235. A. Peyrilloux, S. Février, J. Marcou, L. Berthelot, D. Pagnoux, and P. Sansonetti, "Comparison between the finite element method, the localized function method, and a novel equivalent averaged index method for modeling photonic crystal fibres," J. Opt. A: Pure Appl. Opt. 4, 257-262 (2002).

236. E. Istrate and E. H. Sargent, "Photonic crystal heterostructures—resonant tunnelling, waveguides and filters," J. Opt. A: Pure Appl. Opt. 4, S242-S246 (2002).

237. T. Vallius and M. Kuittinen, "Novel electromagnetic approach to photonic crystals with use of the C method," J. Opt. Soc. Am A 20 (1), 85-91 (2003).

238. B. K. Henderson, V. K. Kinra, and A. W. Gonzales, "Ultrasonic diffraction by a square periodic array of spheres," J. Acoust. Soc. Am. 107 (3), 1759-1761 (2000).

239. M. Kafesaki, R. S. Penciu, and E. N. Economou, "Air bubbles in water: A strongly multiple scattering medium for acoustic waves," Phys. Rev. Lett. 84 (26), 6050-6053 (2000).

240. I. E. Psarobas, N. Stefanou, and A. Modinos, "Scattering of elastic waves by periodic arrays of spherical bodies," Phys. Rev. B 62 (1), 278-291 (2000).

241. I. E. Psarobas, N. Stefanou, and A. Modinos, "Photonic crystals with planar defects," Phys. Rev. B 62 (9), 5536-5540 (2000).

242. I. E. Psarobas, "Viscoelastic response of sonic band-gap materials," Phys. Rev. B 64: 012303 (2001).

243. I. E. Psarobas, N. Stefanou, and A. Modinos, "Acoustic properties of colloidal crystals," Phys. Rev. B 62: 064307 (2002).

244. D. Garcia-Pablos, M. Sigalas, F. R. Montero de Espinosa, M. Torres, M. Kafesaki, and N. Garcia, "Theory and experiment on elastic band gaps," Phys. Rev. Lett. 84 (19), 4349-4352 (2000).

245. L. Sanchis, F. Cervera, J. Sánchez-Dehesa, J. V. Sánchez-Pérez, C. Rubio, and R. Martinez-Sala, "Reflectance properties of two-dimensional sonic band-gap crystals," J. Acoust. Soc. Am. 109 (6), 2598-2605 (2001).

246. F. T. Schulitz, Y. Lu, and H. N. G. Wadley, "Ultrasonic propagation in metal powder-viscous liquid suspensions," J. Acoust. Soc. Am. 103 (3), 1361-1369 (1998).

247. R. Weaver, "Ultrasonics in an aluminum foam," Ultrasonics 36, 435-442 (1998).

248. J. A. Turner, M. E. Chambers, and R. L. Weaver, "Ultrasonic Band Gaps in Aggregates of Sintered Aluminum Beads," Acustica 84, 628-631 (1998).

249. O. I. Lobkis and R. L. Weaver, "Mode counts in an aluminum foam," J. Acoust. Soc. Am. 109 (6), 2636-2641 (2001).

250. D. J. McClements, M. J. W. Povey, M. Jury, and E. Betsanis, "Ultrasonic characterization of a food emulsion," Ultrasonics 28, 266-272 (1990).

251. D. J. McClements and M. J. W. Povey, "Ultrasonic analysis of edible fats and oils," Ultrasonics 30, 383-388 (1992).

252. P. Chen, "Quality Evaluation Technology for Agricultural Products," Proc. Int. Conf. on Agric. Machinery Engineering, Nov. 12-15, 1996, Seoul, Korea, Vol. I: 171-204.

253. A. Mizrach and U. Flitsanov, "Nondestructive ultrasonic determination of avocado softening process," Journal of Food Engineering 40, 139-144 (1999).

254. S. C. Hill, A. C. Hill, and P. W. Barber, "Light scattering by size/shape distributions of soil particles and spheroids," Applied Optics 23 (7), 1025-1031 (1984).

255. Ustin, S. L., E. W. Sanderson, Y. Grossman, Q. J. Hart, and R. S. Haxo, "Relationships between pigment composition variation and reflectance for plant species from a coastal savannah in California," Summaries of the Fourth Annual JPL Airborne Earth Science Workshop: AVIRIS Workshop, Washington, D.C., 1993, pp. 181-184.

256. Govaerts, Y. M., S. Jacquemoud, M. M. Verstraete, and S. L. Ustin, "Modeling plant leaf bidirectional reflectance and transmittance with a 3-D ray tracing approach," IGARSS 95: Proceedings International Geoscience and Remote Sensing Symposium, Greenbelt, MD, Feb. 27-Mar. 1, 1995.

257. Jacquemoud S., S.L. Ustin, J. Verdebout, G. Schmuck, G. Andreoli, B. Hosgood, "Modeling Leaf Optical Properties Using a Radiative Transfer Model," NASA Remote Sensing Science Workshop, Greenbelt, MD, Feb. 27-Mar. 1, 1995.

258. Govaerts, Y.M., S. Jacquemoud, M.M. Verstraete, and S. L. Ustin, "Three-dimensional radiation transfer modeling in a dicotyledon leaf," Applied Optics 35 (33), 6585-6598 (1996).

259. Jacquemoud, S., S.L. Ustin, J. Verdebout, G. Schmuck, G. Andreoli, and B. Hosgood, "Estimating leaf biochemistry using the PROSPECT leaf optical properties model." Remote Sensing of Environment 56 (3), 194-202 (1996).

260. Jacquemoud, S., J.-P. Frangi, Y. Govaerts, and S.L. Ustin, "Three-dimensional representation of leaf anatomy - Application of photon transport," 7th Int. Symp. Physical Measurements and Signatures in Remote Sensing, Vol. 1, Courchevel, France, April 7-11, 1997, pp. 295-302.

261. A. Yodh and B. Chance, "Spectroscopy and imaging with diffusing light," Physics Today, 34-40 (March 1995).

262. J. Chen and J. A. Zagzebski, "Frequency Dependence of Backscatter Coefficient Versus Scatterer Volume Fraction," IEEE Trans. Ultrason., Ferroelect., Freq. Contr. 43 (3), 345-353 (1996).

263. D. A. Benaron, W. Cheong, and D. K. Stevenson, "Tissue Optics," Science 276, 2002-2003 (1997).

264. J. C. Bamber, "Ultrasonic Properties of Tissues," in Ultrasound in Medicine, edited by F. A. Duck, A. C. Baker, and H. C. Starritt (Institute of Physics Publishing, Bristol, 1998), pp. 57-88.

265. D. Phillips, X. Chen, R. Baggs, D. Rubens, M. Violante, and K. J. Parker, "Acoustic backscatter properties of the particle/bubble ultrasound contrast agent," Ultrasonics 36, 883-892 (1998).

266. P. M. Shankar, "A General Statistical Model for Ultrasonic Backscattering from Tissues," IEEE Trans. Ultrason., Ferroelect., Freq. Contr. 47 (3), 727-736 (2000).

267. A. G. Hoekstra and P. M. A. Sloot, "Biophysical and biomedical applications of nonspherical scattering," in Light Scattering by Nonspherical Particles, edited by M. I. Mishchenko, J. W. Hovenier, and L. D. Travis (Academic Press, San Diego, CA, 2000), pp. 585-602.

268. J. S. Allen, D. E. Kruse, and K. W. Ferrara, "Shell waves and acoustic scattering from ultrasound contrast agents," IEEE Trans. Ultrason., Ferroelect., Freq. Contr. 48 (2), 409-418 (2001).

269. D. Savery and G. Cloutier, "A point process approach to assess the frequency dependence of ultrasound backscattering by aggregating red blood cells," J. Acoust. Soc. Am. 110 (6), 3252-3262 (2001).

270. A. Dunn and R. Richards-Kortum, "Three-dimensional computation of light scattering from cells," IEEE Journal of Selected Topics in Quantum Electronics 2 (4), 898-905 (1996).

271. J. R. Mourant, J. P. Freyer, A. H. Hielscher, A. A. Eick, D. Shen, and T. M. Johnson, "Mechanisms of light scattering from biological cells relevant to noninvasive optical-tissue diagnostics," Applied Optics 37 (16), 3586-3593 (1998).

272. R. Drezek, A. Dunn, and R. Richards-Kortum, "Light scattering from cells: finite-difference time-domain simulations and goniometric measurement," Applied Optics 38 (16), 3651-3661 (1999).

273. R. Gurjar, V. Backman, L. T. Perelman, I. Georgakoudi, K. Badizadegan, I. Itzkan, R. R. Dasari, and M. S. Feld, "Imaging human epithelial properties with polarized light-scattering spectroscopy," Nature Medicine 7 (11), 1245-1248 (2001).

274. A. M. K. Enejder, J. Swartling, P. Aruna, and S. Andersson-Engels, "Influence of cell shape and aggregate formation on the optical properties of flowing whole blood," Applied Optics 42 (7), 1384-1394 (2003).

275. G. T. Kuster and M. N. Toksoz, "Velocity and Attenuation of Seismic Waves in Two-Phase Media: Part I. Theoretical Formulations," Geophysics 39 (5), 587-606 (1974).

276. G. T. Kuster and M. N. Toksoz, "Velocity and Attenuation of Seismic Waves in Two-Phase Media: Part I. Experimental Results," Geophysics 39 (5), 607-618 (1974).

277. S. Pride, "Governing equations for the coupled electromagnetics and acoustics of porous media," Phys. Rev. B 50 (21), 15678-15696 (1994).

278. M. J. Buckingham, "Theory of compressional and transverse wave propagation in consolidated porous media," J. Acous. Soc. Am. 106 (2), 575-581 (1999).

279. M. A. Biot, "Generalized Theory of Acoustic Propagation in Porous Dissipative Media," J. Acoust. Soc. Am. 34 (9), 1254-1264 (1962).

280. R. D. Stoll, "Theoretical aspects of sound transmission in sediments," J. Acoust. Soc. Am. 68 (5), 1341-1350 (1980).

281. A. L. Anderson and L. D. Hampton, "Acoustics of gas-bearing sediments I. Background," J. Acoust. Soc. Am. 67 (6), 1865-1889 (1980).

282. C. W. Holland and B. A. Brunson, "The Biot-Stoll sediment model: An experimental assessment," J. Acoust. Soc. Am. 84 (4), 1437-1443 (1988).

283. M. Breitzke and V. Spieß, "An automated Full Waveform Logging System for High-Resolution P-Wave Profiles in Marine Sediments," Marine Geophysical Researches 15, 297-321 (1993).

284. K. C. Leurer, "Attenuation in fine-grained marine sediments: Extension of the Biot-Stoll model by the "effective grain model" (EGM)," Geophysics 62 (5), 1465-1479 (1997).

285. J. Schat, "Multifrequency acoustic measurement of concentration and grain size of suspended sand in water," J. Acoust. Soc. Am. 101 (1), 209-217 (1997).

286. S. G. Kargl, K. L. Williams, and R. Lim, "Double monopole resonance of a gas-filled, spherical cavity in a sediment," J. Acoust. Soc. Am. 103 (1), 265-274 (1998).

287. Z. W. Qian, "Sound Attenuation in Marine Sediments," Acustica 84, 621-627 (1998).

288. M. Breitzke, "Acoustic and elastic characterization of marine sediments by analysis, modeling, and inversion of ultrasonic P wave transmission seismograms," J. Geophys. Res. 105 (B9), 21,411-21,430 (2000).

289. M. J. Buckingham, "Wave propagation, stress relaxation, and grain-to-grain shearing in saturated, unconsolidated marine sediments," J. Acoust. Soc. Am. 108 (6), 2796-2815 (2000).

290. R. H. Mellen, "Sound Propagation in an Inhomogeneous Ocean," in Cavitation and Inhomogeneities in Underwater Acoustics, edited by W. Lauterborn (Springer-Verlag, Berlin, 1980), pp. 272-280.

291. L. Brekhovskikh and Y. Lysanov, Fundamentals of Ocean Acoustics, (Springer-Verlag, Berlin, 1982).

292. L. J. Ziomek, Fundamentals of Acoustic Field Theory and Space-Time Signal Processing, (CRC Press, Boca Raton, 1995), pp. 307-397.

293. M. S. Quinby-Hunt, P. G. Hull, and A. J. Hunt, "Polarized light scattering in the marine environment," in Light Scattering by Nonspherical Particles, edited by M. I. Mishchenko, J. W. Hovenier, and L. D. Travis (Academic Press, San Diego, CA, 2000), pp. 525-554.

294. Z. Ye, "Recent developments in underwater acoustics: Acoustic scattering from single and multiple bodies," Proc. Natl. Sci. Counc. ROC(A) 25 (3), 137-150 (2001).

295. Z. Ye and A. Alvarez, "Acoustic Localization in Bubbly Liquid Media," Phys. Rev. Lett. 80 (16), 3503-3506 (1998).

296. F. S. Henyey, "Corrections to Foldy's effective medium theory for propagation in bubble clouds and other collections of very small scatterers," J. Acoust. Soc. Am. 105 (4), 2149-2154 (1999).

297. J. L. Leander, "Wavefront and group velocity in relaxing and bubbly fluids," J. Acoust. Soc. Am. 105 (6), 3044-3048 (1999).

298. C. Feuillade, "Acoustically coupled gas bubbles in fluids: Time-domain phenomena," J. Acoust. Soc. Am. 109 (6), 2606-2615 (2001).

299. T. K. Stanton, "Sound scattering by cylinders of finite length. I. Fluid cylinders," J. Acoust. Soc. Am. 83 (1), 55-63 (1988).

300. T. K. Stanton, "Sound scattering by cylinders of finite length. II. Elasic cylinders," J. Acoust. Soc. Am. <u>83</u> (1), 64-67 (1988).

301. T. K. Stanton, "Sound scattering by cylinders of finite length. III. Deformed cylinders," J. Acoust. Soc. Am. <u>86</u> (2), 691-705 (1989).

302. T. K. Stanton, "Simple approximate formulas for backscattering of sound by spherical and elongated objects," J. Acoust. Soc. Am. <u>86</u> (4), 1499-1510 (1989).

303. T. K. Stanton, "Sound scattering by spherical and elongated shelled bodies," J. Acoust. Soc. Am. <u>88</u> (3), 1619-1633 (1990).

304. D. T. DiPerna and T. K. Stanton, "Sound scattering by cylinders of noncircular cross section: A conformal mapping approach," J. Acoust. Soc. Am. <u>96</u> (5), 3064-3079 (1994).

305. T. K. Stanton, D. Chu, P. H. Wiebe, L. V. Martin, and R. L. Eastwood, "Sound scattering by several zooplankton groups. I. Experimental determination of dominant scattering mechanisms," J. Acoust. Soc. Am. <u>103</u> (1), 225-235 (1998).

306. T. K. Stanton, D. Chu, and P. H. Wiebe, "Sound scattering by several zooplankton groups. II. Scattering models," J. Acoust. Soc. Am. <u>103</u> (1), 236-253 (1998).

307. T. K. Stanton, P. H. Wiebe, and D. Chu, "Differences between sound scattering by weakly scattering spheres and finite-length cylinders with applications to sound scattering by zooplankton," J. Acoust. Soc. Am. <u>103</u> (1), 254-264 (1998).

308. T. K. Stanton, D. Chu, P. H. Wiebe, R. L. Eastwood, and J. D. Warren, "Acoustic scattering by benthic and planktonic shelled animals," J. Acoust. Soc. Am. <u>108</u> (2), 535-550 (2000).

309. T. K. Stanton, "On acoustic scattering by a shell-covered seafloor," J. Acoust. Soc. Am. <u>108</u> (2), 551-555 (2000).

310. W. J. Wiscombe, "Improved Mie scattering algorithms," Applied Optics <u>19</u> (9), 1505-1509 (1980).

311. G. C. Gerace and E. K. Smith, "A comparison of cloud models," IEEE Antennas and Propagation Magazine <u>32</u> (5), 32-38 (October 1990).

312. P. Yang and K. N. Liou, "Geometric-optics-integral-equation method for light scattering by nonpsherical ice crystals," Applied Optics <u>35</u> (33), 6568-6584 (1996).

313. K. Sassen, "Lidar backscatter depolarization technique for cloud and aerosol research," in <u>Light Scattering by Nonspherical Particles</u>, edited by M. I. Mishchenko, J. W. Hovenier, and L. D. Travis (Academic Press, San Diego, CA, 2000), pp. 393-416.

314. K. N. Liou, Y. Takano, and P. Yang, "Light scattering and radiative transfer in ice crystal clouds: Applications to climate research," in <u>Light Scattering by Nonspherical Particles</u>, edited by M. I. Mishchenko, J. W. Hovenier, and L. D. Travis (Academic Press, San Diego, CA, 2000), pp. 417-449.

315. K. Aydin, "Centimeter and millimeter wave scattering from nonspherical hydrometeors," in <u>Light Scattering by Nonspherical Particles</u>, edited by M. I. Mishchenko, J. W. Hovenier, and L. D. Travis (Academic Press, San Diego, CA, 2000), pp. 451-479.

316. J. L. Haferman, "Microwave scattering by precipitation," in <u>Light Scattering by Nonspherical Particles</u>, edited by M. I. Mishchenko, J. W. Hovenier, and L. D. Travis (Academic Press, San Diego, CA, 2000), pp. 481-524.

317. D. R. Huffman, "Interstellar grains: The interaction of light with a small-particle system," Adv. Phys. <u>26</u>, 129-230 (1977).

318. C. Rogers and P. G. Martin, "On the shape of interstellar grains," Astrophys. J. <u>228</u> (2, pt.1), 450-464 (1979).

319. C. B. Vaidya and H. C. Bhatt and J. N. Desai, "Interstellar extinction and polarization by spheroidal dust grains," Astrophys. Space Sci. <u>104</u> (2), 323-336 (1984).

320. M. I. Mischenko, "Extinction of light by randomly-oriented non-spherical grains," Astrophys. Space Sci. <u>164</u> (1), 1-13 (1990).

321. M. Matsumura and M. Seki, "Light scattering calculations by the Fredholm integral equation method," Astrophys. Space Sci. <u>176</u> (2), 283-295 (1991).

322. N. V. Voshchinnikov and V. G. Farafonov, "Optical properties of spheroidal particles," Astrophys. Space Sci. <u>204</u> (1), 19-86 (1993).

323. M. I. Mischenko, "On the nature of the polarization opposition effect exhibited vy Saturn's rings," Astrophys. J. <u>411</u>, 351-361 (1993).

324. S. J. Ostro, "Planetary radar astronomy," Rev. Mod. Phys. <u>65</u> (4), 1235-1279 (1993).

325. K. Lumme, "Scattering properties of interplanetary dust particles," in <u>Light Scattering by Nonspherical Particles</u>, edited by M. I. Mishchenko, J. W. Hovenier, and L. D. Travis (Academic Press, San Diego, CA, 2000), pp. 555-583.

326. N. Makris, "Probing for an ocean on Jupiter's moon Europa with natural sound sources," Echoes <u>11</u> (3), 1-3 (2001).

327. C. J. Braak, J. F. de Haan, J. W. Hovenier, and L. D. Travis, "Spatial and temporal variations of Venus haze properties obtained from Pioneer Venus Orbiter polarimetry," Journal of Geophysical Research <u>107</u> (E5), 10.1029/2001JE001502 (2002).

328. R. P. Graham, I. L. Davis, L. H. Pearson, J. W. Sinclair, and R. S. Hyde, *Service Life Prediction Technology Interim Technical Report*, Report No. AFRL-PR-ED-TR-2000-0021, Air Force Research Laboratory, Edwards Air Force Base, CA, January 2001.

329. R. P. Graham, I. L. Davis, T. E. Doyle, J. W. Sinclair, and R. S. Hyde, *Service Life Prediction Technology Interim Technical Report*, Report No. AFRL-PR-ED-TR-2001-0016, Air Force Research Laboratory, Edwards Air Force Base, CA, September 2001.

330. A. B. Davis, R. F. Cahalan, S. P. Love, J. D. Spinhirne, and M. McGill, "Off-Beam Lidar: An Emerging Technique in Cloud Remote Sensing Based on Radiative Green-Function Theory in the Diffusion Domain," Phys. Chem. Earth (B) <u>24</u>, 757-765 (1999).

331. N. D. Aparicio and A. C. F. Cocks, "On the representation of random packings of spheres for sintering simulations," Acta Metall. Mater. <u>43</u> (10), 3873-3884 (1995).

332. T. Aste, "Circle, sphere, and drop packings," Phys. Rev. E <u>53</u> (3), 2571-2579 (1996).

333. A. Yang, C. T. Miller, and L. D. Turcoliver, "Simulation of correlated and uncorrelated packing of random size spheres," Phys. Rev. E 53 (2), 1516-1524 (1996).

334. A. A. Gusev, "Representative volume element size for elastic composites: A numerical study," J. Mech. Phys. Solids 45 (9), 1449-1459 (1997).

335. S. Torquato, "Mean nearest-neighbor distance in random packings of hard D-dimensional spheres," Phys. Rev. Lett. 74 (12), 2156-2159 (1995).

336. M. D. Rintoul and S. Torquato, "Algorithm to compute void statistics for random arrays of disks," Phys. Rev. E 52 (3), 2635-2643 (1995).

337. J. Quintanilla and S. Torquato, "Microstructure functions for a model of statistically inhomogeneous random media," Phys. Rev. E 55 (2), 1558-1565 (1997).

338. S. Torquato, "Exact conditions on physically realizable correlation functions of random media," J. Chem. Phys. 111 (19), 8832-8837 (1999).

339. S. Torquato, T. M. Truskett, and P. G. Debenedetti, "Is random close packing of spheres well defined?," Phys. Rev. Lett. 84 (10), 2064-2067 (2000).

340. I. L. Davis, "Particle pack influence on highly filled material properties," Current Opinion in Solid State and Materials Science 4, 505-513 (1999).

341. I. L. Davis and R. G. Carter, "Random particle packing by reduced dimension algorithms," J. Appl. Phys. 67 (2), 1022-1029 (1990).

342. C. L. Y. Yeong and S. Torquato, "Reconstructing random media," Phys. Rev. E 57 (1), 495-506 (1998).

343. C. L. Y. Yeong and S. Torquato, "Reconstructing random media. II. Three-dimensional media from two-dimensional cuts," Phys. Rev. E 58 (1), 224-233 (1998).

344. S. Torquato, "Modeling of physical properties of composite materials," Int. J. Solids Structures 37, 411-422 (2000).

345. M. I. Mishchenko, W. J. Warren, J. W. Hovenier, and L. D. Travis, "Overview of scattering by nonspherical particles," in Light Scattering by Nonspherical Particles, edited by M. I. Mishchenko, J. W. Hovenier, and L. D. Travis (Academic Press, San Diego, CA, 2000), pp. 29-60.

346. J. A. Stratton, P. M. Morse, L. J. Chu, and R. A. Hutner, Elliptic, Cylinder, and Spheroidal Wave Functions, (John Wiley and Sons, Inc., New York, 1941).

347. J. A. Stratton, P. M. Morse, L. J. Chu, J. D. C. Little, and F. J. Corbató, Spheroidal Wave Functions, (John Wiley and Sons, Inc., New York, 1956).

348. Carson Flammer, Spheroidal Wave Functions, (Stanford University Press, Stanford, California, 1957).

349. Le-Wei Li, Xiao-Kang Kang, and Mook-Seng Leong, Spheroidal Wave Functions in Electromagnetic Theory, (Wiley, New York, 2002).

350. L. J. Chu and J. A. Stratton, "Steady-State Solutions of Electromagnetic Field Problems. III. Forced Oscillations of a Prolate Spheroid," J. Appl. Phys. 12, 241-248 (1941).

351. S. Asano and G. Yamamoto, "Light Scattering by a Spheroidal Particle," Appl. Opt. 14 (1), 29-49 (1975).

352. S. Asano and G. Yamamoto, "Light Scattering Properties of Spheroidal Particles," Appl. Opt. 18 (5), 712-723 (1979).

353. T. J. Herbert, "Alternating electric field light scattering from spheroidal macromolecules," Journal of Colloid and Interface Science 69 (1), 122-127 (1979).

354. G. H. Meeten, "Refractive index of colloidal dispersions of spheroidal particles," Journal of Colloid and Interface Science 77 (1), 1-5 (1980).

355. A. R. Holt, "Electromagnetic wave scattering by spheroids: A comparison of experimental and theoretical results," IEEE Transactions on Antennas and Propagation AP-30 (4), 758-760 (1982).

356. I. R. Ciric and F. R. Cooray, "Separation of variables for electromagnetic scattering by spheroidal particles," in Light Scattering by Nonspherical Particles, edited by M. I. Mishchenko, J. W. Hovenier, and L. D. Travis (Academic Press, San Diego, CA, 2000), pp. 89-130.

357. Y. Han and Z. Wu, "Absorption and scattering by an oblate particle," J. Opt. A: Pure Appl. Opt. 4, 74-77 (2002).

358. A. F. Stevenson, "Light scattering by spheroidal particles oriented by streaming," J. Chem. Phys. 49 (10), 4545-4550 (1968).

359. W. Heller and M. Nakagaki, "Light scattering of spheroids. I. Extension of the Rayleigh-Gans-Stevenson functions and their application for molecular weight and shape determinations at theta = 90 degrees," J. Chem. Phys. 60 (10), 3889-3895 (1974).

360. M. Nakagaki and W. Heller, "Light scattering of spheroids. II. Angular dispersion and dissymetry of light scattering," J. Chem. Phys. 61 (8), 3297-3303 (1974).

361. W. Heller and M. Nakagaki, "Light scattering of spheroids. III. Depolarisation of the scattered light," J. Chem. Phys. 61 (9), 3619-3625 (1974).

362. D.-S. Wang and P. W. Barber, "Scattering by inhomogeneous nonspherical objects," Applied Optics 18 (8), 1190-1197 (1979).

363. P. Latimer, "Predicted scattering by spheroids: Comparison of approximate and exact methods," Applied Optics 19 (18), 3039-3041 (1980).

364. S. Asano and M. Sato, "Light scattering by randomly oriented spheroidal particles," Applied Optics 19 (6), 962-974 (1980).

365. D. W. Schuerman, R. T. Wang, B. A. S. Gustafson, and R. W. Schaefer, "Systematic studies of light scattering. I. Particle shape," Applied Optics 20 (23), 4039-4050 (1981).

366. J.-C. Ravey and P. Mazeron, "Light scattering in the physical optics approximation: Application to large spheroids," J. Opt. 13 (5), 273-282 (1982).

367. J.-C. Ravey and P. Mazeron, "Light scattering by large spheroids in the physical optics approximation: Numerical comparison with other approximate and exact results," J. Opt. 14 (1), 29-41 (1983).

368. S. Asano, "Light scattering by horizontally oriented spheroidal particles," Applied Optics 22 (9), 1390-1396 (1983).

369. K. N. Liou, Q. Cai, P. W. Barber, and S. C. Hill, "Scattering phase matrix comparison for randomly hexagonal cylinders and spheroids," Applied Optics 22 (11), 1684-1687 (1983).

370. M. F. Iskander and A. Lakhtakia, "Extension of the iterative EBCM to calculate scattering by low-loss or lossless elongated dielectric objects," Applied Optics 23 (6), 948-953 (1984).

371. G. R. Fournier and B. T. N. Evans, "Approximation to extinction efficiency for randomly oriented spheroids," Applied Optics 30 (15), 2041-2048 (1991).

372. M. I. Mishchenko, "Light scattering by randomly oriented axially axially symmetric particles," J. Opt. Soc. Am. A, Opt. Image Sci. 8 (6), 871-882 (1991).

373. W. Vargas, L. Cruz, L. F. Fonseca, and M. Gomez, "T-matrix approach for calculating local fields around clusters of rotated spheroids," Applied Optics 32 (12), 2164-2170 (1993).

374. M. I. Mishchenko, "Light scattering by size-shape distributions of randomly oriented axially symmetric particles of a size comparable to a wavelength," Applied Optics 32 (24), 4652-4666 (1993).

375. M. I. Mishchenko and L. D. Travis, "Light scattering by polydispersions of randomly oriented spheroids with sizes comparable to wavelengths of observation," Applied Optics 33 (30), 7206-7225 (1994).

376. M. I. Mishchenko and L. D. Travis, "T-matrix computations of light scattering by large spheroidal particles," Opt. Commun. 109 (1-2), 16-21 (1994).

377. B. T. N. Evans and G. R. Fournier, "Analytic approximation to randomly oriented spheroid extinction," Applied Optics 33 (24), 5796-5804 (1994).

378. Z.-F. Xing and J. M. Greenberg, "Efficient method for the calculation of mean extinction. II. Analyticity of the complex extinction efficiency of homogeneous spheroids and finite cylinders," Applied Optics 33 (24), 5783-5795 (1994).

379. B. P. Sinha and R. H. MacPhie, "Electromagnetic scattering by prolate spheroids for plane waves with arbitrary polarization and angle of incidence," Radio Science 12, 171-184 (1977).

380. B. P. Sinha and R. H. MacPhie, "Electromagnetic plane wave scattering by a system of two parallel conducting prolate spheroids," IEEE Trans. Antennas Propag. AP-31, 294-304 (1983).

381. J. Dalmus and R. Deleuil, "Multiple scattering of electromagnetic waves from two infinitely conducting prolate spheroids which are centered in a plane perpendicular to their axes of revolution," Radio Science 20, 575-581 (1985).

382. J. Dalmus and R. Deleuil, "Translational addition theorems for prolate spheroidal vector wavefunctions M' and N'," Q. Appl. Math. 44, 213-222 (1986).

383. R. H. MacPhie, J. Dalmus, and R. Deleuil, "Rotational-translational addition theorems for scalar spheroidal wave functions," Q. Appl. Math. 44, 737-749 (1987).

384. B. L. Merchant, P. J. Moser, A. Nagl, and H. Uberall, "Complex pole patterns of the scattering amplitude for conducting spheroids and finite-length cylinders," IEEE Trans. Antennas Propag., AP-36, 1769-1777 (1988).

385. M. F. R. Cooray and I. R. Ciric, "Electromagnetic wave scattering by a system of two spheroids of arbitrary orientation," IEEE Trans. Antennas Propag., AP-37, 608-618 (1989).

386. M. F. R. Cooray and I. R. Ciric, "Scattering of electromagnetic waves by a system of two dielectric spheroids of arbitrary orientation," IEEE Trans. Antennas Propag., AP-39, 680-684 (1991).

387. S. Nag and B. P. Sinha, "Electromagnetic plane wave scattering by a system of two uniformly lossy dielectric prolate spheroids in arbitrary orientation," IEEE Trans. Antennas Propag., AP-43, 322-327 (1995).

388. R. D. Spence and Sara Granger, "The Scattering of Sound from a Prolate Spheroid," J. Acous. Soc. Am. 23 (6), 701-706 (1951).

389. Alexander Silbiger, "Scattering of Sound by an Elastic Prolate Spheroid," J. Acous. Soc. Am. 35 (4), 564-570 (1963).

390. G. C. Kokkorakis and J. A. Roumeliotis, "Acoustic Eigenfrequencies in Concentric Spheroidal-Spherical Cavities," J. Sound Vib. 206 (3), 287-308 (1997).

391. G. C. Kokkorakis and J. A. Roumeliotis, "Acoustic Eigenfrequencies in Concentric Spheroidal-Spherical Cavities: Calculation by Shape Perturbation," J. Sound Vib. 212 (2), 337-355 (1998).

392. G. C. Kokkorakis and J. A. Roumeliotis, "Acoustic eigenfrequencies in a spheroidal cavity with a concentric penetrable sphere," J. Acous. Soc. Am. 105 (3), 1539-1547 (1999).

393. J. P. Barton, N. L. Wolff, H. Zhang, and C. Tarawneh, "Near-field calculations for a rigid spheroid with an arbitrary incident acoustic field," J. Acous. Soc. Am. 113 (3), 1216-1222 (2003).

394. E. G. Lawrence, "Diffraction of Elastic Waves by a Rigid Inclusion," Quart. J. Mech. Appl. Math. 23 (3), 389-397 (1970).

395. E. G. Lawrence, "Diffraction of Elastic Waves by a Rigid Ellipsoid," Quart. Journ. Mech. And Applied Math. 25 (2), 161-172 (1972).

396. F. M. Arscott, P. J. Taylor, and R. V. M. Zahar, "On the Numerical Construction of Ellipsoidal Wave Functions," Mathematics of Computation 40 (161), 367-380 (1983).

397. T. Levitina and E. J. Brändas, "Scattering by a Potential Separable in Ellipsoidal Coordinates," Int. J. Quant. Chem. 65, 601-608 (1997).

398. T. Levitina and E. J. Brändas, "Perturbed Ellipsoidal Wave Functions for Quantum Scattering," Int. J. Quant. Chem. 70, 1017-1022 (1998).

399. A. V. Goncharenko, Y. G. Semenov, and E. F. Venger, "Effective scattering cross section of an assembly of small ellipsoidal particles," J. Opt. Soc. Am. A 16 (3), 517-522 (1999).

400. G. Dassios and F. Kariotou, "Magnetoencephalography in ellipsoidal geometry," Journal of Mathematical Physics 44 (1), 220-241 (2003).

401. C. Yeh, Perturbation Approach to the /diffraction of Electromagnetic Waves by Arbitrarily Shaped Dielectric Obstacles," Phys. Rev. 135 (5A), A1193-A1201 (1964).

402. V. A. Erma, "Exact Solution for the Scattering of Electromagnetic Waves from Conductors of Arbitrary Shape. I. Case of Cylindrical Symmetry," Phys. Rev. 173 (5), 1243-1257 (1968).

403. V. A. Erma, "Exact Solution for the Scattering of Electromagnetic Waves from Conductors of Arbitrary Shape. II. General Case," Phys. Rev. 176 (5), 1544-1553 (1968).

404. V. A. Erma, "Exact Solution for the Scattering of Electromagnetic Waves from Conductors of Arbitrary Shape. II. Obstacles with Arbitrary Electromagnetic Properties," Phys. Rev. 179 (5), 1238-1246 (1969).

405. M. Tran Van Nhieu, "A singular perturbation problem: Scattering by a slender body," J. Acoust. Soc. Am. 83 (1), 68-73 (1988).

406. K.-U. Machens, "On radiation from elliptic-cylinder geometries," Acustica 85, 449-463 (1999).

407. F. M. Schulz, K. Stamnes, and J. J. Stamnes, "Point-group symmetries in electromagnetic scattering," J. Opt. Soc. Am. A 16 (4), 853-865 (1999).

408. K. Muinonen, "Light scattering by stochastically shaped particles," in Light Scattering by Nonspherical Particles, edited by M. I. Mishchenko, J. W. Hovenier, and L. D. Travis (Academic Press, San Diego, CA, 2000), pp. 323-352.

409. P. L. Marston, "Generalized optical theorem for scatterers having inversion symmetry: Applications to acoustic backscattering," J. Acoust. Soc. Am. 109 (4), 1291-1295 (2001).

410. F. M. Kahnert, J. J. Stamnes, and K. Stamnes, "Can simple particle shapes be used to model scalar optical properties of an ensemble of wavelength-sized particles with complex shapes?" J. Opt. Soc. Am. A 19 (3), 521-531 (2002).

411. V. K. Varadan, V. V. Varadan, and Y.-H. Pao, "Multiple scattering of elastic waves by cylinders of arbitrary cross section. I. SH waves," J. Acoust. Soc. Am. 63 (5), 1310-1319 (1978).

412. R.-B. Yang and A. K. Mal, "Multiple scattering of elastic waves in a fiber-reinforced composite," J. Mech. Phys. Solids, 42 (12), 1945-1968 (1994).

413. L.-W. Cai and J. H. Williams, Jr., "Large-scale multiple scattering problems," Ultrasonics 37, 453-462 (1999).

414. L.-W. Cai and J. H. Williams, Jr., "Full-scale simulations of elastic wave scattering in fiber-reinforced composites," Ultrasonics 37, 463-482 (1999).

415. L.-W. Cai and J. H. Williams, Jr., "NDE via stop band formation in fiber reinforced composites having square fiber arrangement," Ultrasonics 37, 483-492 (1999).

416. A. Y. Perelman, "Scattering in spherically symmetric media," Applied Optics 18 (13), 2307-2314 (1979).

417. O. B. Toon and T. P. Ackerman, "Algorithms for the calculation of scattering by stratified spheres," Applied Optics 20 (20), 3657-3660 (1981).

418. S. R. Aragon S. and M. Elwenspoek, "Mie scattering from thin spherical bubbles," J. Chem. Phys. 77 (7), 3406-3413 (1982).

419. R. Bhandari, "Scattering coefficients for a multilayered sphere: analytic expressions and algorithms," Applied Optics 24 (13), 1960-1967 (1985).

420. R. L. Hightower and C. B. Richardson, "Resonant Mie scattering from a layered sphere," Applied Optics 27 (23), 4850-4855 (1988).

421. D. K. Cohoon, "An exact solution of Mie type for scattering by a multilayer anisotropic sphere," J. Electromagn. Waves Appl. 3 (5), 421-448 (1989).

422. J. Baldauf, S. W. Lee, H. Ling, and R. Chou, "On physical optics for calculating scattering from coated bodies," J. Electromagn. Waves Appl. 3 (8), 725-746 (1989).

423. D. W. Mackowski, R. A. Altenkirch, and M. P. Menguc, "Internal absorption cross sections in a stratified sphere," Applied Optics 29 (10), 1551-1559 (1990).

424. Z. S. Wu and Y. P. Wang, "Electromagnetic scattering for multilayered sphere: Recursive algorithms," Radio Science 26 (6), 1393-1401 (1991).

425. A.-K. Hamid, I. R. Ciric, and M. Hamid, "Analytic solution of the scattering by two multilayered dielectric spheres," Can. J. Phys. 70 (9), 696-705 (1992).

426. T. Kaiser and G. Schweiger, "Stable algorithm for the computation of Mie coefficients for scattered and transmitted fields of a coated sphere," Computers in Physics 7 (6), 682-686 (1993).

427. T. Kaiser, S. Lange, and G. Schweiger, "Structural resonances in a coated sphere: Investigation of the volume-averaged source function and resonance positions," Applied Optics 33 (33), 7789-7797 (1994).

428. J. Sinzig and M. Quinten, "Scattering and absorptionby spherical multilayer particles," Appl. Phys. A Solids Surf. A58 (2), 157-162 (1994).

429. B. R. Johnson, "Exact theory of electromagnetic scattering by a heterogeneous multilayer sphere in the infinite-layer limit: effective-media approach," J. Opt. Soc. Am. A 16 (4), 845-852 (1999).

430. R. T. Wang and J. M. Greenberg, "Scattering by spheres with nonisotropic refractive indices," Applied Optics 15 (5), 1212-1217 (1976).

431. P. Chýlek, G. Videen, D. J. W. Geldart, J. S. Dobbie, and H. C. W. Tso, "Effective medium approaches for heterogeneous particles," in Light Scattering by Nonspherical Particles, edited by M. I. Mishchenko, J. W. Hovenier, and L. D. Travis (Academic Press, San Diego, CA, 2000), pp. 273-308.

432. A. Macke, "Monte Carlo calculations of light scattering by large particles with multiple internal inclusions," in Light Scattering by Nonspherical Particles, edited by M. I. Mishchenko, J. W. Hovenier, and L. D. Travis (Academic Press, San Diego, CA, 2000), pp. 309-322.

433. J. A. Fawcett, "Scattering from a partially fluid-filled, elastic-shelled sphere," J. Acoust. Soc. Am. 109 (2), 508-513 (2001).

434. D. D. Smith and K. A. Fuller, "Photonic bandgaps in Mie scattering by concentrically stratified spheres," J. Opt. Soc. Am. B 19 (10), 2449-2455 (2002).

435. R. C. Gauthier, "Laser-trapping properties of dual-component spheres," Applied Optics 41 (33), 7135-7144 (2002).

436. J. C. Maxwell, A Treatise on Electricity and Magnetism, (Clarendon, London, 1873; Dover, New York, 1954).

437. R. S. Rayleigh, Phil. Mag. 34, 481-502 (1892).

438. R. C. McPhedran and D. R. McKenzie, "The Conductivity of Lattices of Spheres, I. The Simple Cubic Lattice," Proc. R. Soc. Lond., A. 359, 45-63 (1978).

439. A. P. Roberts and M. A. Knackstedt, "Structure-property correlations in model composite materials," Phys. Rev. E 54 (3), 2313-2328 (1996).

440. H. Cheng and S. Torquato, "Effective Conductivity of Periodic Arrays of Spheres with Interfacial Resistance," Proc. R. Soc. Lond., A. 453, 145-161 (1997).

441. V. I. Kushch, "Conductivity of a Periodic Particle Composite with Transversely Isotropic Phases," Proc. R. Soc. Lond., A. 453, 65-76 (1997).

442. S. Torquato, I. C. Kim, and D. Cule, "Effective conductivity, dielectric constant, and diffusion coefficient of digitized composite media via first-passage-time equations," J. Appl. Phys. 85 (3), 1560-1571 (1999).

443. I. L. Davis, "Electric Field in an Arbitrary Random Pack of Spherical Particles," J. Appl. Phys. 67 (2), 955-964 (1990).

444. L. Fu and L. Resca, "Electrical response of heterogeneous systems containing inclusions with permanent multipoles," Phys. Rev. B 50 (21), 15719-15732 (1994).

445. L. Fu and L. Resca, "Electrical response of heterogeneous systems and Debye's problem," Phys. Rev. B 50 (21), 15733-15738 (1994).

446. D. Cule and S. Torquato, "Electric-field distribution in composite media," Phys. Rev. B 58 (18), R11829-R11832 (1998).

447. I. L. Davis, R. L. Hatch, M. Yener, and K. Chompooming, "Elastic fields in a random pack of rigid bonded spheres," Phys. Rev. B 47 (5), 2530-2545 (1993).

448. W. M. Suen, S. P. Wong, and K. Young, "The Lattice Model of Heat Conduction in a Composite Material," J. Phys. D: Appl. Phys. 12, 1325-1338 (1979).

449. A. S. Sangani and C. Yao, "Bulk Thermal Conductivity of Composites with Spherical Inclusions," J. Appl. Phys. 63 (5), 1334-1341 (1988).

450. W. Friederich, "Inferring the orientation-distribution function from observed seismic anisotropy: General considerations and an inversion of surface-wave dispersion curves," Pure Appl. Geophys. 151, 649-667 (1998).

451. F. J. Zerilli, "Tensor harmonics in canonical form for gravitational radiation and other applications," J. Math. Phys. 11 (7), 2203-2208 (1970).

452. G. A. Prodi, "Acoustic detectors of gravitational radiation," Rivelatori Acustici di Onde Gravitazionali – XI Giornate di Studio Sui Rivelatori, Torino, Italy, 2001.

CURRICULUM VITAE

Timothy Edwin Doyle
(August 2003)

CAREER OBJECTIVE

A research faculty position at a university, emphasizing research in the development and application of computational and theoretical models for complex media, including advanced materials (composites, amorphous solids, *etc.*) nanostructured matter (photonic crystals, quantum dots, *etc.*), living systems (biophysics), and geophysical media (solid earth, ocean, and atmosphere).

EDUCATION

B.S. in Physics, Utah State University, Logan, Utah (1982) GPA: 3.81 (4.0 = A)
M.S. in Physics, Utah State University, Logan, Utah (1992) GPA: 3.77 (4.0 = A)
Ph.D. in Physics, Utah State University, Logan, Utah (2004) GPA: 4.00 (4.0 = A)

RESEARCH EXPERIENCE

<u>Senior Research Scientist</u>, Physics Department, Utah State University (2003-present)
- Research emphasis: Computational modeling of wave propagation in complex media

<u>Principal Scientist</u>, NDE Research and Analysis Section, R&D Laboratories, ATK-Thiokol Propulsion (1991-2002)
- Principal investigator for US Air Force and US Navy solid rocket motor aging programs
- R&D of nondestructive evaluation methods for solid rocket motors. Research emphasis:
  - Spectroscopic and ultrasonic methods for health monitoring
  - Computational models for scattering in particulate media
  - Ultrasonic tomography and other imaging methods

<u>Research Assistant</u>, Physics Department, Utah State University (1990-1991)
- Modeling of microscopic electric fields in solid rocket propellants for Thiokol Corporation

<u>Research Assistant</u>, Center for Atmospheric and Space Sciences, Utah State University (1988-1989)
- Feasibility study of the application of imaging Doppler interferometry to medical ultrasonography

<u>Scientist</u>, Applied Physics, Chemical Sciences, and Materials Sciences Divisions, EG&G Idaho, Inc., Idaho National Engineering Laboratory (1981-1988)
- Microstructural characterization of metals, ceramics, and glasses with the use of scanning transmission electron microscopy
- Development of Raman and luminescence microanalysis methods for characterization of debris from nuclear accidents
- Collection and analysis of seismological data for eastern Idaho

TEACHING EXPERIENCE

<u>Teaching Assistant</u>, Utah State University, Physics Department
- Instruction, grading, and testing for 2nd year general physics course (1988)
- Instruction, grading, and testing for 1st year general physics course (1981)

PUBLICATIONS

Dissertation and Thesis

1. T. E. Doyle, <u>Computational Scattering Models for Elastic and Electromagnetic Waves in Particulate Media</u>, (Ph.D. Dissertation, Utah State University, Logan, Utah, 2003).

2. T. E. Doyle, <u>An Embedded Ring Approach to the Vibrational Dynamics of Disordered Two-Dimensional Materials</u>, (M.S. Thesis, Utah State University, Logan, Utah, 1992).

Articles

1. J. R. Dennison, T. E. Doyle, "An Embedded Ring Approach to the Vibrational Dynamics of Low-Dimensional Amorphous Solids with Applications to Graphitic Carbon Materials," Carbon <u>35</u> (10-11), 1465-1477 (1997).

2. T. E. Doyle, "Using Acoustic Waveguides to Probe Materials Ultrasonically," NASA Tech Briefs <u>20</u> (9), 66 (1996).

3. T. E. Doyle, J. R. Dennison, "Vibrational Dynamics and Structure of Graphitic Amorphous Carbon Modeled using an Embedded Ring Approach," Phys. Rev. B <u>51</u> (1), 196-200 (1995).

4. D. N. Coon, T. E. Doyle, J. R. Weidner, "Refractive Indices of Glasses in the Y-Al-Si-O-N System," Journal of Non-Crystalline Solids <u>108</u>, 180-186 (1989).

5. R. N. Wright, T. E. Doyle, J. E. Flinn, G. E. Korth, "Microstructure and Bonding of Dynamically Consolidated Al and Al-1.4Co Powders," Materials Science and Engineering <u>94</u>, 428-429 (1987).

6. J. J. King, T. E. Doyle, S. M. Jackson, "Seismicity of the Eastern Snake River Plain Region, Idaho, Prior to the Borah Peak, Idaho, Earthquake: October 1972-October 1983," Bulletin of the Seismological Society of America <u>77</u> (3), 809-818 (1987).

Conference Papers

1. T. E. Doyle, "Ultrasonic Tomography of Multilayer Structures of High Contrast Materials," in <u>Review of Progress in Quantitative Nondestructive Evaluation, Vol. 20A</u>, (American Institute of Physics, Melville, New York, 2001), pp. 687-694.

2. T. E. Doyle, A. D. Degtyar, K. P. Sorensen, M. J. Kelso, T. A. Berger, "Ultrasonic Method for Inspection of the Propellant Grain in the Space Shuttle Solid Rocket Booster," in <u>Review of Progress in Quantitative Nondestructive Evaluation, Vol. 19B</u>, (American Institute of Physics, Melville, New York, 2000), pp. 1833-1840.

3. T. E. Doyle, L. G. Porter, L. H. Pearson, D. G. Gill, "Ultrasonic Reflection Tomography of Inhomogeneous Materials," in <u>Review of Progress in Quantitative Nondestructive Evaluation, Vol. 18A</u>, (Plenum Press, New York, 1999), pp. 959-966.

4. T. E. Doyle, "Ultrasonic Reflection Tomography of Low Density Inclusions in Solid Rocket Propellant," 1998 JANNAF Non-Destructive Evaluation Subcommittee Meeting, 16-20 March 1998, Salt Lake City, Utah.

5. L. H. Pearson, T. E. Doyle, R. S. Hamilton, I. L. Davis, "The Role of NDE in Service Life Prediction of Solid Rocket Propellant," 87th Symposium of the Propulsion and Energetics Panel on Service Life of Solid Propellant Systems, NATO Advisory Group for Aerospace Research and Development (NATO-AGARD), 6-10 May 1996, Athens, Greece.

6. T. E. Doyle, "Acoustic Waveguide Probe for Aging Surveillance of Solid Propellants and Liners," 1995 JANNAF Non-Destructive Evaluation Subcommittee Meeting, 4-8 December 1995, Tampa, Florida.

7. J. R. Dennison, T. E. Doyle, "Vibrational Dynamics and Structure of Carbon Materials Determined using an Embedded Ring Approach," Bulletin of the American Physical Society 40 (1), 751 (1995).

8. T. E. Doyle, L. H. Pearson, "Application of Ultrasonic Damage Evaluation Testing to Aging in Minuteman Propellants," 1994 JANNAF Structures & Mechanical Behavior Subcommittee Meeting, 24-28 October 1994, Hill Air Force Base, Ogden, Utah.

9. L. H. Pearson, T. E. Doyle, R. S. Hamilton, "Ultrasonic Method for in-situ Monitoring of Filled Polymeric Materials during Tensile Loading," 1994 JANNAF Structures & Mechanical Behavior Subcommittee Meeting, 24-28 October 1994, Hill Air Force Base, Ogden, Utah.

10. T. E. Doyle, L. H. Pearson, "Embedded Health Sensor Characterization of Solid Propellant Aging," 1994 JANNAF Propellant Development and Characterization Subcommittee Meeting, 13-15 April 1994, NASA Kennedy Space Center, Kennedy Space Center, Florida.

11. T. E. Doyle, J. R. Dennison, "An Embedded Ring Approach to the Vibrational Dynamics of Disordered Two-dimensional Materials," Bulletin of the American Physical Society 37 (1), 289 (1992).

12. J. R. Dennison, T. E. Doyle, "Structure and Vibrational Dynamics of Amorphous Carbon Modeled with the Embedded Ring Approach," Bulletin of the American Physical Society 37 (1), 289 (1992).

13. J. C. Debsikdar, T. E. Doyle, R. M. Neilson, Jr., "Microstructure Development in Oxynitride Glass Interlayers During Joining of Silicon Nitride Ceramics," 1988 Annual Meeting of the American Ceramic Society.

14. J. E. Flinn, T. E. Doyle, "Structure/Properties of Extrusion Consolidated Fe-16Ni-9Cr and Fe-16Ni-9Cr-5Mo-2Cu Powders Containing Entrapped Argon," The Metallurgical Society Annual Meeting, Phoenix, Arizona, January 25-28, 1988.

15. J. E. Flinn, T. E. Doyle, R. N. Wright, "The Influence of NbC on Annealing Behavior and Mechanical Properties of Wrought Fe-40Ni Alloys," Materials Week, Cincinnati, Ohio, October 10-15, 1987.

16. J. E. Flinn, G. E. Korth, T. E. Doyle, "Particle Interaction and Bonding for Dynamically Consolidated Fe-40Ni Powders," in Proceedings of the APS 1987 Topical Conference on Shock Waves in Condensed Matter, (Elsevier Science Publishers B.V., Amsterdam, 1987).

17. T. E. Doyle, R. N. Wright, J. E. Flinn, G. E. Korth, "Microstructures in Explosively Consolidated Rapidly Solidified Aluminum Powders," in Proceedings of the 44th Annual Meeting of the Electron Microscopy Society of America, (San Francisco Press, Inc., 1986), pp. 428-429.

18. T. E. Doyle, J. L. Alvarez, "Raman and Luminescence Spectroscopy of Zirconium Oxide with the use of the MOLE Microprobe," in Materials Science and Research, Vol. 19: Advances in Materials Characterization II, (Plenum Press, New York, 1985), pp. 155-165.

19. T. E. Doyle, J. L. Alvarez, "Microluminescence Spectra of Ti-Activated ZrO_2-Y_2O_3," in Microbeam Analysis—1985, (San Francisco Press, Inc., 1985), pp. 71-74.

20. J. L. Alvarez, T. E. Doyle, "Development of a Luminescence Microprobe," in Microbeam Analysis—1985, (San Francisco Press, Inc., 1985), pp. 65-67.

21. T. E. Doyle, J. L. Alvarez, "Microfluorescence Studies of Zirconium Oxide," in Microbeam Analysis—1984, (San Francisco Press, Inc., 1984), pp. 103-106.

22. K. Vinjamuri, D. J. Osetek, R. R. Hobbins, T. E. Doyle, "Characterization of Solid Debris Transported in the Coolant during the First Two Severe Fuel Damage Tests," American Nuclear Society Topical Meeting on Fission Product Behavior and Source Term Research, Snowbird, Utah, July 15-19, 1984.

23. T. E. Doyle, J. L. Alvarez, "Micro-Raman Analysis of Three Mile Island Samples," in Microbeam Analysis—1983, (San Francisco Press, Inc., 1983), pp. 277-279.

24. J. J. King, T. E. Doyle, "Seismicity of the Eastern Snake River Plain Region, Idaho (43.0°-44.5° N, 111.5°-114.0° W), October 1972-June 1982," Earthquake Notes 54 (1), 99 (1983).

25. T. E. Doyle, J. L. Alvarez, "Analysis of TMI-2 Samples Using the Molecular Optical Laser Examiner," Transactions of the American Nuclear Society 43, 16-17 (1982).

Reports

1. R. P. Graham, R. K. Kunz, D. Gutierrez-Lemini, I. L. Davis, L. H. Pearson, T. E. Doyle, J. W. Burns, and R. S. Hyde, *Service Life Prediction Technology Interim Technical Report #4*, Draft, Air Force Research Laboratory, Edwards Air Force Base, CA, February 2002.

2. R. P. Graham, I. L. Davis, T. E. Doyle, J. W. Sinclair, and R. S. Hyde, *Service Life Prediction Technology Interim Technical Report #3*, Report No. AFRL-PR-ED-TR-2001-0016, Air Force Research Laboratory, Edwards Air Force Base, CA, September 2001.

3. R. P. Graham, I. L. Davis, T. E. Doyle, J. W. Sinclair, and R. S. Hyde, *Service Life Prediction Technology Interim Technical Report #2*, Air Force Research Laboratory, Edwards Air Force Base, CA, July 2001.

4. T. E. Doyle, *Thiokol Report TR-12120: Consolidated Motor Aging Program (CMAP) Progress Report: Ultrasonic Testing of C4 and D5 Motors in 1999*, Thiokol Propulsion, Alcoa, May 2000.

5. T. E. Doyle, *Thiokol Report TR-12064: IR&D Final Report—CY99—NDE of Bonded Systems*, Thiokol Propulsion, Cordant Technologies, March 2000.

6. T. E. Doyle, *Thiokol Report TR-11651: Consolidated Motor Aging Program (CMAP) Progress Report: Ultrasonic Testing of C4 and D5 Motors in 1998*, Thiokol Propulsion, Cordant Technologies, April 1999.

7. T. E. Doyle, *Thiokol Report TR-11577: IR&D Final Report—FY98—NDE Detection of Defects in Bonded Elastomeric Materials*, Thiokol Propulsion, Cordant Technologies, December 1998.

8. T. E. Doyle, D. G. Gill, B. W. Sermon, L. A. Martinez, *Thiokol Report TR-11208: Consolidated Motor Aging Program (CMAP) Progress Report: Ultrasonic Testing (UT) of Trident II (D5) Motors*, Thiokol Propulsion, October 1997.

9. T. E. Doyle, L. H. Pearson, B. A. Fairbourn, *Thiokol Report TR-11086: Ultrasonic Inspection of Castor 120® DM-2 Propellant Grain*, Thiokol Propulsion, April 1997.

10. T. E. Doyle, L. H. Pearson, W. J. Murri, R. N. Andersen, E. J. Vanderheiden, L. A. Martinez, B. W. Sermon, D. S. Gardiner, *Thiokol Report TR-11052: Bore-Side Ultrasonics for Aging Surveillance of C4 Third Stage Fleet Ballistic Motors*, Thiokol Propulsion, February 1997.

11. T. E. Doyle, M. C. Hawkins, K. C. Jensen, D. G. Shook, J. W. Sinclair, *Report No. PL-TR-95-3031: Life Assessment Technology Evaluation (LATE)*, Phillips Laboratory, Edwards Air Force Base, California, December 1996.

12. L. G. Porter, T. E. Doyle, L. H. Pearson, *Thiokol Report TR-10683: Ultrasonic Inspection of the RSRM 38A Aft Segment Inhibitor*, Thiokol Propulsion, June 1995.

13. T. E. Doyle, "Acoustic Waveguide Probe for Detecting Changes in the Shear Properties of Liners and Propellants" *NASA Solid Propulsion Integrity Program (SPIP) Bondline Work Package 4.0: Annual Report — 1993, Technical Papers*, Report No. 443/1293/39, March 11, 1994.

14. T. E. Doyle, "Acoustic Waveguide Probe for Detecting Changes in the Shear Properties of Liners and Propellants" *NASA Solid Propulsion Integrity Program (SPIP) Bondline Work Package 4.0: New Technology Report — Option Year 3 C December 1992-December 1993*, Report No. 4431/0194/05, January 26, 1994.

15. R. P. Graham, T. E. Doyle, R. S. Hamilton, K. L. Laheru, L. H. Pearson, A. S. Allen, *Report No. PL-TR-94: Extended Service Life Prediction — Final Report for Period November 1990 to January 1994*, Phillips Laboratory, Edwards Air Force Base, California, 1994.

16. R. P. Graham, K. L. Laheru, R. S. Hamilton, L. H. Pearson, T. E. Doyle, *Report No. PL-TR-93-3022: Extended Service Life Prediction — R&D Annual Report*, Phillips Laboratory, Edwards Air Force Base, California, September 1993.

17. T. E. Doyle, G. W. Adams, J. W. Brosnahan, *CASS Report #GR-12: Feasibility Study of the Application of Imaging Doppler Interferometry to Medical Ultrasonography*, Center for Atmospheric and Space Sciences, Utah State University, September 1989.

18. J. E. Flinn, R. N. Wright, G. E. Korth, M. D. Harper, T. E. Doyle, *U.S. Bureau of Mines Topical Report*, EG&G Idaho, Inc., 1986.

19. T. E. Doyle, J. L. Alvarez, *Raman and Luminescence Analyses for Severe Fuel Damage Tests SFD 1-3 and SFD 1-4*, EG&G Idaho, Inc., for the Nuclear Regulatory Commission, November 1986.

20. T. E. Doyle, J. L. Alvarez, V. A. Deason, *Raman and Luminescence Development for SFD 1-3 and SFD 1-4 Tests*, EG&G Idaho, Inc., for the Nuclear Regulatory Commission, March 1986.

21. T. E. Doyle, V. A. Deason, J. L. Alvarez, *Luminescence Detection of Cesium Iodide*, EG&G Idaho, Inc., September 1984.

22. C. S. Olsen, R. E. Mason, T. E. Doyle, R. R. Hobbins, *TMI Particle Characterization Determined from Filter Examinations--Draft*, EG&G Idaho, Inc., September 1984.

23. J. J. King, T. E. Doyle, *Earthquake Catalog for the Eastern Snake River Plain Region, Idaho (43.0°-44.5° N, 111.5°-114.0° W), October 1972-June 1982*, EG&G Idaho, Inc., December 1982.

24. J. J. King, T. E. Doyle, *Idaho National Engineering Laboratory Quarterly Seismic Report: July 1—September 30, 1982*, EG&G Idaho, Inc., October 1982.

25. T. E. Doyle, J. J. King, *Idaho National Engineering Laboratory Quarterly Seismic Report: April 1—June 30, 1982,* EG&G Idaho, Inc., July 1982.

26. T. E. Doyle, J. J. King, *Idaho National Engineering Laboratory Quarterly Seismic Report: January 1—March 31, 1982,* EG&G Idaho, Inc., April 1982.

27. T. E. Doyle, J. J. King, *Idaho National Engineering Laboratory Quarterly Seismic Report: October 1—December 31, 1981,* EG&G Idaho, Inc., January 1982.

28. J. J. King, T. E. Doyle, *Idaho National Engineering Laboratory Quarterly Seismic Report: July 1—September 30, 1981,* EG&G Idaho, Inc., October 1981.